LES AND HYBRID RANS/LES TURBULENCE MODELLING IN UNSTRUCTURED FINITE VOLUME CODE AND APPLICATIONS TO NUCLEAR REACTOR FUEL BUNDLES

A thesis submitted to the University of Manchester
for the degree of Doctor of Philosophy
in the Faculty of Engineering and Physical Sciences

2010

By
Stefano Rolfo
Mechanical, Aerospace and Civil Engineering

CONTENTS

Word count 37524

List of Tables

List of Figures

The University of Manchester

Stefano Rolfo
Doctor of Philosophy
LES and Hybrid RANS/LES Turbulence Modelling in unstructured Finite Volume Code and Applications to Nuclear Reactor Fuel Bundles
October 29, 2010

Rod bundle is a typical constitutive element of a very wide range of nuclear reactor designs. This thesis describes the investigation of such geometry with wall-resolved Large Eddy Simulation (LES). In order to alleviate the mesh constraint, imposed by the near wall resolution, the usage of embedded refinements and polyhedral meshes is analysed firstly with a inviscid laminar case (Taylor Green vortices) and secondly with a fully turbulent case (channel flow only with embedded refinement). The inviscid test case shows that the addition of embedded refinements decreases the conservation properties of the code. Indeed the accuracy decreases from second order in a structured conformal mesh, to something in between first and second order depending on the quality of the unstructured mesh. Better results are obtained when the interface between refined and coarse areas presents a more regular and structured pattern, reducing the generation of skewed and stretched cells. The channel flow simulation shows that the Reynolds stresses, of some embedded refined meshes, are affected by spurious oscillations. Surprisingly this effect is present in the unstructured meshes with the best orthogonal properties. Indeed analysis of Reynolds stress budgets shows that terms, where the gradient in the wall normal direction is dominant, have a largely oscillatory behaviour. The cause of the problem is attributed to the convective term and in particular in the method used for the gradient reconstruction.

As a consequence of these contradictory signs between the inviscid and the fully turbulent cases, the rod bundle test case is analysed using a conventional body fitted multiblock mesh. Two different Reynolds numbers are investigated reporting Reynolds stresses and budgets. The flow is characterised by an energetic and almost periodic azimuthal flow pulsation in the gap region between adjacent sub-channels, which makes turbulent quantities largely different from those in plane channel and pipes and enhances mixing. Experiments found that a constant Strouhal number, with the variation of the Reynolds number, characterises the phenomenon. The frequency analysis finds that present simulations are distinguished by three dominant frequencies, the first in agreement with the experimental value and two higher ones, which might be due to the correlation of the azimuthal velocity in the streamwise direction. Several passive temperature fields are added at the simulations in order to study the effects of the variation of the Prandtl number and the change in boundary conditions (Neumann and Dirichlet). A simplified case where an imbalance of the scalar between adjacent sub-channels is also investigated in order to evaluate the variation of the heat fluxes with respect to the homogeneous case.

An alternative solution, to reduce the mesh constraint imposed by the wall, is to hybridize LES with RANS. The main achievement of this work is to integrate the heat transfer modelling to the already existing model for the dynamic part. Further investigations of the blending function, used to merge the two velocity fields, are carried out in conjunction with a study of the model dependency on the mesh resolution. The validation is performed on a fully developed channel flow at different Reynolds numbers

and with constant wall heat flux. On coarse meshes the model shows an improvement of the results for both thermal and hydraulic parts with respect to a standard LES. On refined meshes, suitable for wall-resolved LES, the model suffers from a problem of double counting of modelled Reynolds stresses and heat fluxes because the RANS contribution does not naturally disappear as the mesh resolution increases.

DECLARATION

No portion of the work referred to in this thesis has been submitted in support of an application for another degree or qualification of this or any other university or other institution of learning.

COPYRIGHT

1. The author of this thesis (including any appendices and/or schedules to this thesis) owns certain copyright or related rights in it (the “Copyright”) and s/he has given The University of Manchester certain rights to use such Copyright, including for administrative purposes.

2. Copies of this thesis, either in full or in extracts and whether in hard or electronic copy, may be made **only** in accordance with the Copyright, Designs and Patents Act 1988 (as amended) and regulations issued under it or, where appropriate, in accordance with licensing agreements which the University has from time to time. This page must form part of any such copies made.

3. The ownership of certain Copyright, patents, designs, trade marks and other intellectual property (the “Intellectual Property”) and any reproductions of copyright works in the thesis, (for example graphs and tables the “Reproduction”), which may be described in this thesis, may not be owned by the author and may be owned by third parties. Such Intellectual Property and Reproductions cannot and must not be made available for use without the prior written permission of the owner(s) of the relevant Intellectual Property and/or Reproductions.

4. Further information on the conditions under which disclosure, publication and commercialisation of this thesis, the Copyright and any Intellectual Property and/or Reproductions described in it may take place is available in the University IP Policy (see http://www.campus.manchester.ac.uk/medialibrary/policies/intellectual-property.pdf), in any relevant Thesis restriction declarations deposited in the University Library, The University Library’s regulations (see http://www.manchester.ac.uk/library/aboutus/regulations) and in The University’s policy on presentation of Theses.

ACKNOWLEDGEMENTS

I am finally arrived at the end of this work and I would like to acknowledge all the people that help me during this time. First of all I would like to thanks my supervisor Prof D. Laurence: sometimes we had some different points of view, but his guidance and his patience with me were really appreciated. Many thanks to the UK Engineering and Physical Sciences Research Council for funding under grant EP/C549465/1 Keeping the Nuclear Option Open. I would like also to thanks all the KNOO team at the School of MACE: Dr M. Cotton, Dr. Y. Addad and Mr. A. Keshmiri. Thanks to the EDF R&D department in Chatou (Paris) for the grant for the investigation of SFR fuel bundle and for the usage of the BlueGene machine. In particular I would like to thanks Mr C. Peniguel and Dr F. Archambeau (EDF R&D). A very big thanks is going to Dr J.C. Uribe for the fundamental help with the Hybrid model and to solve all the issues related to *Code_Saturne*. I am very grateful to Dr. C. Moulinec and Dr A. Revell for the all advices about work, and not only, and for the corrections of this manuscript. Big thanks to all my housemates of these years in Manchester and in particular to Rui and Flavien with whom I have shared both office and home life; it was a pleasure to live with you. Thanks also to all others office mates and colleagues of these and to the Italian community in my department (Ruggero, Raffaello and Riccardo) Thanks to you Gisella for your encouragement and support. My last thought is going to my family back in Italy, to my mum, to my dad, to my sister, to my niece and to my brother-in-law.

Nomenclature

Capital Roman Symbols

C_D	Smagorinsky constant for the Germano's Dynamic Model.
C_s	Smagorinsky constant
D	Diameter
D/Dt	Substantial derivative $(\partial/\partial t + u_j\,\partial/\partial x_j)$
D_h	Hydraulic diameter $(4S/P)$
$\overrightarrow{G}_{c,I}$	Gradient evaluated with Up-Wind definition (eq. (3.12))
H	Heaviside Step Function
$\overrightarrow{IF}$	Distance vector between point I and point F.
I	Index of cell centre of the I^{th} cell
I'	Index of the point obtained by the projection of the I^{th} cell centre on the line perpendicular to a face between cell I and J and passing through the face centre (see figure 3.1)
K	Total kinetic energy $((u_i u_i/2)$
L	Charactheristic length of largest eddies
L_t	RANS turbulent length scale
L_{ij}	Resolved stress (Eq. (2.32))
L_{ij}^a	Anisotropic resolved stress (Eq. (2.29))
M_{ij}	Scaled composite rate-of-strain tensor (Eq. (2.31))
Nu	$\frac{hD_h}{k}$ Nusselt number

P	Perimeter
P	Pitch distance (fuel rod bundle test case, see figure 6.1)
P/D	Pitch-to-diameter-ratio
Pr	Prandtl number
Pr_t	Turbulent Prandtl number
Pr_{SGS}	Sub-grid Prandtl number
$Pr_{t,\gamma}$	Turbulent Prandtl number for the homogeneous part of the hybrid RANS/LES model
$Pr_{t,a}$	Turbulent Prandtl number for the anisotropic part of the hybrid RANS/LES model
$R_{ij,R}$	Reduced Reynolds stresses $R_{ij} - \frac{1}{3}R_{kk}\delta_{ij}$
Re	Reynolds number (Eq (1.2))
$\overline{S_{ij}}$	Filtered rate-of-strain $\frac{1}{2}\left(\frac{\partial \overline{u_i}}{\partial x_j} + \frac{\partial \overline{u_j}}{\partial x_i}\right)$
$\widetilde{\overline{S_{ij}}}$	Filtered rate-of-strain $\frac{1}{2}\left(\frac{\partial \widetilde{\overline{u_i}}}{\partial x_j} + \frac{\partial \widetilde{\overline{u_j}}}{\partial x_i}\right)$
S	Cross section area
S_w	Wall surface
St	Strouhal number (see Eq. (6.8))
T^+	$\left(T_w - T\right)/T_\tau$ Dimensionless temperature
T_B	Bulk Temperature
T_τ	Local friction temperature
T_{ij}	Doubly filtered SGS stress tensor (Eq. (2.27))
T_{ij}^a	Anisotropic double filtered SGS stress tensor (Eq. (2.29))
U_B	Bulk velocity
U_L	Velocity scale of largest eddies
$\left\Vert\overrightarrow{V}\right\Vert$	Intensity secondary motion

Lower-case Roman Symbols

c_p	Specific heat capacity at constant pressure
c	Constant (see Eq. (2.56))
f	Dominant frequency
f	Elliptic relaxation factor (see Chapter A)
h	$\dfrac{q_w}{(T_w - T_B)}$ Heat transfer coefficient
k	wave number cutoff ($k = 1/\eta$), or turbulent kinetic energy ($u_i^{\prime} u_i^{\prime}/2$)
k_η	wave number cutoff for the scalar field ($1/\eta_\eta$)
l	Charactheristic length of an eddy
l_{ei}	demarcation length scale between the energy-containig range of eddies ($l > l_{ei}$) and smaller eddies ($l < l_{ei}$)
m_{IJ}	mass flux evaluated at the face centre between cell I and cell J.
$\overrightarrow{n}_{IJ}$	Normal vector to the face
n_i	Normal vector to the surface
$\overline{p}$	Filtered pressure
p	Pressure
$p^{\prime}$	Pressure fluctuation
q_w	Wall heat flux
s	Subgrid-activity parameter
$s_{ij}^{\prime}$	Filtered fluctuating rate-of-strain $\left(\overline{S_{ij}} - \left\langle \overline{S_{ij}} \right\rangle\right)$
s^*	Modified subgrid-activity parameter
s_ϕ	Volumetric source term
t	Time
$\langle u \rangle_{GAP}$	Bulk velocity in the gap region (Fuel Rod Bundle test case)
$\overline{u_i}$	Filtered velocity
$\overrightarrow{u^*}$	Predicted velocity in the SIMPLEC velocity pressure coupling

$\overrightarrow{u}$	Velocity vector
$\overrightarrow{u}_{IJ}$	Velocity vector evaluated at the face centre between cell I and cell J
u'_i	Velocity fluctuation or subgrid velocity component in i^{th} direction with $i = 1, 2, 3$
u, v, w	Velocity components is a Cartesian system of reference (used in channel flow, see Chapter 5)
u, v, w	Velocity components is a curvilinear system of reference (used for fuel rod bundle, see Chapter 6)
u_i	Velocity componenets in i^{th} direction with $i = 1, 2, 3$
u_η	Kolmogorov's velocity scale
$\overline{v^2}$	Normal velocity fluctuations to the wall
x, r, θ	Curvilinear system of reference (used for furl rod bundle, see Chapter 6.1)
x, y, z	Cartesian coordinates (used in channel flow, see Chapter 5)
x_i	Cartesian coordinate in the i^{th} direction with $i = 1, 2, 3$

Capital Greek Symbols

Δ	Grid filter with the Smagorinsky model (see Eq. (2.25))
$\overline{\Delta}$	Grid filter with the Germano's Dynamic model (see Eq. (2.26))
$\widetilde{\overline{\Delta}}$	Effective filter with the Germano's Dynamic model (see Eq. (2.26)).
Γ_a	Turbulent diffusivity for Schumann's decomposition (Eq (2.46))
Γ_r	Sub-grid diffusivity for Schumann's decomposition (Eq (2.46))
Γ_θ	Molecular diffusivity for the scalar θ
Γ_{SGS}	Sub-grid diffusivity
Ω_I	Volume of the I^{th} cell

Lower-case Greek Symbols

α	Blending parameter
α_{IJ}	Geometrical factor $\dfrac{\left\Vert\overrightarrow{FJ}\right\Vert}{\left\Vert\overrightarrow{IJ}\right\Vert}$

η	Kolmogorov's length scale
η_θ	Obukhov-Corrsin scale (Eq. (2.43))
ε	Dissipation
λ	Thermal conductivity
λ	Wavelength
μ	Molecular viscosity
ν	Kinematic viscosity
ν_a	Turbulent viscosity in Schumann's decomposition (Eq. (2.40))
ν_r	Sub-grid viscosity in Schumann's decomposition (Eq. (2.40))
ν_{SGS}	Subgrid eddy discosity (Eq (.2.23))
ϕ	Generic scalar
ϕ_I	Generic scalar evaluated at the cell centre of the I^{th} cell
ϕ_{IJ}	Generic scalar evaluated at the face centre between cell I and cell J
ρ	Fluid density
σ	dT_b/dx_1 Bulk temperature variation along the streamwise direction (see Eq.(6.10))
$\overline{\theta}$	Filtered scalar
τ_{ij}^a	Subgrid anisotropic stress tensor (Eq. (2.17))
τ_{ij}^R	Subgrid stress tensor (Eq. (2.16))
τ_j^R	Subgrid scalar flux (Eq. (2.16))
τ_L	Time scale of largest eddies
τ_η	Kolmogorov's time scale
θ	Conserved passive scalar
φ	$\overline{v^2}/k$ (see section A.1.1)

Abbreviations

BC	Boundary conditions

CD	Central difference
CFD	Computational Fluid Dynamics
CFL	Courant-Friedrichs number $\frac{u\Delta t}{\Delta x}$
DNS	Direct Numerical Simulation
FD	Finite Difference
FV	Finite Volume
HPC	High Performing Computing
LES	Large Eddy Simulation
RANS	Reynolds Averaged Navier-Stokes
$SOLU$	Second Order Linear Up-Wind
UW	Up-Wind
URANS	Unsteady Reynolds Averaged Navier-Stokes
WP	Work Package

Mathematical Symbols

$\mathcal{F}_b$	Blending function (see Eq.(2.54))
∇	Nabla operator $\sum_{i=1}^{n} \hat{x}_i \frac{\partial}{\partial x_i}$
$\partial\Omega_I$	Surface of the I^{th} cell

Chapter 1

INTRODUCTION

De' Fiumi

"Dove il canale è più stretto, ivi corre l'acqua più forte, e nell'uscire dallo stretto si allarga con furia e percote e consuma le vicine rive traverse, e spesso muta corso d'uno in altro loco" [1]

The above statement is taken from the Codex Atlanticus where Leonardo Da Vinci annotated his observations about the flowing of the river Arno in Tuscany. Leonardo had a very wide range of interests: from philosophy to astronomy, from anatomy to military engineering, from mechanics to bird flight and, of course, fluid mechanics. Leonardo was hundreds of years ahead with respect to his age: for example in the *Codex E* Leonardo gave a very precise description of how birds fly, explaining very accurately the mechanisms responsible for lift generation. Leonardo can be considered the father of modern fluid dynamics, for example the first part of the above statement can be interpreted as the first enunciation of the principle of mass conservation. Continuing in his study Leonardo was able to formulate the following general rule "*where the flow carries large quantity of water, the speed of the water is greater and vice versa*"[2] which can be mathematically express as:

$$U_B S = const \tag{1.1}$$

where U_B is the fluid velocity and S is the cross sectional area. During his work Leonardo also approached turbulence. Figure 1.1 shows the flow around an obstacle,

---

[1] On Rivers " Where the channel is narrow, the water proceeds faster, and coming out from the straight it expands with anger and hits and erodes the near cross bank, and frequently it changes stream from one place to another " Leonardo Da Vinci, Codex Atlanticus, 1483-1518, 403 pages about various topics. The translation from Italian is done by the author of this work. The original text is taken from *e-Leo*, electronic scansion of the original manuscript conserved at *Biblioteca Ambrosiana*, Milan.

[2] Translation from Tokaty (1971) page 39.

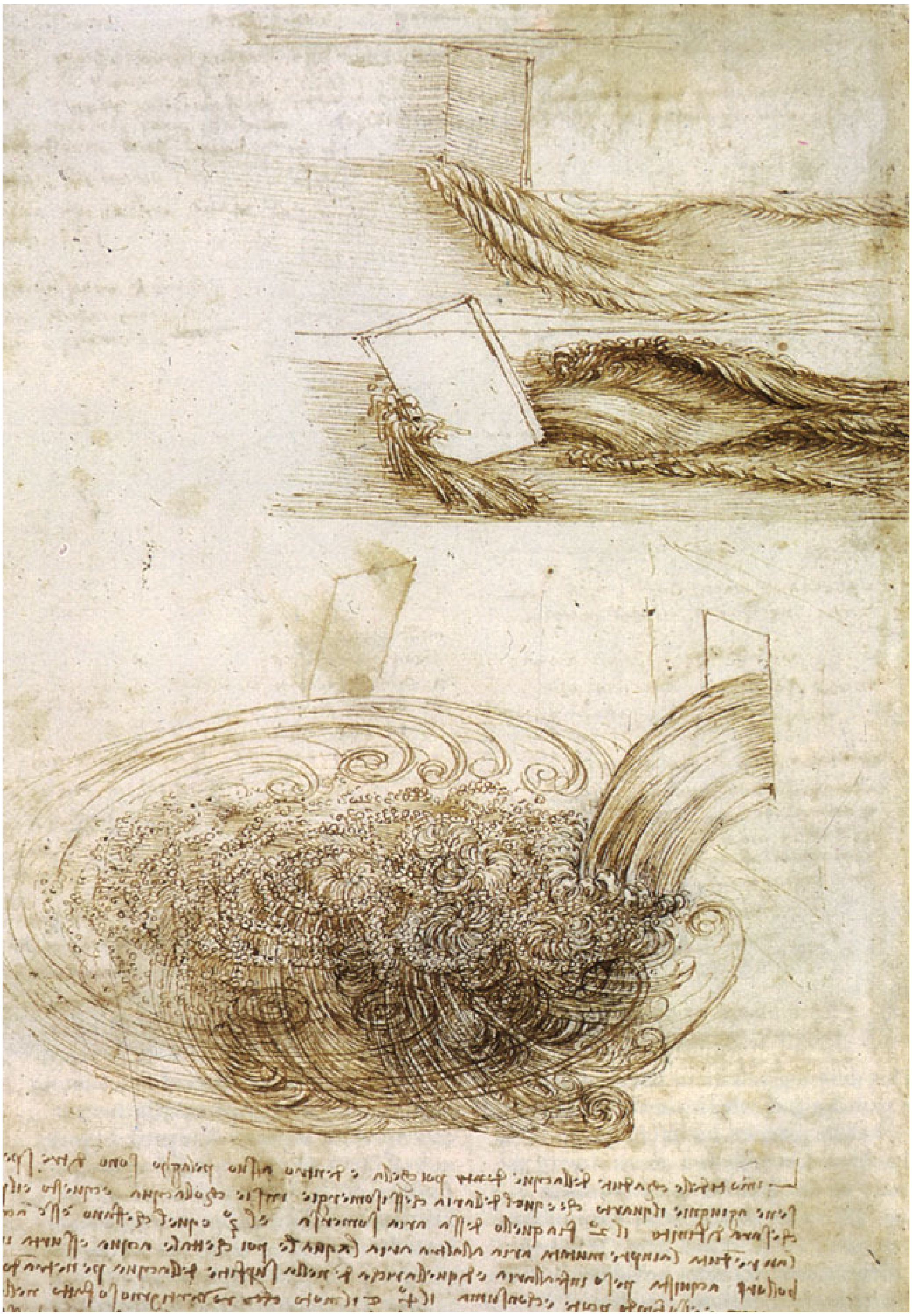

Figure 1.1: Sketches from the Codex Atlanticus of Leonardo Da Vinci. In the upper part of the image a complex turbulent flow is showed, which is generated by an obstacle introduced in a-free stream. The bottom part shows a waterfall and the consequent recirculation, generated in the underneath basin (Figure from Reuteler (2006))

where the separation and the consecutive wake are very clear. In the bottom part instead a waterfall is drawn and with the following quotation:

> *"L'acqua che caderà da alto in basso, si farà profondo pelago, il quale sempre accrescerà, e spesso le sue argini vi ricaderanno dentro. E la ragion si é che l'acqua che cade sopra l'altra acqua, per la velocità del colpo del peso si fa dar loco, viene a passare insino sul fondo, dove cava, e per la percussione e per l'aria che nel cadere sommerge insieme con seco, viene a resurgere, a elevarsi in alto per varie vie, le quali fanno gargugliamento, ...".*[3]

The interesting part of the statement is the second one, where Leonardo describes two mechanisms, the collision between the falling water and the water at the bottom and the imprisoned air that is moving upward, that give rise to the turbulent motion ("*gargugliamento"*).

After Leonardo a number of other scientists approached fluid mechanics, but was not until the end of the nineteenth century that turbulence was spoken about in the work of Reynolds (1883). Reynolds carried out series of experiments, employing horizontal pipes and inserting a colour liquid inside the main flow, in order to visualise the streamlines. He observed that for low speed the pattern of the streamlines was regular: they were all parallel and aligned with the flow direction. By increasing the speed of the fluid, eddies formed at the end of the pipe and this destroyed the regular streamline pattern in the region. By increasing the velocity further the eddy formation moved upstream and after a certain value of the velocity the flow was chaotic everywhere. He plotted also the head loss as function of the velocity (Fig. 1.2) and he found that the relationship was linear until point 1, random between points 1 and 2 and, after 2, again a smooth curve, with a possible quadratic relation with the velocity. From this description the flow can be clearly divided into three different regimes: a *laminar regime* before point 1, a *transitional regime* between 1 and 2 and a *fully turbulent regime* after 2. Reynolds investigated the transitional point, he carried out his experiments with pipes of different diameters and he came up with the following dimensionless parameter, later called the Reynolds number:

$$Re = \frac{\rho U_B D}{\mu} = \frac{U_B D}{\nu}. \tag{1.2}$$

---

[3] "The water falling down from the top to the bottom will create a deep cavity, which will always grow, and frequently its bank-side will fall into. And the reason is due to the velocity of the knock and the weight of the water falling onto other water. The falling water is getting room and proceeding to the bottom (" *viene a passare insino sul fondo"*), where it digs in. And due to the hitting and the air imprisoned (*"per la percussione e per l'aria che nel cadere sommerge"*) into the fall that after the water is rising again (*"viene a resurgere"*), moving upward, generating a chaotic motion ("*gargugliamento"*),...", Leonardo Da Vinci, Codex Atlanticus. Translation by the author of this work.

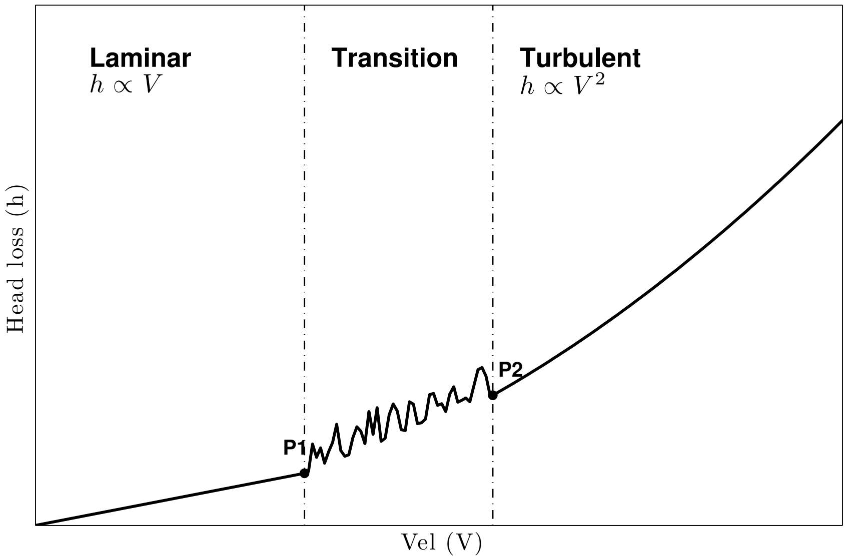

Figure 1.2: Reynolds diagram showing the loss of head as function of the velocity.

He observed that the flow regime was dependent only on this number; he assigned at $P1$ a Reynolds number between 1900 and 2000 (Reynolds (1895)). The Reynolds number has a fundamental importance in fluid mechanics because it permits to compare similar flows around similar configurations, even if the geometrical dimensions are different.

A fundamental tool in order to understand turbulence is the concept of the energy cascade. The concept was introduced by Richardson in 1922 and the great Russian scientist Kolmogorov perfected it. First of all the concept of eddy has to be introduced as turbulent motion localised within a region of size l, which is at least moderately coherent over the region. A typical example is a vortex. The flow is divided into large and small scales. The former has a typical dimension L of the same order as the geometry under investigation (for example the diameter of the pipe) and at this level the kinetic energy enters the turbulence through the production mechanism. The energy is then transferred to the small scales by an inviscid process and is dissipated at the smallest scales (in general named as Kolmogorov's scale). A more complete description of the phenomenon is given in Chapter 2. This concept of energy cascade has a fundamental role in modern numerical simulation such as Large Eddy Simulation.

1.1 Types of analysis in a CFD framework

With the introduction and the continuing development of computer science, Computational Fluid Dynamics (CFD) is becoming more and more popular in many branches of research and engineering. CFD is based on the approximation, discretization and the solution of the Navier-Stokes equations (N.S.).

The main problem of a turbulent flow is that even if the equations are deterministic the consequent velocity field is random[4]. The reason has to be found in unavoidable perturbations in initial conditions, boundary conditions and material properties. As was demonstrated by Reynolds in his experiments the flow field, after a certain speed, is very sensitive to these perturbations.

The direct resolution of the N.S. equations is called Direct Numerical Simulation (DNS). In this approach all the time and space scales are resolved as shown in Fig. (1.3). In order to resolve small scales (Kolmogorov scales) the mesh has to be very fine. DNS is becoming increasingly popular because the information that can be provided is, in same cases, not even achievable by experiments. This method is now widely used in research and in particular in turbulence modelling. As a consequence of its extremely fine level of description, DNS is very time consuming. Table 1.1reports the CPU time needed for a simulation of isotropic turbulence as function of the Reynolds number, showing that CPU time is proportional to the Re^3. Consequently simulations of relatively complicated geometries at very high Reynolds number are still not feasible, even using High Performing Computing (HPC). The second failing of DNS is that high order schemes, in the discretization of equations, have to be employed in order to minimise the numerical dispersion and dissipation. Implementation of these schemes is relatively easy in block-structured meshes, but their formulation on general unstructured grids, as required in very complex engineering flows, is not straightforward. In Chapter 4 all these points will be discussed in more detail. Some examples of DNS are reported in Kim et al. (1987); Kawamura et al. (1999); Abe et al. (2001, 2004)

A second type of approach consists in calculating the statistical average of the solution. In this method, which is based on Reynolds observations, the solution is divided into two parts: a mean part and a fluctuating part. Mathematically the decomposition is:

$$\underbrace{u_i}_{instant\,value} = \underbrace{\overline{u_i}}_{mean} + \underbrace{u'_i}_{fluctuating} \tag{1.3}$$

where the mean value is obtained as:

$$\overline{u_i} = \lim_{T\to\infty} \frac{1}{2T} \int_{t-T}^{t+T} u(x,t')dt' \tag{1.4}$$

This is called Reynolds Averaged Navier-Stokes (RANS), where turbulence effects are

---

[4] Random event: considering a certain event A (for example $A \equiv \{u_1 < 10\,ms^{-1}\}$), if the event A inevitably occurs, then A is certain, If A never occurs, then it is impossible, if A may or may not occur, then it is *random*.

fully modelled as presented in Figure (1.4). The computational resources required are far less than in DNS. Consequently very high Reynolds numbers and very complex geometries are feasible to be resolved even on a simple laptop. These characteristics make the approach very attractive for engineering applications, and in fact it is the base of most commercial and industrial codes. For a more detailed description of RANS method and models refer to Pope (2000); Wilcox (1993).

A very similar approach to RANS is the Unsteady Reynolds Averaged Navier-Stokes (URANS), or Semi-Deterministic Simulation (SDS), or Very Large-Eddy Simulation (VLES). In this case the resolved part is only constituted by some low frequency modes in time, and all turbulence is modelled following a RANS approach (Fig. 1.5). In this case the level of information given by the solution is more detailed than RANS. This approach is used frequently when there is a superimposition on the mean flow of an external unsteadiness, for example a pulsating flow or vortex shedding.

An intermediate approach between RANS and DNS is Large Eddy Simulation (LES). As the name suggests the flow is divided into large and small scales. The former are resolved and the latter, instead, are modelled (Fig. 1.6). In order to separate the two scales a cut-off length has to be defined. The methodology to do this scale separation is presented in Chapter 2. The same chapter also presents governing equations for LES and some commonly used turbulence models. A more complete introduction to the topic could be found in Pope (2000) and in particular in the book of Sagaut (2001), which is entirely devoted to the subject. Clearly the level of approximation, given by LES, is more accurate than what RANS can provide. In the past, LES was entirely devoted to research about turbulence when DNS was still too expensive. More recently, with the increase of the computational CPU power, LES has started to become attractive also for industrial and engineering applications. In some applications, for example nuclear power plant, the results given by RANS calculations do not give enough details about the fluctuating forces or temperatures which are important for the circa fifty years lifespan of major components. LES becomes feasible and more accurate than RANS when it can be applied to a sub-component such as pipe bends, T-junction, flow between tubes. As a consequence several commercial codes (Fluent, Star-CD are only two examples) and industrial ones (*Code_Saturne*) are introducing this type of approach among their turbulence model options.

1.2 Ph.D. motivations and objective

This Ph.D. is part of the KNOO project (Keep Nuclear Option Open), a five year initiative to enhance research in the nuclear field. The project is divided in four work packages (WP):

$Re_L = \frac{kL}{\nu}$	$Re_\lambda = \frac{u'_{rms}\lambda}{\nu}$	CPU Time
94	25	20 min
375	50	9 h
1500	100	13 days
6000	200	20 months
24000	400	90 years
96000	800	5000 years

Table 1.1: Estimation of the CPU time for DNS of isotropic turbulence at different Reynolds number. The estimation was done at 1 gigaflops (1000 operations per mode per time step). The data are taken from Pope (2000) .

1. Fuel Thermal-hydraulics and reactor systems;
2. Materials performances and monitoring reactors conditions;
3. An integrate approach to waste immobilisation;
4. Safety and performances for a new generation of reactor design.

This work is enclosed in WP1. The aim of this work is to use LES to generate a reliable data-set for RANS validation. The main drawback of LES in wall bounded flows is the very fine mesh resolution required by the small near wall structures. Therefore one of the main objective of this work is to relax the near wall mesh constraints employing some of the recent techniques such as embedded refinements or Hybrid RANS/LES turbulence modelling.

1.3 Outline of the thesis

This thesis is divided into two parts: the first is a theoretical review of fundaments of turbulence models and numerical analysis, whereas the second presents the results.

Chapter 2 recalls the Navier-Stokes equation, the concept of energy cascade and some concepts of turbulence modelling. The turbulence modelling section is mainly concentrated on the filtering approach, which is the theoretical base of Large Eddy Simulation. The Smagorinsky model and Germano's Dynamic approach are introduced, underlining their strengths and weaknesses. Because the main focus of this work is toward wall bounded flow some elements of anisotropic modelling are also brought up, in particular focusing on Schumann's decomposition. Heat transfer modelling is also considered, along with different thermal regimes as function of the Prandtl number variation. Finally the chapter presents a Hybrid RANS/LES model based on the Schumann's decomposition, where heat transfer is taken into account. Appendix A briefly reviews the equations for the RANS approach.

In this work the numerical analysis is performed using *Code_Saturne*, a CFD code developed by R&D at EDF. The solver is based on a Finite Volume discretization and the computational methods used are described in Chapter 3.

A considerable part of this work investigates the influence of the mesh requirements for LES type of calculations and Section 3.1 gives a briefly overview of the available mesh strategies, focusing in particular on the comparison between structured and unstructured approaches.

In Chapter 4 the concept of kinetic energy conservation in conjunction with an inviscid bi-dimensional test case (Taylor-Green vortices) is used in order to compare structured and unstructured mesh performances. During the comparison embedded refined and polyhedral meshes are tested against a well known structured conformal grid. The use of unstructured meshes increases the level of error, but performance can be recovered if the unstructured mesh presents a low level of non-orthogonalities. Indeed results show the large importance of the accuracy of the gradient reconstruction, which is used in the evaluation of the explicit part of the convective and diffusive terms when the mesh is non-orthogonal.

The comparison between mesh arrangements is carried on in Chapter 5, but using a 3D fully turbulent flow at $Re_\tau = 395$. Several types of mesh are employed and compared with a structured grid. Some of the unstructured meshes presented some non-physical oscillations in the Reynolds stresses profiles. Budgets of turbulent kinetic energy and Reynolds stresses are also evaluated in order to find a possible explanation for the problem.

Chapter 5 presents a validation of a Hybrid RANS/LES model, which includes heat transfer modelling. The model is tested against wall resolved LES on coarse meshes and it has been proved to be beneficial. An investigation of the model dependency to the mesh resolution is also carried out. In the validation process the effect of the Prandtl number variation is also considered.

Chapter 6 presents the fuel rod bundle test case. Firstly the quality of simulations is evaluated using some LES quality indices and after the results are presented. The flow presents coherent structures that are flowing in the streamwise direction in the gap region between two adjacent sub-channels. This generates a phenomena called flow pulsations, which is enhancing mixing between sub-channels. Budgets of turbulent kinetic energy and Reynolds stresses are computed and reported. Heat transfer results are also presented taking into account different boundary conditions for the scalars: Neumann (constant wall heat flux) and Dirichlet (constant wall Temperature). Effects of the Prandtl number variation on the thermal field are also taken into account. Finally a case with scalar imbalance between adjacent sub-channels is investigated. A similar geometry, where a spacer wire is wrapped around every fuel rod, in presented into

Appendix D. The test case is analysed with RANS turbulence models therefore it is inserted into appendix.

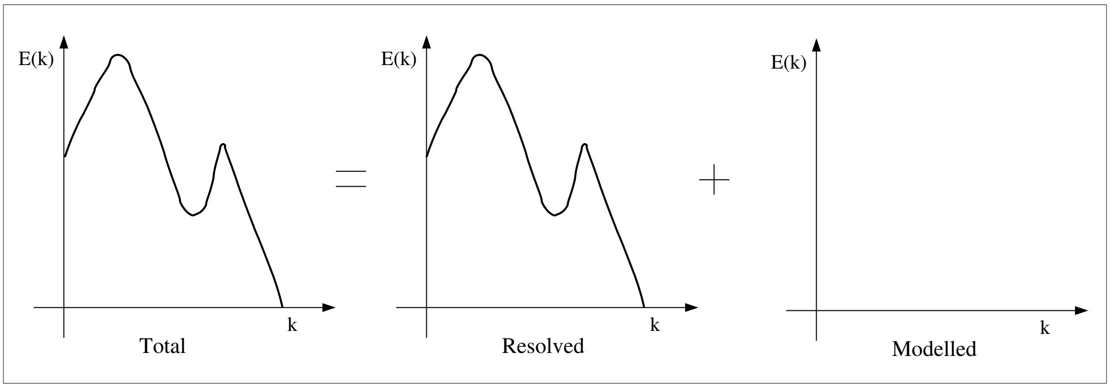

Figure 1.3: Decomposition of the energy spectrum into resolved and modelled parts for a DNS analysis.

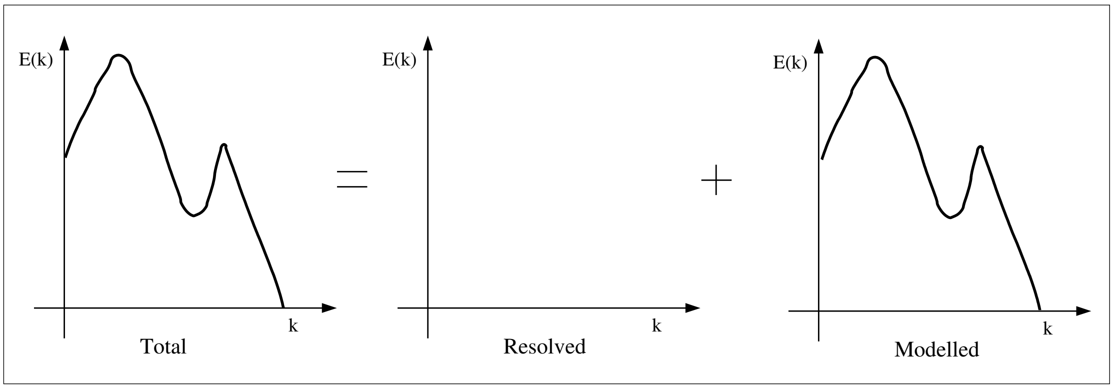

Figure 1.4: Decomposition of the energy spectrum into resolved and modelled parts for a RANS analysis.

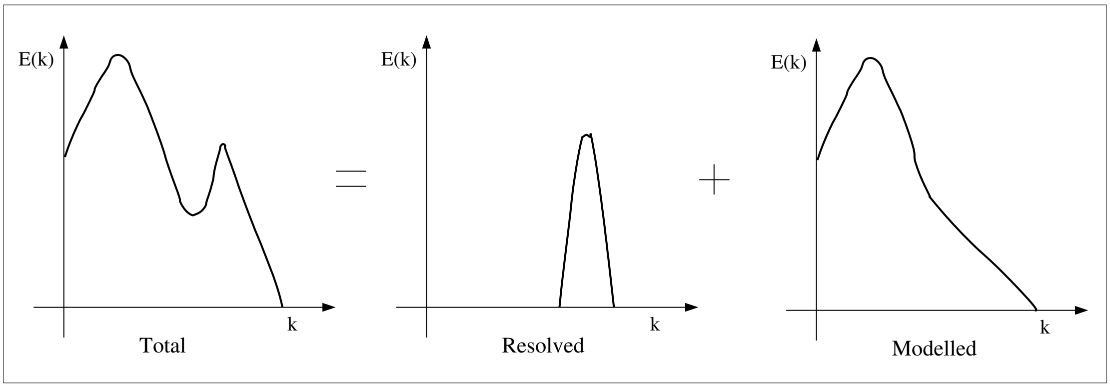

Figure 1.5: Decomposition of the energy spectrum in resolved part and modelled part for a URANS analysis.

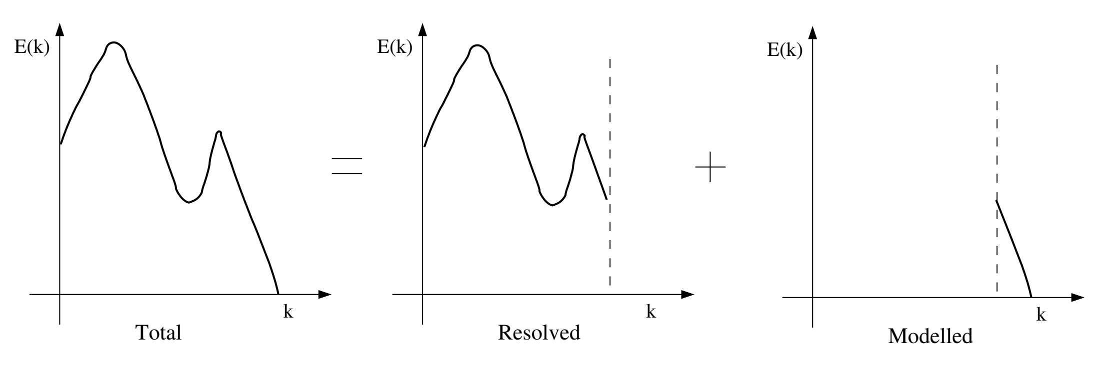

Figure 1.6: Decomposition of the energy spectrum into resolved and modelled parts for a LES analysis.

Part I

Theoretical overview

Chapter 2

GOVERNING EQUATIONS AND TURBULENCE MODELLING

In this chapter the governing equations for fluid motion and heat transfer are presented. The concept of energy cascade is also briefly revised in order to have a more complete introduction to turbulence modelling. Secondly LES modelling is introduced and some of the most popular models are presented. RANS modelling is not considered in this chapter, but a very quick overview is given in Appendix A. Finally Hybrid RANS/LES is introduced in conjunction with a new Hybrid model for the heat transfer. More details about fluid mechanics and turbulence modelling can be found in several books, for example Tritton (1988) and Pope (2000), whereas a complete description of LES and Hybrid modelling can be found in Sagaut (2001).

2.1 GOVERNING EQUATIONS

The intrinsic physical meaning of thermodynamic quantities must be found in the statistical description of a gas. Consequently the governing equations for fluid motion can be derived using a statistical mechanics approach. Such rigorous derivation of mass, momentum and energy conservation can be found in the book of Vincenti and Kruger (1965).

In this work the starting point is the Navier-Stokes equations[1] in their incompressible form [2] and with assumption of constant fluid properties. The energy balance is consequently reduced to a transport equation of a passive scalar. The system of equations being solved is therefore:

---

[1] In this context Einstein's notation is used.

[2] In case of constant density the buoyant term in the momentum equation is neglected and the thermal field is only acting as a passive scalar, without any feedback in the momentum.

$$\begin{cases} \dfrac{\partial u_i}{\partial x_i} = 0 \\ \dfrac{\partial u_i}{\partial t} + \dfrac{\partial u_j u_i}{\partial x_j} = -\dfrac{1}{\rho}\dfrac{\partial p}{\partial x_i} + \nu \dfrac{\partial^2 u_i}{\partial x_j \partial x_j} \\ \dfrac{\partial \theta}{\partial t} + \dfrac{\partial u_j \theta}{\partial x_j} = \Gamma \dfrac{\partial^2 \theta}{\partial x_j \partial x_j} \end{cases} \tag{2.1}$$

where x_i is the coordinate in the i^{th} direction, u_i the velocity component in the i^{th} direction, t the time, ρ the density, p the pressure, ν the kinematic viscosity, θ a scalar (i.e. temperature) and $\Gamma = \nu/Pr$ is the diffusivity of θ with Pr being the Prandtl number.

In general the pressure is seen as a thermodynamic variable and thus can be related to density and temperature using an equation of state. In the case of a constant density flow this link is lost and a different interpretation for the role of pressure is required. Taking the divergence of the second equation of the system 2.1 leads to

$$\left(\frac{D}{Dt} - \nu \nabla^2\right) \nabla \cdot \overrightarrow{u} = -\frac{1}{\rho}\nabla^2 p - \frac{\partial u_i}{\partial x_j}\frac{\partial u_j}{\partial x_i} \tag{2.2}$$

In the case of a divergence free flow $\nabla \cdot \overrightarrow{u} = 0$ and this is true if and only if the RHS of Eq. (2.2) is equal to zero everywhere, which implies that the following Poisson equation for the pressure has to be verified:

$$\frac{\partial^2 p}{\partial x_i^2} = -\rho \frac{\partial u_i}{\partial x_j}\frac{\partial u_j}{\partial x_i} \tag{2.3}$$

Thus: the satisfaction of Equation (2.3) is a necessary and sufficient condition for the velocity field to be solenoidal.

2.2 THE ENERGY CASCADE

The concept of energy cascade was first introduced by Richardson (1922). It is based on the concept of an eddy defined as turbulent motion localized in a region of size l, which has a moderately coherent structure over this region. The Richardson point of view can be summarized as:

- Turbulence can be considered composed by eddies of different sizes;
- The largest eddies are characterized by a length scale L, which is comparable with the flow scale and by a velocity U_L comparable with the root mean square (r.m.s.) value of the turbulent fluctuating velocity;

- The Reynolds number of the large eddies is large enough for the viscosity effects to be negligible;
- The large eddies are unstable and they break down, transferring their energy to smaller eddies;
- The same procedure of breaking and energy transfer affects also these new small eddies, creating even smaller eddies;
- This process of energy cascade continues until the Reynolds number of the eddies is small enough for the molecular viscosity to take place and dissipate the kinetic energy; at this stage the smallest scales of the turbulent motion are reached;
- Dissipation takes place only at the end of the energy cascade, the dissipation rate can be determinate by this process in sequence and it scales as[3]

$$\varepsilon \equiv \frac{U_L^3}{L} \tag{2.4}$$

Two main questions remain still unanswered: what is the size of the smaller eddies? As the characteristic length scale of an eddy decreases what happens to the characteristic velocity $u(l)$ and time scale $\tau(l)$? Answers were given by Kolmogorov (1941a,b,c, 1962)[4] when he formulated his hypotheses.

- **Kolmogorov's hypothesis of local isotropy:** *at sufficiently high Reynolds number, the small-scale turbulent motions are statistically isotropic*[5]. The separation length scale between anisotropic large eddies and isotropic small eddies is in general referred as l_{ei}[6].
- **Kolmogorov's first similarity hypothesis**: *in every turbulent flow at sufficiently high Reynolds numbers, the statistics of the small scale motion ($l < l_{ei}$) have a universal form that is uniquely determined by the kinematic viscosity ν and the dissipation rate ε.* l_{ei} demarcates the so called Universal Equilibrium range.

---

[3] The large scales have energy of order U_L^2 and then the time scale τ is

$$\tau_L = \frac{L}{U_L}$$

so the rate of transfer of energy scales as:

$$\frac{U_L^2}{\tau_L} = \frac{U_L^3}{L}$$

[4] A translation from Russian to English of Kolmogorov's work can be found in Kolmogorov (1991)

[5] Statistically isotropy: all the statistics of u_i' does not change if the coordinate system is rotated by an arbitrary angle.

[6] A rough estimation is $l_{ei} \approx \frac{1}{6}L$ (Pope (2000)).

Combining ν and ε yields:

$$\begin{cases} \eta \equiv \left(\frac{\nu^3}{\varepsilon}\right)^{1/4} \\ u_\eta \equiv (\varepsilon\nu)^{1/4} \\ \tau_\eta \equiv \left(\frac{\nu}{\varepsilon}\right)^{1/2} \end{cases} \tag{2.5}$$

where η is the length scale of the smallest eddies (also called Kolmogorov's scale), u_η the velocity scale and τ_η the time scale. Using the definition of the dissipation rate given by Eq. (2.4), the following estimations of ratios between small and large scales can be derived:

$$\begin{cases} \frac{\eta}{L} \sim Re^{-3/4} \\ \frac{u_\eta}{U_L} \sim Re^{-1/4} \\ \frac{\tau_\eta}{\tau_L} \sim Re^{-1/2} \end{cases} \tag{2.6}$$

- **Kolmogorov's second similarity hypothesis**: *in every turbulent flow at sufficiently high Reynolds numbers, the statistics of the motion of scale l in the range $L \gg l \gg \eta$ have a universal form that is uniquely determined by ε and independent from ν.* Now it is convenient to introduce a length scale l_{di} ($l_{di} \backsimeq 60 \cdot \eta$) that divides the universal equilibrium range into an inertial sub-range where inertia still dominates, and a viscous range where the dissipation acts. In the inertial sub-range the velocity and time scales are:

$$\begin{cases} u(l) = (\varepsilon l)^{1/3} \\ \tau(l) = \left(\frac{l^2}{\varepsilon}\right)^{1/3} \end{cases} \tag{2.7}$$

Figure (2.1) visualizes all the different scales and ranges.

2.3 LARGE EDDY SIMULATION

As a consequence of the energy cascade presented in the previous section, a turbulent flow could be divided into small, or sub-grid, scales and large scales. In LES the decomposition is applied through a filtering operation. The equations obtained are the

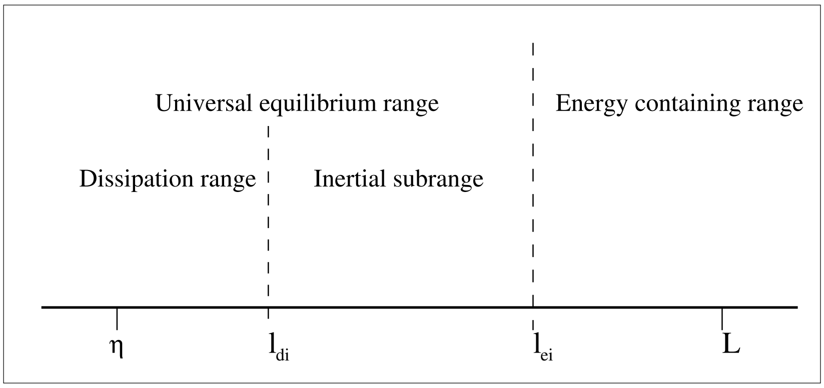

Figure 2.1: Visualization of the typical length scales of a turbulent motion at high Reynolds number.

usual mass, momentum and energy conservation with the addition of a new term the Sub-Grid Scale (SGS) stress tensor that represents the effect of small scales on the large ones. This term has to be modelled and many options are possible, starting from a simply eddy viscosity model (Smagorinsky model) to more complex models where several transport equations are solved for different sub-grid quantities. A very complete and comprehensive description of LES modelling and related issues is given in Sagaut (2001).

2.3.1 Filtering

A filtering operation can be mathematically defined as a convolution product:

$$\overline{u}_i(\overrightarrow{x},t) = \int_{-\infty}^{\infty} u_i(\overrightarrow{r},t) G(\overrightarrow{x} - \overrightarrow{r},t) d\overrightarrow{r} \tag{2.8}$$

where $\overline{u_i}$ is the filtered velocity, G is the kernel of the convolution and depends on the type of the filter.

The residual field is defined as:

$$u'_i(\overrightarrow{x},t) \equiv u_i(\overrightarrow{x},t) - \overline{u}_i(\overrightarrow{x},t) \tag{2.9}$$

and the velocity field can be decomposed as

$$u_i(\overrightarrow{x},t) \equiv \overline{u}_i(\overrightarrow{x},t) + u'_i(\overrightarrow{x},t). \tag{2.10}$$

This decomposition appears to be similar to the Reynolds one, but in this case the filtered velocity $\overline{u}(\overrightarrow{x},t)$ is random and time dependent. The second difference is that the filtering operation applied to the residual field is not zero:

$$\overline{u'_i}(\vec{x},t) \neq 0. \tag{2.11}$$

The filter must verify the following properties:

1. Conservation of constant:

$$\overline{a} = a \Longleftrightarrow \int_{-\infty}^{\infty} G(\vec{r},t)\, d\vec{r} = 1 \tag{2.12}$$

2. Linearity:

$$\overline{u_1 + u_2} = \overline{u}_1 + \overline{u}_2 \tag{2.13}$$

3. Commutation with differentiation[7]:

$$\overline{\frac{\partial u_i}{\partial s}} = \frac{\partial \overline{u}_i}{\partial s} \tag{2.14}$$

General	$G(r)$
Box	$\frac{1}{\Delta} H\left(\frac{1}{2}\Delta - \lvert r \rvert\right)$
Gaussian	$\sqrt{\frac{6}{\pi\Delta^2}} \exp\left(-\frac{6r^2}{\Delta^2}\right)$
Sharp spectral	$\frac{\sin(\pi r/\Delta)}{\pi r}$

Table 2.1: Example of one-dimensional filter functions. H is the Heaviside Step Function.

Table 2.1 reports some examples of filter functions in one-dimension (for simplicity). For a more detailed treatment of the filter operation, its properties and its applications refer to the book of Sagaut (2001).

2.3.2 LES FORMULATION

Using the velocity decomposition of Eq. (2.10) for both velocities and pressure, the system of Equations (2.1) becomes:

$$\left\{ \begin{array}{c} \frac{\partial \overline{u}_i}{\partial x_j} = 0 \quad \frac{\partial u'_i}{\partial x_j} = 0 \\ \frac{\partial \overline{u}_i}{\partial t} + \frac{\partial \overline{u_i u_j}}{\partial x_j} = -\frac{1}{\rho}\frac{\partial \overline{p}}{\partial x_i} + \nu \frac{\partial^2 \overline{u}_i}{\partial x_j \partial x_j} \\ \frac{\partial \overline{\theta}}{\partial t} + \frac{\partial \overline{u_j \theta}}{\partial x_j} = \Gamma \frac{\partial^2 \overline{\theta}}{\partial x_j \partial x_j}. \end{array} \right. \tag{2.15}$$

---

[7] The commutation with differentiation holds only if G is homogeneous in space.

From equations in the first line of system (2.15) it is immediately possible to observe that both the filtered and the sub-grid field are solenoidal. Now the problem comes from the term $\overline{u_i u_j}$ that is not simply equal to the product of the filtered single velocities. The non-linear term can be expressed as:

$$\tau_{ij}^R = \overline{u_i u_j} - \overline{u}_i\,\overline{u}_j. \tag{2.16}$$

The residual stress tensor could be divided into an isotropic and anisotropic part as:

$$\tau_{ij}^a = \tau_{ij}^R - \frac{1}{3}\tau_{kk}^R \delta_{ij} \tag{2.17}$$

and the isotropic part could be added to the pressure obtaining:

$$\overline{p} \equiv \overline{p} + \frac{1}{3}\rho\tau_{kk}^R \delta_{ij}. \tag{2.18}$$

The momentum equation can be rewritten as:

$$\frac{\partial \overline{u}_i}{\partial t} + \frac{\partial \overline{u_j}\,\overline{u}_i}{\partial x_j} = -\frac{1}{\rho}\frac{\partial \overline{p}}{\partial x_i} - \frac{\partial \tau_{ij}^a}{\partial x_j} + \nu \frac{\partial^2 \overline{u}_i}{\partial x_j \partial x_j}. \tag{2.19}$$

Same issue also affects the sub-grid scalar flux, which can be expressed as:

$$\tau_j^R = \overline{u_j \theta} - \overline{u_j}\,\overline{\theta} \tag{2.20}$$

and the transport equation for the scalar can be rewritten as:

$$\frac{\partial \overline{\theta}}{\partial t} + \frac{\partial \overline{u}_j\,\overline{\theta}}{\partial x_j} = -\frac{\partial \tau_j^R}{\partial x_j} + \Gamma \frac{\partial^2 \overline{\theta}}{\partial x_j \partial x_j}. \tag{2.21}$$

The filtered quantities depend also on the type and the width of the filter. Filtered quantities can also appear indirectly in the model of τ_{ij}^a and τ_j^R.

2.3.3 S.G.S. Modelling

2.3.3.1 The Smagorinsky model

The simplest model to express τ_{ij}^a was proposed by Smagorinsky (1963) and is based on a mixing length hypothesis:

$$\tau_{ij}^a = -2\left(C_s \Delta\right)^2 \left|\overline{S}\right| \overline{S}_{ij} \tag{2.22}$$

where C_s is the Smagorinsky constant, Δ the filter width, $\overline{S}_{ij} = \frac{1}{2}\left(\frac{\partial \overline{u}_i}{\partial x_j} + \frac{\partial \overline{u}_j}{\partial x_i}\right)$ is the filtered rate of strain tensor and $\left|\overline{S}\right| = \sqrt{2\overline{S}_{ij}\,\overline{S}_{ij}}$. The sub-grid viscosity (ν_{SGS}) is:

$$\nu_{SGS} = (C_s\Delta)^2 \left|\overline{S}\right| \tag{2.23}$$

and the model has a total viscosity equal to:

$$\nu_{TOT} = \nu + \nu_{SGS} \tag{2.24}$$

The theoretical value of the Smagorinsky constant is still an open debate. Pope (2000) gives a value of 0.17 for isotropic turbulence. A common way to evaluate is to use the decay of the isotropic turbulence in order to take into account the numerical dissipation. For inhomogeneous flow a smaller value is used, for example in channel flow a common value is $C_s = 0.1$ or $C_s = 0.065$ (see Benhamadouche (2006)) and they are in general related to conservative properties of the code.

This model presents many drawbacks:

- Different values of C_s are used to describe different flows;
- The sub-grid stresses do not vanish in laminar regions. Consequently damping functions must be introduced in order to take into account near wall effects;
- Intermittency functions must be introduced for transitional flow in order to modify C_s;
- The model does not take into account the back-scatter that occurs when the energy flows from small scales to the large ones. The phenomenon sometimes can be significant;
- Anisotropy of small scales in the near wall region is not considered;
- The model needs also to be modified in the case of a strong density stratification or rotation, even if the Reynolds number is high.

In the framework of *Code_Saturne* the value used for $C_s = 0.065$ and the filter width is defined as:

$$\Delta = 2\sqrt[3]{\Omega_I} \tag{2.25}$$

Where Ω_I is the cell volume. The Van Driest (1956) damping is used to damp the SGS viscosity in wall-bounded flows.

2.3.3.2 The Germano Dynamic model

The dynamic model introduced by Germano et al. (1991) can be interpreted as an evolution of the Smagorinsky model, where the Smagorinsky constant becomes a coefficient that depends on space and time. The model is based on a double filtering operation. The first filtering operation is defined as the implicit mesh induced filter and it is denoted here with an over-line symbol. This filter is characterised by a filter width $\overline{\Delta}$. The second filtering operation is called test filtering. It is indicated by a tilde and it is characterized by an effective filter width $\widetilde{\overline{\Delta}}$. Both filter widths are related as:

$$\widetilde{\overline{\Delta}} > \overline{\Delta}. \tag{2.26}$$

In general literature $\widetilde{\overline{\Delta}} = 2\overline{\Delta}$ (see Moin et al. (1991)), but for example Benhamadouche (2006) in his PhD thesis uses a ratio of 1.5, computed as the optimal value from tests on isotropic turbulence. Applying the second filtering operation to the residual stress tensor defined in Eq. (2.16) the corresponding residual stress tensor is obtained as:

$$T_{ij} = \widetilde{\overline{u_i u_j}} - \widetilde{\overline{u_i}}\,\widetilde{\overline{u_j}}. \tag{2.27}$$

The model is based on Germano's identity (Germano (1992)) that is written as:

$$L_{ij} = T_{ij} - \widetilde{\tau^R_{ij}} = \widetilde{\overline{u_i}\,\overline{u_j}} - \widetilde{\overline{u_i}}\,\widetilde{\overline{u_j}}. \tag{2.28}$$

The same decomposition on isotropic and anisotropic parts used in (2.17) for τ_{ij} can be applied also for T_{ij} and L_{ij} obtaining:

$$\begin{cases} T^a_{ij} = T_{ij} - \frac{1}{3}T_{kk}\delta_{ij} \\ L^a_{ij} = L_{ij} - \frac{1}{3}L_{kk}\delta_{ij} \end{cases} \tag{2.29}$$

The residual stress tensors τ^R_{ij} and T_{ij}, obtained from the two filtering levels, can be modelled using the same constant C_D. This leads to:

$$\begin{cases} \tau^a_{ij} = -2C_D\overline{\Delta}^2 \left|\overline{S}\right| \overline{S_{ij}} \\ T^a_{ij} = -2C_D\widetilde{\overline{\Delta}}^2 \left|\widetilde{\overline{S}}\right| \widetilde{\overline{S_{ij}}} \end{cases} \tag{2.30}$$

Taking C_D to be uniform and defining

$$M_{ij} = 2\widetilde{\overline{\Delta}^2 \left|\overline{S}\right| \overline{S_{ij}}} - 2\widetilde{\overline{\Delta}}^2 \left|\widetilde{\overline{S}}\right| \widetilde{\overline{S_{ij}}}. \tag{2.31}$$

Substituting Eq. (2.30) into the second of Eq. (2.29) and taking into account definition (2.31) gives:

$$L^S_{ij} = T^a_{ij} - \widetilde{\tau^a_{ij}} = C_D M_{ij} \tag{2.32}$$

where L^S_{ij} represents the Smagorinsky model for the anisotropic part of the resolved stress L_{ij}. A single value of the coefficient C_D cannot be chosen to satisfy the six independent components of the tensor defined as:

$$E_{ij} = L^a_{ij} - L^S_{ij}. \tag{2.33}$$

A possible solution is presented by Lilly (1992), where C_D is evaluated using a mean square minimisation of the error between the deviatoric stress L^a_{ij} and its Smagorinsky prediction L^S_{ij} obtaining[8]:

$$C_D = \frac{L^a_{ij} M_{ij}}{M_{kl} M_{kl}} = \frac{L_{ij} M_{ij}}{M_{kl} M_{kl}} \tag{2.34}$$

From this definition of C_D some considerations can be made:

- C_D can assume a negative value: this is in general interpreted as a synonym of the back-scatter;
- If $M_{kl} \rightarrow 0 \Rightarrow C_D \rightarrow \infty$.

These two situations lead to instability of the solution. A common practice to overcome the problem (see for example Piomelli and Liu (1995)) is to average, in time and/or along homogeneous directions, the numerator and the denominator of Eq. (2.34).

In addition the following conditions need also to be verified in order to obtain a physically acceptable solution:

$$\begin{cases} \nu + \nu_t \geq 0 \\ C_D \leq C_s^2 \end{cases} \tag{2.35}$$

where C_s is the value of the Smagorinsky constant used for isotropic turbulence. With the Germano Dynamic Model no damping function is required in the near wall region.

2.3.4 Non isotropic modelling

The development of most LES models is done under the framework of isotropic flows. In a case where the flow is anisotropic some adaptations are required. A common example is the introduction of the Van Driest (1956) damping function for the turbulent viscosity in case of a wall bounded flow. In these types of flows the cells, and in particular in the near wall region, are far from isotropic (i.e. perfect cube) and the usual filter width proposed by Deardorff (1970), where the filter width is simply the cube root of the cell volume[9], is questionable.

$$\Delta(\overrightarrow{x}) = (\Delta_1(\overrightarrow{x})\Delta_2(\overrightarrow{x})\Delta_3(\overrightarrow{x}))^{1/3} \tag{2.36}$$

---

[8] Since M_{ij} is deviatoric $\Rightarrow M_{ij} L_{ij} = M_{ij} L^a_{ij}$.

[9] Most authors use twice the cube root of the volume because the smallest eddy which can be resolved has to be composed by at least two cells.

where $\Delta_i(\overrightarrow{x})$ is the filter width in the i^{th} direction. Some simple modifications, in order to take into account mesh stretching, could be (see Sagaut (2001)):

$$\Delta(\overrightarrow{x}) = \sqrt{\frac{1}{3}\left(\Delta_1^2(\overrightarrow{x}) + \Delta_2^2(\overrightarrow{x}) + \Delta_3^2(\overrightarrow{x})\right)} \tag{2.37}$$

$$\Delta(\overrightarrow{x}) = \max\left(\Delta_1(\overrightarrow{x}), \Delta_2(\overrightarrow{x}), \Delta_3(\overrightarrow{x})\right) \tag{2.38}$$

A more complex modification of the filter width due to cell stretching is proposed by Scotti et al. (1993) where the filter width is computed as:

$$\Delta(\overrightarrow{x}) = \Delta(\overrightarrow{x})_{iso} f\left(a_1, a_2\right) \tag{2.39}$$

where $\Delta(\overrightarrow{x})_{iso}$ is defined in Eq. (2.36), f is a function depending on the ratios a_1 and a_2, which are computed as $a_i = \Delta_i/\Delta_{max}$[10].

All these approaches can be brought back to the isotropic modelling where just only one length is defined for the filter width. Another possibility, when cells are extremely stretched in one direction, is to introduce several lengths and have a variable filter width depending on the direction. An example is presented in Bardina et al. (1983) where a tensorial formulation related with the cell geometry is proposed for the filter width. Of course the modelling stages becomes more complex with this latter option. However the validity of LES performed on very stretched grid can be questionable.

Schumann's decomposition

Another way to approach inhomogeneous flow is proposed by Schumann (1975). The method consists of splitting the velocity field into locally isotropic and inhomogeneous parts. The model can consequently be formulated as follows:

$$\tau_{ij}^a = \underbrace{-2\nu_r\left(\overline{S_{ij}} - \left\langle\overline{S_{ij}}\right\rangle\right)}_{Locally\,isotropic} - \underbrace{2\nu_a\left\langle\overline{S_{ij}}\right\rangle}_{inhomogeneous} \tag{2.40}$$

where ν_r can be considered as a sub-grid viscosity which is computed from a transport equation for the sub-grid kinetic energy. The inhomogeneous term is instead treated in a RANS way and the turbulent viscosity ν_a is evaluated with a mixing length model. The angular parentheses $\langle\rangle$ denote an average quantity.

Other authors, instead, treat both terms in a "LES fashion", using for both viscosities a sub-grid formulation. An example is presented by Moin and Kim (1982) where both viscosities are evaluated as:

---

[10] Δ_{max} is computed using Eq. (2.38) and Δ_i are the other two smaller filter widths.

$$\begin{cases} \nu_r = (C_1\Delta)^2 \sqrt{2\left(\overline{S_{ij}} - \langle \overline{S_{ij}} \rangle\right)\left(\overline{S_{ij}} - \langle \overline{S_{ij}} \rangle\right)} \\ \nu_a = (C_2\Delta_y)^2 \sqrt{\langle \overline{S_{ij}} \rangle \langle \overline{S_{ij}} \rangle} \end{cases} \tag{2.41}$$

where C_1 and C_2 are two arbitrary constants and the two filter widths are defined as:

$$\begin{cases} \Delta = (\Delta_1\Delta_2\Delta_3)^{1/3}\left(1 - \exp\left(y^+/A^+\right)\right) \\ \Delta_y = \Delta_y \left(1 - \exp\left(\left(y^+/A^+\right)^2\right)\right) \end{cases} \tag{2.42}$$

where y is the wall normal direction Δ and Δ_y are two filter widths associated with ν_r and ν_y. Both filter widths are damped using the Van Driest damping for Δ and a modified Van Driest with quadratic argument for the exponential for Δ_y. A^+ is a constant equal to 25 and y^+ is the dimensionless distance from the wall.

2.3.5 PASSIVE SCALAR MODELLING

In the same manner as for the hydrodynamic field, presented in Sec. 2.2, a length scale needs to be introduced in order to describe scalar dynamics. This scale is named after Corrsin (1951):

$$\eta_\theta = \left(\frac{\varepsilon}{\Gamma^3}\right)^{1/4} = \left(\frac{1}{Pr}\right)^{3/4} \eta \tag{2.43}$$

with η the Kolmogorov scale defined in Eq. (2.5). The ratio between cut-off wave numbers consequently scales as:

$$\frac{k_\theta}{k} = Pr^{3/4} \tag{2.44}$$

with $k_\theta = 2\pi/\eta_\theta$ wave cut-off number for the scalar field and $k = 2\pi/\eta$ wave number cut-off for the velocity. [11]

Three different regimes can be encountered:

1. $Pr \ll 1$: when the diffusivity is much bigger than the kinematic viscosity. In this case the scalar cut-off wave number is smaller than the one for the velocity. Thinking in terms of boundary layer (B.L.) thickness the velocity B.L. is smaller than thermal one.

2. $Pr \simeq 1$: in this case both cut-off wave numbers are comparable. Consequently the two boundary layers have similar thickness.

---

[11] The Obukhov-Corrsin definition is not valid at very high Prandtl numbers, for which Batchelor (1959) derived a wave number defined as:

$$k_B = \left(\frac{\varepsilon}{\nu\lambda^2}\right)^{1/4}$$

3. $Pr \gg 1$: when the velocity cut-off is larger that the one for scalar. This case is more complex because the scalar length is smaller than the velocity length, with the consequence that the thermal boundary layer has a smaller thickness.

The simplest closure approach for the scalar modelling is to use a *gradient diffusion hypothesis,* where a sub-grid Prandtl number is introduced and the sub-grid diffusivity is defined as:

$$\Gamma_{SGS} = \frac{\nu_{SGS}}{Pr_{SGS}} \tag{2.45}$$

Pr_{SGS} is in general a constant and is evaluated in order to better fit reference results. In the literature the value varies between 0.1 and 1, with a common value around 0.7 [12]. This option is also the most used in most of the CFD codes even if it is a crude approximation.

Moin et al. (1991) present a generalization of the dynamic model (see 2.3.3.2) including scalar transport. The same dynamic procedure is applied to the calculation of a sub-grid Prandtl number. It is interesting to notice that, in the case of a turbulent channel flow at $Re_\tau = 180$ (Reynolds number based on the friction velocity), Pr_{SGS} has a wide variation ranging from more than 1 in the near wall region, to 0.6 at the centre of the channel.

Schumann's decomposition of Section 2.3.4, can be also applied to the heat transfer modelling (see Grötzbach (1979); Grötzbach and Schumann (1979)) leading to the following formulation for the heat fluxes:

$$\tau_j^R = -\Gamma_r \frac{\partial}{\partial x_j} \left(\overline{\theta} - \langle \overline{\theta} \rangle \right) - \Gamma_a \frac{\partial \langle \overline{\theta} \rangle}{\partial x_j} \tag{2.46}$$

2.4 HYBRID RANS/LES COUPLING

The use of LES to study 3D transient flows has been in huge growth, in particular because of the ability of the method to give quantitatively better information than those provided by a usual RANS calculation. Despite this the application of LES to high Reynolds number wall bounded flow is still an issue due to computational constraints. For those types of flows a large amount of control volumes is necessary in order to capture all the scales responsible for the turbulent production and to avoid the deficiencies of most of the LES models to take into account anisotropy and non-equilibrium.

Wall modelling is necessary to keep the computational cost of the simulation reasonable. A first simple approach is to use the so called "wall-function" approach to

---

[12] The reason of a Pr_{SGS} smaller that 1 is often explained because the ability of temperature hot spot to diffuse more with respect to a velocity peak, without counter action from pressure.

provide the right amount of shear stress at the first cell, which is located far above the laminar sub-layer ($y^+ \gg 5$). Wall functions can range from simple models based on the "log law", to a resolution of simplified equations in the near wall region. For a detailed presentation about wall model requirements refer to Baggett (1997).

Another way to reduce LES mesh requirements is to hybridise it with another type of computational technique able to provide lower frequency solution at cheaper computational cost. The obvious candidate is RANS. Hybrid RANS/LES models can be divided into three main groups following Sagaut (2001):

1. *Non-linear disturbance equations*: the method is firstly proposed by Morris et al. (1997) in which the flow field is divided into a steady or low frequency part and a high frequency or fluctuating part. The first is computed with a RANS approach and the second with a LES method. The result is a generalized form of the Navier-Stokes equations written in a perturbation form.

2. *Universal modelling*: in this case the sub-grid model is generalised by including a combination of RANS and usual LES modelling. Those models are designed in a way to recover asymptotically the behaviour of typical RANS, with the inclusion of some LES capabilities. The aim is to make the sub-grid model able to deal with coarse meshes and then move the cut-off to lower frequencies. An example of this type of modelling is Germano's Hybrid model presented in Germano (1999, 2004).

   The model starts from the definition of a hybrid filter as a sum of LES and RANS filters. The main outcome is that the residual stress tensor has three contributions: the LES term, the RANS term and an extra term, which arises from the blending between the two types of filters.

3. *Zonal decomposition*: with this approach the domain is divided into sub-domains, with some domains treated with RANS and the remaining with LES.

The zonal decomposition has received most attention by many different research groups and can be divided into two main types: the sharp and the smooth transition. In the first family the RANS and the LES parts are divided by a defined interface. The communication between the two regions is in general done by exchanging boundary conditions. A problem arises because the fluctuating part, ignored by the RANS sub-domain, has to be reconstructed in order to have proper boundary conditions for the LES domain. An example of this type of technique is presented in Davidson and Peng (2003), where both plane channel flow and flow over a periodic hill are considered. The near wall region ($y^+ \leq 60$) is computed with a $k - \omega$ model and the inner region is modelled with a one equation model for the sub-grid stress tensor. The interface is fixed and Neumann boundary conditions are applied for the RANS sub-domain. The results are better than LES on the same coarse meshes but some problems are pointed out. Firstly results are dependent from the location of the matching plane between RANS and LES and, secondly, the velocity shows a sudden acceleration at this interface. This problem is more evident in the channel flow simulation. This may be, according to the authors, due to the smoothing produced by the convective and diffusive transport in the latter case. As already mentioned, RANS domain does not contain enough turbulent characteristics and the LES part is not supplied with the right amount of fluctuations. Improvements in the results for the channel flow calculation are obtained in Davidson and Dahlstrom (2005); Davidson and Billson (2006), where fluctuations are imposed at the interface. In the first case, fluctuations are computed from a DNS database for a generic boundary layer, in the second case they are computed with a Synthetic Eddy Method (SEM). The same method is also used for the plane diffuser finding better results than usual RANS simulation.

Another sharp transition approach is presented by Temmerman et al. (2005). In this case the key feature is to impose a continuity constraint to the turbulent viscosity at the interface. The coefficient C_μ (see Appendix A for definition) is computed at the interface as ratio between average LES turbulent viscosity and RANS viscosity and after it is used to increase the RANS viscosity, via an exponential function, as the wall is approached. Many different RANS models and different locations of the interface have been tested finding better results than analogue coarse LES. The model is also tested on a series of periodic hills finding, instead, worse results than pure LES on same meshes. The approach gives an excessively long recirculation zone with respect to the reference solution. Evidence suggests that the problem is caused by defects in the wall shear stress provided by the RANS model. The same method is also compared with LES with wall functions (standard log law and zonal two-layer strategy) in Tessicini et al. (2006) for different test cases. The Hybrid method in general provides better results because it permits to place the interface further away from the wall. On the other hand the two-layers approach is very simple, economical and far more accurate than a standard log-law wall function.

Keating et al. (2006) applied Hybrid RANS/LES to attached boundary layers. Authors found that a Synthetic Eddy Method is not sufficient to reconstruct the fluctuating field because the method needed long distance (about 10-20 times the boundary layer thickness) to develop proper phase relationships between the modes. A forcing term was introduced with the result of a decrease of the development distance to 1-2 boundary layer thicknesses.

A very popular technique, that can be included in the smooth transition family, is the so-called Detached Eddy Simulation (DES). The method consists in an unsteady RANS model in which the turbulent length scale is switched to a LES filtered type when a separation occurs. This is actuated by damping the turbulent viscosity. The original formulation of DES model is presented by Spalart et al. (1997) using a one equation Spallart-Allmaras model, but later many other models are incorporated in the same framework e.g. Mockett et al. (2005). The drawback for this type of approach is when the near wall region is approached and fine meshes are employed. In this part of the domain the RANS length scales might become much larger than those imposed by the mesh, leading the method to a grid induced separation as proved by Menter et al. (2003). As the name suggests the model works with highly separated flows, but it does not performs very well with wall bounded flow. The problem is taken into account and corrected in Spalart et al. (2006) where the concept of Delayed Detached Eddy Simulation (DDES) is introduced.

Another type of smooth transition model can be extended from the splitting technique proposed by Schumann (1975) and also briefly recalled in Section 2.3.4. In this case the anisotropic part of the residual stress tensor is corrected with a term computed with a RANS approach. The two terms that compose the stress tensor, are blended using a blending function, in order to obtain a smooth transition between the RANS and the LES sub-domains. This method was first proposed by Baggett (1998), finding some controversial results: unphysical very elongated streaks in the streamwise direction were formed in the RANS region. As a consequence there is a decorrelation of the fluctuation in the streamwise and wall normal direction that must be compensated by a larger velocity gradient. The result is a shift toward higher distance from the wall of the intercept of the logarithmic region. The reason of all this seems to be more caused by the low resolution in the near wall region rather than a modelling deficiency. Many authors try to alleviate the problem by introducing different types of corrections. Piomelli et al. (2003) move the interface more close to the wall in combination with a less dissipative sub-grid model without a big improvement of the results. On the other hand the introduction of a back-scatter forcing term in the region immediately below the interface is proven beneficial. Good results are also found by Hamba (2003), introducing an overlap region in which the model switches smoothly from the RANS to the LES.

In the family of the smooth transition models a very interesting model is presented by Abe (2005). In this case a non-linear eddy viscosity model is used in both domains. In the RANS part uses a $k-\epsilon$ base model, whereas the LES part employs an algebraic definition. The blending function is parameterised using the wall distance and the grid size. Several channel flows are computed finding good results in terms of mean velocity profiles, but with a stronger stress anisotropy caused by some suppression of energy redistribution from the streamwise to the wall normal and the spanwise directions.

A complete review of different Hybrid methods and their application can be found in Fröhlich and von Terzi (2008).

2.4.1 Hybrid RANS/LES formulation

This section presents the Hybrid model used in this work. The model is based on Schumann's decomposition recalled in Section 2.3.4. This model was originally formulated by Uribe et al. (2009). Here the model is extended with some improvements in the blending function definition and the addition of the heat transfer modelling (Rolfo et al. (2010)).
From Equations (2.40) and (2.46) the sub-grid terms can be expressed as:

$$\begin{cases} \tau^a_{ij} = -2\nu_r \left(\overline{S_{ij}} - \left\langle \overline{S_{ij}} \right\rangle\right) - 2\nu_a \left\langle \overline{S_{ij}} \right\rangle \\ \tau_j = -\Gamma_r \dfrac{\partial}{\partial x_j} \left(\overline{\theta} - \left\langle \overline{\theta} \right\rangle\right) - \Gamma_a \dfrac{\partial \left\langle \overline{\theta} \right\rangle}{\partial x_j} \end{cases} \tag{2.47}$$

For the homogeneous part a simple Smagorinsky model based on the fluctuating strain is used (Moin and Kim (1982)), leading to the following expression for the sub-grid turbulent viscosity:

$$\nu_r = \left(C_s \Delta\right)^2 \sqrt{2 s'_{ij} s'_{ij}} \tag{2.48}$$

with $s'_{ij} = \overline{S_{ij}} - \left\langle \overline{S_{ij}} \right\rangle$ and a filter width equal to twice the cubic root of the cell volume ($\Delta = 2 \cdot \Omega_I^{1/3}$). The $\varphi - \overline{f}$ model of Laurence et al. (2005) is used to compute the average viscosity ν_a, and the description of the model can be found in Section A.1.1 of the Appendix.

For the eddy conductivity a simple gradient diffusion hypothesis has been employed, obtaining the following expressions:

$$\begin{cases} \Gamma_r = \nu_r / Pr_{t,\gamma} \\ \Gamma_a = \nu_a / Pr_{t,a} \end{cases} \tag{2.49}$$

where $Pr_{t,\gamma}$ is the Turbulent Prandtl number for the locally isotropic (i.e LES) contribution and $Pr_{t.a}$ the one for the inhomogeneous part. This model allows the possibility to have two different control parameters for both contributions to the modelled heat flux. The influence of these two constants on the thermal field is investigated in Chapter 5, Section 5.3.1. However in order to have an idea about the turbulent Prandtl number variation the reader should refer to Moin et al. (1991). The paper shows a large variation of the parameters moving from the near wall region to the centre of the channel. For coarse meshes a variation depending of the molecular Prandtl number is also observed.

In order to introduce a smooth transition between the resolved and the ensemble average turbulent parts a blending function is introduced and the sub-grid terms of Eq. (2.47) are rewritten as:

$$\begin{cases} \tau^a_{ij} = \overbrace{-\mathcal{F}_b 2\nu_r \left(\overline{S_{ij}} - \left\langle \overline{S_{ij}} \right\rangle\right)}^{Locally\,Isotropic} - \overbrace{(1-\mathcal{F}_b)\, 2\nu_a \left\langle \overline{S_{ij}} \right\rangle}^{Inhomogeneous} \\ \tau^R_j = -\mathcal{F}_b \Gamma_r \dfrac{\partial}{\partial x_j}\left(\overline{\theta} - \left\langle \overline{\theta} \right\rangle\right) - (1-\mathcal{F}_b)\,\Gamma_a \dfrac{\partial \left\langle \overline{\theta} \right\rangle}{\partial x_j} \end{cases} \tag{2.50}$$

The average of the sub-grid modelled terms can be expressed as:

$$\begin{cases} \left\langle \tau^a_{ij} \right\rangle = -\,(1-\mathcal{F}_b)\, 2\nu_a \left\langle \overline{S_{ij}} \right\rangle \\ \left\langle \tau^R_j \right\rangle = -\,(1-\mathcal{F}_b)\,\Gamma_a \dfrac{\partial \left\langle \overline{\theta} \right\rangle}{\partial x_j} \end{cases} \tag{2.51}$$

where only the RANS contribution takes place. Consequently the total Reynolds stresses and heat fluxes take the following formulation:

$$\begin{cases} \left\langle u'_i u'_j \right\rangle_{TOT} = \left\langle u'_i u'_j \right\rangle_{RES} - 2\nu_a (1-\mathcal{F}_b) \left\langle \overline{S_{ij}} \right\rangle \\ \langle u'_i \theta' \rangle_{TOT} = \langle u'_i \theta' \rangle_{RES} - (1-\mathcal{F}_b)\,\Gamma_a \dfrac{\partial \left\langle \overline{\theta} \right\rangle}{\partial x_j} \end{cases} \tag{2.52}$$

where $\left\langle u'_i u'_j \right\rangle_{RES}$ are the resolved Reynolds stresses and $\langle u'_i \theta' \rangle_{RES}$ the resolved heat fluxes. The rate of energy transfer from the filtered motion to the residual is estimated as[13]:

$$\begin{aligned} -\left\langle \tau^a_{ij} \overline{S_{ij}} \right\rangle &= 2\left\langle \nu_r \mathcal{F}_b \left(\overline{S_{ij}} - \left\langle \overline{S_{ij}} \right\rangle\right) \overline{S_{ij}} \right\rangle + 2(1-\mathcal{F}_b)\left\langle \nu_a \left\langle \overline{S_{ij}} \right\rangle \overline{S_{ij}} \right\rangle \\ &= 2\nu_r \mathcal{F}_b \left(\left\langle \overline{S_{ij} S_{ij}} \right\rangle - \left\langle \overline{S_{ij}} \right\rangle \left\langle \overline{S_{ij}} \right\rangle\right) + 2(1-\mathcal{F}_b)\,\nu_a \left\langle \overline{S_{ij}} \right\rangle \left\langle \overline{S_{ij}} \right\rangle \end{aligned} \tag{2.53}$$

Eq. (2.53) shows that RANS viscosity contributes to the dissipation only in association with the mean motion, consequently the LES resolved turbulent fluctuations are free to develop independently.

2.4.2 Blending Function

The blending function $\mathcal{F}_b$ can be parameterised using the ratio between a turbulent length scale computed from the average field and the filter width of LES, leading to:

$$\mathcal{F}_b = \tanh\left(C_l \frac{L_t}{\Delta}\right)^n \tag{2.54}$$

---

[13] It is assumed that $\left\langle \nu_r \overline{S_{ij} S_{ij}} \right\rangle \approx \nu_r \left\langle \overline{S_{ij} S_{ij}} \right\rangle$ as proposed by Nicoud et al. (2001).

where $L_t = \varphi k^{3/2}/\varepsilon$ is a turbulent length computed from the RANS field. In the original formulation (Uribe et al. (2009)) the empirical constants were set to $C_l = 1$ and $n = 1.5$. In this work their values are changed to $C_l = 1.3$ and $n = 2$, in order to have a better agreement with the velocity profile for channel flow at $Re_\tau = 395$. Furthermore a new definition of the filter width Δ is introduced:

$$\Delta = \max\left(2\Omega_I^{1/3}, \frac{2}{3}\left(\Delta_1 + \Delta_2 + \Delta_3\right)\right) \tag{2.55}$$

where Δ_1, Δ_2, Δ_3 are the max cell dimensions in directions x_1, x_2, x_3. When $\Delta_1 \approx \Delta_2 \approx \Delta_3 \Rightarrow 2\Omega_I^{1/3} \approx \frac{2}{3}\left(\Delta_1 + \Delta_2 + \Delta_3\right)$. When instead a cell is stretched in one or two directions or a cell is highly skewed $2\Omega_I^{1/3} \ll \frac{2}{3}\left(\Delta_1 + \Delta_2 + \Delta_3\right)$. In these cases the filter width Δ is kept bigger and consequently more "RANS" is performed. The changing of the definition for the filter width is used only for the calculation of the blending function. If this new filter width is applied also to the LES part a new validation of the Smagorinsky model employing the new constant should be necessary. The objective of this small modification is only to trust more the RANS model than the LES in case of a very skewed or stretched cell.

2.4.3 AVERAGING PROCEDURE

In order to compute the sub-grid stress tensor, heat fluxes (Eq. 2.50) RANS viscosity ν_a, average velocities and temperature are necessary. A first possibility could be to perform a space averaging along homogeneous directions. This procedure is relatively easy in the case of channel flow and structured mesh, but in a fully 3D flow and unstructured mesh this operation is no more possible. A second possibility is to perform a standard time average defined as:

$$\langle u_i \rangle = \frac{1}{N}\sum_{i=1}^{N} u_i \tag{2.56}$$

Where N is the number of samples. In this work instead a time running average is performed, making the model respond quickly to changes:

$$\langle u_i \rangle^{n+1} = c u_i^{n+1} + (1 - c)\langle u_i \rangle^{n} \tag{2.57}$$

Where c is a constant used to control the time window size[14] and superscripts indices stand for the time step. In the case of channel flow, the use of a running or a usual ensemble average does not affect the results. The window size for the running average also does not affect largely the results as long as it is kept well above the eddy turn over

---

[14] Time window is the time over which is performed the running average and it is composed by a fixed number of time steps decided a priori.

time[15]. The main advantage of the running average, with respect to the time average, is the save in CPU time. In the case of very small windows for the running average, the mean values have strange fluctuations and the mean strain becomes large in the region far from the wall. A good practice is to initialize the running average with a mean value computed with a precursor RANS simulation, in order to reduce the time necessary to have constant values for the variables.

---

[15] In the case of channel flow a value of $10\frac{\delta}{u_\tau}$ is used as optimum size for the time window. In order to have good and stable results the time window has to be no smaller than $5\frac{\delta}{u_\tau}$ seconds. δ is the channel height and u_τ is the shear velocity.

Chapter 3

NUMERICAL METHODS

In this chapter the discretization techniques employed in *Code_Saturne* are briefly introduced. More details about the code are given in Archambeau et al. (2004). A complete overview of the most common computational methods for CFD, using finite volume or Finite Differences, is available in the book of Ferziger and Peric (1997). In the case of Finite Elements refer to the books of Chung (1978) and Ern and Guermond (2004).

3.1 MESH GENERATION

Grid generation is often considered as the most important and most time consuming part of CFD simulation. The quality of the grid plays a direct role on the final quality of the analysis, regardless of the flow solver used. Additionally, the solver will be more robust and accurate when using a well-constructed mesh. It is important for the CFD user to know and understand all of the various grid generation methods. Only by knowing all the methods can the right tool be selected to solve the problem at hand. It is possible to distinguish several ways of discretising a complex geometry:

- Coordinate transformations
- Structured grids
  - Hexahedral grids
  - Multi-blocks grids
  - Overlapping grids
- Unstructured grids
- Hybrid grids.

A more comprehensive review with many sharp cues can be found in Baker (2005), or in the book of Thompson et al. (1999).

3.1.1 GENERALIZED CURVILINEAR COORDINATES

The computation of flow-fields in and around a complex shape involves computational boundaries that do not coincide with coordinate lines in physical space. For finite difference methods, the imposition of boundary conditions for such problems has required a complicated interpolation of the data on local grid lines and, typically, a local loss of accuracy in the computational solution. Such difficulties motivate the introduction of a mapping or transformation from physical (x, y, z) space to a generalised curvilinear coordinate (ξ, η, ζ) space. This technique is used since the beginning of CFD when it was still performed by hand calculations like in Thom (1933). The generalized coordinate domain is constructed so that a computational boundary in physical space coincides with a coordinate line in generalised coordinate space. The use of generalised coordinates implies that a distorted region in the physical domain is mapped into a rectangular region in the generalized coordinate space. The governing equations are expressed in terms of generalised coordinates as independent variables and the discretization is undertaken in the generalised coordinate space. Thus the computation is performed in the generalised coordinate space, effectively. The concept of generalised coordinates suggests additional possibilities. First, the computational grid in generalised-coordinate space can correspond to a moving grid in physical space as would be appropriate for an unsteady flow with boundary movement. The mapping between physical and generalised-coordinate space permits grid lines to be concentrated in parts of the physical domain where severe gradients are expected. If the severe gradient region changes with time (e.g. shock-wave propagation) the physical grid can be adjusted in time to ensure that the local grid is sufficiently refined to obtain a accurate solution. The use of generalised coordinates introduces some specific complications; it is necessary to consider what form the governing equations take in generalized coordinates. In this case they contain additional terms that define the mapping between the physical and the generalised-coordinate domains. These additional terms usually need to be discretised and this introduces an additional source of error in the solution.

3.1.2 STRUCTURED GRIDS

Structured meshes in general display a very regular pattern composed by quadrilateral elements in 2D and hexahedral elements in 3D. Structured grids depend on the creation of blocks, which are shaped in order to fit the geometry (body fitted meshes). In order to improve the orthogonality and the uniformity of the grid, mesh optimization algorithms, based on sophisticated elliptic equations, were extensively developed and can be found in most of the commercial mesh generators (for example Gambit, or ICEM CFD refer to Thompson et al. (1999)). In the past, structured meshes could only consist of one block, and various cell flagging schemes were used to "turn off" portions of the block to model obstacles. Later, multi-block was developed allowing several blocks to be connected together in order to discretise the whole geometry (Lee et al. (1980)). Several types of block connections were developed and this gives more freedom in the mesh generation, but the block connection can still place some limitations in the meshing procedure.

A possible solution to the problem is to use Chimera or overset grids (see for example Chesshire and Henshaw (1990)), where blocks are free from the physical boundary and can overlap. This technique uses interpolation of data between different meshes and can generate a large source of error. However in case of very complicated geometries, where usual meshing techniques produce high degree of distortion, or moving meshes, Chimera grids can guarantee a high level of orthogonality.

The main advantage of structured grids is high degree of control over the mesh. In addition, hexahedral and quadrilateral elements can support a certain amount of skewness and stretching without affecting the quality of the solution. This allows the user to concentrate control points in key areas, for example in regions of sharp gradients. Another important feature is that the mesh is, in general, aligned with the main flow direction increasing the accuracy of the solver. Structured codes are, in general, faster than unstructured codes and the implementation of high order schemes is easier.

The major drawback is the requirement of very experienced users in order to build a suitable mesh. Indeed the meshing procedure can be extremely long and measured in days if not weeks. Another disadvantage is that the refinement in one area can results in an addition of points where not necessary. In case of singularities in the geometry structured mesh does not perform well, displaying a high degree of skewness which might affect dramatically the solution.

3.1.3 Unstructured grids

Unstructured grids employ arbitrary elements to map the domain and because the arrangement of cells does not have a specific pattern, the mesh is called unstructured. In general this technique employs triangles in 2D and tetrahedra in 3D. Unstructured mesh techniques have a large degree of automatization, requiring very little input from the user. Automatic meshing procedures are in general divided into two steps: first the meshing of the boundary and after the interior. This second step can be performed with two different types of strategies:

- *the advancing front* where elements touching the boundary are constructed (Thompson et al. (1999));
- *Delaunay* where points are added in the domain and afterwards connected (George and Borouchaki (1998)).

The main advantage is the already mentioned high level of automatization. The user does not need to worry about laying out block structure or connections. There is no need for the user to create structured blocks and also inexperienced users can produce suitable meshes for most applications. Indeed the mesh generation time is short in comparison with other techniques, measurable in minutes or hours.

A very attractive type is polyhedral cells, which possesses very interesting properties, is illustrated in Peric (2004). The starting point is a conventional tetrahedral mesh from where a dual-mesh is generated: edge mid points, face centroids and cell centres are connected forming new quadrilateral faces. Those faces are linked in order to form a polyhedron. At this stage a large number of faces is generated, consequently an optimization has to be performed which consists of merging the quadrilateral faces which lie between two original nodes of the primitive tetrahedral mesh. In comparison with tetrahedral, polyhedral cells have more neighbours (in general ten cells) making the local gradient calculation approximation better. Moreover polyhedral cells are also less sensitive to stretching with respect to usual tetrahedral. The main problem of this type of cells is the creation of warped faces, where the face centre lays out of the face plane.

The major drawback of unstructured grids is the lack of user control when laying out the mesh. In general the user has some control of the mesh generation of the boundary, typically on the edges of the geometry, but the program fills automatically the interior. Moreover, triangle and tetrahedral elements are not very suitable for skewing or stretching, and in general the grids are largely isotropic, creating problems when a refinement has to be placed in a specific direction, like across a boundary layer. This problem is frequently resolved by over-refining the mesh, with an obvious impact of the simulation speed up. Another more recent solution is the introduction of a prism layer close to the wall, where cells retain their unstructured form (both triangular or polyhedron) in planes parallel to the wall, but in the wall normal plane the cell cross-section has a quadrilateral shape (Ferziger and Peric (1997)). This solution is now extensively used in most of the commercial packages like ICEM-CFD and STARCCM+. The success of the meshing stage highly depends on very precise CAD models. In fact most of the mesh generation failures are due to imperfections, sometimes even microscopic, of the CAD model. Unstructured solvers are typically slower than structured codes and the implementation of high order schemes is complicated. Post processing of the solution is difficult and requires specific and very powerful tools.

3.1.4 Hybrid grids

Hybrid grids are obtained by combining structured and unstructured meshes, trying to combine the positive aspects of the two types. Hybrid grids can contain every single type of element presented above according to their strengths and weaknesses. An example is embedded refined meshes, using so-called hanging nodes. These meshes can be considered as a particular type of Hybrid grid, where a structured multi-block approach is employed, but without the need of mesh matching at the interface. This procedure improves the flexibility of the multi-block approach and it is widely used in case of wall refinements (see Kravchenko et al. (1996)). In this framework, adaptive mesh refinements (AMR) gain a certain degree of popularity (see Iaccarino and Ham (2005)) and can be found in commercial meshing packages like ICEM-CFD and STARCCM+. The method consists in a successive decomposition of a Cartesian grid. A parent cell is divided into four (eight in 3D) children, and the connectivity follows a typical tree-like structure also called OCTAL-TREE.

3.2 DISCRETIZATION TECHNIQUES

Mathematical models presented in Chapter 2 have now to be discretised using a suitable numerical method. For the sake of clarity the discretization will be applied to the passive scalar equation only.

A general transport equation for a generic variable ϕ, can be written as:

$$\frac{\partial \rho\phi}{\partial t} + \frac{\partial}{\partial x_i}\left(\rho u_i \phi\right) - \frac{\partial}{\partial x_i}\left(\Gamma_\phi \frac{\partial \phi}{\partial x_i}\right) = s_\phi \tag{3.1}$$

where u_i is the fluid velocity vector, Γ_ϕ is the diffusivity of ϕ and s_ϕ is the associated source term. Applying a Finite Volume Discretization Eq. (3.1) can be rewritten as:

$$\underbrace{\frac{\partial}{\partial t}\int_{\Omega_I} \rho\phi dV}_{T_I} + \underbrace{\int_{\partial\Omega_I} \rho u_i \phi n_i dS}_{C_I} - \underbrace{\int_{\partial\Omega_I} \Gamma \frac{\partial \phi}{\partial x_i} n_i dS}_{D_I} = \underbrace{\int_{\Omega_I} s_\phi dV}_{S_I} \tag{3.2}$$

where Ω_I is the volume of the I^{th} cell[1], $\partial\Omega_I$ is its boundary and with n_i are the components of the normal vector to the surface. T_I is the time dependent term, C_I the convection term, D_I the diffusion term and S_I the source term.

The next three sections provide details of discretization of different terms in Eq. (3.2). In an unstructured code a very important point is the gradient reconstruction. Details about its implementation are given in Sec. 3.2.4. LES is essentially a transient type of approach, therefore some details about time discretization are given in Section 3.3. The visualization of the discretization nomenclature is plotted in Fig. 3.1.

---

[1] Capital letters, in subscript position, denote a variable evaluated at the cell centre. Two capital letters point to a surface between two cells (refer to Fig. 3.1)

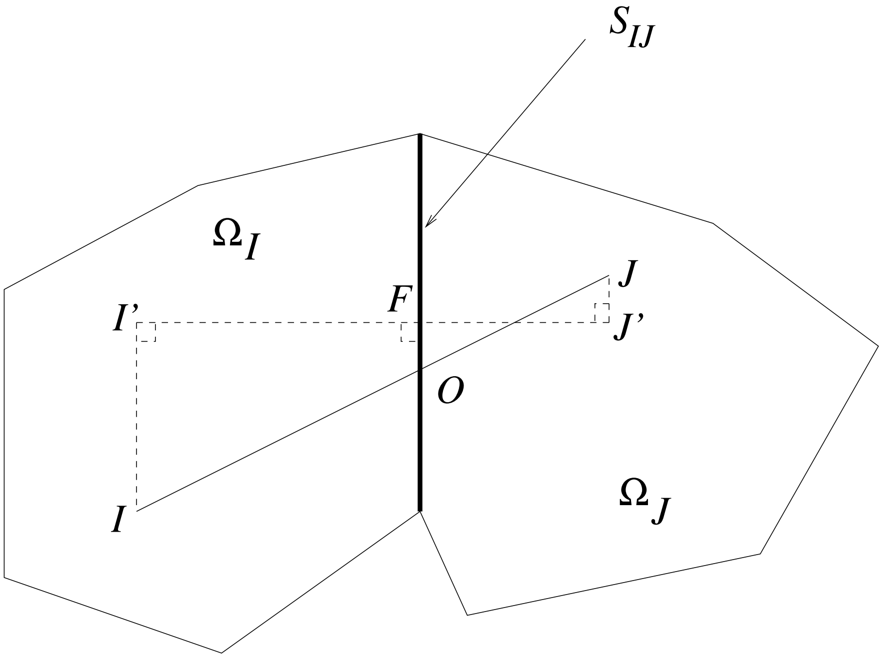

Figure 3.1: Labelling for the computation of the convection-diffusion term.

3.2.1 Temporal and source terms

The first approximation consists of computing the volume integral as:

$$\int_{\Omega_I} \phi dV \approx \phi_I \Omega_I \tag{3.3}$$

which is leading to rewrite terms T_I and S_I of Eq. (3.2) as:

$$T_I \approx \frac{\partial \phi_I \rho_I \Omega_I}{\partial t} \qquad S_I \approx s_{\phi_I} \Omega_I \tag{3.4}$$

3.2.2 Convection term

The convective term of Eq. (3.2) can be written as:

$$C_I = \int_{\partial \Omega_I} \rho u_i \phi n_i dS \approx \sum_{J \in \aleph(\Omega_I)} \phi_{IJ} (\overrightarrow{u}_{IJ} \cdot \overrightarrow{n}_{IJ}) S_{IJ} = \sum_{J \in \aleph(\Omega_I)} \phi_{IJ} m_{IJ} \tag{3.5}$$

where $\aleph(I)$ represents the set of cells that are neighbours of the volume Ω_I, ϕ_{IJ} is the value of the scalar at the face centre between cell I and cell J, $\overrightarrow{n}_{IJ}$ is the vector normal to the face and m_{IJ} is the mass flux between these two adjacent cells. In *Code_Saturne* the convective term is discretised with the following schemes:

1. Up-Wind (UW): this is a first order scheme, which is based on the nearest upwind neighbour

$$\phi_{IJ}^{UW} \equiv \begin{cases} \phi_I & \text{IF } m_{IJ} \geq 0 \\ \phi_J & \text{IF } m_{IJ} < 0 \end{cases} \tag{3.6}$$

   This interpolation preserves the correct physical bounds on ϕ under all conditions, but it leads to numerical diffusion;

2. Linear upwind (SOLU): this is a special adapted, second order accurate scheme derived for an original proposal for structured meshes:

$$\phi_{IJ}^{SOLU} \equiv \begin{cases} \phi_I + \overrightarrow{IF} \cdot (\nabla\phi)_I & \text{IF } m_{IJ} \geq 0 \\ \phi_J + \overrightarrow{JF} \cdot (\nabla\phi)_J & \text{IF } m_{IJ} < 0 \end{cases} \tag{3.7}$$

   where $\overrightarrow{IF}$ and $\overrightarrow{JF}$ are distances between the cell and the face centre expressed in vectorial form. The gradient is computed explicitly from the solution at the previous time step.

3. Central Difference (CD): this scheme is also second order and it is based on a linear interpolation on the nearest neighbour value.

$$\phi_{IJ}^{CD} = \alpha_{IJ}\phi_I + (1 - \alpha_{IJ})\phi_J \tag{3.8}$$

   where $\alpha_{IJ} = \left\|\overrightarrow{FJ}\right\| / \left\|\overrightarrow{IJ}\right\|$. For regular meshes it is equal to 1/2. In the case of a non skewed mesh, where the line connecting the two cell centres does not pass through the face centre, the variable is firstly projected in points $I'$and J' (see Fig. 3.1) as:

$$\phi_{K'} = \phi_K + \frac{1}{2}\left((\nabla\phi)_I + (\nabla\phi)_J\right) \cdot \overrightarrow{KK'} \quad K = I \,\text{or}\, J \tag{3.9}$$

   and the interpolation at the face is performed as:

$$\phi_{IJ} = \alpha'_{IJ}\phi_{I'} + (1 - \alpha'_{IJ})\phi_{J'} \tag{3.10}$$

   being $\alpha^{'} = \left\|\overrightarrow{FJ'}\right\| / \left\|\overrightarrow{I'J'}\right\|$. In Eq. (3.9) a factor of 1/2 is used instead of the more appropriate α' and $(1 - \alpha')$ because of stability reason (see Benhamadouche (2006)).

4. Blended Differencing (BD): this is a scheme in which SOLU or CD is blended with UW as:

$$\phi_{IJ}^{BD} = \gamma \phi_{IJ}^{CD\, or\, SOLU} + (1-\gamma)\phi_{IJ}^{UW} \tag{3.11}$$

where γ is the weight coefficient for the CD or SOLU schemes.

A slope test, in order to verify if the variable ϕ is non-monotonic, is also present and **locally** reverts the convective term from a second order scheme (CD or SOLU) to a UW. The test is based on the calculation of an upwind gradient defined as:

$$\overrightarrow{G}_{c,I} \equiv \sum_{J \in \aleph(I\Omega_I)} \phi_{IJ}^{IIUW} \overrightarrow{n} S_{IJ} \tag{3.12}$$

where ϕ_{IJ}^{IIUW} is the variable at the interface using a second order upwind interpolation like:

$$\phi_{IJ}^{IIUW} \equiv \begin{cases} \phi_I + \overrightarrow{IF} \cdot (\nabla\phi)_I \;\; IF\ m_{ij} \geq 0 \\ \phi_J + \overrightarrow{JF} \cdot (\nabla\phi)_J \;\; IF\ m_{ij} < 0 \end{cases} \tag{3.13}$$

The first condition for the test to be activated is to verify that the dot product between the upwind gradient computed in I and J is negative or mathematically:

$$\overrightarrow{G}_{c,I} \cdot \overrightarrow{G}_{c,J} < 0 \tag{3.14}$$

In the case of a 1D problem the monotonicity of the solution can be also studied using the dot product of the function at the previous $I-1$ and the following $I+1$ discretization points. In a 3D FV context this is equivalent to projecting the gradient on the face. The final formulation of the slope test criteria is:

$$\begin{cases} \left(\left(\dfrac{\partial\phi}{\partial x_i}\right)_I \cdot \overrightarrow{n} S_{IJ}\right)^2 - \left(\overrightarrow{G}_{c,I} \cdot \overrightarrow{n} S_{IJ} - \dfrac{\phi_i - \phi_j}{\left\|\overrightarrow{I'J'}\right\|} S_{IJ}\right)^2 \;\; IF\ m_{ij} \geq 0 \\ \left(\left(\dfrac{\partial\phi}{\partial x_i}\right)_J \cdot \overrightarrow{n} S_{IJ}\right)^2 - \left(\overrightarrow{G}_{c,J} \cdot \overrightarrow{n} S_{IJ} - \dfrac{\phi_i - \phi_j}{\left\|\overrightarrow{I'J'}\right\|} S_{IJ}\right)^2 \;\; IF\ m_{ij} < 0 \end{cases} \tag{3.15}$$

The slope test is used to switch locally from a second order scheme to a first order upwind scheme when the solution is non-monotone. This might help in case of non-stable solutions, but with a reduction to first order of the accuracy. In the case of LES calculations reverting to first order accuracy has the effect to delay the transition from the laminar state to the turbulent state of the solution. The use of the slope test is investigated in Chapters 4 and 5 using a small but substantial modification: the slope test is reverted to a blended scheme as defined in Eq. (3.11) with a small percentage of up-winding. The percentage is chosen to keep the computation stable or to damp spurious oscillation due to numerical instability.

3.2.3 Diffusion term

The diffusive term D_I is computed as follows:

$$D_I = \int_{\partial\Omega_I} \Gamma_\phi \frac{\partial \phi}{\partial x_i} n_i dS = \sum_{J\in\aleph(\Omega_I)} \Gamma_{IJ} \left(\nabla\phi\right)_{IJ} \cdot \overrightarrow{n_{IJ}} S_{IJ} = \sum_{J\in\aleph(\Omega_I)} \Gamma_{IJ} \frac{\phi_{J'} - \phi_{I'}}{\left\| \overrightarrow{I'J'} \right\|} S_{IJ} \tag{3.16}$$

where the variable at the projection points I' and J' is computed using (3.9).

3.2.4 Gradient reconstruction

A key issue not yet developed is the gradient calculation. As stated in Eq. (3.9) the explicit value of the gradient at the cell centre is used to correct the effect of the non-orthogonality. An accurate approximation of the gradient is consequently a necessary requirement. In *Code_Saturne* several options are possible:

1. A least square method;
2. A generalized least square method based on extended neighbours (all cells sharing a cell vertex, but necessary a face);
3. An iterative reconstruction of the non-orthogonality based on the Green-Gauss theorem.

In this context only the last option is considered. Methods based on the least square method are not reviewed because of their diffusive effects and their high inaccuracy in cases of non-conformal meshes (see Ham and Iaccarino (2004)).

The starting point is the Green-Gauss theorem:

$$\int_{\Omega_I} \frac{\partial \phi}{\partial x_i} dV = \int_{\partial\Omega_I} \phi \vec{n} dS \approx \sum_{J\in\aleph(\Omega_I)} \phi_{IJ} \, \vec{n}_{IJ} \, S_{IJ} \tag{3.17}$$

Firstly the volume integral is approximated as in Eq. (3.3) giving:

$$\int_{\Omega_I} \frac{\partial \phi}{\partial x_i} dV = \frac{\partial \phi}{\partial x_i} \Omega_I \tag{3.18}$$

secondly the value ϕ_{IJ} is interpolated at the interface as:

$$\phi_{IJ} = \alpha'_{IJ}\phi_I + \left(1 - \alpha'_{IJ}\right)\phi_J + \frac{1}{2}\left((\nabla\phi)_I + (\nabla\phi)_J\right)\cdot\overrightarrow{FO} \tag{3.19}$$

where the factor $\frac{1}{2}$ is used for stability reasons. Combining Eq. (3.18) and (3.19) into (3.17) leads to the following formulation:

$$(\nabla\phi)_I\,\Omega_I = \sum_{J\in\aleph(\Omega_I)}\left[\alpha'_{IJ}\phi_I + \left(1 - \alpha'_{IJ}\right)\phi_J + \frac{1}{2}\left((\nabla\phi)_I + (\nabla\phi)_J\right)\cdot\overrightarrow{FO}\right]\overrightarrow{n}_{IJ}S_{IJ} \tag{3.20}$$

where the unknown is the gradient $(\nabla\phi)_I$ evaluated at the centre of mass of the cell. This system of equations can be solved with an iterative procedure as follows:

$$\begin{aligned}(\nabla\phi)_I^{\tau+1}\,\Omega_I - \sum_{J\in\aleph(\Omega_I)}\left[\frac{1}{2}\left((\nabla\phi)_I^{\tau+1}\cdot\overrightarrow{FO}\right)\overrightarrow{n}_{IJ}S_{IJ}\right] &= \\ \sum_{J\in\aleph(\Omega_I)}\left[\alpha'_{IJ}\phi_I + \left(1 - \alpha'_{IJ}\right)\phi_J + \frac{1}{2}(\nabla\phi)_J^{\tau}\cdot\overrightarrow{FO}\right]\overrightarrow{n}_{IJ}S_{IJ}\end{aligned} \tag{3.21}$$

where τ denotes the sub-iterations and the initial guess is done without taking into account the correction term due to non-orthogonality.

3.3 Time discretization

Time schemes are in general divided into two main categories: explicit and implicit. In *Code_Saturne* a combination of second order explicit and implicit time schemes, namely Adam-Bashforth (AB) and Crank-Nicolson (CN), are used Benhamadouche (2006). The formulation assumes constant time step and it fits well with LES, where time averaging is important. All terms are centred in time hence they are expressed at the time $n + \frac{1}{2}$.

Temporal term

The time term T_I of Eq. (3.4) is discretised using a fully implicit Euler scheme:

$$T_1 = \frac{\partial}{\partial t}\int_{\Omega_I}\rho\phi dV = \frac{\partial}{\partial t}\left(\phi_I\Omega_I\right) = \Omega_I\frac{\phi_I^{n+1} - \phi_I^n}{\Delta t} \tag{3.22}$$

where Δt is the time step. The time term has first order accuracy, but in case of right hand side (RHS) also expressed at $n + \frac{1}{2}$ the formulation becomes second order (see Benhamadouche (2006)).

Convection term

The mass flux in the convective term of Eq. (3.5) is evaluated explicitly at the time step $n + \frac{1}{2}$ using an AB scheme:

$$m_{IJ}^{n+\frac{1}{2}} = \frac{3}{2} m_{IJ}^{n} - \frac{1}{2} m_{IJ}^{n-1} \tag{3.23}$$

The variable ϕ_{IJ} at the face centre is instead evaluated with CN, which leads to:

$$\phi_{IJ}^{n+\frac{1}{2}} = \frac{1}{2} \left(\phi_{IJ}^{n+1} + \phi_{IJ}^{n} \right) \tag{3.24}$$

The convection term can be rewritten as:

$$\int_{\partial\Omega_I} \phi \vec{n} dS \approx \sum_{J \in \aleph(\Omega_I)} \left[\frac{1}{2} \left(\phi_{IJ}^{n+1} + \phi_{IJ}^{n} \right) \left(\frac{3}{2} m_{IJ}^{n} - \frac{1}{2} m_{IJ}^{n-1} \right) \right] \tag{3.25}$$

Diffusion term

In this case the CN scheme is applied to the main variable ϕ only. The diffusivity Γ is always explicit (i. e. evaluated with AB scheme) in order to avoid negative values, which may affect the stability of the solution.

$$\int_{\partial\Omega_I} \Gamma_\phi \frac{\partial \phi}{\partial x_i} n_i dS = \sum_{J \in \aleph(\Omega_I)} \left[\frac{1}{2} \Gamma_{IJ}^{n} \left((\nabla\phi)_{IJ}^{n+1} + (\nabla\phi)_{IJ}^{n} \right) \cdot \vec{n}_{IJ} S_{IJ} \right] \tag{3.26}$$

Source term

In general the source terms (i.e. the buoyant term in the momentum equations) are treated explicitly using the AB scheme.

$$S_I = s_\phi \Omega_I = \Omega_I \left(\frac{3}{2} s_{\phi_I}^{n} - \frac{1}{2} s_{\phi_I}^{n-1} \right) \tag{3.27}$$

For the pressure gradient term in the momentum equation a special treatment is used and is discussed in Section 3.5, where the velocity-pressure coupling is presented.

3.4 Transport equation

Finally the equation for the resolution of the unknown ϕ is discretised as follows:

$$
\begin{aligned}
\Omega_I \frac{\phi_I^{n+1}}{\Delta t} + \sum_{J\in\aleph(\Omega_I)} \Bigg[\frac{1}{2} \left(\frac{1}{2} \left(m_{IJ} + |m_{IJ}| \right) \phi_I^{n+1} + \frac{1}{2} \left(m_{IJ} - |m_{IJ}| \right) \phi_J^{n+1} \right) & \quad + \\
-\frac{1}{2} \Gamma_{IJ} \frac{\phi_J^{n+1} - \phi_I^{n+1}}{\left\| \overrightarrow{IJ} \right\|} S_{IJ} \Bigg] & \quad = \\
+\Omega_I \frac{\phi_I^{n}}{\Delta t} - \sum_{J\in\aleph(\Omega_I)} \left[\frac{1}{2} \phi_{IJ}^{n} m_{IJ} - \frac{1}{2} \Gamma_{IJ} \frac{\phi_{J'}^{n} - \phi_{I'}^{n}}{\left\| \overrightarrow{I'J'} \right\|} S_{IJ} \right] & \quad + \\
\Omega_I s_\phi &
\end{aligned}
\tag{3.28}
$$

where all the implicit terms are placed in the LHS and the explicit in the RHS. The implicit part of the LHS is evaluated using an UW scheme. The CD scheme and the reconstruction terms appear only on the RHS following the equations presented in Section 3.2. The mass flux and the physical properties are evaluated explicitly using the AB scheme of Eq. (3.23).

Equation (3.28) is solved in an iterative and incremental way because this allows to treat implicitly part of the correction term for the convection-diffusion term. Let us introduce the following increments of the variable ϕ as:

$$
\begin{cases}
\delta\phi^{n+1,k+1} = \phi^{n+1,k+1} - \phi^{n+1,k} \\
\delta\phi^{n+1,k} = \phi^{n+1,k} - \phi^{n+1,0}
\end{cases}
\tag{3.29}
$$

where, by definition, $\phi^{n+1,0} = \phi^n$ is the value at the previous time step and k the index for the sub-iteration. Applying the variations of Eq. (3.29) to the scalar solver (3.28) leads to:

$$
\begin{aligned}
\Omega_I \frac{\delta\phi_I^{n+1,k+1}}{\Delta t} + \sum_{J\in\aleph(\Omega_I)} \left[\frac{1}{2} \left(m_{IJ} + |m_{IJ}| \right) \delta\phi_I^{n+1,k+1} + \frac{1}{2} \left(m_{IJ} - |m_{IJ}| \right) \delta\phi_J^{n+1,k+1} \right] + \\
+ \sum_{J\in\aleph(\Omega_I)} \left[-\frac{1}{2} \Gamma_{IJ} \frac{\delta\phi_J^{n+1,k+1} - \delta\phi_I^{n+1,k+1}}{\left\| \overrightarrow{IJ} \right\|} S_{IJ} \right] = \\
+ \Omega_I \frac{\delta\phi_I^{n+1,k}}{\Delta t} - \sum_{J\in\aleph(\Omega_I)} \left[\frac{1}{2} \delta\phi_{IJ}^{n+1,k} m_{IJ} - \frac{1}{2} \Gamma_{IJ} \frac{\delta\phi_{J'}^{n+1,k} - \delta\phi_{I'}^{n+1,k}}{\left\| \overrightarrow{I'J'} \right\|} S_{IJ} \right] + \Omega_I s_\phi^n
\end{aligned}
\tag{3.30}
$$

This is equivalent to the resolution of a linear system of the type $\mathbf{Ax} = \mathbf{b}$ where $\mathbf{x}$ is the vector of the unknown, **b** is the RHS of Eq. (3.30) and **A** is a non symmetric matrix, but conditioned with an up-wind scheme. This discretization permits to reconstruct the RHS with the updated values $\phi^{n+1,k}$.

3.5 Velocity pressure coupling

In the case conservation of the momentum velocity and pressure are coupled and this has to be taken into account by the algorithm. In *Code_Saturne* a SIMPLEC algorithm is used. Rhie and Chow interpolation is applied to the Poisson equation in order to avoid the odd-even decoupling problem. The method consists of three different steps named: prediction, correction and test. Firstly the following increments have to introduced:

$$\begin{cases} \delta\vec{u} = \vec{u} - \vec{u}^{*} \\ \delta p^{k+1} = p^{k+1} - p^{k} \end{cases}$$

1. **Predictor step:** the momentum is resolved using an explicit pressure gradient computed from a known pressure field (i.e. from the previous iteration or sub-iteration). The predicted velocity $\vec{u}^{*}$ is resolved as:

$$\Omega_I \frac{\vec{u}_I^{*k+1}}{\Delta t} + \sum_{J \in \aleph(\Omega_I)} \left[m_{IJ} \vec{u}_{IJ}^{*k+1} - (\nu + \nu_T) \frac{\vec{u}_{J'}^{*k+1} - \vec{u}_{I'}^{*k+1}}{\left\| \overrightarrow{I'J'} \right\|} S_{IJ} \right] = \Omega_I s_{\vec{u}} - \Omega_I \left(\nabla p \right)_I^k \tag{3.31}$$

2. **Corrector step:** the discrete version of the Poisson equation (2.3) is resolved for the unknown pressure variation δp^{k+1}. Firstly the discrete version of Poisson Equation (2.3) has to be introduced as:

$$\nabla_{dis} \cdot (\mathbf{T}^{u} \nabla_{dis} \delta p) = \nabla_{dis} \cdot (\delta \overrightarrow{u_I}) \tag{3.32}$$

   where $\mathbf{T}^{u}$ is a matrix which contains the temporal terms and the subscript *dis* stands for discrete. The discrete divergence is defined as

$$\nabla_{dis} \cdot (\delta \overrightarrow{u_I}) = \sum_{J \in \aleph(\Omega_I)} \delta \overrightarrow{u_{IJ}} \cdot \overrightarrow{u_{IJ}} S_{IJ} \tag{3.33}$$

   Finally also the interpolation suggested by Rhie and Chow (1983) is added and the final equation for pressure being solved is:

$$\begin{aligned}\sum_{J\in\aleph(\Omega_I)} \mathbf{T}^u\left(\nabla\delta p^{k+1}\right)_{IJ}\cdot\overrightarrow{n_{IJ}}S_{IJ} &= -\nabla_{dis}\cdot\left(\overrightarrow{u}_I^{*k+1}\right)-\nabla_{dis}\cdot\left[\mathbf{T}^u\left(\nabla p^k\right)_I\right]+\\ &\quad+\sum_{J\in\aleph(\Omega_I)}\mathbf{T}^u\left(\nabla p^k\right)_{IJ}\cdot\overrightarrow{n_{IJ}}S_{IJ}\end{aligned} \tag{3.34}$$

With this value of the pressure correction the pressure and the velocity are corrected as:

$$\begin{cases} p^{k+1}=p^k+\delta p^{k+1} \\ \overrightarrow{u}_I^{k+1}=\overrightarrow{u}_I^{*k+1}-\mathbf{T}^u\left(\nabla\delta p^{k+1}\right)_I \end{cases} \tag{3.35}$$

3. **Test**: checking of the convergence using a least square norm defined as

$$\left\|\overrightarrow{u}_I^{k+1}-\overrightarrow{u}_I^{k}\right\|_{L^2}>\epsilon \tag{3.36}$$

If the test is positive the procedure is restarted from point 1.

Part II

RESULTS

Chapter 4

KINETIC ENERGY CONSERVATION

The numerical conservation of kinetic energy is a crucial point for all calculations and particularly for turbulence simulation approaches, which aim to reproduce a good part of the energy spectrum. Discretization schemes that conserve energy have been proved to produce accurate results (Ham and Iaccarino (2004)); moreover energy conservation ensures that the contribution from the sub-grid model is not obscured by numerical errors. With the increase of LES type approaches in industrial engineering problems, the geometry becomes more complicated and the mesh quality might deteriorate. Indeed the generation of an optimal mesh might result in a long procedure, which might account up to $50 - 80\%$ of the total CFD process. An automatic meshing procedure might be desirable, considerably reducing the time required by the mesh generation step. Additionally there is a constraint for the near wall resolution, which, in the case of a wall-resolved simulation, imposes a fine near wall mesh distribution.

The aim of this chapter is to use the concept of kinetic energy conservation in order to investigate the use of embedded refinements in the context of a finite volume unstructured code. Kinetic energy conservation is recalled in Section 4.2 in both continuous and discrete sense. The test case considered is the well-known Taylor-Green vortices, which consist of an infinite array of vortices. Firstly some results for conformal structured meshes are recalled, in order to introduce a reference solution. Afterwards embedded refinements are taken into consideration, varying the configuration of the mesh at the interface between the coarse and refined area. In this context an attempt to perform a simple mesh optimization is also presented. Finally polyhedral meshes are considered. The use of a blended CD-UPWIND convective scheme when the slope test fails (see Section 3.2.2) is also investigated. As pointed out by many authors (see Section 4.1) the role of the gradient reconstruction is fundamental in order to minimize the numerical dissipation. Indeed the introduction of non-orthogonalities can increase the error of the gradient calculation up to more than one order of magnitude, largely deteriorating the accuracy of the solution.

4.1 INTRODUCTION

The incompressible Navier-Stokes equations, conserve mass, momentum and, in their inviscid limit, kinetic energy (see Section 4.2). A sufficient but not necessary condition to help improve energy conservation is to employ high order schemes as presented by Vasilyev (2000), where high order finite differences (FD) schemes for a staggered pressure-velocity arrangement are generalized for non-uniform grids. These schemes do not conserve simultaneously mass, momentum, and kinetic energy. However, depending on the form of the convective term, conservation of either momentum or energy, in addition to mass, can be achieved. Conservation properties of these schemes are as good as those of standard second order finite difference, but their accuracy is far superior. Finite difference can, in principle, be applied to any type of grid, however in most cases reported in literature, are applied to structured meshes. Therefore FD is in general restricted to the analysis of relatively simple geometries.

The finite volume method (FV) can more easily accommodate any type of cell geometry and it is the most widely used approach for unstructured cell-based solvers. The method conserves mass and momentum by construction. The main advantage is the flexibility of the method, which permits to concentrate the control volumes only in the needed parts of the domain. Indeed, the unstructured approach permits to adapt the mesh size to the local length-scales avoiding unnecessary refinements. A good example of LES applied to the study of the flow past a cylinder is reported in Liang and Papadakis (2007). Thanks to the use of hanging nodes, the work takes into account the effects of mesh refinement close to the cylinder without refining over all the domain. A similar technique is also applied in Liang et al. (2009), in order to study the effect of tube spacing on vortex shedding in in-line tube arrays. The investigation is carried out at very low Reynolds number, therefore no turbulence modelling is employed. The principle disadvantage is that high-order numerical schemes are relatively difficult to develop on 3D unstructured meshes because the formulation requires three level of approximation: interpolation, differentiation and integration (see Section 3.2).

Ham and Iaccarino (2004) demonstrate that a co-located arrangement of the variable might not conserve kinetic energy. The non-conservative term arises from the discretization of the pressure and it can be demonstrated that it is dissipative. A similar conclusion is also reported by Benhamadouche (2006), where the author demonstrates that kinetic energy conservation in a co-located arrangement can be achieved using low order (i.e. 2^{nd} order) scheme only without the use of Rhie and Chow interpolation and on regular grids (see Sec. 4.2.2). Additionally Ham and Iaccarino (2004) pointed out the importance of the gradient reconstruction method, devising an alternative reconstruction based on the Green-Gauss theorem, where a correction term is introduced in order to minimize the non-conservation of the kinetic energy due to pressure term. This method is compared with a face-area-weighted least-squares minimisation to reconstruct the pressure gradient. For the case of inviscid Taylor-Green vortices on skewed mesh the Green-Gauss reconstruction shows to be a necessary requirement to obtain a stable solution, whereas the least-squares method displays an increase of the total kinetic energy, which is unphysical.

The effect of different mesh types in energy conservation is presented by Moulinec et al. (2005). Three different types of mesh are assessed and results indicate that polyhedral meshes have conservation properties similar to those of hexahedral and considerably better than tetrahedral meshes, if no special treatment is performed.

An important question arises: what is the order of accuracy of a standard finite volume discretization, when a CD scheme is used to evaluate the convective term on an unstructured or irregular mesh? Svard et al. (2008) propose an answer to the problem, by evaluating the accuracy of the discretization of second and first derivatives on different mesh types, both from a theoretical point of view and via numerical verification. The outcome is that the approximation of second derivatives is inconsistent[1] in case of unstructured tetrahedral meshes. Consistency can be recovered using "high level grids" such as rectangles or regular polygons (in 2D). Another important conclusion of the work is that, on mixed grids (hexahedra plus tetrahedra or mesh with hanging nodes), the order of accuracy for first order derivatives, evaluated with a 2^{nd} order CD scheme, drops to 1.5 in case of a smooth interface (face to face matching) and to 0.5 in non-smooth (presence of hanging nodes). Eriksson and Nördstrom (2009) report similar findings in their analysis of both hyperbolic and elliptic problems with Dirichlet boundary conditions. The hyperbolic problem has been proved to have a rate of convergence, in L_2 norm, equal to 0.5 on a completely random mesh (casual distribution of cells and face centres). However, in the case of an advection-diffusion problem, the order of accuracy of the error remains (in the case without forcing term) second order for any type of mesh and drops to 1.5 on a random mesh with forcing term[2]. In the paper an interesting statement is also reported in the conclusions:

"The most significant feature of a "good" grid is that the control volumes are centred, i.e. that the flux points[3] *are positioned right between the solution points. Note that this centring is very easy to create in one dimension, but it is not clear how to achieve the same thing in multiple dimensions".*

A first approach to solve this issue is to combine unstructured finite volumes with high order finite difference schemes. An example is presented in Nördstrom and Gong (2006) where a hyperbolic problem is studied. The finite volume is predominantly used

---

[1] Consistency: the rate of the error decrease follows the theoretical value given by the Taylor expansion.

[2] The forcing term is constituted by a trigonometric function.

[3] The flux points can be interpreted as the face centre in a more standard finite volume nomenclature.

close to the wave source, where the geometry is more complex and non-linear phenomena are present. The high order finite difference is instead used for wave propagation. In both domains strict stability is achieved using a Summation-By-Part (SBP) in conjunction with a penalty procedure to impose boundary conditions called Simultaneous Approximation Term (SAT, see Nördstrom et al. (2003)). Strict stability implies that the growth rate of the semi-discrete solution is less than or equal to the growth rate of the analytic solution. Satisfying this condition ensures that the error does not grow with time. The coupling is based on energy estimates and stable conditions are enforced at the FV-FD interface, modifying the dual mesh of the FV domain at the interface. This method is generalized for convection-diffusion problems in complex geometries in Gong and Nördstrom (2007).

Another approach consists of switching from a co-located to a staggered arrangement. Perot (2000) presents a staggered formulation for unstructured meshes, which conserve mass, momentum, kinetic energy and vorticity at machine precision. Velocity is located at the face centre, whereas pressure is located at the circumcentre. This scheme is proven, both analytically and numerically, to be first order on unstructured grids and second on regular Cartesian meshes. Another important feature of the approach is its ability to avoid spurious oscillation in the solution: the scheme takes advantage by the creation of a “co-volume” mesh (Nicolaides (1993)), which is created using a Voronoi tessellation: every single unstructured (triangles in 2D and tetrahedra in 3D) has associated an orthogonal “dual mesh”. The method is generalized for fully 3D applications in Zhang et al. (2002) and for moving mesh with free surface flow in Perot and Nallapati (2003). Following almost the same formulation an algorithm for LES computations on arbitrary grid is presented in Mahesh et al. (2004). Several test cases are taken into consideration ranging from simple laminar flow i.e. Taylor-Green vortices, to simple LES like decay of isotropic turbulence to a very complex flow in a Pratt and Whitney gas turbine combustor.

Another interesting staggered formulation is presented in Benhamadouche and Laurence (2002), where pressure is stored at both the cell centre and cell vertex and instead the velocity is located at the face centre. The discretization uses a hybrid FV/FE formulation: the velocity is linear over the discretization element (triangles in 2D or tetrahedra in 3D), whereas the pressure is $P1$ over the diamond obtained joining two nodes and the centre of gravity. The name of the velocity-pressure element is of the type $P1 - non - conform - P1 - bubble$. The discretization is verified to be completely conservative both analytically and numerically.

The combination of SBP and SAT, introduced earlier, is applied to a staggered arrangement by Ham et al. (2006). Staggered solvers display a more consistent second order reduction of the error, without dropping to smaller orders in case of non conformal meshes, making the discretization suitable for accurate LES or DNS in complex geometries. An extension of the formulation including also scalar transport equations is introduced in Ham (2008).

4.2 Conservation of the global properties

As introduced in the previous section the Navier-Stokes equations, in their incompressible form, conserve mass, momentum and (in the inviscid limit) the kinetic energy. The energy conservation equation is obtained from the scalar product between the momentum equations and the velocity vector.

4.2.1 Kinetic energy conservation in a continuous sense

The Navier-Stokes equations, in their incompressible form and neglecting the diffusive term, could be rewritten as:

$$\begin{cases} \dfrac{\partial u_i}{\partial x_i} = 0 \\ \dfrac{\partial u_i}{\partial t} + \dfrac{\partial u_i u_j}{\partial x_j} = -\dfrac{1}{\rho}\dfrac{\partial p}{\partial x_i} \end{cases} \tag{4.1}$$

Thus the energy equation is derived as:

$$u_i \left(\frac{\partial u_i}{\partial t} + \frac{\partial u_i u_j}{\partial x_j} = -\frac{1}{\rho}\frac{\partial p}{\partial x_i} \right) \tag{4.2}$$

If the kinetic energy is introduced as $K = u_i u_i / 2$ Equation (4.2) could be divided into three terms:

1. Temporal term:

$$u_i \frac{\partial u_i}{\partial t} = \frac{\partial \left(u_i u_i / 2 \right)}{\partial t} = \frac{\partial K}{\partial t} \tag{4.3}$$

2. Convective term:

$$u_i \frac{\partial u_i u_j}{\partial x_j} = \frac{\partial \left(u_i u_i u_j / 2 \right)}{\partial x_j} - \frac{u_i^2}{2}\frac{\partial u_j}{\partial x_j} = \frac{\partial K u_j}{\partial x_j} - K \frac{\partial u_j}{\partial x_j} \tag{4.4}$$

3. Pressure term:

$$-\frac{u_i}{\rho}\frac{\partial p}{\partial x_i} = -\frac{1}{\rho}\frac{\partial u_i p}{\partial x_i} + \frac{p}{\rho}\frac{\partial u_i}{\partial x_i} \tag{4.5}$$

Substituting (4.3), (4.4) and (4.5) into (4.2) and keeping in mind that the flow is divergence free (first equation of (4.1)), the following formulation for the energy conservation is obtained:

$$\frac{\partial K}{\partial t} = -\frac{\partial K u_i}{\partial x_i} - \frac{\partial u_i p}{\partial x_i} = -\frac{\partial}{\partial x_i}\left[\left(K + \frac{p}{\rho}\right) u_i\right] \tag{4.6}$$

If the flow is periodic in all directions the integral of the total kinetic energy, over all the domain, is constant therefore:

$$\int_V \frac{\partial K}{\partial t} dV = 0 \tag{4.7}$$

4.2.2 Kinetic energy conservation in a discrete sense

Now the same procedure can be applied to verify the conservation of energy in a discrete sense. The different terms are approximated with formulae presented in Chapter 3.

1. Temporal term:

$$\begin{aligned}\int_{\Omega_I} u_i \frac{\partial u_i}{\partial t} dV &= \overrightarrow{u}_I^{n+1/2} \cdot \frac{\overrightarrow{u}_I^{n+1} - \overrightarrow{u}_I^{n}}{\Delta t}\Omega_I = \frac{\overrightarrow{u}_I^{n+1} + \overrightarrow{u}_I^{n}}{2} \cdot \frac{\overrightarrow{u}_I^{n+1} - \overrightarrow{u}_I^{n}}{\Delta t}\Omega_I \\ &= \frac{\Omega_I}{\Delta t}\left[\left(\frac{1}{2}\overrightarrow{u}_I^{n+1} \cdot \overrightarrow{u}_I^{n+1}\right) - \left(\frac{1}{2}\overrightarrow{u}_I^{n} \cdot \overrightarrow{u}_I^{n}\right)\right] \\ &= \frac{\Omega_I}{\Delta t}\left[K_I^{n+1} - K_I^{n}\right] \end{aligned} \tag{4.8}$$

where $K_I = \frac{1}{2}\left(u_i u_i\right)_I$.

2. Convective term:

$$\begin{aligned}\int_{\Omega_I} u_i \frac{\partial u_i u_j}{\partial x_j} dV &= \overrightarrow{u}_I^{n+1/2} \cdot \sum_{J\in\aleph(\Omega_I)} \overrightarrow{u}_{IJ}^{n+1/2} m_{IJ}^n \\ &= \overrightarrow{u}_I^{n+1/2} \cdot \sum_{J\in\aleph(\Omega_I)} \left[\alpha \overrightarrow{u}_{I'}^{n+1/2} + (1-\alpha)\overrightarrow{u}_{J'}^{n+1/2}\right] m_{IJ}^n \\ &= \underbrace{\overrightarrow{u}_I^{n+1/2} \cdot \overrightarrow{u}_{I'}^{n+1/2} \sum_{J\in\aleph(\Omega_I)} \alpha m_{IJ}^n}_{A} \\ &+ \underbrace{\sum_{J\in\aleph(\Omega_I)} (1-\alpha)\left(\overrightarrow{u}_I^{n+1/2} \cdot \overrightarrow{u}_{J'}^{n+1/2}\right) m_{IJ}^n}_{B} \end{aligned} \tag{4.9}$$

The term A disappears if α is constant over the entire domain (i.e. $\alpha = 1/2$ is the value for a conformal mesh) because of the discrete divergence $\sum_{J \in \aleph(\Omega_I)} m_{IJ}^n = 0$. The term B does not necessarily vanish if α is constant, but requires also to have $\overrightarrow{u}_I = \overrightarrow{u}_{J'}$ in order to have the velocity evaluated at the same point in cell I and J. This only happens in the case of a uniform and constant mesh.

3. Pressure term:

$$\int_{\Omega_I} -u_i \frac{\partial p}{\partial x_i} dV = -\overrightarrow{u}_I^{n+1/2} \cdot \sum_{J \in \aleph(\Omega_I)} p_{IJ}^{n+1/2} \overrightarrow{n}_{IJ} S_{IJ}$$

$$\begin{aligned} &= -\overrightarrow{u}_I^{n+1/2} \cdot \sum_{J \in \aleph(\Omega_I)} \left(\alpha p_{I'}^{n+1/2} + (1-\alpha)\, p_{J'}^{n+1/2} \right) \overrightarrow{n}_{IJ} S_{IJ} \\ &= \underbrace{-\overrightarrow{u}_I^{n+1/2} p_{I'}^{n+1/2} \cdot \sum_{J \in \aleph(\Omega_I)} \alpha \overrightarrow{n}_{IJ} S_{IJ}}_{A} \\ &- \underbrace{\sum_{J \in \aleph(\Omega_I)} (1-\alpha)\, p_{J'}^{n+1/2} \overrightarrow{u}_I^{n+1/2} \cdot \overrightarrow{n}_{IJ} S_{IJ}}_{B} \end{aligned} \tag{4.10}$$

The comments already made for Eq. (4.9) are applicable also for Eq. (4.10). The A term vanishes when α is constant (i.e $\alpha = 1/2$). This condition is necessary but not sufficient for term B, which requires also to have the Rhie and Chow interpolation, presented in Section (3.5), deactivated as demonstrated in Benhamadouche (2006).

4.3 TAYLOR-GREEN VORTICES

The test case of the Taylor-Green vortices is employed in this chapter to study the effect of unstructured meshes (meshes with embedded refinements and polyhedral cells are considered), in the framework of a FV second order accurate code in time and space. The concept of kinetic energy conservation is used to measure the effect of mesh distortion. Comparison with regular Cartesian grid is performed. In the case of embedded refined meshes different patterns of the interface between the coarse and the fine areas are investigated in order to find possible best practice guidelines for mesh generation. An attempt to obtain a mesh optimization of a particular configuration will be presented.

It is commonly accepted to use second order accurate, FV codes on structured meshes in order to perform LES / "quasi DNS" computations. On the other hand, in this context, the use of unstructured meshes is questionable. The evaluation of the conservation properties of *Code_Saturne* is not the object of this study, consequently conservation of angular momentum or other types of conservative verifications is not presented herein. The purpose is to compare advantages and disadvantages of unstructured meshes with the well known structured meshes. Differences are very clear in the inviscid limit of the test case, therefore only this is presented. In conclusion the question, which we are trying to address is:

Is it possible to perform LES/DNS using an unstructured mesh and, if so, under which conditions?

4.3.1 Test case definition

The $2D$ Taylor-Green vortices are an infinite array of vortices. Because of periodicity only a square $2\pi \times 2\pi$ is considered. The velocity field has the following analytical expression:

$$\begin{cases} u_1 = -\cos(kx_1)\cdot\sin(kx_2)\cdot e^{-2k^2\nu t} \\ u_2 = \sin(kx_1)\cdot\cos(kx_2)\cdot e^{-2k^2\nu t} \end{cases} \tag{4.11}$$

and the pressure is expressed by:

$$p = -\frac{1}{4}\left[\cos\left(2kx_1\right) + \cos\left(2kx_2\right)\right]\cdot e^{-4k^2\nu t} \tag{4.12}$$

where $k = \frac{2\pi}{2l}$ and l is the size of the vortex (in this case $k = 1$ with l equal to π). The number of vortices in each direction is equal to $2 \times k$. Table 4.1 lists all grids used, whereas Table 4.2 defines the numerical options used in this analysis. The calculation are performed with a time step equal to $0.01\,s$, which correspond to a maximum CFL number of 0.095 in the conformal mesh and 0.19 in the mesh RR050 which is the mesh with the largest CFL number.

A possible strategy to improve the results without over-refining could be to localize the refinements in the most needed regions. In the present test the refinement is placed in the middle of the domain, in order to avoid the connection between hanging nodes and periodic boundary conditions on the external edges. Figure 4.1 shows a sketch of the domain, highlighting the refined area (which is also referred as slave block, whereas the coarse is referred as master block). Fig. 4.2 illustrates a practical example of a mesh 60 × 60 with an embedded refinement. The refinements can be characterised by the refined ratio (RR) parameters defined as (and referring to Fig. 4.1(b)):

$$RR = \frac{\overline{AB}}{\overline{AC}} \equiv \frac{N_{Master}}{N_{Slave}} \tag{4.13}$$

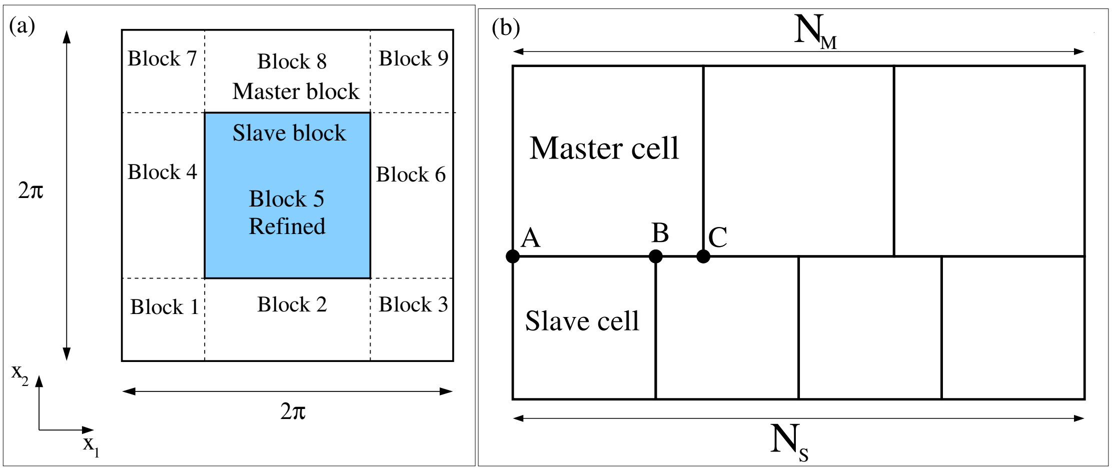

Figure 4.1: (a) Presentation of the block structure for the Taylor-Green vortices. The domain is $2\pi \times 2\pi$ with the refined block positioned in the middle with dimensions $\pi \times \pi$. (b) Schematic sketch of the interface between master and slave block.

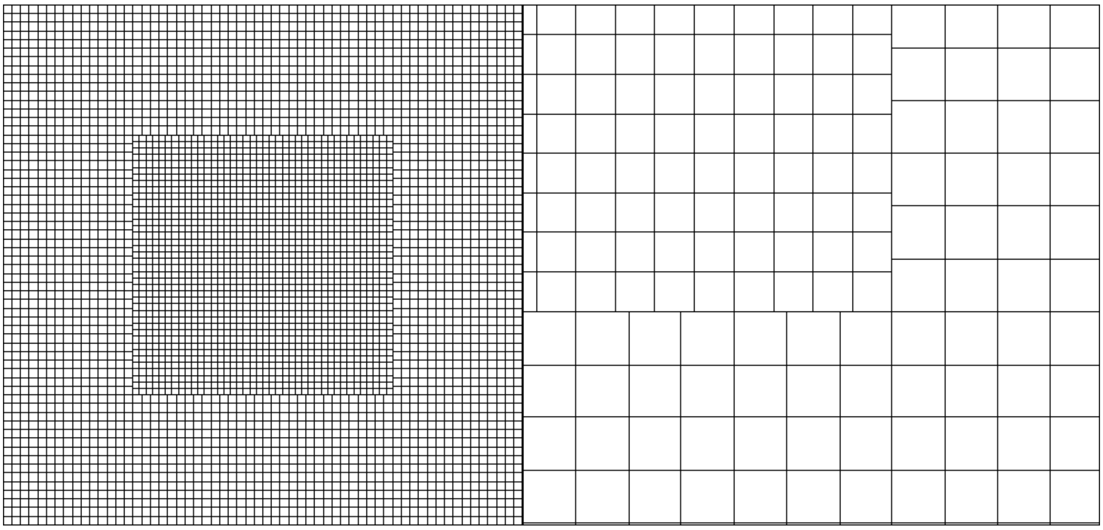

Figure 4.2: Example of an embedded refined mesh. The base resolution is 60 × 60 and the refinement has a 3-4 structure. On the left hand side global view of the domain, on the right hand side a close up view on the refined area.

Mesh	*RR*	Type of refinement	n cells	n faces
CONF60	1.00	60×60 + no ref. in slave blk	3600	7440
RR097	0.97	$60 \times 60 + 31 \times 31$ in slave blk	3661	7433
RR094	0.94	$60 \times 60 + 32 \times 32$ in slave blk	3724	7558
RR091	0.91	$60 \times 60 + 33 \times 33$ in slave blk	3789	7695
RR088	0.88	$60 \times 60 + 34 \times 34$ in slave blk	3856	7824
RR077	0.77	$60 \times 60 + 39 \times 39$ in slave blk	4221	8553
RR075	0.75	$60 \times 60 + 40 \times 40$ in slave blk, 3-4 sub pattern	4300	8840
RR073	0.73	$60 \times 60 + 41 \times 41$ in slave blk	4381	8879
RR068	0.68	$60 \times 60 + 44 \times 44$ in slave blk	4636	9394
RR067	0.66	$60 \times 60 + 45 \times 45$ in slave blk	4725	9555
RR065	0.65	$60 \times 60 + 46 \times 46$ in slave blk	4816	9756
RR062	0.625	$60 \times 60 + 48 \times 48$ in slave blk	5004	10134
RR061	0.61	$60 \times 60 + 49 \times 49$ in slave blk	5101	10282
RR060	0.60	$60 \times 60 + 50 \times 50$ in slave blk	5200	10520
RR050	0.50	$60 \times 60 + 60 \times 60$ in slave blk, 1-2 sub pattern	6300	12840
POLY1	/	/	2119	10593
POLY2	/	/	2050	10251
POLY3	/	/	4157	20786

Table 4.1: List of all the meshes used for the Taylor-Green vortices. In the *Type of refinement* column is described the resolution used for the base conformal mesh and the type of refinement used in the slave block (Fig. 4.1).

Run	n it vel/pres	R&C	$\nabla\phi$	Conv. Term.
R1	1	1	G&G rec.	CD
R2	2	1	G&G rec.	CD
R3	5	1	G&G rec.	CD
R4	2	0.5	G&G rec.	CD
R5	2	0	G&G rec.	CD
R6	2	1	L2 ext.	CD
R7	2	1	G&G rec.	CD + Slope 10%

Table 4.2: List of the numerical options adopted for the different runs of the Taylor-Green vortices test case. Col. 1: acronym of the run; col. 2: iterations for the velocity pressure coupling (SIMPLEC, see sec. 3.5); col. 3: Arakawa constant controlling the R&C interpolation (1 full interpolation, 0 no interpolation); col. 4: gradient reconstruction (G&G is Green and Gauss with reconstruction of the non-orthogonalities, see Sec. 3.2.4, L2 ext stands for least squares method with extended neighbours); col. 5: convective scheme (see Sec. 3.2.2).

TOTAL KINETIC ENERGY.

The kinetic energy (K) for the Taylor-Green vortices reads:

$$K = \frac{1}{2}\left(u_1^2 + u_2^2\right) = \frac{1}{2}\left(\cos^2(kx_1)\sin^2(kx_2) + \sin^2(kx_1)\cos^2(kx_2)\right)e^{-4k^2\nu t} \tag{4.14}$$

The integral of Eq. (4.14) over the whole domain leads to[4]:

$$\begin{aligned} K_{TOT} &\equiv \frac{1}{V_{TOT}}\int_0^{2\pi}\int_0^{2\pi} K \cdot dx_1 dx_2 \\ &= \frac{1}{(2\pi)^2}\int_0^{2\pi}\int_0^{2\pi}\frac{1}{2}\left(\cos^2(kx_1)\sin^2(kx_2) + \sin^2(kx_1)\cos^2(kx_2)\right)e^{-4k^2\nu t}dx_1dx_2 \\ &= \left[\frac{x_1x_2}{16\pi^2} - \frac{\sin(2kx_1)\sin(2kx_2)}{64\pi^2k^2}\right]_{x_1,x_2=0}^{x_1,x_2=2\pi} e^{4k^2\nu t}\left[\frac{1}{4} - \frac{\sin^2(4\pi k)}{64\pi^2k^2}\right]e^{-4k^2\nu t} \\ &= \frac{1}{4}e^{-4\nu t} \end{aligned} \tag{4.15}$$

where $k = 1$ and V_{TOT} is the total volume. In the inviscid limit[5] the result of (4.15) reads:

$$K_{TOT} = \frac{1}{4} = K_0 \tag{4.16}$$

4.3.2 CONFORMAL MESH

This section briefly recalls results for energy conservation on a conformal structured mesh. Figures 4.3 and 4.4 report the results as function of time for an increased for different values of the Rhie and Chow constant and for an increased number of iterations of the velocity/pressure coupling. Figures report on the top rights the decay of the total kinetic energy, the error of velocity u_1 (bottom left) and pressure p (bottom right) computed using a least squares definition[6]:

---

[4] The unit of measure of the total kinetic energy K is $\left[{}^{m^2}/{}_{s^2}\right]$. The argument of the exponential is $\left(-4k^2\nu t\right)$ which is dimensionless because $\left[{}^{1}/{}_{m}\right]^2\left[{}^{m^2}/{}_{s}\right][s]$. The final results of Eqs. (4.15) and (4.16) could be misleading because some factors cancel out or are equal to 1 and therefore dropped in order to obtain an simpler formulation for K.

[5] $\nu \to 0$

[6] In the case of error distribution on all the computational domain (see for example Fig. 4.5) the error is evaluated as:

$$err\left[\psi^i(\vec{x})\right] = \frac{\left\|\psi^i(\vec{x}) - \psi^0(\vec{x})\right\|}{\left\|\psi^0(\vec{x})\right\|_\infty}. \tag{4.17}$$

This formulation is necessary in order to avoid division by 0.

$$L2(\psi^i) = \sqrt{\frac{\sum_{n=1}^{N} \left(\psi^0(n) - \psi^i(n)\right)^2}{\sum_{n=1}^{N} \left(\psi^0(n)\right)^2}} \tag{4.18}$$

where N is the total amount of cells, ψ^i is a general variable at time step i and ψ^0 is its initial solution, which correspond to the analytical definition of Eqs. (4.11) and (4.12). As already stated in Section 4.2.2 full conservation is achieved only when the Rhie and Chow interpolation is deactivated[7] as can be seen from Fig. 4.3. In other cases there is a decay of kinetic energy due to numerical diffusion. A simple estimation of this numerical diffusion is obtained by inverting Eq. (4.15) as:

$$\nu_{num} = \frac{\ln\left(K_{TOT}/K_0\right)}{-4t} \tag{4.19}$$

where $K_0 = 1/4$ is given by Eq. (4.16). This definition of equivalent numerical viscosity is used to measure the diffusivity of the code and it is reported on the top right of the Figures 4.3 and 4.4. Ham and Iaccarino (2004) demonstrate that the decay of total kinetic energy follows:

$$\frac{\partial K}{\partial t} + \frac{\partial}{\partial x_i}(...) = -\left(\frac{\Delta x_i^2 \Delta t}{4}\right) p \frac{\partial^4 p}{\partial x_i^4} \tag{4.20}$$

Integrating (4.20) over the entire domain and using the expression of the Taylor-Green vortices in the inviscid limit we have:

$$\frac{\partial K_{TOT}}{\partial t} = \frac{1}{V_{TOT}} \int_0^{2\pi} \int_0^{2\pi} -\left(\frac{\Delta x_i^2 \Delta t}{4}\right) p \frac{\partial^4 p}{\partial x_i^4} dx_1 dx_2 = -\left(\frac{\Delta x_i^2 \Delta t}{4}\right) \approx -0.275 \cdot 10^{-4} \tag{4.21}$$

assuming as $\Delta t = 0.01$ and a constant $\Delta x_i = \frac{2\pi}{60}$. This value is in fair agreement with $0.25 \cdot 10^{-4}$, value that can be found in Fig. 4.3 (top right).

On the other hand the effect of increasing the number of iterations on the velocity/pressure coupling does not have a major impact on the solution (Fig. 4.4), in fact the change in slope of the kinetic energy can be appreciated only in the close up view. The effect is more evident on the equivalent numerical viscosity ν_{num}, which converges immediately to a constant value when more than one iteration is used.

The global error of the u_1 velocity component has a linear increase with time (this error is always reported on the bottom left of the figure). Indeed after 17-18 rotations the error has a sudden jump and starts to increase rapidly in addition with a large oscillatory behaviour. This point roughly corresponds to an abrupt discontinuity in the kinetic energy conservation. The reason of this phenomenon is a loss of coherence of the

---

[7] Under *Code_Saturne* the Rhie & Chow interpolation is controlled using the Arakawa constant. A value equal to 1 mean a full activation, 0 the interpolation is deactivated.

solution as can be seen in Fig. 4.5, which reports the velocity field and the distribution of the u_1 velocity error after 240 seconds. Figure 4.6 reports the same quantities after only forty seconds. Large errors are located in areas where the velocity is small and among them the most critical zone is located in the middle of the domain. A problem of chessboard oscillations of the pressure arises in the middle of the domain as can be seen in the pressure field of Fig. 4.5. *This point, where the solution starts to diverge*[8]*, is fundamental in this analysis because it is the major point of comparison between unstructured (embedded refinement and polyhedral meshes) and structured conformal mesh performances.*

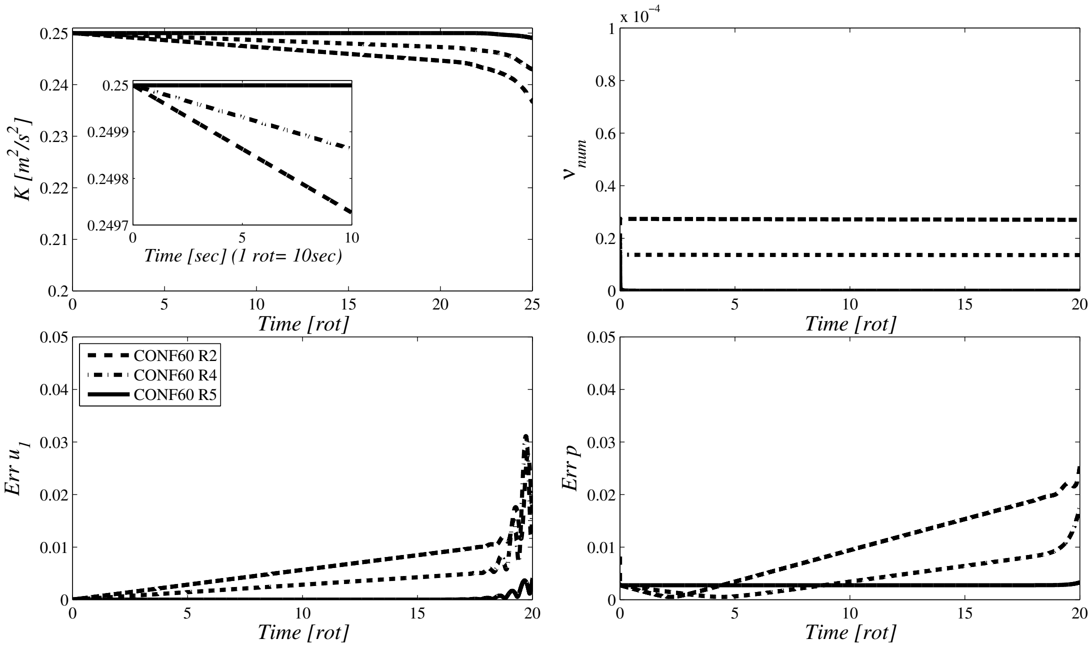

Figure 4.3: Taylor Green vortices: results as function of the number of Rhie & Chow constant for mesh CONF60. Total kinetic energy (top left), equivalent viscosity (top right), global error on u_1 (bottom left), global error on p (bottom right). Time is expressed in number of vortex rotations ($1\,rot = 10\,s$). See Table 4.2 for run definitions.

---

[8] Divergence of the solution is characterized by an abrupt decrease of the total kinetic energy (top right), or, equivalently by a sudden increase of the error (two bottom graphs).

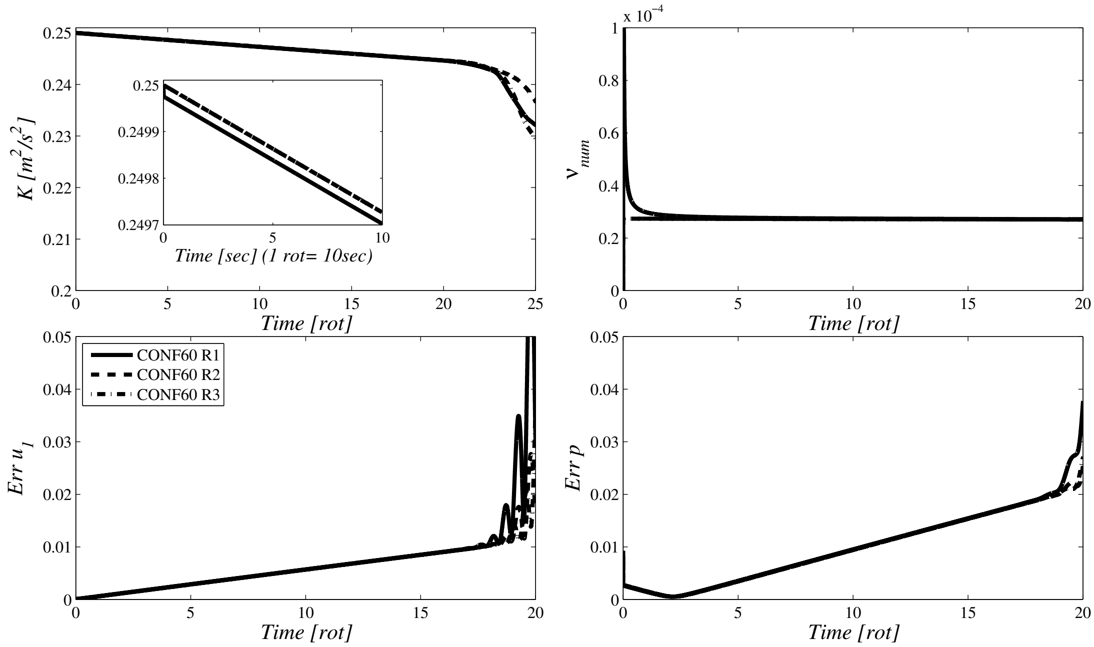

Figure 4.4: Taylor Green vortices: results as function of the number of velocity/pressure coupling iterations for mesh CONF60. Total kinetic energy (top left), equivalent viscosity (top right), global error on u_1 (bottom left), global error on p (bottom right). Time is expressed in number of vortex rotations ($1\,rot = 10\,s$). See Table 4.2 for run definitions.

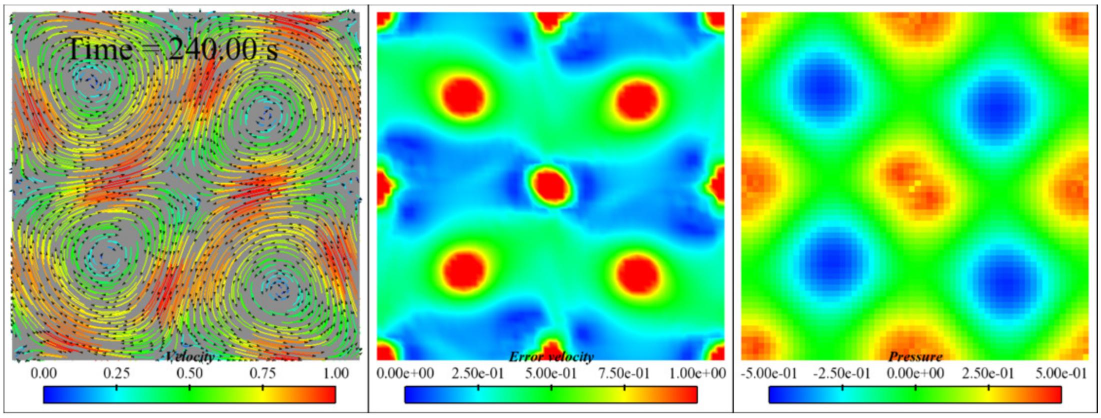

Figure 4.5: Taylor Green vortices: Velocity vectors (left), error of u_1 (middle) and pressure field (right) for the conformal mesh 60×60 (CONF60). The solution is at time $240\,s$ (approximately 24 complete vortex rotations). The error is evaluated using Eq. (4.17).

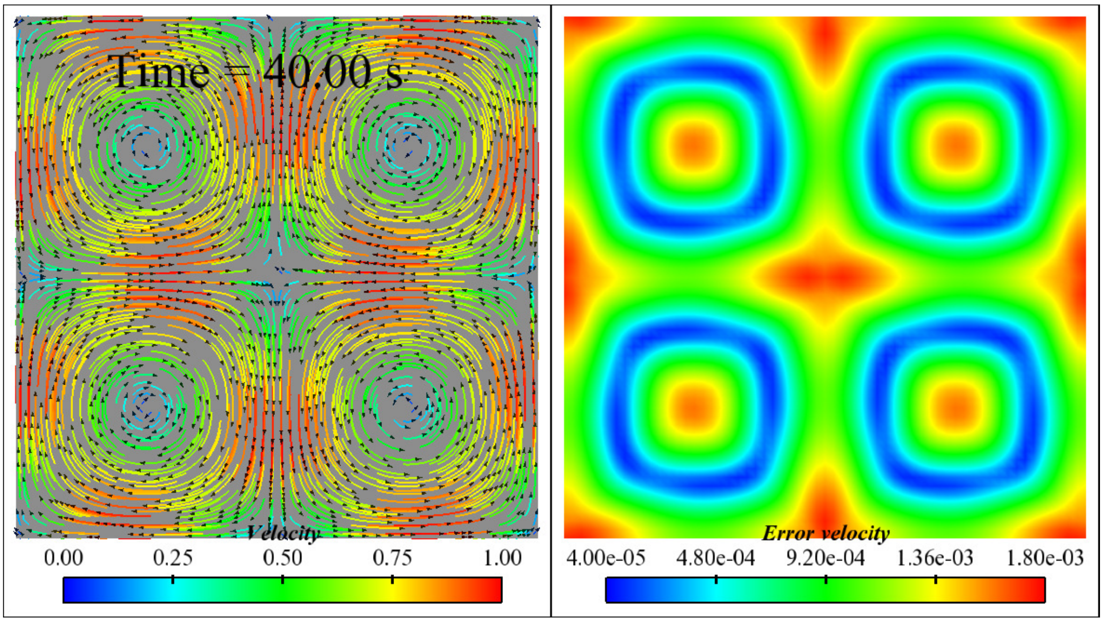

Figure 4.6: Taylor Green vortices: velocity field and error of the u_1 velocity component computed using Eq. (4.17) after 40 s (approximately 4 complete rotations) for the conformal mesh 60 × 60 (CONF60). Velocity vectors (left), velocity error (right).

4.3.3 EMBEDDED REFINED MESH

In this study the refinement ratio RR varies between 1 (structured conformal mesh) and 0.5 (1-2 sub-pattern). Table 4.1 lists all the meshes investigated, whereas the numerical options used are reported in Table 4.2. The results concerning the kinetic energy conservation, the equivalent viscosity and the error for the u_1 velocity and pressure are reported from Fig. 4.7 to 4.14. The following observations can be made.

- The addition of the refinement is bringing forward the point at which the solution is loosing coherence with respect to the conformal mesh. This is true for all the cases but there is a strong variation between meshes and two main points can be made:
  - The presence of a structured sub-pattern (i.e. a $3-4$ refinement) at the interface between master and slave areas improves the conservative properties. This is clear in Fig. 4.9, where the 3-4 sub-pattern of the RR075 mesh produces significantly better results than RR077 and RR073. A structured sub-pattern avoids the presence of small surfaces reducing the non-orthogonalities of the grid.

  - Embedded refinements characterised by $RR \approx 1$ also display better conservation properties because of the smaller stretching of the mesh at the interface. The α' parameter, defined in Eq. (3.10), is consequently closer to the ideal value of 0.5. Although this effect is less important than mesh sub-pattern structure.

- More iterations on the velocity-pressure coupling are necessary to have constant equivalent viscosity ν_{num} (Fig. 4.13) in the first part of the simulation.

- With more cells in the slave block, the kinetic energy has a slower decay. This is a consequence of the increase of the global resolution. The objective herein is not to find the best conservative meshes, but to analyze the effect of the addition of non-conformities with respect to a reference solution (i.e. structured conformal mesh). A more appropriate procedure could have been to keep constant the number of cells across all the meshes. On the other hand the methodology adopted is faster and because of a large number of grids generated, this last option was chosen. Indeed this methodology shows that even increasing the mesh resolution does not automatically lead to more accurate results.

- The method used for the gradient reconstruction is fundamental as already stated by Ham and Iaccarino (2004). Using a least square method on such type of meshes might lead to unstable solutions as can be seen from Fig. 4.14.

- The RR050 mesh, which corresponds to a 1-2 type of refinement, shows the worst conservation properties among all meshes characterized by a regular sub-pattern. This is not surprising because the mesh at the interface is over-stretched and skewed. However this type of refinement is widely used in many commercial grid generators (Star-CCM, ICEM-CFD) and academic as well for reasons of its simplicity and automatisation.

We now analyse the reasons for the reduced performance of the embedded refined meshes with respect to the conformal grid. From Fig. 4.15 to 4.17 the contours of errors of u_1 velocity and its gradient in the x_1 direction are plotted along with a complete visualization of the velocity field for different time steps. The addition of the refinement induces an increase of the error at the interface between master and slave regions. The error is subsequently convected to the centre of the domain bringing forward the loss of coherence of the solution. Table 4.3 reports the global error of first velocity component and its gradient in the direction x_1. Here it is clear that in the case of the unstructured mesh the accuracy decreases; for instance the u_1 error has a jump of about one order of magnitude. A fundamental part is played by the error in the gradient calculation. The gradient is used in the explicit evaluation of the convection-diffusion term, in order to correct the effect of non-orthogonalities (see Chapter 3), therefore small errors in the solution are amplified in the gradient reconstruction and they are subsequently used to correct the solution. A confirmation is provided by Figure 4.18 shows the error reduction for the CONF and RR075 meshes as function of the mesh size. RR075 not only shows a higher error but also the order of accuracy moves from the second order of the conformal to 1.71. An interesting point to look at is the CPU time required by the different meshes, which is reported in Table 4.3. CPU time is divided by the number of cells and number of faces in order to have a more fair comparison. A common statement is that the reduction of cells achievable using an unstructured mesh makes also the calculation faster. From Table 4.3 it does not seem the case: the conformal mesh is always the fastest, independent of the way in which the comparison is carried out. The reason is simple: embedded meshes need to iterate in order to reconstruct the gradient making the calculation slower. Further consideration about speed up of the solution as a function of the mesh characteristics can be found in Chapter 5 where a turbulent case is analysed.

Mesh	CPU [s]	CPU/n cells	CPU/n faces	Global err u_1	Global err $\partial u_1/\partial x_1$
CONF60	6.4	0.0010	0.0009	$0.90 \cdot 10^{-5}$	$0.18 \cdot 10^{-2}$
RR097	11.2	0.0031	0.0015	$0.93 \cdot 10^{-4}$	$0.23 \cdot 10^{-2}$
RR075	16.3	0.0038	0.0018	$0.15 \cdot 10^{-3}$	$0.20 \cdot 10^{-2}$
RR050	30.9	0.0049	0.0025	$0.25 \cdot 10^{-3}$	$0.19 \cdot 10^{-2}$
POLY1	20.0	0.0094	0.0019	$0.40 \cdot 10^{-3}$	$0.83 \cdot 10^{-2}$
POLY2	19.9	0.0097	0.0019	$0.19 \cdot 10^{-3}$	$0.61 \cdot 10^{-2}$

Table 4.3: List of the CPU time for different type of meshes, global error for the first velocity component and its gradient in the x_1 direction. The CPU time is evaluated after 100 time steps. In order to make the comparison more fair the elapsed time is also divided by the total number of cells and faces. Errors are instead computed after 1 iteration using run R2 (see Table 4.2).

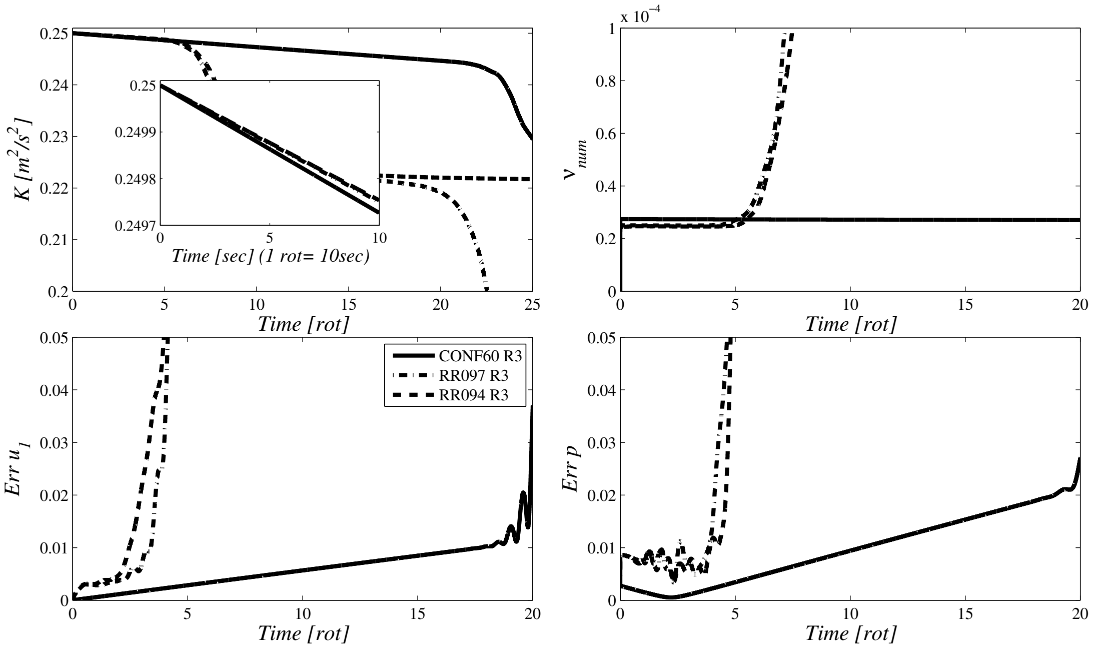

Figure 4.7: Taylor Green vortices: results for meshes RR097 and RR094. Total kinetic energy (top left), equivalent viscosity (top right), global error on u_1 (bottom left), global error on p (bottom right). Time is expressed in number of vortex rotations ($1\,rot = 10\,s$). See Table 4.2 for run definitions.

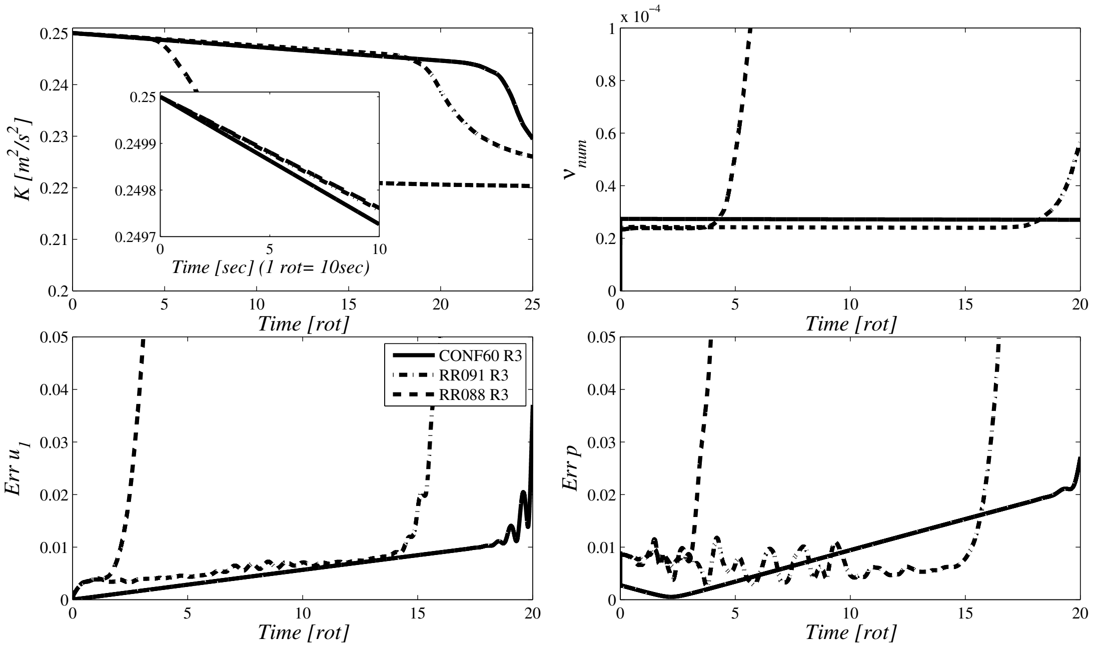

Figure 4.8: Taylor Green vortices: results for meshes RR091 and RR088. Total kinetic energy (top left), equivalent viscosity (top right), global error on u_1 (bottom left), global error on p (bottom right). Time is expressed in number of vortex rotations ($1\,rot = 10\,s$). See Table 4.2 for run definitions.

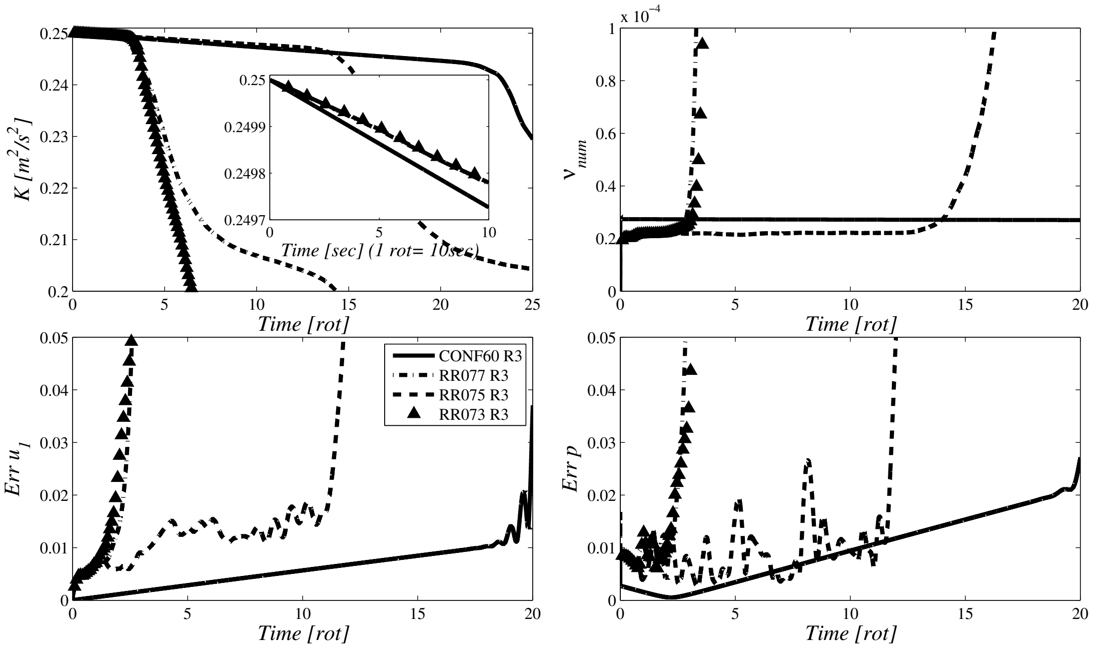

Figure 4.9: Taylor Green vortices: results for meshes RR077, RR075 and RR073. Total kinetic energy (top left), equivalent viscosity (top right), global error on u_1 (bottom left), global error on p (bottom right). Time is expressed in number of vortex rotations ($1\,rot = 10\,s$). See Table 4.2 for run definitions.

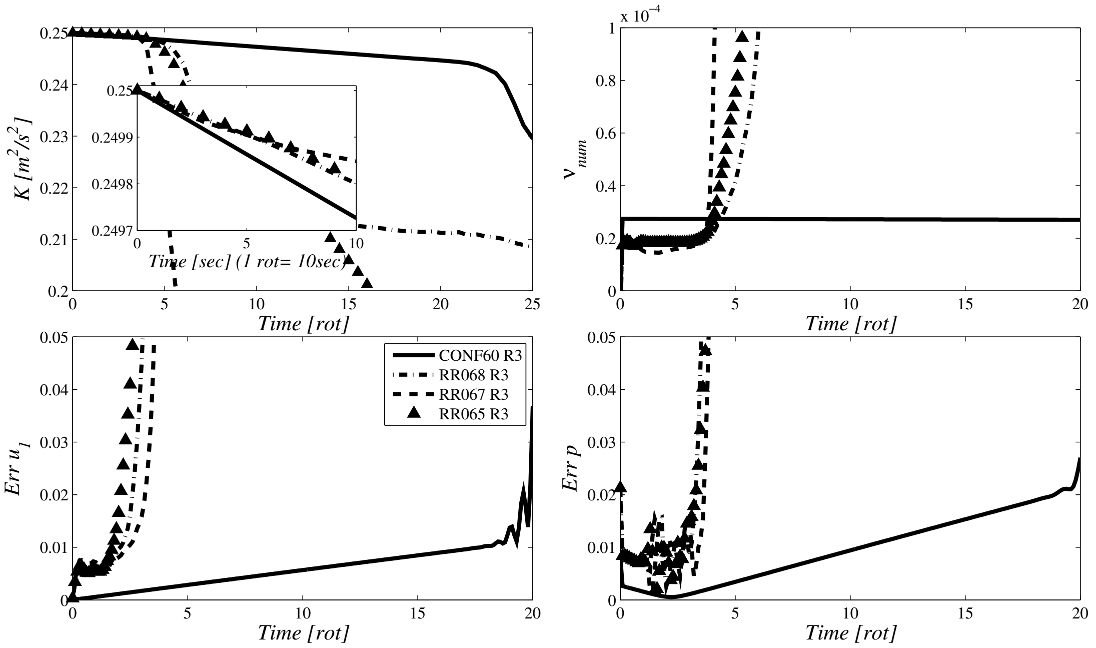

Figure 4.10: Taylor Green vortices: results for meshes RR068, RR067 and RR065. Total kinetic energy (top left), equivalent viscosity (top right), global error on u_1 (bottom left), global error on p (bottom right). Time is expressed in number of vortex rotations ($1\,rot = 10\,s$). See Table 4.2 for run definitions.

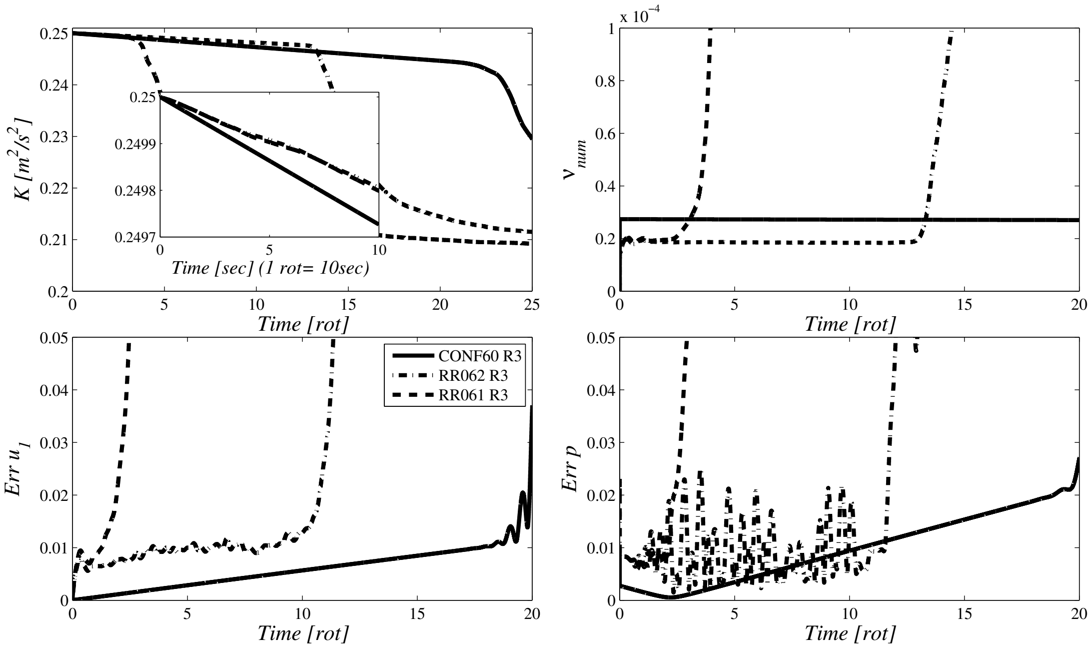

Figure 4.11: Taylor Green vortices: results for meshes RR062 and RR061. Total kinetic energy (top left), equivalent viscosity (top right), global error on u_1 (bottom left), global error on p (bottom right). Time is expressed in number of vortex rotations ($1\,rot = 10\,s$). See Table 4.2 for run definitions.

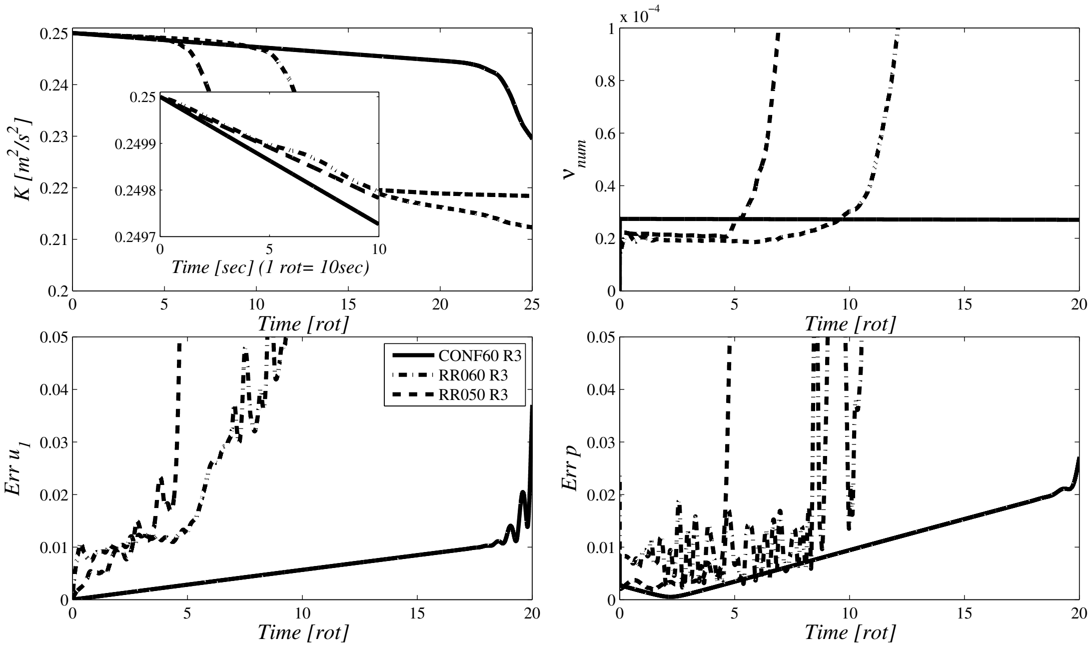

Figure 4.12: Taylor Green vortices: results for meshes RR060 and RR050. Total kinetic energy (top left), equivalent viscosity (top right), global error on u_1 (bottom left), global error on p (bottom right). Time is expressed in number of vortex rotations ($1\,rot = 10\,s$). See Table 4.2 for run definitions.

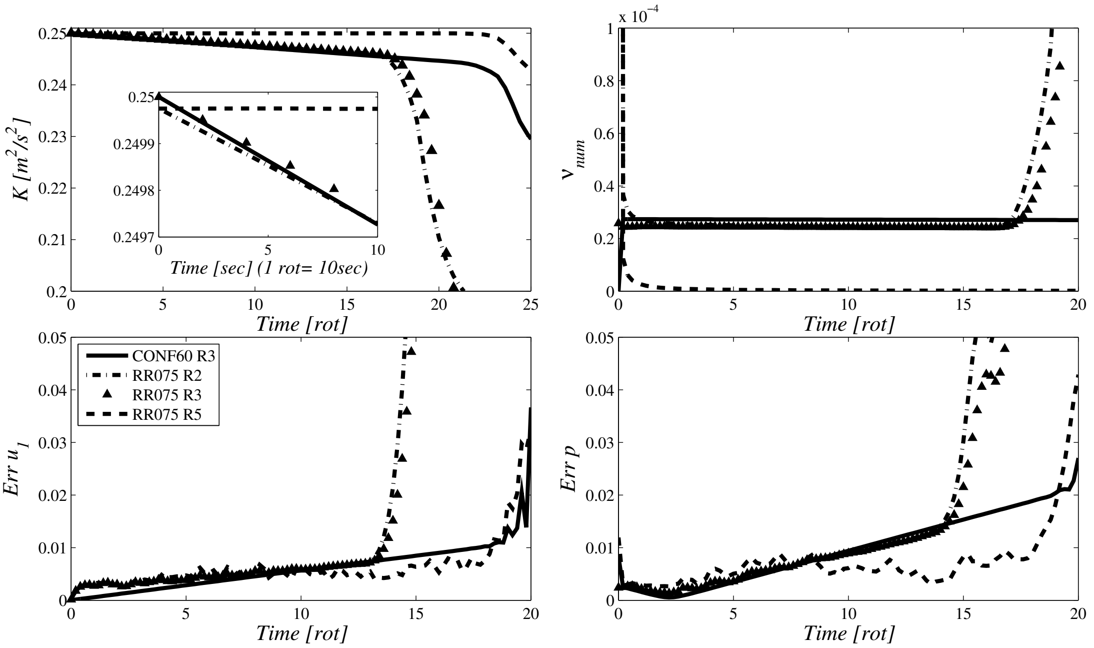

Figure 4.13: Taylor Green vortices: results as function of the number of Rhie & Chow interpolation and number of velocity/pressure coupling for mesh RR075 . Total kinetic energy (top left), equivalent viscosity (top right), global error on u_1 (bottom left), global error on p (bottom right). Time is expressed in number of vortex rotations ($1\,rot = 10\,s$). See Table 4.2 for run definitions.

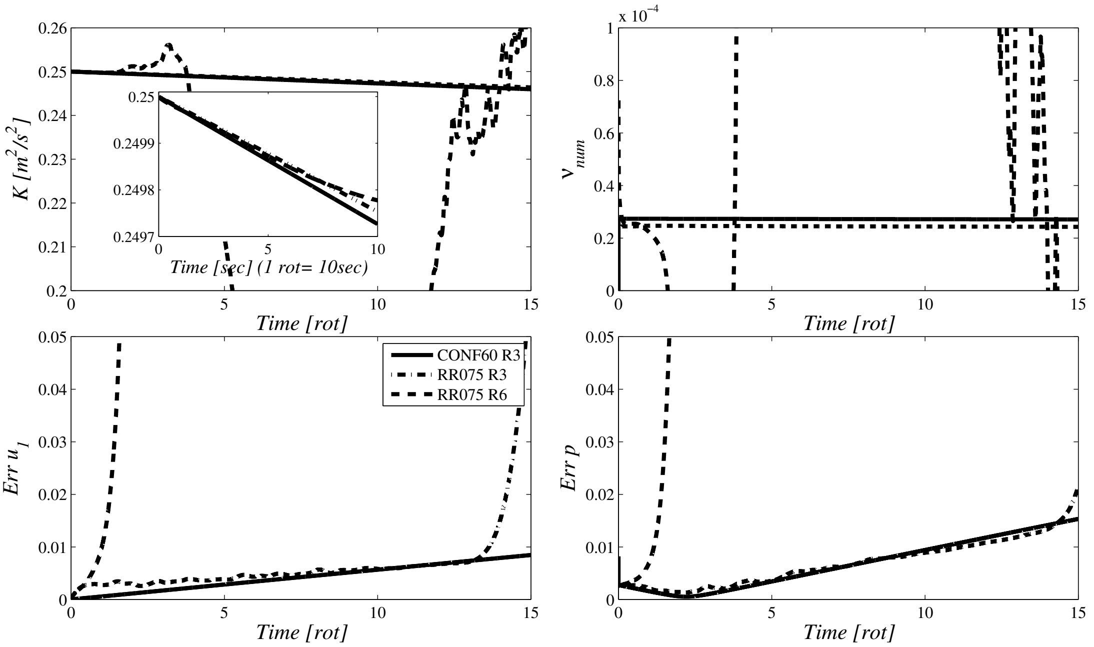

Figure 4.14: Taylor Green vortices: results as function of the gradient reconstruction method for mesh RR075 . Total kinetic energy (top left), equivalent viscosity (top right), global error on u_1 (bottom left), global error on p (bottom right). Time is expressed in number of vortex rotations ($1\,rot = 10\,s$). See Table 4.2 for run definitions.

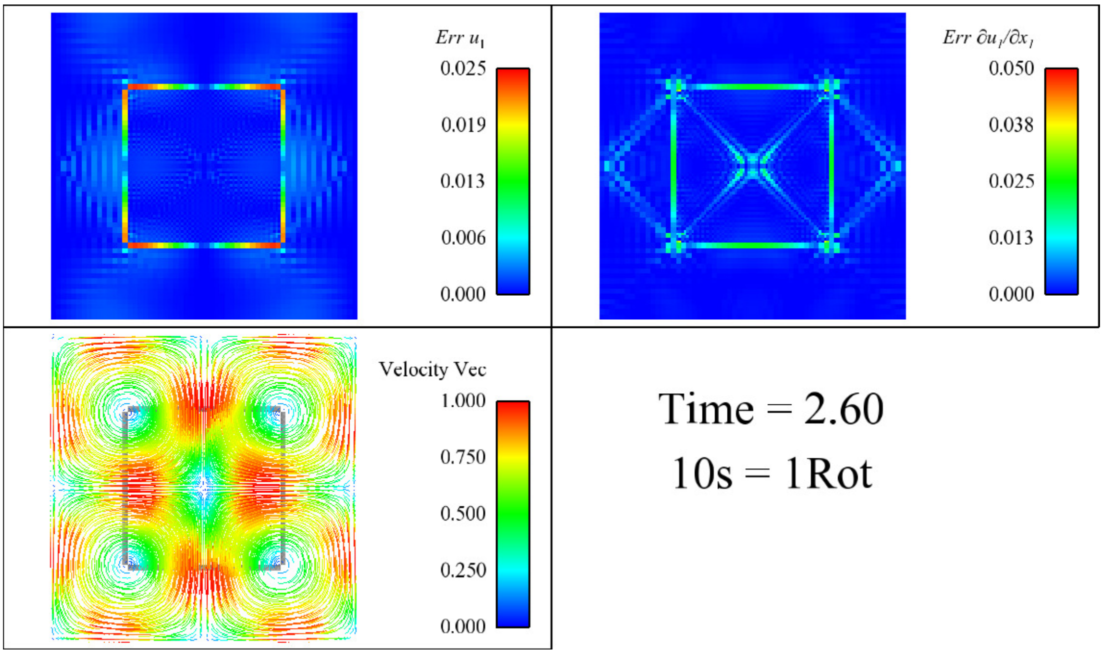

Figure 4.15: Taylor Green vortices: errors and velocity fields after 2.6 s for the mesh RR050. On top left error of the u_1 velocity component; on top right error of the $\partial u/\partial x$ derivative; on the bottom left the corresponding velocity field.

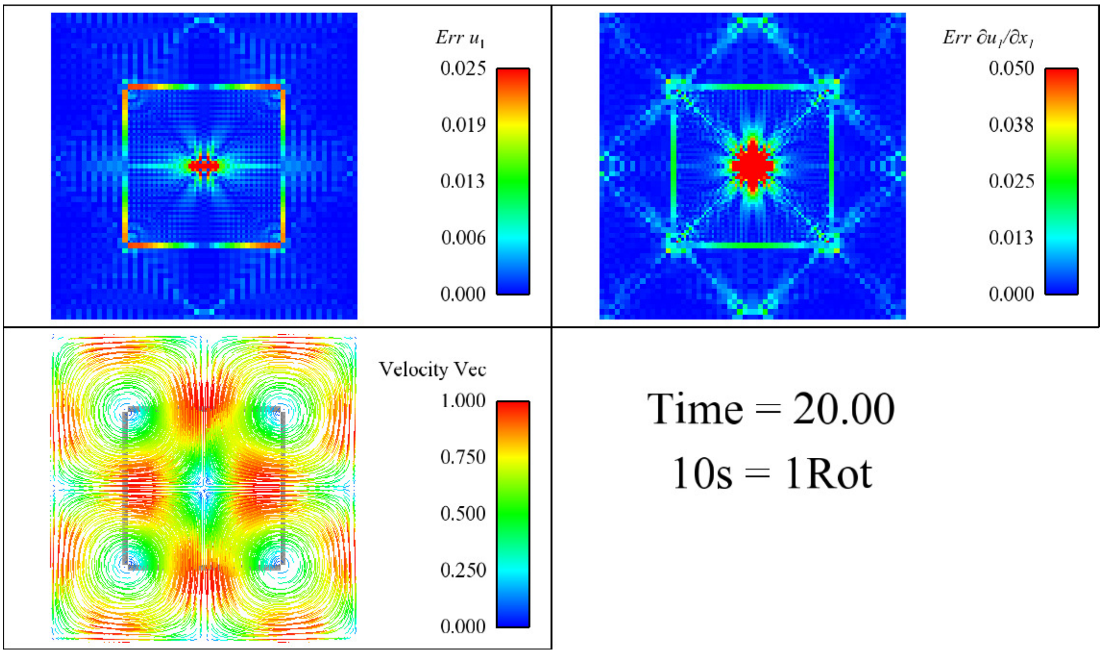

Figure 4.16: Taylor Green vortices: errors and velocity fields after 20 s for the mesh RR050. On top left error of the u_1 velocity component; on top right error of the $\partial u_1/\partial x_1$ derivative; on the bottom left the corresponding velocity field.

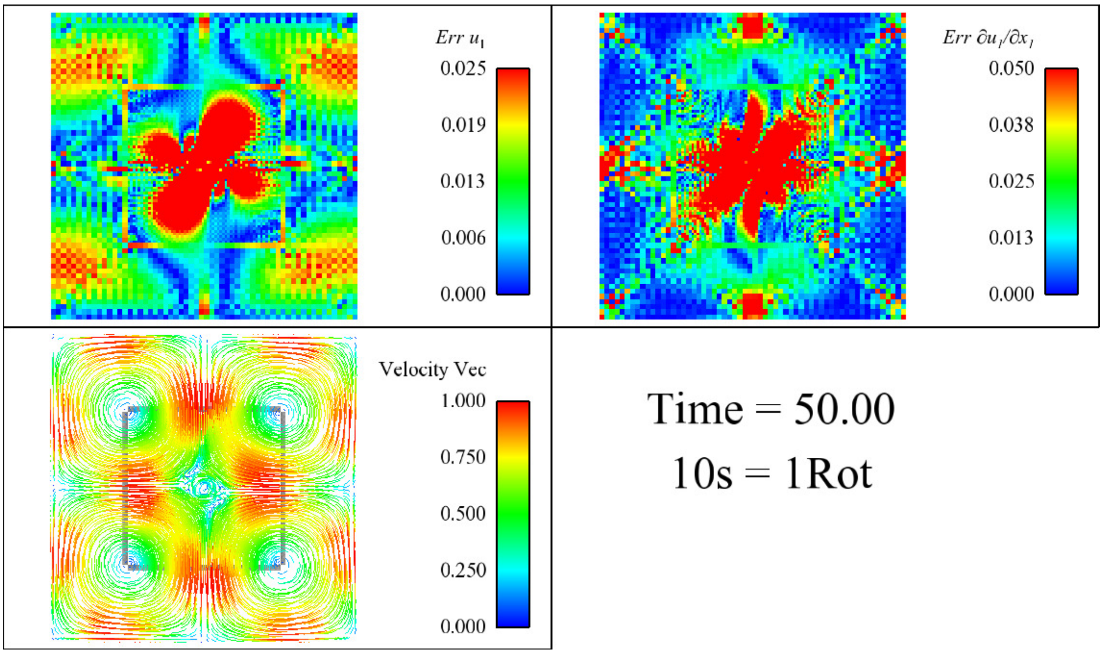

Figure 4.17: Taylor Green vortices: errors and velocity fields after 50 s for the mesh RR050. On top left error of the u_1 velocity component; on top right error of the $\partial u_1/\partial x_1$ derivative; on the bottom left the corresponding velocity field.

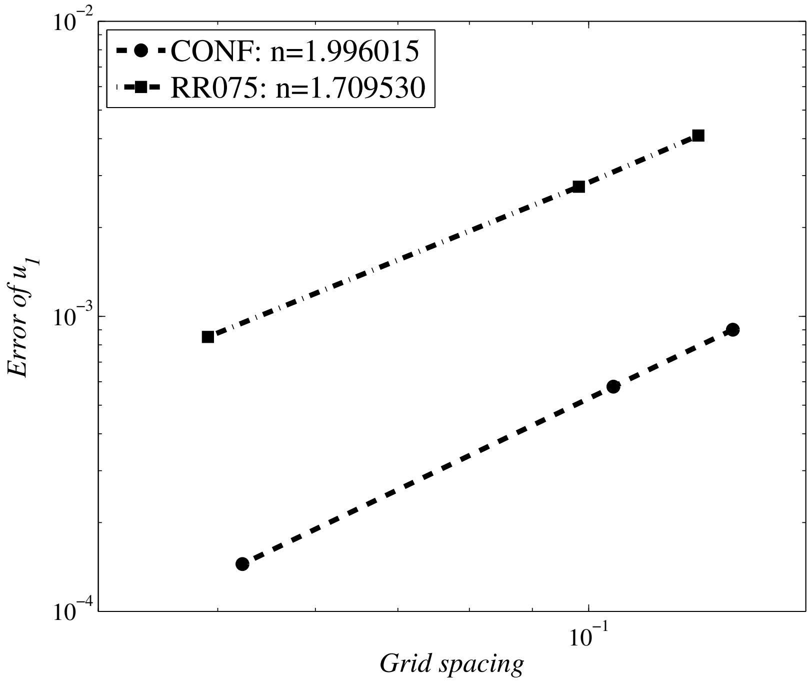

Figure 4.18: Taylor Green vortices: error reduction as function of the grid spacing for the conformal and the RR075 meshes. The base resolutions used are 48 × 48, 60 × 60 and 120 × 120. The base size is computed as weighted average of the different cell sizes. The error is evaluated after one hundred time steps (0.1 s in real time).

RR050 MESH OPTIMIZATION

Among all the embedded meshes the RR050 shows some of the worst properties in terms of energy conservation, displaying the earliest loss of coherence of the solution. However this type of refinement is widely used by commercial mesh generators. This section presents an attempt to improve conservation properties by moving the nodes at the interface between master and slave blocks. The mesh at the interface can be reduced to the one presented in Fig. 4.19. The optimization is carried out moving in the vertical direction the nodes y_l and y_r in order to have the face lying exactly half way between the two cell centres, which can be mathematically expressed as:

$$\frac{\overline{C_f G"_1}}{\overline{C_f G"_2}} = \frac{\overline{O_2 G_3}}{\overline{O_2 G_2}} = \frac{\overline{O_3 G_4}}{\overline{O_3 G_1}} = 1 \tag{4.22}$$

where C_f is the face centre at the interface, G is the cell centre, $G"$ is the projection of the cell centre on the line passing through the face centroid and perpendicular to the face, O is the intersection point between the line connecting two cell centres and the face and subscript numbers stands for the cell number. Note that in a not highly skewed cell (i.e. square or rectangle) $O \cong C_f$. The variation of the three ratios, defined by Eq. (4.22), as functions of y_l and y_r is drawn in the map of Figure 4.19 (left). The map presents two more lines: a thick black which represents the condition $y_l = y_r$ and a thin red which is the limiting condition where the cell centre G_1 has the same vertical distance y_r.

Obviously all conditions expressed by Eq. (4.22) cannot be achieved simultaneously because the three optimal lines do not intersect each other at one location. Consequently different "optimal points" are defined. P_1 and P_2 tries to improve the ratio $\overline{C_f G"_1}/\overline{C_f G"_2}$ shifting upwards y_l and y_r by the same amount. Point $P3$ tries to make the value of all the three ratios as close as possible to 1 maintaining the master cell convex. The condition expressed by (4.22) is achieved by point $P4$, but making concave the master cell. Finally point $P5$, where only the master-slave interface is considered, $\overline{C_f G"_1}/\overline{C_f G"_2} = 1$ and the line connecting $\overline{G"_1 G"_2}$ or $\overline{G_1 G_2}$ is exactly orthogonal with respect to the face at the interface.

Results are reported in Fig. 4.20 where it is obvious that the best "optimised" configurations can produce the same results of the original 1-2 configuration (RR050). In the original configuration the ratios $\overline{O_2 G_3}/\overline{O_2 G_2}$ and $\overline{O_3 G_4}/\overline{O_3 G_3}$ are already equal to 1 and the optimisation procedure spreads the non-orthogonality, distorting the mesh where was conformal before doing the optimisation. Eriksson and Nördstrom (2009) pointed out that the optimal condition is to have a flux point in the middle of the face centroid, which is easy to impose in 1D but not always possible in 2D and very difficult to achieve in 3D. Using a more complex mesh optimization as presented by Iaccarino and Ham (2005) could lead to better results, but there will always be areas where the optimizing algorithm will not produce perfectly orthogonal or slightly stretched meshes. As shown in this work, even if small, this imperfection could have a great impact on the solution.

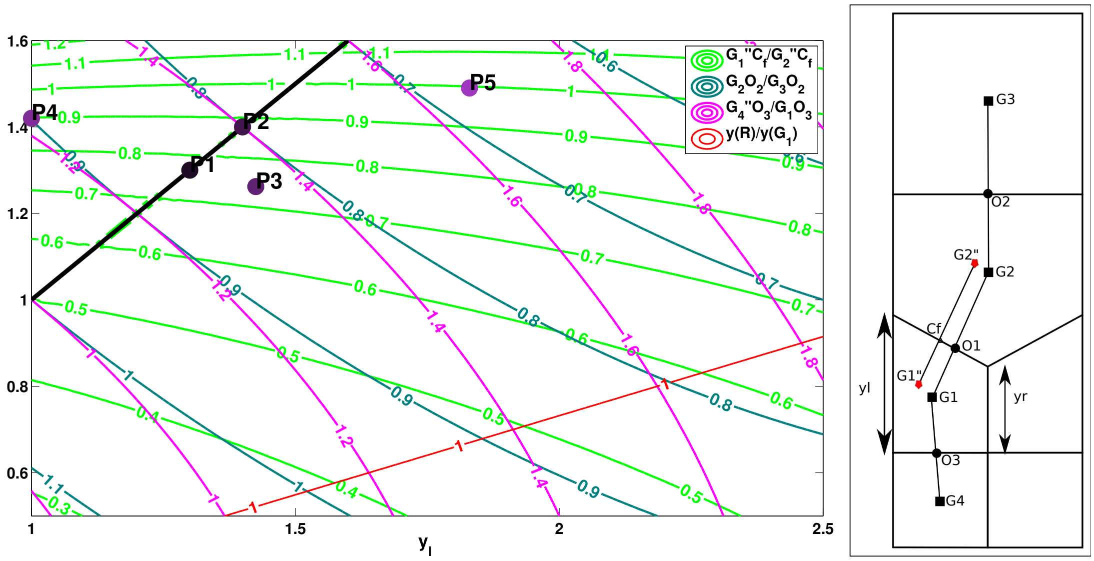

Figure 4.19: $RR050$ mesh optimization: map with the value of different ratios as function of y_r and y_l vertical distance.

4.3.4 POLYHEDRAL MESH

Finally, the Taylor-Green vortices test case is simulated with a fully unstructured mesh. Tetrahedral meshes, under *Code_Saturne* , are already investigated by Benhamadouche (2006). Polyhedral cells are considered in Moulinec et al. (2005) but using the Code Comet of M. Peric (see Ferziger and Peric (1997))

In this work three different meshes are considered and their characteristics are listed in Table 4.1. The mesh marked by POLY1 is generated directly from the mesh generator imposing periodic faces to topologically match. The reference size used by the grid generator is equal to the diagonal of a cell in the CONF60 mesh. The resulting mesh can be seen in Fig. 4.21. The mesh displays a high level of skewing and polygons are not regular. In order to improve the mesh quality another mesh is generated (see Fig. 4.22) and marked as POLY2. In this case a regular pre-triangulation of surfaces is created and, at the periodic faces, hanging nodes are allowed. The mesh POLY3 is similar to POLY2, but with a base size half the one in POLY2.

All meshes display a very early divergence of the solution, after only 2 vortex rotations. Moreover the POLY1 mesh shows an oscillatory behaviour (clear in the close up view) and the total kinetic energy overshoots the maximum theoretical value of 0.25. This unphysical behaviour can be fixed by adding the SLOPE test for the convective term as described in Section 3.2.2 (run R7 in Table 4.2). On the other hand the addition of the up-wind term increases the numerical dissipation, increasing the negative slope of the kinetic energy decay. A higher and more spread error, over all the domain, can be seen if error contours of u_1 velocity and x_1 derivative for the poly mesh (see Figs. 4.21 and 4.22) are compared with ones in an embedded refined mesh (see Fig. 4.15) . The non-orthogonalities of the mesh are distributed over the entire domain making the error no longer located in a specific area. A more regular grid like POLY2 produces better results as also reported in Table 4.3. The run times for the polyhedral meshes are also higher with respect to all the others not only because more iterations are necessary to reconstruct the non-orthogonalities, but also because of the high number of faces required to build this type of grid: all loops to compute convective and diffusion terms are performed on faces.

4.4 CONCLUSIONS

In this chapter kinetic energy conservation on embedded refined and polyhedral meshes is investigated and performances are compared against a structured conformal mesh simulation. The main outcome is that performances are degraded. All meshes lead to a divergence of the solution due to a loss of coherence of the solution. Unstructured meshes bring forward this phenomenon mainly because of the larger error committed in the reconstruction of the gradient. The evolution of the solution divergence depends on mesh quality: meshes with less skewness and stretching conserve energy for a longer period. This feature is characteristic of refinements with a structured sub-pattern like the 3-4. A value close to one of the refinement ratio RR also improves the conservation because of the stretching reduction at the interface. The importance of an orthogonal mesh is clear, in particular in the polyhedral mesh, where the non-regular mesh POLY1 displays a non-physical increase of the total kinetic energy. The problem is corrected using a CD convective scheme with the addition of a test on the slope, but which comes with an increase of the numerical viscosity. The most regular polyhedral mesh shows a large amount of error in comparison with the embedded refinements.

An attempt to optimize the 1-2 configuration is carried out with not much success. The reduction of non-orthogonalities at the interface is obscured by the addition of non-orthogonalities in adjacent areas. Better results might be obtained if a more complex algorithm is employed as the one presented in Iaccarino and Ham (2005), but it is very difficult to obtain a perfect orthogonality everywhere in the domain.

With the current availability of HPC facilities, and the chance to run meshes with millions or even billions of cells, automatic or semi-automatic mesh generation is inevitable. Unstructured meshes will be a requirement and, even using mesh optimization algorithms, the mesh will not be perfect all over the domain. Therefore author's moot point is that the approach to the problem has to be reversed from mesh optimization to numeric improvements. Numerical codes must be able to deal also with bad constructed grids, not only displaying a stable but also accurate solution. A possible alternative methodology is the use of auxiliary points in order to locally rebuild orthogonality as presented by Moulinec and Wesseling (2000). For every face centre two auxiliary points are created in order to have the flux point lying exactly in the middle. Afterward the solution is interpolated on the auxiliary points using a predefined support. The advantage of the method is that the convection-diffusion term can be evaluated using exactly a second order discretization and all the error is concentrated only in the interpolation phase. Many other solutions can be implemented, like the SBP (Summation-By-Part) operators in conjunction with a penalty procedure to impose boundary conditions as presented in the introduction (Sec. 4.1).

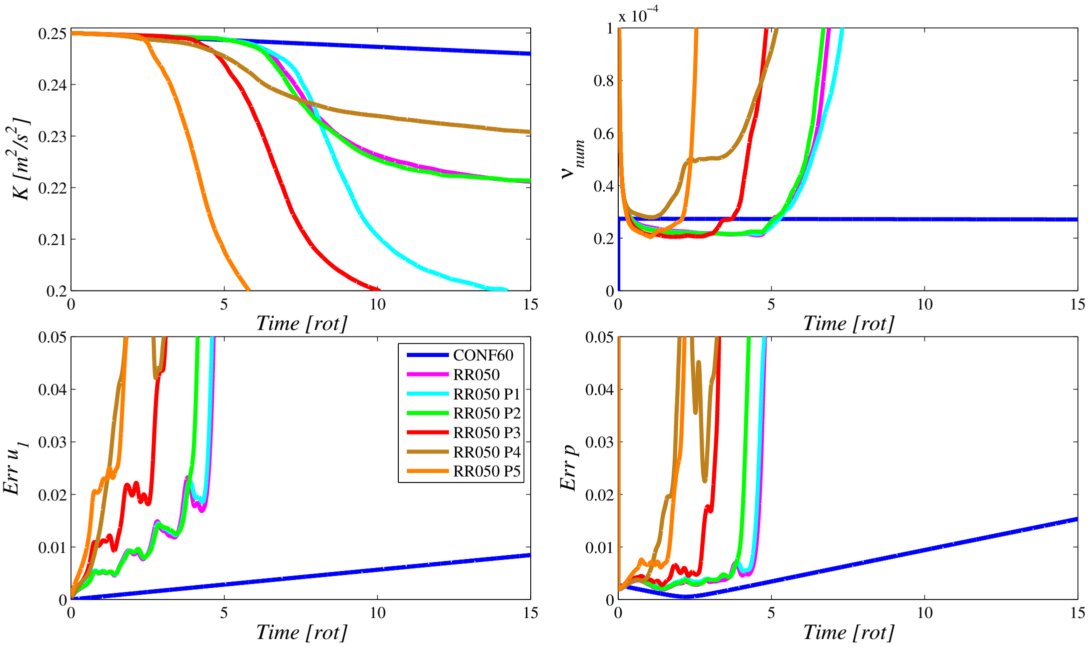

Figure 4.20: Taylor Green vortices: results for the optimization of mesh RR050. Total kinetic energy (top left), equivalent viscosity (top right), global error on u_1 (bottom left), global error on p (bottom right). Time is expressed in number of vortex rotations ($1\,rot = 10\,s$). See Table 4.2 for run definitions.

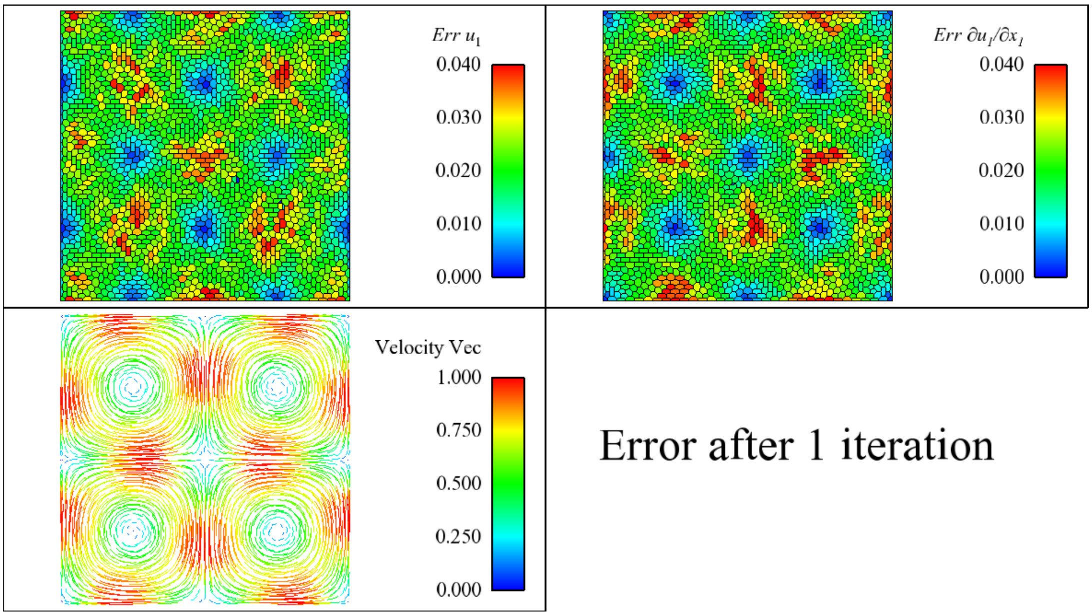

Figure 4.21: Taylor Green vortices: errors and velocity fields after one iteration for the mesh POLY1 On top left the error on the u velocity component; on top right the error on the $\partial u_1/\partial x_1$ derivative; on the bottom left the correspondent velocity field.

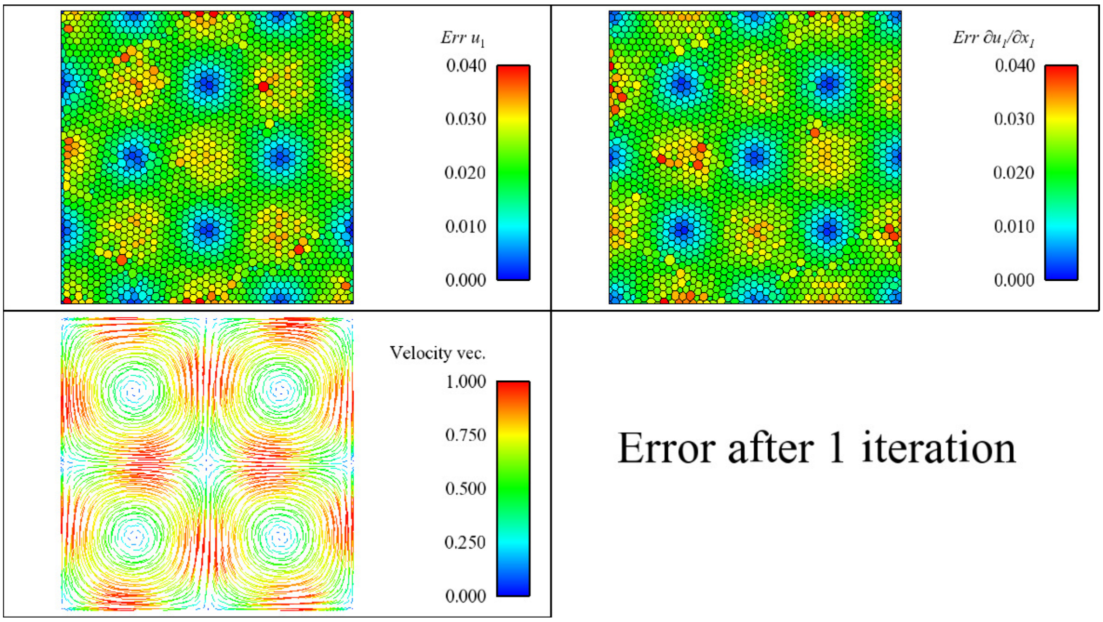

Figure 4.22: Taylor Green vortices: errors and velocity fields after one iteration for the mesh POLY2. On top left the error on the u velocity component; on top right the error on the $\partial u_1/\partial x_1$ derivative; on the bottom left the correspondent velocity field.

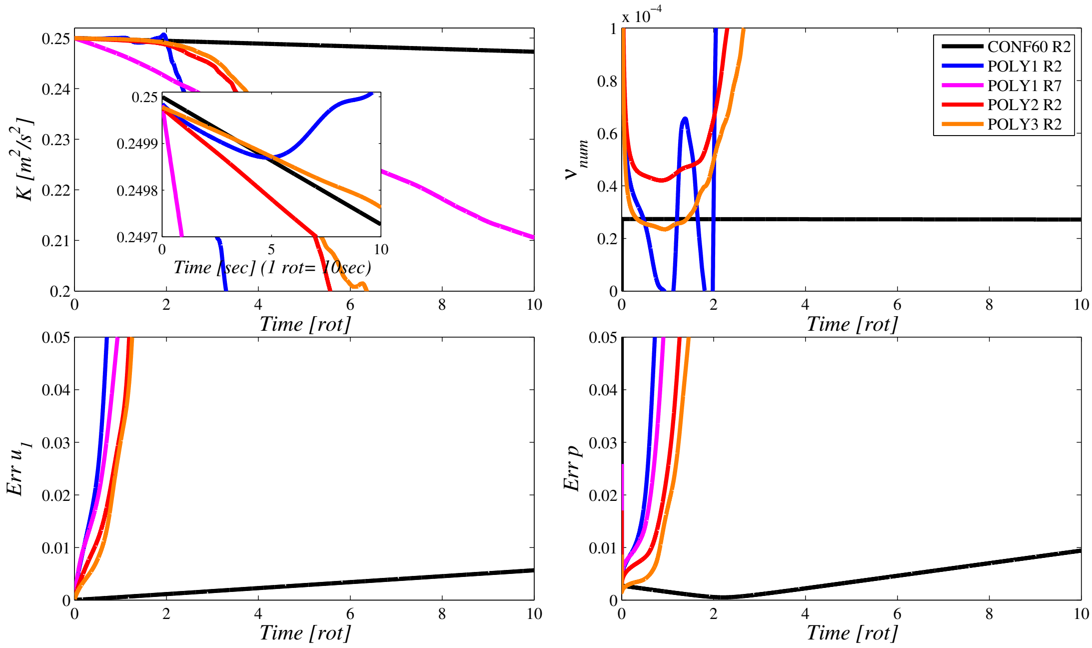

Figure 4.23: Taylor Green vortices: results for the polyhedral meshes. Total kinetic energy (top left), equivalent viscosity (top right), global error on u_1 (bottom left), global error on p (bottom right). Time is expressed in number of vortex rotations ($1\,rot = 10\,s$). See Table 4.2 for run definitions.

Chapter 5

CHANNEL FLOW

The turbulent channel flow has been used for many years as a reference for turbulence modelling. Indeed, with the increase of computing power, several DNS studies have been carried out in order to gain a better understanding of near wall turbulence. Examples of DNS studies of channel flow can be found in Kim et al. (1987); del Alamo and Jimenez (2003). In the present work Kawamura et al. (1999); Abe et al. (2001, 2004) are used as references because of the availability of heat transfer data.

This chapter is divided into three main sections: first an introduction, secondly the use of unstructured meshes in wall bounded LES is analysed; finally the Hybrid RANS/LES model of Sec. 2.4 is validated. In the case of unstructured meshes the focus is mainly on embedded refinements, trying to verify some of the findings of Chapter 4. In the case of the Hybrid model the main focus is to investigate some possible modifications of the blending function and the effect of mesh resolution. Additionally an extensive validation of the heat transfer modelling is also carried out.

5.1 INTRODUCTION

The geometry representing a plane channel, with the definition of all geometrical parameters, is sketched in Fig. 5.1. The top and bottom walls are located at $y = 0$ and $y = 2\delta$. The streamwise direction[1] is $x_1 = x$ and the maximum velocity is located at the centre line $y = \delta$. The mean velocity field is only dependent on the wall-normal direction and is driven by a constant pressure gradient in the stream-wise direction. All other statistical derivatives in the span-wise and streamwise directions are zero.

The mean momentum equations of A.2 can be simplified to:

---

[1] In this context a Cartesian system of reference (x, y, z) is used instead (x_1, x_2, x_3) adopted in Chapter 2. Consequently the velocity components are (u, v, w).

$$\begin{cases} -\dfrac{1}{\rho}\dfrac{\partial\langle p\rangle}{\partial x} = \dfrac{\partial\langle u'v'\rangle}{\partial y} - \nu\dfrac{\partial^2\langle u\rangle}{\partial y^2} \\ -\dfrac{1}{\rho}\dfrac{\partial\langle p\rangle}{\partial y} = \dfrac{\partial\langle v'v'\rangle}{\partial y} \end{cases} \tag{5.1}$$

being $\langle w\rangle = 0$, $\langle v\rangle = 0$, $\langle u\rangle$ function on the wall normal coordinate ($\langle u\rangle = f(y)$). If the lateral momentum equation is integrated in the y direction, between 0 and a generic coordinate y, and as boundary condition at the wall $\langle v'v'\rangle_{y=0} = 0$ is used, the following relation can be obtained:

$$\langle v'v'\rangle + \frac{\langle p\rangle}{\rho} = \frac{p_w(x)}{\rho} \tag{5.2}$$

where p_w is the average pressure at the wall as function of x, hence the mean axial pressure gradient is uniform across the flow which can be express as:

$$\frac{\partial\langle p\rangle}{\partial x} = \frac{dp_w}{dx} \tag{5.3}$$

If Eq. (5.3) is inserted into the mean axial momentum the following ordinary differential equation can be written:

$$-\frac{1}{\rho}\frac{dp_w}{dx} = \frac{d\langle u'v'\rangle}{dy} - \nu\frac{d^2\langle u\rangle}{dy^2} \tag{5.4}$$

now the total shear stress can be introduced as:

$$\tau = \rho\nu\frac{d\langle u\rangle}{dy} - \langle u'v'\rangle \tag{5.5}$$

the axial momentum becomes:

$$\frac{d\tau}{dy} = \frac{dp_w}{dx} \tag{5.6}$$

Equation (5.6) is solved with separation of variable and introducing the wall shear stress as:

$$\tau(0) \equiv \tau_w \equiv \rho\nu\left(\frac{d\langle u\rangle}{dy}\right)_{y=0} \tag{5.7}$$

The total shear is antisymmetric with respect to the channel mid plane, hence $\tau(\delta) = 0$ and $\tau(2\delta) = -\tau_w$ giving the following solution for Eq. (5.6):

$$\begin{cases} \tau(y) = \tau_w \left(1 - \dfrac{y}{\delta}\right) \\ -\dfrac{dp_w}{dx} = \dfrac{\tau_w}{\delta} \end{cases} \tag{5.8}$$

In the near wall region viscosity is the dominant parameter, therefore a set of viscous scales can be defined as follows:

$$\begin{cases} \text{friction velocity} & u_\tau \equiv \sqrt{\dfrac{\tau_w}{\rho}} \\ \text{viscous length} & \delta_\nu \equiv \dfrac{\nu}{u_\tau} \\ \text{friction } Re & Re_\tau \equiv \dfrac{u_\tau \delta}{\nu} \\ \text{wall units} & y^+ \equiv \dfrac{u_\tau y}{\nu} \quad u^+ \equiv \dfrac{\langle u \rangle}{u_\tau} \end{cases} \tag{5.9}$$

The channel flow can be divided, as a function of the wall distance, into different regions and layers, which have different properties:

- *viscous sublayer* ($y^+ < 5$): the Reynolds stress $\langle u'v' \rangle$ is negligible and the dimensionless wall velocity u^+ is a linear function of y^+ as follows:

$$u^+ = y^+ \tag{5.10}$$

- *buffer layer* ($5 < y^+ < 30$): blending region between the viscous sublayer and the log-law region;
- *log-law region* ($y^+ > 30 \wedge y/\delta < 0.3$): the dimensionless wall velocity u^+ holds a logarithmic profile as follows:

$$u^+ = \frac{1}{\kappa} \ln y^+ + B \tag{5.11}$$

  where $\kappa = 0.41$ is the von Karman constant and $B = 5.2$;

- *outer layer* ($y^+ > 50$): the shear stress is mainly dominated by the Reynolds shear stress;
- *inner layer* ($y/\delta < 0.1$): the mean velocity profile $\langle u \rangle$ is mainly dominated by u_τ and y^+ and independent from velocity at the centre line U_0 and δ;
- *overlap region* ($y^+ > 50 \wedge y/\delta < 0.1$): overlap region between the inner and the outer layers.

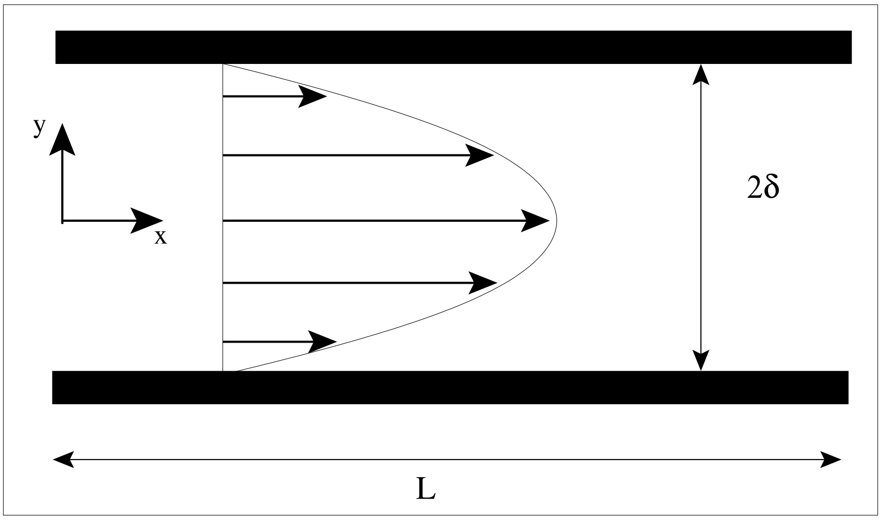

Figure 5.1: Sketch of the geometry of a plane channel flow.

5.2 LES

5.2.1 Mesh description

In this section the objective is to investigate the use of unstructured meshes for LES calculations. Five different meshes for channel flow at $Re_\tau = 395$ are employed and the characteristics are summarized in Table 5.1. The STRUCT mesh is a structured mesh where, in the wall normal direction, a hyperbolic node distribution is employed. The TAYLOR mesh is an embedded refined mesh built following the Taylor micro-scales[2] as described in Addad et al. (2008). Taylor micro-scales are estimated from DNS databases and lengthscales in streamwise and span-wise directions are used to define the cell sizes at different wall distances. Below $y^+ \approx 70$ the wall normal spacing does not follow the Taylor micro-scales, but the distribution follows a geometrical expansion with a ratio of about 1.1, starting from a position of the first cell centre at $y^+ = 1$. The mesh presents an almost continuous coarsening as the wall distance increases. The RR075 mesh is characterized by embedded refinements but only four coarsening steps are applied and they follow a 3-4 sub-pattern as presented in Chapter 4 as the best ratio for embedded refinements. The four interfaces are placed around $y^+ = 14$, 45, 100 and 205. In the wall normal direction a geometrical distribution with an expansion ratio around 1.1 is

---

[2] The Taylor micro-scale λ_f is defined as:

$$\lambda_f = \left[-\frac{1}{2} f'' (0,t) \right]^{-1/2}$$

where f is the velocity auto-correlation function and $f''(0,t)$ its second derivative evaluated at $r = 0$.

used. The RANDOM mesh has the first near wall layer identical to the one of RR075 and it is also identical from $y^+ = 205$ to the centre line. Between $2 < y^+ < 230$ a continuous coarsening is used, following a parabolic decrease[3]. A bar chart with the non-orthogonality coefficients[4] for TAYLOR, RR075 and RANDOM meshes are plotted in Fig. 5.3. Mesh RR075 shows the best orthogonality, having over than 80% of the orthogonality coefficients below 7.5^o, whereas the other two meshes have around, or even more that 50% of faces above this limit.

Table 5.2 lists the numerical parameters used for all the different simulations. The time step is $0.2{\cdot}10^{-2}\ s$ and constant for all cases, which gives an instantaneous $CFL_{max} \leq 1.5$ and an average value $\langle CFL_{max}\rangle \leq 1$. All cases employ the Smagorinsky model (see Sec. 2.3.3.1) with a constant $C_s = 0.065$. The anisotropy is taken into account using the Van Driest damping as described into Sec. 2.3.4).

Mesh	Mesh resolution	Δx^+, Δy^+, Δz^+	n^o cells $[10^3]$
STRUCT	128 × 64 × 96	20 × 2 × 13	786
TAYLOR	200 × 46 × 100	13 × 2 × 13	443
RR075	216 × 44 × 112	12 × 2 × 11.5	493
RANDOM	216 × 44 × 112	12 × 2 × 11.5	344

Table 5.1: List of all the meshes used for the LES of channel flow at $Re_\tau = 395$. In the cases of the three embedded refined meshes the number of cells in the streamwise and span-wise direction refers only to the first layer at the wall. For the subsequent layers a coarsening of the mesh is employed following different strategies (see Sec. 5.2.1). The number of cells in the wall-normal direction stands for the number of layers from wall-to-wall.

---

[3] A parabola is fitted between the number of cell at the first layer and at the layer placed at $y^+ = 205$. The number of cells was calculated finding the zero of the following:

$$\begin{cases} \textit{streamwise dir} \Rightarrow 67.2n_x^2 - 1.82n_x - y_c = 0 \\ \textit{spanwise dir} \Rightarrow 81.2n_z^2 - 2.10n_z - y_c = 0 \end{cases}$$

where n_x is the number of cells in the streamwise direction, n_z in the span-wise and y_c is the location of the cell centre. n_x and n_z were subsequently truncated to the closest integer number. The coefficients of the two parabolas are obtained using a parabolic fitting between the number of cells in the streamwise and span-wise directions in the first layer at the wall ($n_x = 212$ $n_z = 112$) and at $y^+ = 230$ ($n_x = 66$ $n_z = 36$). The location of the cell centre $y_c$is the same of the $RR075$ mesh.

[4] Non-orthogonality coefficient is the angle between the line connection two cell centres of adjacent cells and the line perpendicular to the face and passing through the face centre.

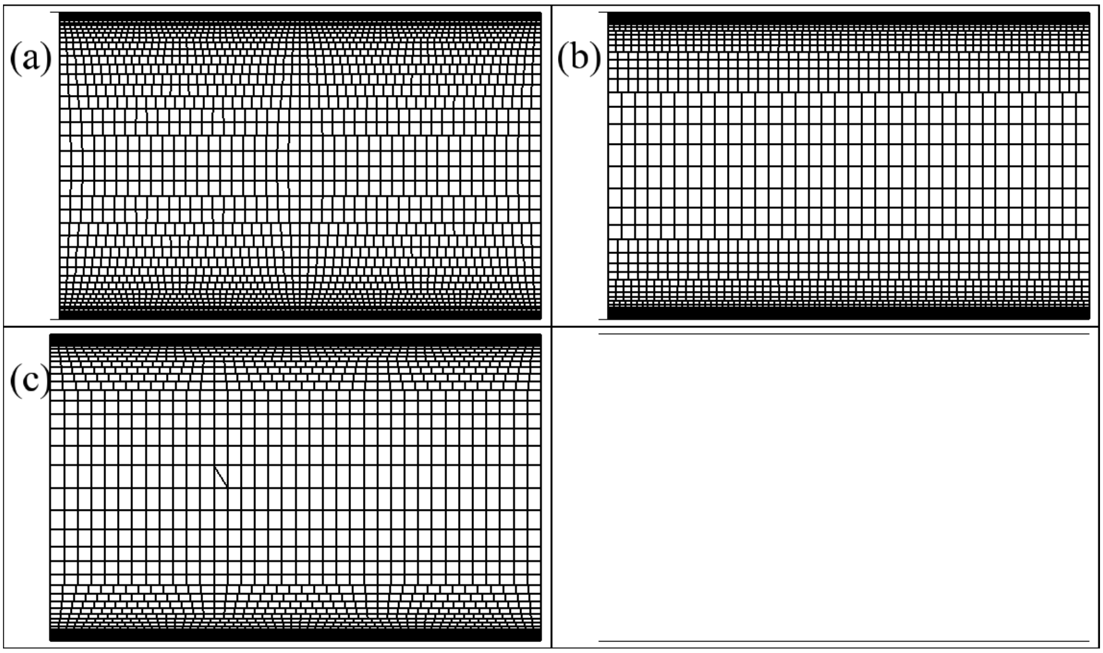

Figure 5.2: Visualization of the unstructured meshes used for the LES of channel flow.(a)TAYLOR mesh; (b) $RR075$ mesh; (c) RANDOM mesh.

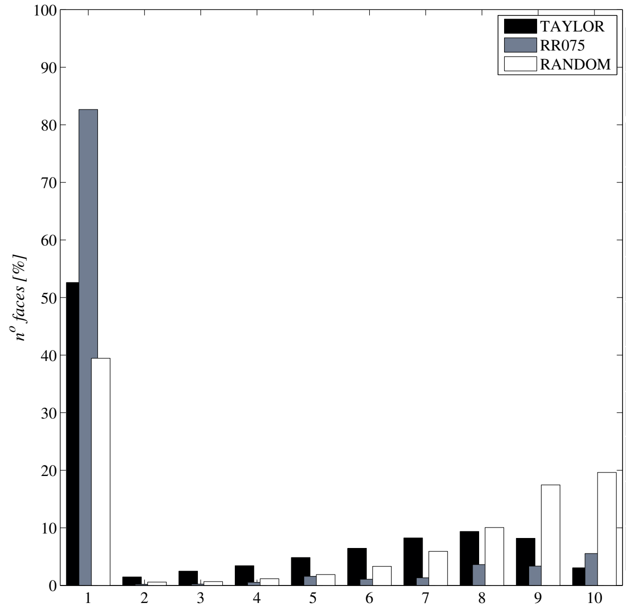

	Non-orthogonality coeff. [^{o}]		
	TAYLOR	$RR075$	RANDOM
1	0-7.5	0-7.5	0-8.25
2	7.5-15	7.5-15	8.25-16.5
3	12-22.5	12-22.5	16.5-24.75
4	22.5-30	22.5-30	24.77-33
5	30-37.5	30-37.5	33-41.25
6	37.5-45	37.5-45	41.25-49.5
7	45-52.5	45-52.5	49.5-57.75
8	52.5-60	52.5-60	57.75-66
9	60-67.5	60-67.5	66-74.25
10	67.5-75	67.5-75	74.25-82.5

Figure 5.3: Non-orthogonality coefficients for the meshes TAYLOR, RR075 and RANDOM. The coefficient is measured in [^{o}] and it represents the angle between the line connecting two face centres and the line orthogonal to the face passing through the face centre.

Parameter	Value
Convective scheme	CD
Residual resolution linear system	$p \Rightarrow \epsilon = 1e-5$ $vel \Rightarrow \epsilon = 1e-5$
Number vel/pres coup.	1
Grad. reconstruction	$n_{max}\, rec = 100$ $\epsilon = 1e-6$
Reconstruction of the RHS	$p = 10$ $vel = 5$
Time step	$0.2 \cdot 10^{-2}\, s$

Run	n^o vel/pres
STx	1
STx + VP	3

Run	Conv. scheme
ST4	CD + 4% UW(fail ST)
ST2 + VP	CD + 2% UW(fail ST)

Table 5.2: List of the default numerical settings used for the LES calculations. ST means addition of up-winding (UW) is case of slope test failure (see Sec. 3.2.2). VP stands for an increase of the iterations in the velocity-pressure coupling.

5.2.2 Results

In most papers the resolved quantities given by the LES are directly compared with the ones given by DNS or experiment. In Winckelmans et al. (2002) authors suggested that, instead, the reduced or anisotropic Reynolds stresses should be used for the comparison as follows:

$$R^{EXP}_{ij,R} \approx R^{LES}_{ij,RES} + \langle \tau^a_{ij} \rangle \tag{5.12}$$

where $R_{ij,R} = R_{ij} - \frac{1}{3} R_{kk}\delta_{ij}$ and $\langle \tau^a_{ij} \rangle$ is the average of the modelled part of the Reynolds stresses. In this context an effective eddy viscosity model is used and the anisotropic part of the sub-grid contribution is given by Eq. (2.22).

Figure 5.4 reports both the resolved and the modelled part of the Reynolds stresses for the TAYLOR mesh. For normal stresses u'^{+}_{rms}, v'^{+}_{rms} and w'^{+}_{rms} the modelled contribution is negligible. In the case of the shear stress $\langle u'v' \rangle^+$ the inclusion of the modelled part is relevant only for $y^+ \leq 100$, and the contribution around the peak value is of the order of 3%. Therefore this contribution can be neglected without a large impact on the final quality of the results. Indeed, as will be clear form the following coverage, the main point is not to obtain a perfect comparison with the reference DNS, but to analyse if the the solution has some oscillatory behaviour. As suggested by Winckelmans et al. (2002) reduced stresses are reported in order to have a wider comparison.

Figure 5.5 reports a comparison between different meshes. The shear stress $\langle u'v' \rangle^+$ reaches the required DNS level in the log-layer ($y^+ \approx 50$) with the TAYLOR grid, but the mesh RR075 shows an oscillatory behaviour of the solution between $15 < y^+ < 200$ which corresponds to the region between the refined layers. Normal stresses u'^{+}_{rms} and w'^{+}_{rms} , for the same mesh, do not display any clear oscillatory behaviour whereas v'^{+}_{rms}

does. Figure 5.6 reports two attempts to remove the oscillations: the first one by increasing the number of iterations of the velocity/pressure coupling and second one by using the test on the slope for the convective scheme as presented in Section 3.2.2. Both attempts fail to correct the problem. The phenomenon has been already described in Benhamadouche (2006) in conjunction with a $1-2$ type of refinement and it was credited to this particular type of refinement. On the other hand the RANDOM mesh does not display the same problem (see Fig. 5.7). The mesh has in common with RR075 the first layer of cells at wall and middle parts, but the structure of the refinement is more similar to the TAYLOR mesh. Indeed results for the RANDOM mesh are satisfactory taking into account that the global resolution is almost one quarter less with respect to the TAYLOR or RR075 meshes[5].

When the CD convective scheme with slope test is used, it is of interest to visualize where the test fails. This is achieved using an average counter for every internal face: a value close to zero stands for no failure of the slope test for the face; on the contrary a value close to one indicates that the face fails the test every time the variable is resolved. An example is plotted in Fig. 5.8 for u and in Fig. 5.9 for v. In the near wall region the slope test is rarely active. Moving toward the centre of the channel, where the flow is turbulent, more up-winding is added, in particular where the mesh is more stretched or where the non-orthogonality, introduced by the refinement process, is large. This is clear looking at the interfaces, close to the channel centre line, and in particular where small faces are adjacent to large ones (Fig. 5.8). Two interesting points are observed: first the slope test fails also in regions where the mesh is structured (around the centre of the channel), consequently up-winding is added where, in theory, it should not be (structured part in the centre of the domain). In a turbulent flow, high level of oscillations are present and it is very difficult to distinguish between turbulent and spurious oscillations. The second point is that oscillations affects more v velocity component with respect to others. This is not surprising because the coarsening is perpendicular to this velocity component, whereas it is parallel to the other two. More figures about the distribution of up-winding use can be found in Appendix B (Figs. B.2, B.3 and B.4).

Table 5.4 lists the average CPU time for the STRUCT, TAYLOR and RR075 meshes. The average is performed over 40000 time steps on an 8 Dual-Core AMD Opteron Processor 8220. Although the TAYLOR mesh has less cells than the other two, it has the highest CPU time per iteration. This is not surprising, because the TAYLOR grid has the highest amount of non-orthogonalities and the reconstruction of the gradient requires more time to converge. Moreover iterations necessary to resolve a linear system

---

[5] The RR075 mesh displays the same oscillatory behaviour also in others code, i.e. STAR-CD, as can be seen from Fig. B.1 in appendix. Therefore the issue is not code related but resides in the specific meshing strategy employed to generate the mesh RR075.

increase, for example in the STRUCT mesh only 88 iterations are required to converge, whereas 265 are necessary for the TAYLOR mesh.

In order to better understand the nature of the spurious oscillations budgets of kinetic energy and Reynolds stresses are evaluated using the equations of Appendix B.1. More about modelling effects on budgets can be found in Howard and Addad (2009). The budgets are computed in a "DNS mode", therefore modelling effects are not taken into account, because the focus of this analysis is to identify possible oscillatory behaviours and not to exactly reproduce the DNS data-set. Budgets are computed only for TAYLOR and RR075 in order to compare the behaviour of two unstructured meshes. As mentioned before dissipation is underestimated, but the simple addition of the model does not compensate, because numerical dissipation is also relevant. The only possibility to reduce numerical dissipation is to increase the mesh resolution moving toward a DNS. Despite the absence of model contributions, turbulent kinetic energy k budget compares with a relatively good approximation against the DNS data, beside the dissipation (see Figs. 5.10 and 5.11). Surprisingly $\langle u'v' \rangle$ budget (see Fig. 5.12) does not display any clear oscillatory behaviour, although $\Pi_{u'v'}$ and $P_{u'v'}$ do not have the smooth profiles as the ones of the TAYLOR mesh (Fig. 5.13). Turbulent diffusion $T^u_{u'u'}$ (compare Fig. 5.14 with Fig. 5.15) and the velocity-pressure transfer term $\Pi_{u'u'}$ (compare Fig. 5.16 with Fig. 5.17) show a large oscillatory behaviour. A first possible explanation might be the sparse distribution of the control points in the wall normal direction, but the absence of the phenomenon in the RANDOM mesh (which has the same wall normal cell distribution of RR075) gives evidence of the contrary. The velocity-pressure transfer term $\Pi_{v'v'}$ reduces to:

$$\Pi_{v'v'} = \frac{2}{\rho} \left\langle v' \frac{\partial p'}{\partial y} \right\rangle \tag{5.13}$$

and the turbulent diffusion $T^u_{u'u'}$ leads to:

$$T^u_{u'u'} \approx \left\langle v' \frac{\partial u'u'}{\partial y} \right\rangle = \left\langle 2u'v' \frac{\partial u'}{\partial y} \right\rangle \tag{5.14}$$

In both terms appear a quantity (v' for $\Pi_{v'v'}$ and $u'v'$ for $T^u_{u'u'}$) that has shown a swinging behaviour and which is amplified by a large gradient with the result of an amplification of the phenomenon. The ascription of the spurious oscillations to the wall normal velocity is not surprising because the non-conformal refinements follow the same direction. The main question now remains: *why is this effect not present for the* TAYLOR *or the* RANDOM *mesh?* A possible explanation could be a simple error cancellation. A series of equal coarsening steps can introduce the same error in the solution, while a non-specific pattern produces a more random error. Random errors can cancel out, in particular through the average procedure in time and space. In conclusion in a mesh with series of random refinements the error exists but the averaging process only hides it. The remaining budgets for $\langle w'w' \rangle$ are reported in Section B.1 of appendix.

Mesh	Avg CPU Time $[s]$	Diff. [%]	Avg n^o iter. for p	Diff. [%]
STRUCT	15.8	0	88	0
TAYLOR	18.5	17	265	200
RR075	16.6	5	188	113

Table 5.4: Average iteration time for different meshes and average number of iteration necessary to resolve the linear system for the pressure. The average is performed over 40000 time steps on a 8 Dual-Core AMD Opteron Processor 8220 all grouped in the same blade.

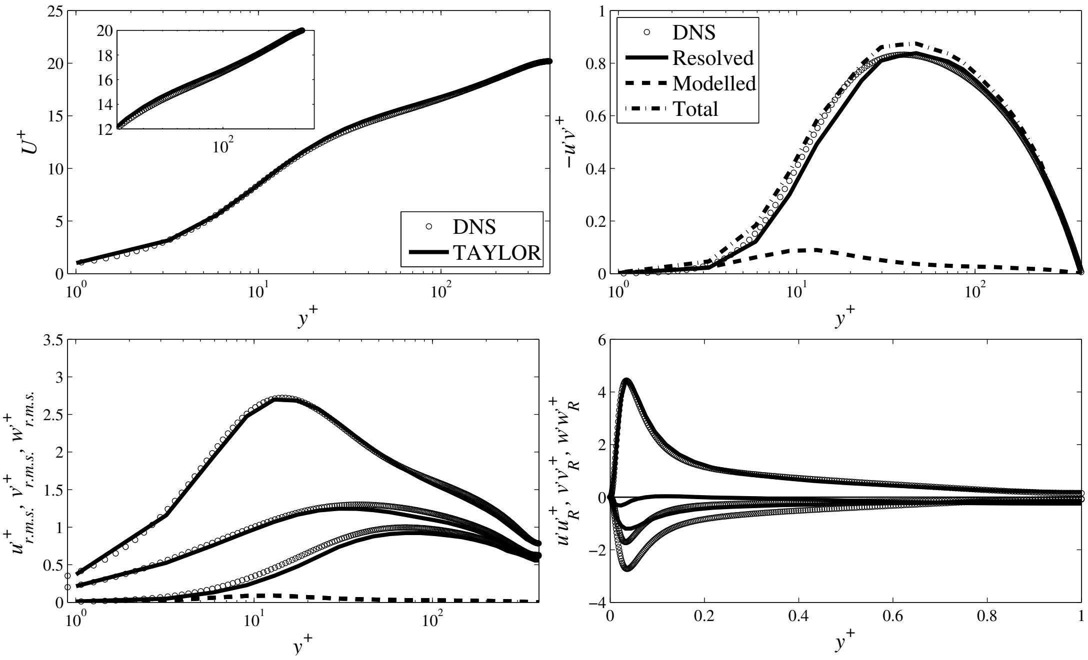

Figure 5.4: LES of channel flow: evaluation of the difference between resolved and modelled. Mean velocity (top left), shear stress (top right), normal stresses (bottom left) and their reduced counterparts (bottom right).

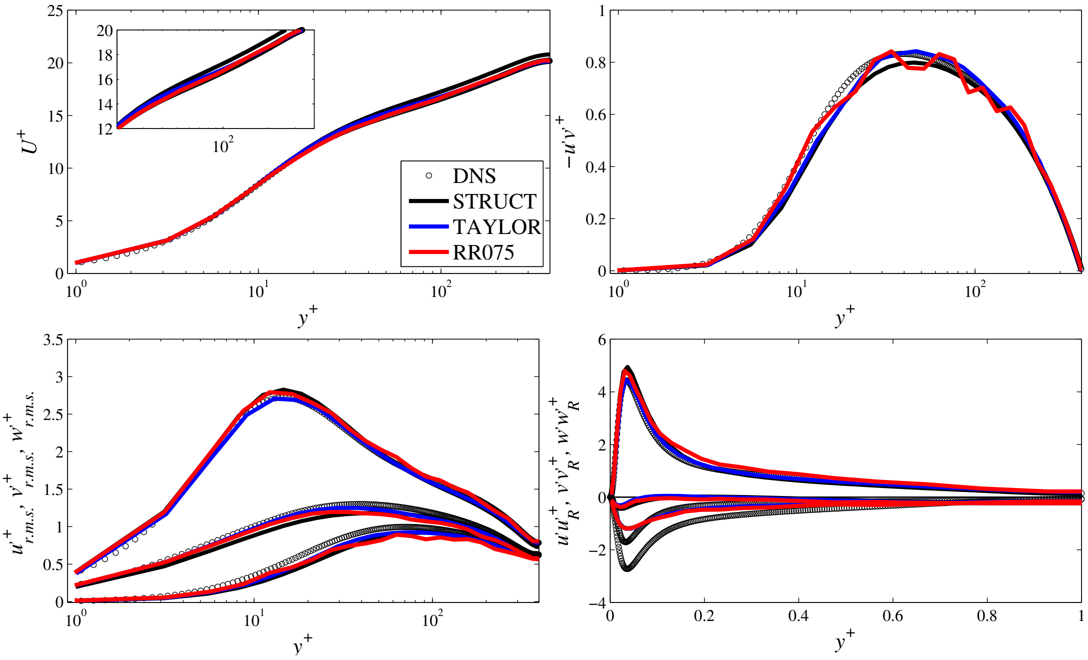

Figure 5.5: LES of channels flow: comparison between meshes (part a). Mean velocity (top left), shear stress (top right), normal stresses (bottom left) and their reduced counterparts (bottom right).

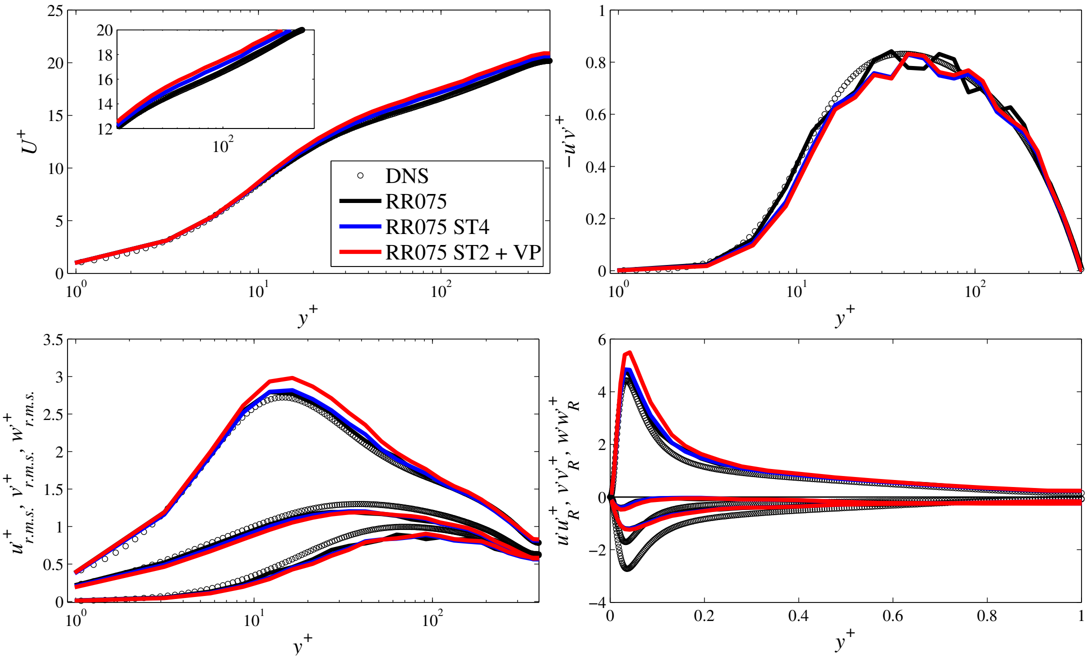

Figure 5.6: LES of channel flow: effect of the numerical treatment. Mean velocity (top left), shear stress (top right), normal stresses (bottom left) and their reduced counterparts (bottom right). ST4 stands for a CD convective scheme with the 4% of UW in case of failure of slope test. ST2 with 2% of UW. VP stands for an increase of the vel./pres iterations from 1 (def. value) to 3.

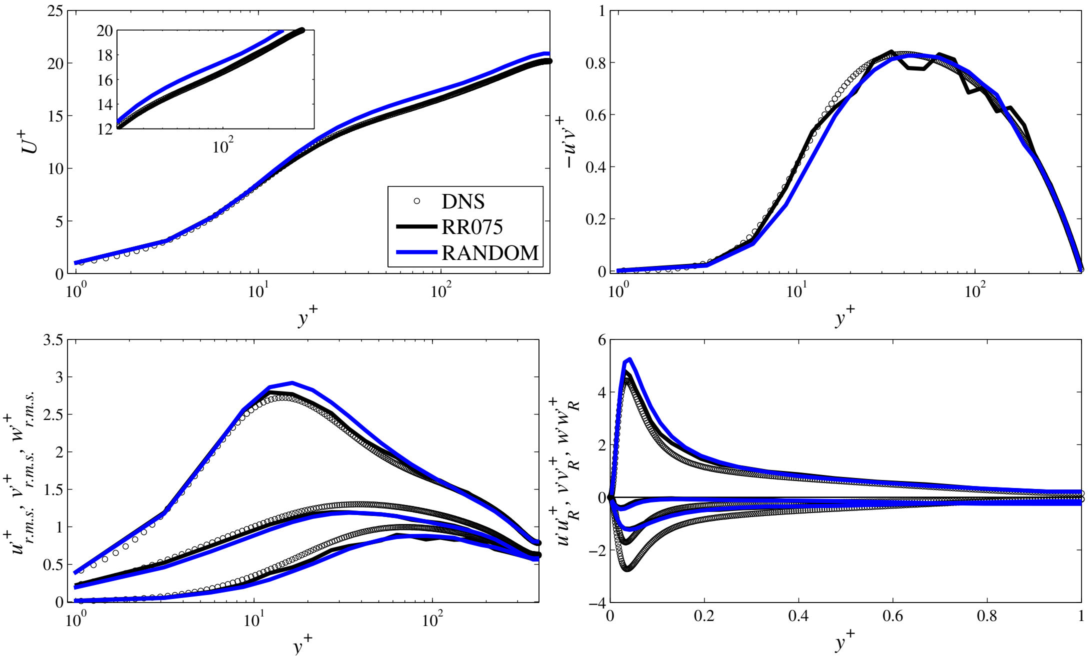

Figure 5.7: LES of channel flow: comparison between meshes (part b). Mean velocity (top left), shear stress (top right), normal stresses (bottom left) and their reduced counterparts (bottom right).

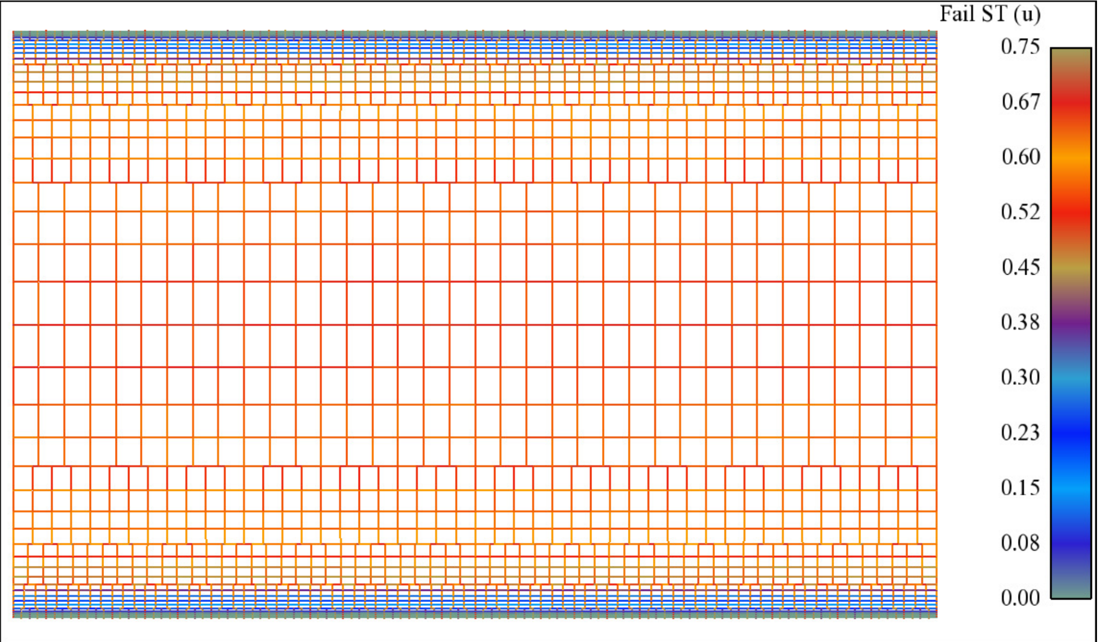

Figure 5.8: LES of channel flow: average counting of the slope test failure in the cross plane for the u velocity component in the span-wise direction. The cut plane is located in the middle of the domain and the average is performed over 20000 time steps ($2\,s$ of physical time). The results are plotted on the cell faces. The amount of UW is equal to 2%.

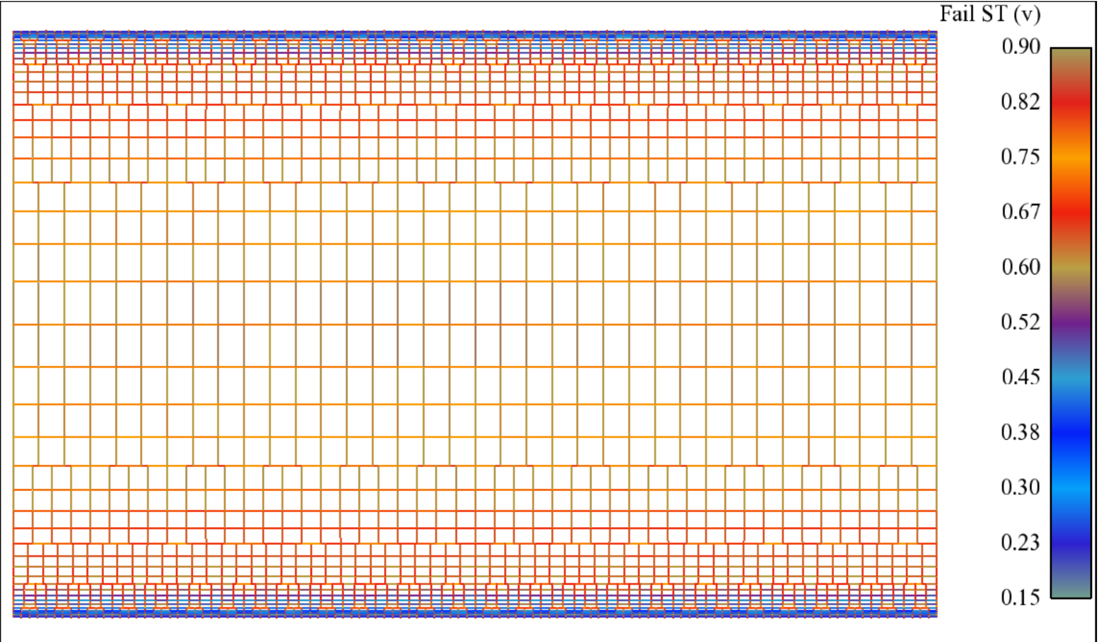

Figure 5.9: LES of channel flow: average counting of the slope test failure in the cross plane for the v velocity component in the span-wise direction. The cut plane is located in the middle of the domain and the average is performed over 20000 time steps ($2\,s$ of physical time). The results are plotted on the cell faces. The amount of UW is equal to 2%.

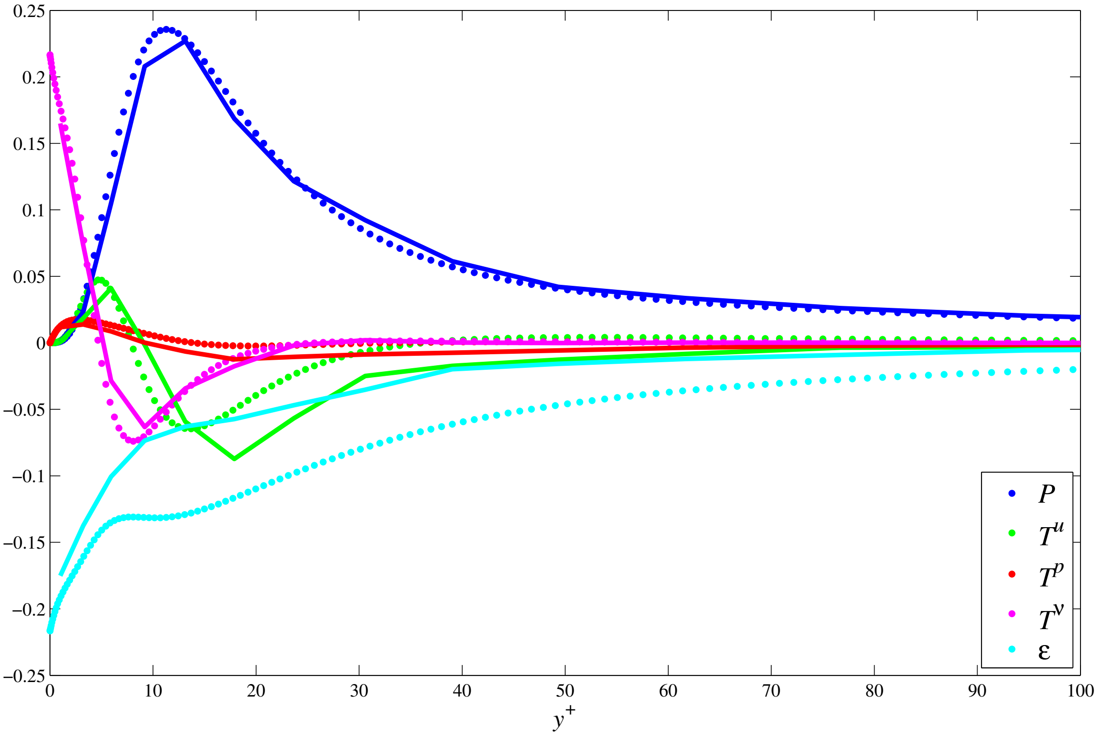

Figure 5.10: LES of channel flow: budget of turbulent kinetic energy k for the RR075 mesh. P production, T^u turbulent transport, T^p pressure transport, T^ν viscous transport, ε dissipation. Bullet points are DNS data, continuous lines LES.

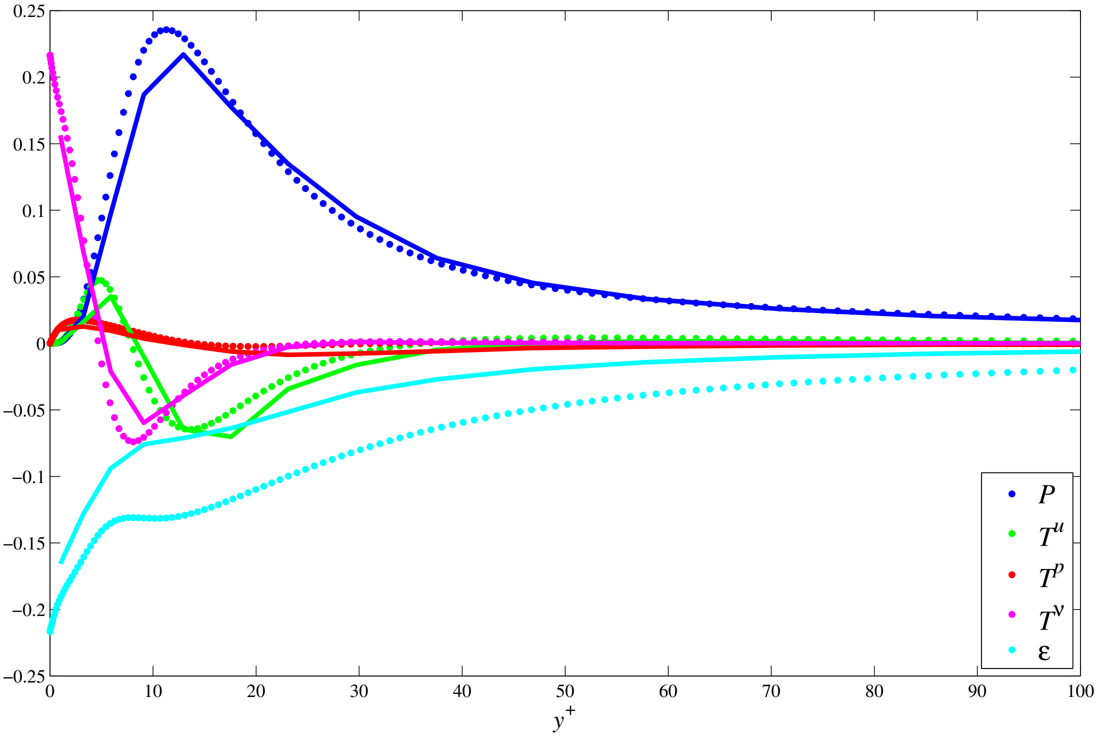

Figure 5.11: Budget of turbulent kinetic energy k for the TAYLOR mesh: P production, T^u turbulent transport, T^p pressure transport, T^ν viscous transport, ε dissipation. Bullets points are DNS data, continuous lines LES.

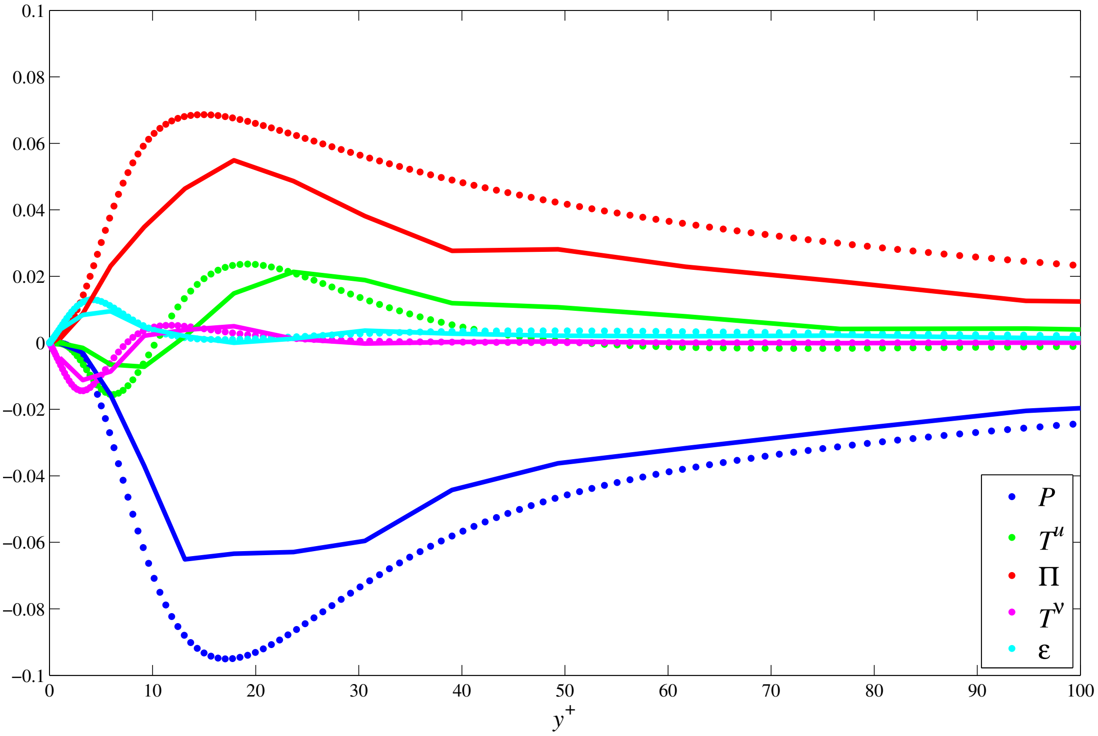

Figure 5.12: LES of channel flow: budget of $\langle u'v' \rangle$ for the RR075 mesh. P production, T^u turbulent transport, Π velocity-pressure transfer, T^ν viscous transport, ε dissipation. Bullet points are DNS data, continuous lines LES.

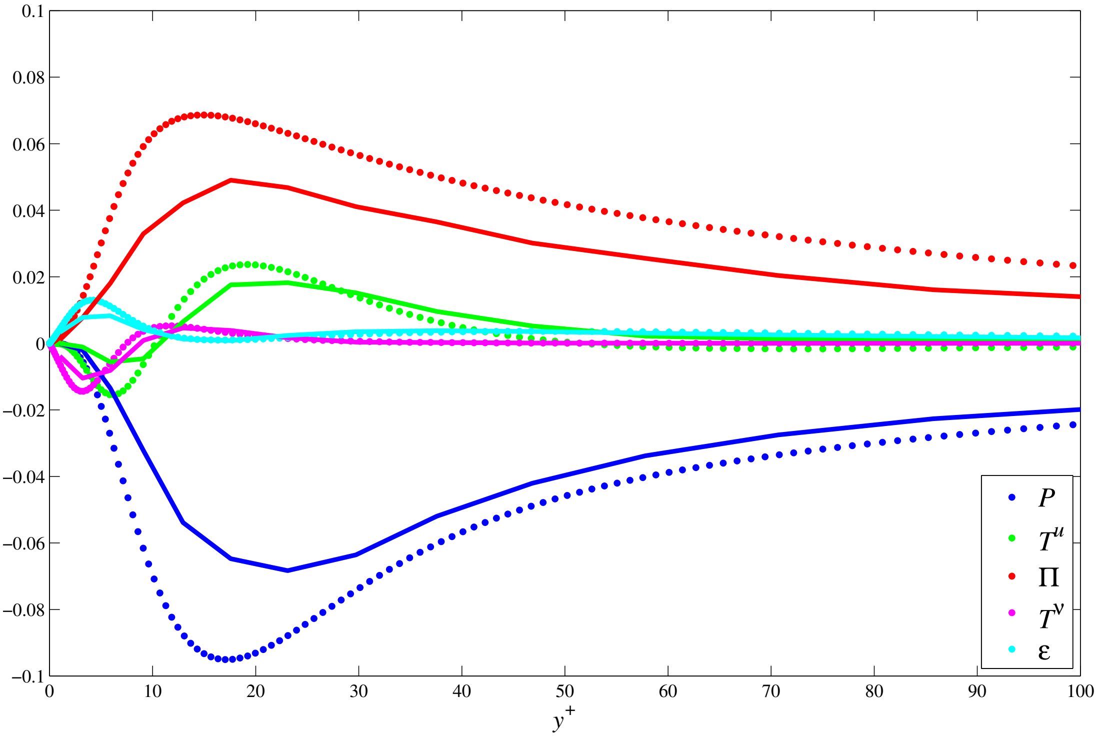

Figure 5.13: LES of channel flow: budget of $\langle u'v' \rangle$ for the TAYLOR mesh. P production, T^u turbulent transport, Π velocity-pressure transfer, T^ν viscous transport, ε dissipation. Bullet points are DNS data, continuous lines LES.

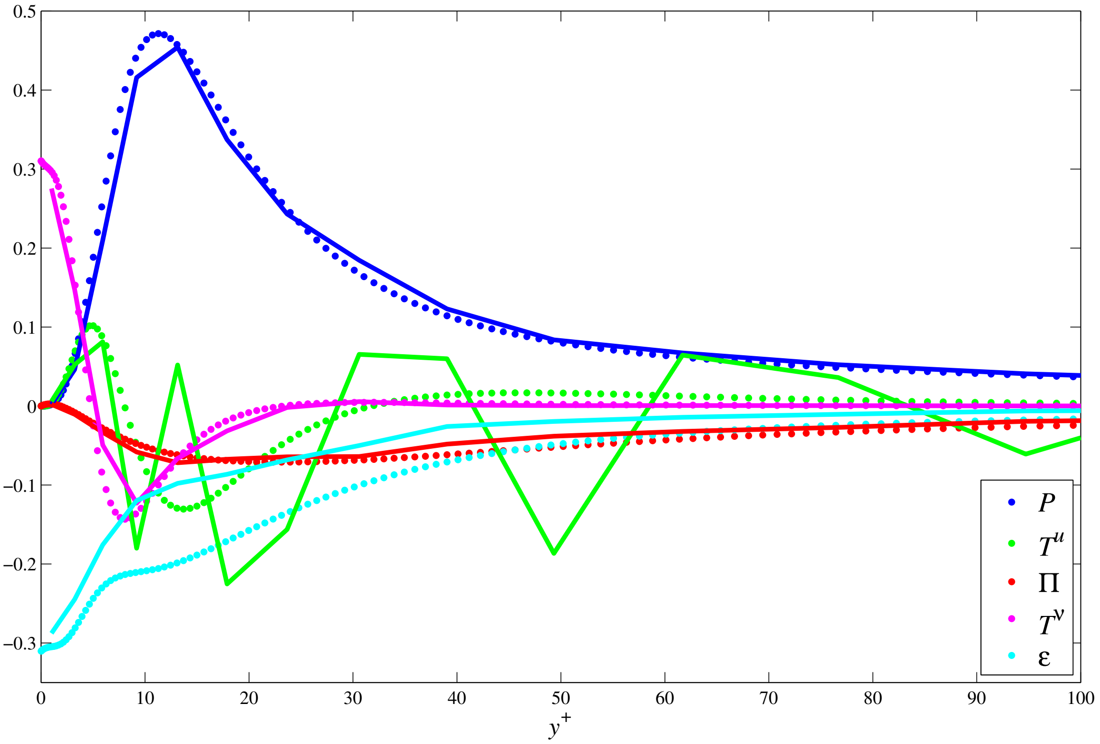

Figure 5.14: LES of channel flow: budget of $\langle u'u' \rangle$ for the $RR075$ mesh. P production, T^u turbulent transport, Π velocity-pressure transfer, T^ν viscous transport, ε dissipation. Bullet points are DNS data, continuous lines LES.

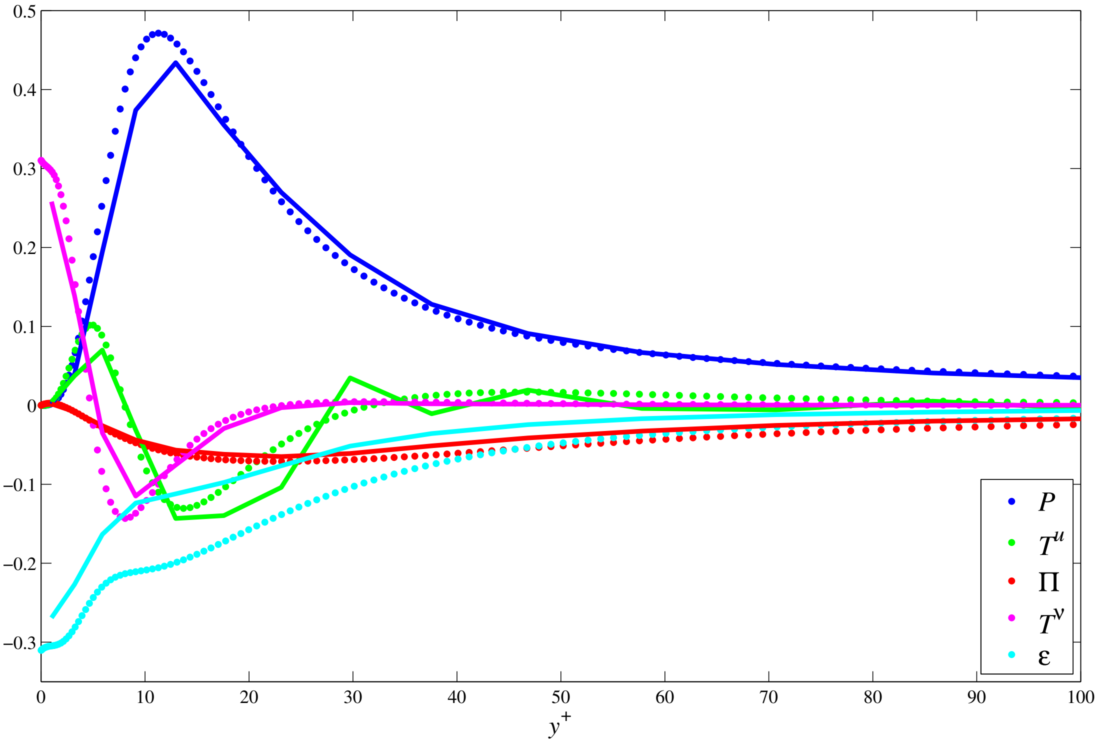

Figure 5.15: Budget of $\langle u'u' \rangle$ for the TAYLOR mesh: P production, T^u turbulent transport, Π velocity-pressure transfer, T^ν viscous transport, ε dissipation. Bullets points are DNS data, continuous lines LES.

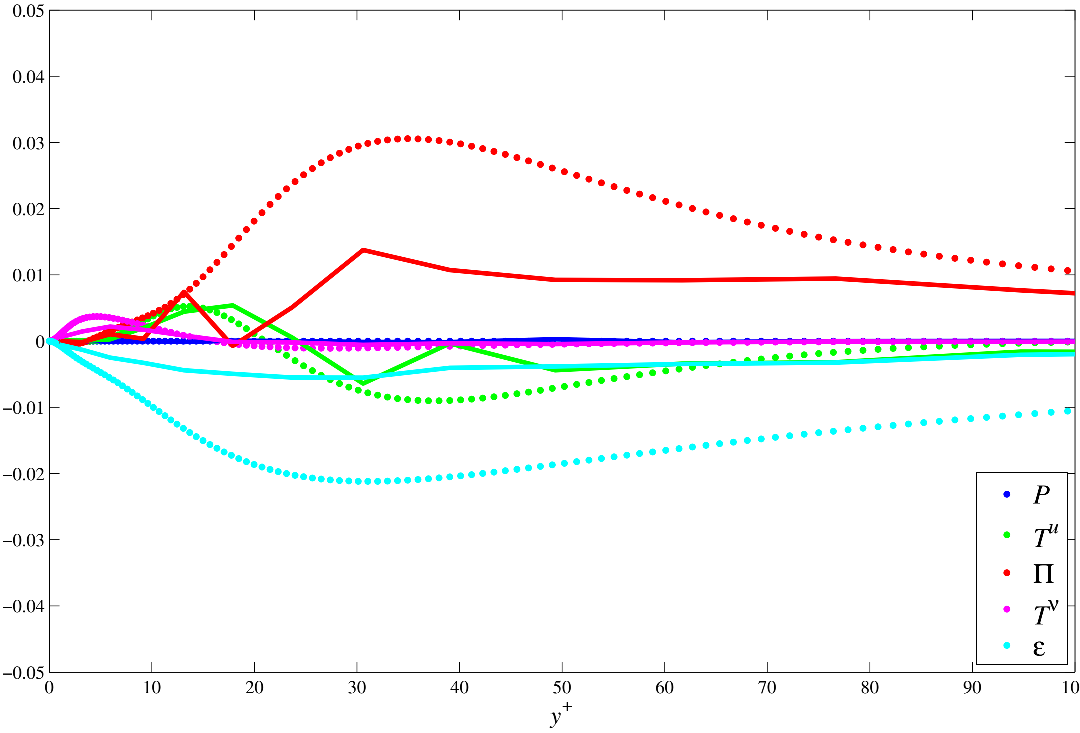

Figure 5.16: LES of channel flow: budget of $\langle v'v' \rangle$ for the $RR075$ mesh. P production, T^u turbulent transport, Π velocity-pressure transfer, T^ν viscous transport, ε dissipation. Bullet points are DNS data, continuous lines LES.

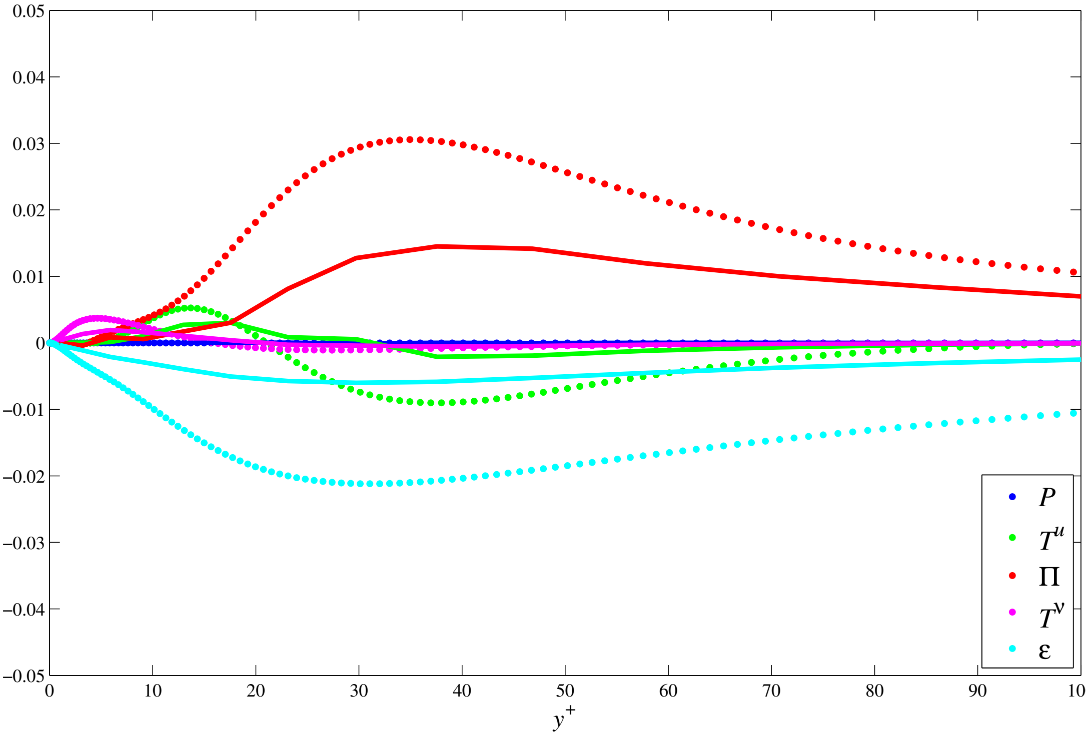

Figure 5.17: Budget of $\langle v'v' \rangle$ for the TAYLOR mesh: P production, T^u turbulent transport, Π velocity-pressure transfer, T^ν viscous transport, ε dissipation. Bullets points are DNS data, continuous lines LES.

5.2.3 PARTIAL CONCLUSIONS

In this part LES of channel flow at $Re_\tau = 395$ is performed with unstructured gridding and compared with the results for a structured mesh. The best results are obtained with the so-called TAYLOR mesh, which is built according to the TAYLOR micro-scales. The criterion of the Taylor micro-scales gives a good estimation of the mesh resolution necessary, avoiding the need for several runs in order understand the mesh requirements. The drawback is that their correct estimation can be done only in presence of DNS results. Scales estimated from RANS computations do not compare very well with those produced by DNS and they tend to zero at the wall. Attempts to use RANS length scales to build the meshes are also presented in Addad et al. (2008). Good results are found also in the case of the RANDOM mesh, where a series of coarsening steps, without following any particular criterion, was used to maintain reasonable the total number of cells.

The embedded refined mesh RR075, which has four coarsening steps following a $3-4$ sub-pattern, is also investigated and shows oscillations of the Reynolds stresses around the refined area. The issue can be ascribed to the wall normal velocity fluctuations, which display a swinging behaviour. This finding is in contrast with the one of Chapter 4 where a structured sub-pattern produces the best results. The reason can be due to error cancellation: meshes with a random structure of the refinement may produce a less accurate instantaneous field, but averaging procedure cancels out this random error. On the other hand, in the case of several layers with the same structure of the refinement (i.e. in the mesh RR075), the error is systematic and the averaging does not remove it. Moreover the addition of the slope test does not solve the problem of the spurious oscillations. In this case it is extremely difficult to separate turbulent from spurious numerical oscillations. As a matter of fact up-winding damping is also activated very frequently in the centre of the channel where the mesh is structured. Findings about mesh requirements, and in particular the choices of the refinement patterns, are in contrast with the ones of Chapter 4. This makes it difficult to formulate general statements for mesh generation because they are highly dependent on the test case considered.

The last, but maybe most important observation about the structured versus embedded refinements can be made from Table 5.4, where the iteration CPU time and the number of iterations necessary to resolve the Poisson equation for pressure for the different grids are listed. Although the TAYLOR mesh has the least number of cells it is 16% slower than the structured mesh, whereas RR075 is 5% slower. The reasons are mainly two: firstly the already mentioned additional time required by the gradient reconstruction to reconstruct the non-orthogonality, and secondly the pressure solver needs more iterations to converge. In general, for incompressible codes, pressure is the variable that requires more iterations to obtain a converged solution. Pressure resolution can take up to $80 - 90\%$ of the total time step. The saving in time because of the mesh size reduction due to the use of unstructured mesh is not always obvious and it might be achievable for significantly higher Reynolds number.

5.3 Hybrid RANS/LES

In this section the Hybrid RANS/LES model introduced in 2.4 is validated. The meshes employed are reported in Table 5.5. A summary of the results, with the percentage error on the bulk velocity and temperature[6], is listed into Table 5.6. Hybrid RANS/LES has an advantage over pure LES with very coarse meshes as can be seen in Figure 5.18. where LES with Smagorinsky model does not capture the logarithmic layer. This leads to an error of about 17% in the bulk velocity estimation for LES whereas on the same mesh, the Hybrid gives at most 2% error, depending on the blending function used (see Table 5.6). Moreover LES shows a consistent underestimation of the shear stress $\langle u'v' \rangle^+$ whereas in the Hybrid method, the anisotropic modelling has a positive effect, making the global shear stress match the DNS. Also, the comparison of normal stresses for LES shows a large overestimation of $u^{;+}_{rms}$ and underestimation of the remaining two components. Despite the fact that Hybrid normal stresses are simply resolved (i.e. no addition of modelling from the anisotropic contribution to the modelled stress) they compared better with DNS with respect to LES. For the sake of completeness, reduced stresses are also reported but they do not compare very well with DNS in all the cases. Among normal stresses the less accurately predicted component is the wall normal $v^{;+}_{rms}$, which can be improved by adding the RANS model contribution as shown in Figure 5.19. In order to make the description easier only the total shear stress $\langle u'v' \rangle^+$ (sum of the resolved plus the modelled) will be displayed in the following of the discussion. Two sets of constants for the blending function of Eq. (2.54) are employed and their definitions are reported in Table 5.5 and plotted in Figure 5.20 for the mesh M1_395 at $Re_\tau = 395$. $BF2$ grows more rapidly toward unity, moving the transition toward LES closer to the wall. The effect of the filter width correction, expressed by Eq. (2.55), is small for this mesh. Results for $Re_\tau = 395$, mesh M1_395 and different blending functions are presented in Figure 5.21. All four formulations of the blending function provide very similar results, which shows low sensitivity to the RANS to LES shift. The comparison with DNS is good for mean velocity and shear stress. In the shear stress is very evident the effect of RANS model addition to the resolved turbulence.

---

[6] As mean pressure gradient and wall heat flux are imposed in the simulation, monitoring the error on the bulk velocity and temperature is equivalent to friction coefficient and Nusselt number.

5.3.1 Heat transfer

Figure 5.22 shows improvement in performances of the Hybrid heat transfer model over the usual LES on a very coarse grid. In this case the error of the bulk temperature is larger than the one for the bulk velocity (see Table 5.6). The same positive effect of the RANS modelling encountered for the shear stress $\langle u'v' \rangle^+$ (Figure 5.18) is also found for the $\langle v'\theta' \rangle^+$ heat flux, which is almost overlapping with the DNS data. The other heat flux $\langle u'\theta' \rangle^+$ and the temperature variance $\theta_{rms}^{;+}$ show an underestimation in the near wall region, until $y^+ \approx 100$ where mainly RANS is performed, since the streamwise heat flux cannot be reproduced by a simple Eddy Viscosity model.For the same reason discussed in the case of the shear stress $\langle u'v' \rangle^+$, the total heat flux $\langle v'\theta' \rangle^+$ is going to be plotted in the continuation of the exposition.

In order to model the eddy conductivities (see Eq (2.49)) two constants are defined, namely $Pr_{t,\gamma}$ and $Pr_{t,a}$, representing the turbulent Prandtl number for the homogeneous and anisotropic parts respectively of the modelled stresses and heat fluxes. In general those constants are kept below one, because of the higher facility of hot spot to diffuse with respect to hydrodynamic structures. The effect of $Pr_{t,\gamma}$ on all the profiles is almost negligible (Fig. 5.23), whereas $Pr_{t,a}$ has a large impact (Fig. 5.24). Low values of the constant allow more RANS in the solution, damping the turbulent oscillations. As a consequence, the mean temperature profile is underestimated. High values increase the fluctuations, making the Hybrid temperature r.m.s compare well with the DNS from $y^+ \approx 10$, but with an overestimation of the bulk temperature. A value of 0.75 was chosen in order to minimize the error of the mean temperature profile. $Pr_{t,\gamma}$ is set equal to 0.70 to be consistent with other LES works (see for example Moin et al. (1991)) which indicates a lower value for the turbulent Prandtl number in the centre of the channel, compared to the near wall region. The model is also tested at very low Pr, typical of liquid metals which are used as coolant for some nuclear reactors. In this case the thermal boundary layer is thicker than the kinematic one, lowering the effect of the meshing. Results for mean temperature profile, fluctuations and heat fluxes improve with respect to the high Pr (Fig. 5.25). The only problem is $\langle v'\theta' \rangle^+$ where the anisotropic modelling addition makes the total overshoot the DNS in the near wall region. Low Prandtl effects need to be introduced in the RANS model or in the blending function. The problem of mesh resolution dependency will be investigated furthermore in section 5.3.3.

5.3.2 Reynolds number effects

From Figures 5.26 to 5.29 the behaviour of the model is tested as the Reynolds number increases. Here the advantages of this model are clear: results display the same level of accuracy as the ones at $Re_\tau = 395$, but without the need of fine mesh resolution, which are required by wall resolved LES. In the case of wall resolved LES the mesh requirement grows with a rate proportional to $Re^{1.8}$ as reported in Piomelli and Balaras (2002). In the Hybrid model presented here the growth rate is instead proportional to $Re^{1.14}$, in fact the mesh used for $Re_\tau = 1020$ (which corresponds to a $Re_b \approx 40,000$) has only 180,000 cells because of the extremely stretched cells used in the near wall region. The anisotropic RANS contribution is relevant only until $y^+ = 100$, which is also the area where the mesh starts to be more isotropic and the length-scales start to be free from wall effects. For the case at very low Reynolds ($Re_\tau = 180$) two different meshes were tested: M1_180 with $30 \times 40 \times 30$ and M2_180 with $40 \times 40 \times 30$ cells. Surprisingly the best results are obtained using the coarse mesh M1_180 as can be seen from Figures 5.30 and 5.31. As the wall heat flux is imposed, so is the sum of molecular plus turbulent heat flux, and, in the end, it is the temperature gradient in the wall normal direction that varies while $\langle v'\theta' \rangle$ is always close to the DNS. The profile of the blending function along with the filter width $\Delta_{\mathcal{F}_b}$, used to compute the blending function and the mesh anisotropy, are plotted in Figure 5.32. More results and considerations on the effects of the mesh resolution are presented in the next section.

5.3.3 Mesh resolution effects

An important point to investigate is the dependency of the Hybrid model on mesh refinement. In the case of a $1D$ channel flow, resolved with a low Reynolds RANS model, at least sixty points in the wall normal direction are necessary to obtain a correct mean velocity profile. Two meshes with such resolution in the wall normal direction are created; M2_395 with the first point located at $y^+ \simeq 1$ and M3_395 with the first point located at $y^+ \simeq 0.2$. Results from those two meshes are reported from Figures 5.33 to 5.38. Mesh M2_395 shows an unusual behaviour, in particular if the filter width correction of Eq. (2.55) is used. There is an increase of the temperature fluctuations (Figures 5.34 and 5.37) in the centre of the channel, making the model overestimate the DNS by an large margin. When the *max* correction is used the r.m.s fluctuations in the streamwise direction $\langle u' \rangle^+_{rms}$ also show the same behaviour. On the other hand these issues are not present in the mesh M3_395, independently of the formulation of the blending function. The reason does not come from the blending function, which is very similar in all the cases (Figs. 5.35 top right and Fig. 5.38), but in the cell stretching. Although after $y^+ = 100$, LES contribution is clearly dominant, cells are stretched in the span- and stream-wise directions (see two graphs at the bottom of Fig. 5.35, which report ratios between the height of the cell over the length in the streamwise and span-wise directions respectively). Mesh M3_395 does not have the same problem: cells are more clustered close to the wall, allowing the central part of the domain (where mainly LES is performed) to regain mesh isotropy. The correction of Eq. (2.55) does not have any positive effect: the correction is acting, increasing the filter width $\Delta_{\mathcal{F}_b}$ as presented in Fig. 5.38, only close to the wall where the cells are stretched and the turbulent length L_t is already small. In the centre of the channel the increase of $\Delta_{\mathcal{F}_b}$ does not compensate the increase of L_t and consequently the blending function grows toward unity almost with the same rate.

Figures 5.39, 5.40 and 5.41 present the results of velocity field, thermal field and blending function for fine meshes. The two meshes employed were those used in the previous part of this chapter for the LES: the first is the structured mesh $128 \times 64 \times 96$ which is now labelled as M4_395, and the second is the TAYLOR mesh, now labelled as MT_395 (see Table 5.5). In this case mean profiles, both velocity and temperature, display a substantial underestimation, which leads to an error of around 15% for the bulk velocity and more than 25% for bulk temperature in both cases. The main difference, with respect to earlier calculations on coarser meshes, is the incorrect prediction of the shear stress $\langle u'v' \rangle^+$ and heat flux $\langle v'\theta' \rangle^+$. The problem can be explained starting from Eq. (2.52), which gives the composition of the total stresses and heat fluxes. The modelled part is controlled by the blending function, whereas the resolved contribution does not have any constraint. In case of very fine meshes the total stresses should be composed only by the resolved part and the model contribution should vanish, as the grid is appropriate for a classical LES. Instead the blending function at the wall does not tend to zero, allowing the RANS (which is proportional to the mean velocity gradient) to contribute to the total solution. This creates a problem of double counting of stresses and heat fluxes, which can be avoid only using coarse meshes at the wall. For example in the mesh MT_395 at $y^+ \approx 30$ the blending function is still around 0.5, where it should be almost one (Figure 5.41).

5.3.4 Conclusions

In the second part of this chapter a Hybrid RANS/LES model is validated, producing good results on very coarse meshes. The main improvement is the addition of heat transfer into the already available model for the dynamic part. The key point of the model is the addition of a RANS contribution in the near wall region, which gradually vanishes as the mesh tends more towards isotropy and the turbulent flow component is more resolved rather than modelled. Because of the relaxed constraint of the near wall resolution the model not only allows the use of coarse meshes but also a growth rate for the mesh size that is proportional to $Re^{1.14}$ instead of the usual $Re^{1.8}$ typical of wall resolved LES.

A new set of constants is proposed for the blending function, showing a better approximation of the bulk velocity and temperature. On the other hand the introduction of the *max* correction of Eq. (2.55) does not have any major impact on the model performance, and in some cases the modification is counterproductive.

In the case of thermal modelling a balance between mean temperature, temperature variance and turbulent heat fluxes must be established. High values of the turbulent Prandtl numbers for the inhomogeneous contribution result in a better approximation of temperature r.m.s. values, along with a noteworthy under-prediction of the mean temperature gradient and, by integration, the temperature profile itself. Low values have, on the other hand, the opposite effect, producing an underestimation of temperature r.m.s. in the near wall region and larger temperature gradient. A balance is found by setting $Pr_{t,\gamma} = 0.75$, which also gave the minimum error in the bulk velocity assessment. The model is also tested for a very low Prandtl number of $Pr = 0.025$ showing very good performances with the exception of $\langle v'\theta' \rangle$, where the RANS addition, on an already relatively well resolved thermal field, makes the Hybrid model overshoot the DNS close to the wall.

Despite many positive features the model shows some shortfalls: some dependency on the mesh and in particular on the relation between cell aspect ratio and blending function. When the blending function tends to unity, cells should also be fairly isotropic. If this condition is not satisfied, an increase in the r.m.s. values in the central part of the domain is observed for both velocity and temperature. A second problem appears when the model is tested on fine meshes, already appropriate for wall-resolved LES. In these cases the mean quantities are underestimated because of an overestimation of the level of turbulence in the solution due to a double counting of the shear stress. As a consequence shear stress $\langle u'v' \rangle$ and heat flux $\langle v'\theta' \rangle$ are wrongly over-predicted in the near wall region. This double counting could be countered by switching off turbulence production, in the LES, by modifying the convecting velocity field with a slip condition at the wall.

The introduction of the blending function is compulsory in order to make possible the natural development of fluctuations. On the other hand its formulation is fairly arbitrary and relied on a careful constant tuning, which might be case dependent. Moreover even in a DNS mesh, near wall cells have aspect ratios far from the unity, making criteria based on cell isotropy not very general. Other specifications based on cell dimensions, expressed in wall units, might be also not universal, but dependant on the test cases used for the definition.

A more pragmatic and better solution should be an “a priori” knowledge of the blending function field, designing the mesh to follows its evolution. In this context RANS models based on elliptic blending can provide an effective solution (see Sec. A.1.2). This model is characterised by a parameter α which takes into account wall effects and is evaluated through an elliptic equation. Therefore a precursor RANS simulation can be performed and used in the mesh construction.

Re_τ	Acronym	Mesh resolution	y^+ 1^{st} cell
180	M1_180	$30 \times 40 \times 30$	1
180	M2_180	$40 \times 40 \times 30$	1
395	M1_395	$40 \times 40 \times 32$	1
395	M2_395	$40 \times 60 \times 32$	1
395	M3_395	$40 \times 60 \times 32$	0.2
395	M4_395	$128 \times 64 \times 96$	1
395	MT_395	$200 \times 46 \times 100$	1
640	/	$50 \times 50 \times 40$	1
1020	/	$60 \times 60 \times 50$	1

Acronym	Coeff.	
	C_l	n
$BF1$	1	1.5
$BF2$	1.3	2
$BF1/2_{max}$	see Eq. (2.55)	

Table 5.5: Mesh acronyms and characteristics for the hybrid calculations (left) and constant used for the blending function $\mathcal{F}_b$ (right).

Re_τ	Mesh	Blending function	U_B error [%]	T_B error [%]
180	M1_180	$BF1$	1.1	0.3
180	M2_180	$BF2$	3.8	5
180	M2_180	$BF2_{max}$	5.5	11
395	M1_395	LES	17.7	51
395	M1_395	$BF1$	1.26	3.33
395	M1_395	$BF2$	0.21	1.32
395	M1_395	$BF2_{max}$	0.38	2.40
395	M2_395	$BF2$	0.21	0.7
395	M2_395	$BF2_{max}$	0.35	4.7
395	M3_395	$BF2_{max}$	0.35	1.22
395	M4_395	$BF2$	14	29
395	MT_395	$BF2$	13	26
395	MT_395	$BF2_{max}$	14	26.6
640	/	$BF2$	1.5	0.11
640	/	$BF2_{max}$	1.18	0.015
1020	/	$BF2$	0.4	1.8
1020	/	$BF2_{max}$	0.2	2.3

Table 5.6: Percentage error with respect to Abe et al. (2004, 2001) DNS for different meshes and blending functions. The turbulent Prandtl number for heat transfer modelling are set to $Pr_{t.\gamma} = 0.70$ and $Pr_{t,a} = 0.75$.

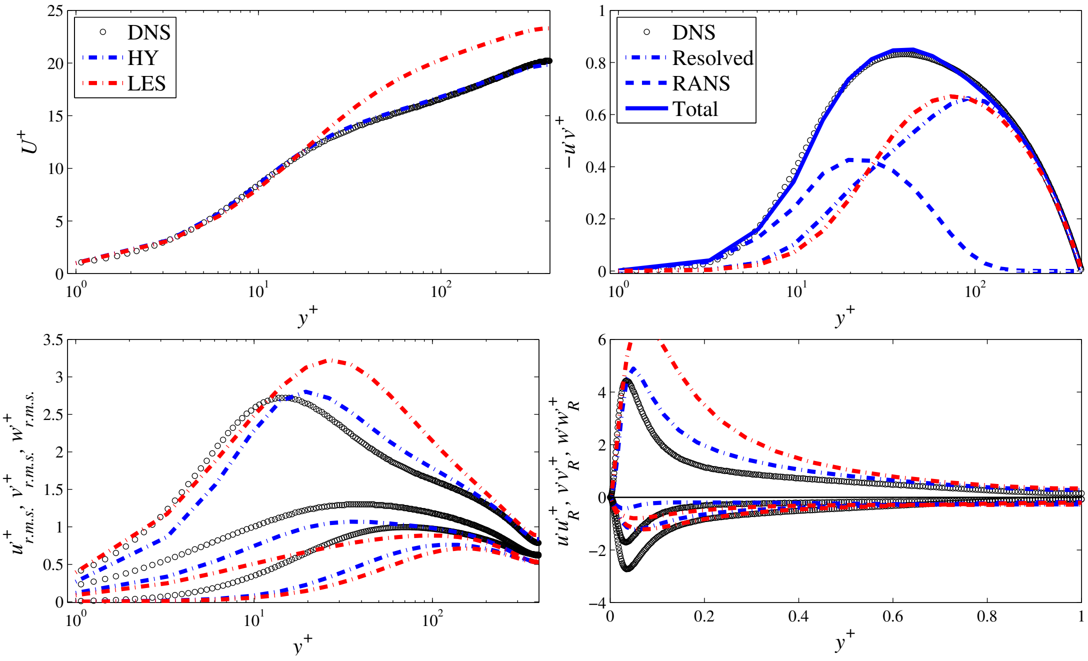

Figure 5.18: Hybrid channel flow ($Re_\tau = 395$): comparison between LES and Hybrid for mesh M1_395 (see Table 5.5). The blending function used is $BF2$ (see table 5.5 (left)). Mean velocity (top left), shear stress (top right), normal stresses (bottom left) and their reduced counterparts (bottom right). .

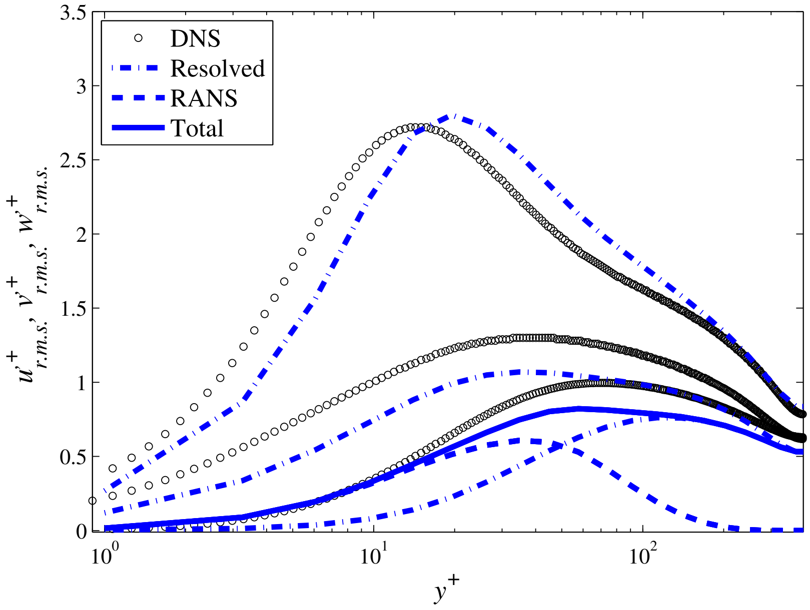

Figure 5.19: Hybrid channel flow ($Re_\tau = 395$): normal Reynolds stresses with the addition of RANS Reynolds stresses. The RANS addition is equal to $(1 - \mathcal{F}_b)\, v^2$, where v^2 is the one given by the EVM $\varphi - \overline{f}$ model of Laurence et al. (2005).

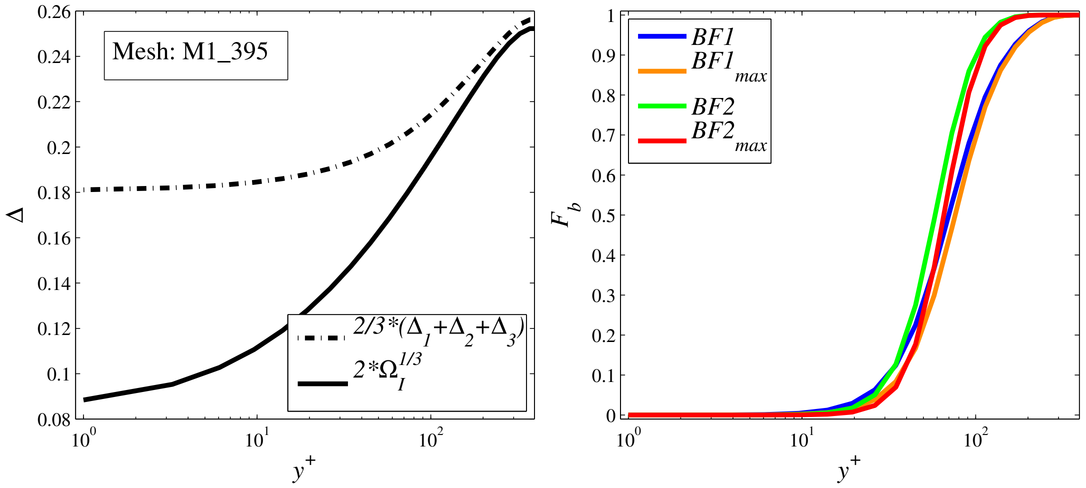

Figure 5.20: Hybrid channel flow: comparison between blending function for channel flow at $Re_\tau = 395$ on mesh M1_395.

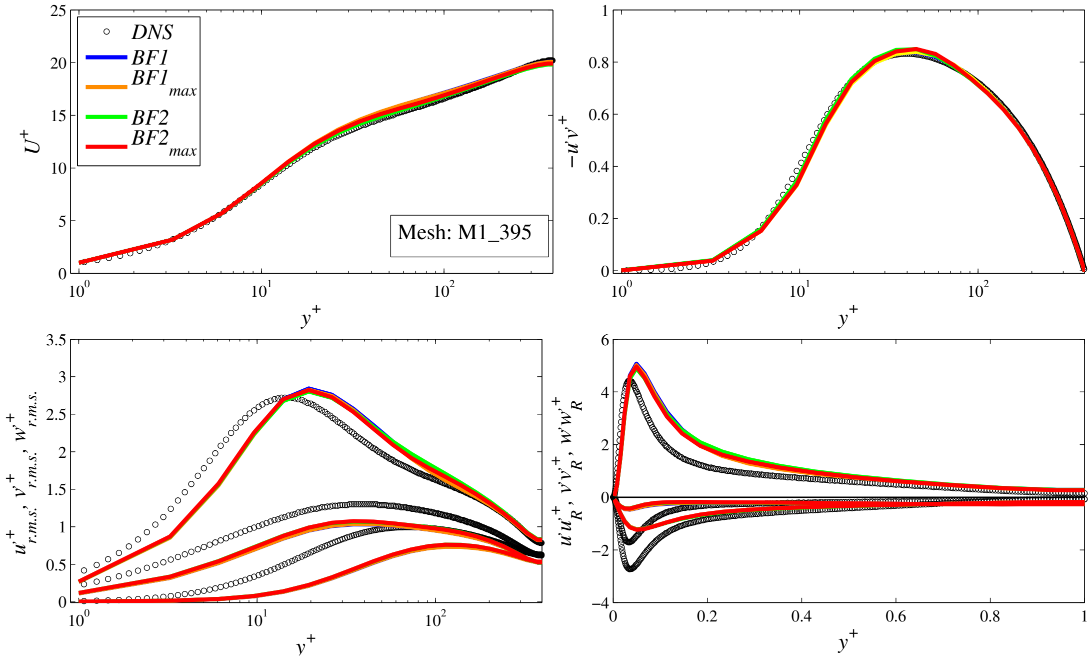

Figure 5.21: Hybrid channel flow ($Re_\tau = 395$): effect of blending function for mesh M1_395 (see Table 5.5). Mean velocity (top left), shear stress (top right), normal stresses (bottom left) and their reduced counterparts (bottom right). Comparison between different blending functions .

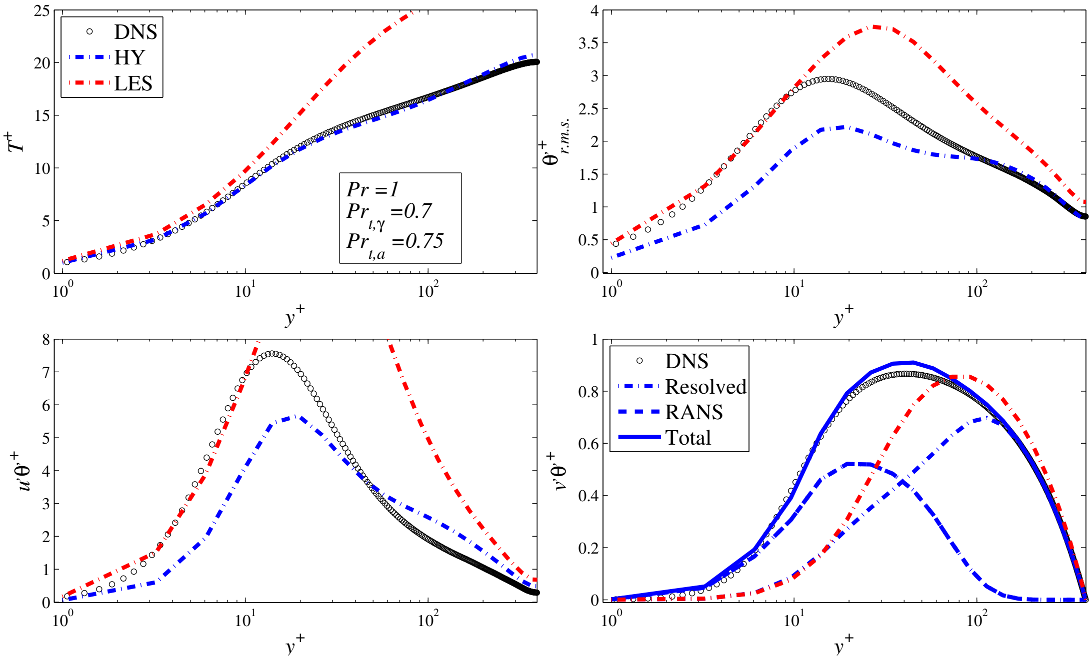

Figure 5.22: Hybrid channel flow: comparison with LES (heat transfer) on mesh M1_395 and using $BF1$ for the hybrid (see Table 5.5). Temperature profile (top left), temperature r.m.s. (top right), heat fluxes (bottom).

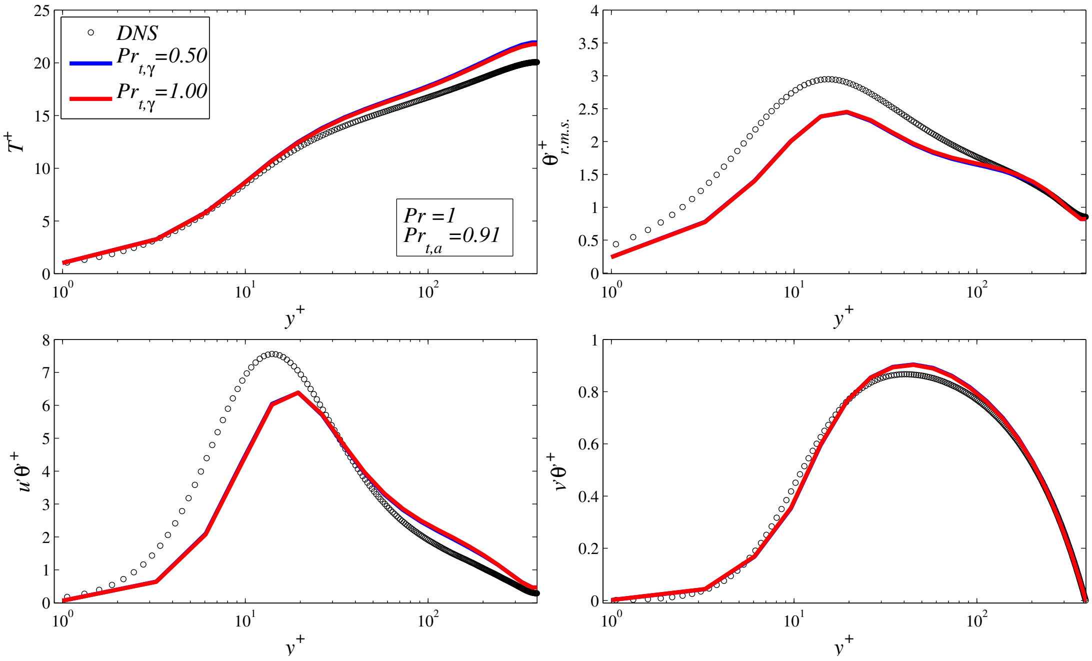

Figure 5.23: Hybrid channel flow heat transfer ($Re_\tau = 395$): effect of variation of $Pr_{t,\gamma}$. Temperature profile (top left), temperature r.m.s. (top right), heat fluxes (bottom). The mesh employed is M1_395 and $BF1$ is used as blending function (see Table 5.5).

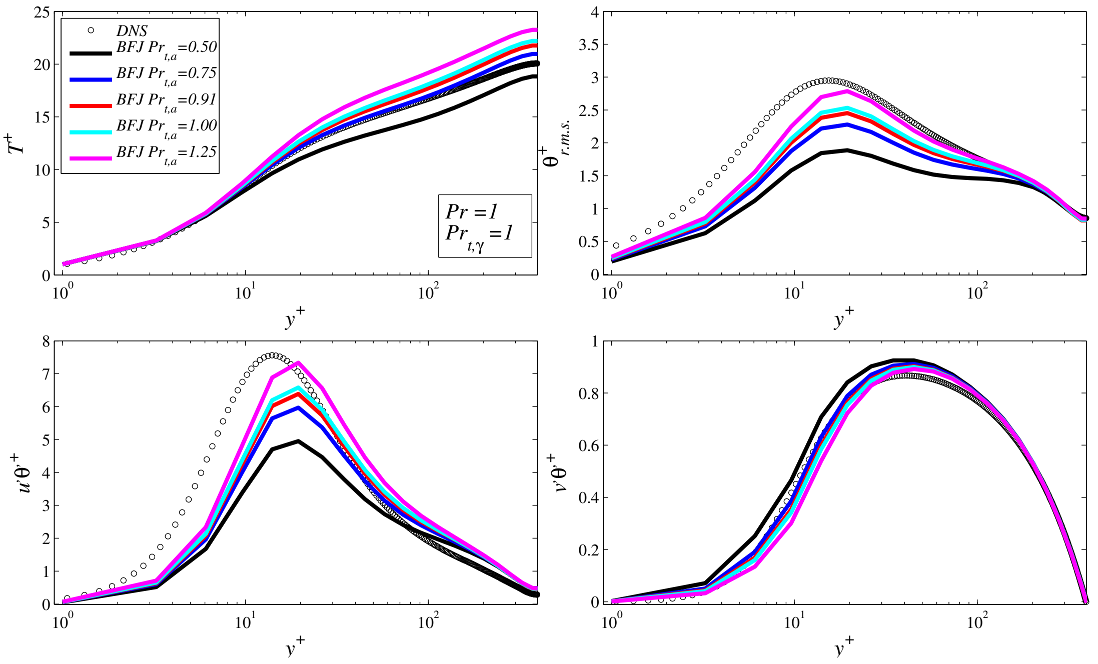

Figure 5.24: Hybrid channel flow heat transfer ($Re_\tau = 395$): effect variation of $Pr_{t,a}$. Temperature profile (top left), temperature r.m.s. (top right), heat fluxes (bottom). The mesh employed is M1_395 and $BF1$ is used as blending function (see Table 5.5).

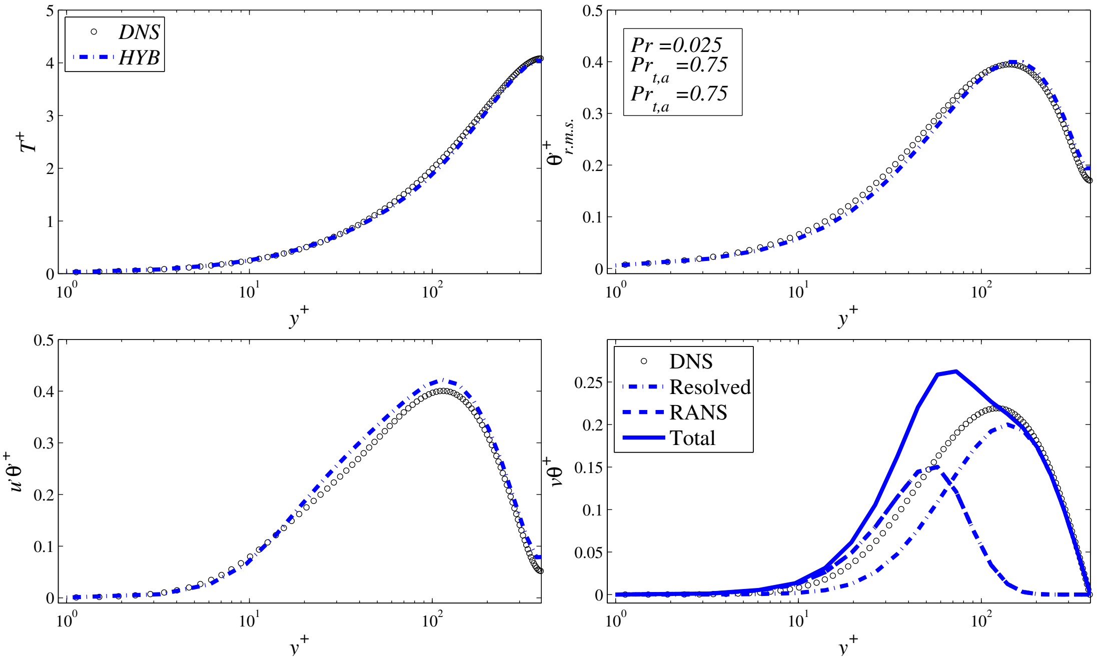

Figure 5.25: Hybrid channel flow heat transfer ($Re_\tau = 395$): effect of low Prandtl number. Temperature profile (top left), temperature r.m.s. (top right), heat fluxes (bottom). The mesh employed is M1_395 and $BF2$ is used as blending function (see Table 5.5).

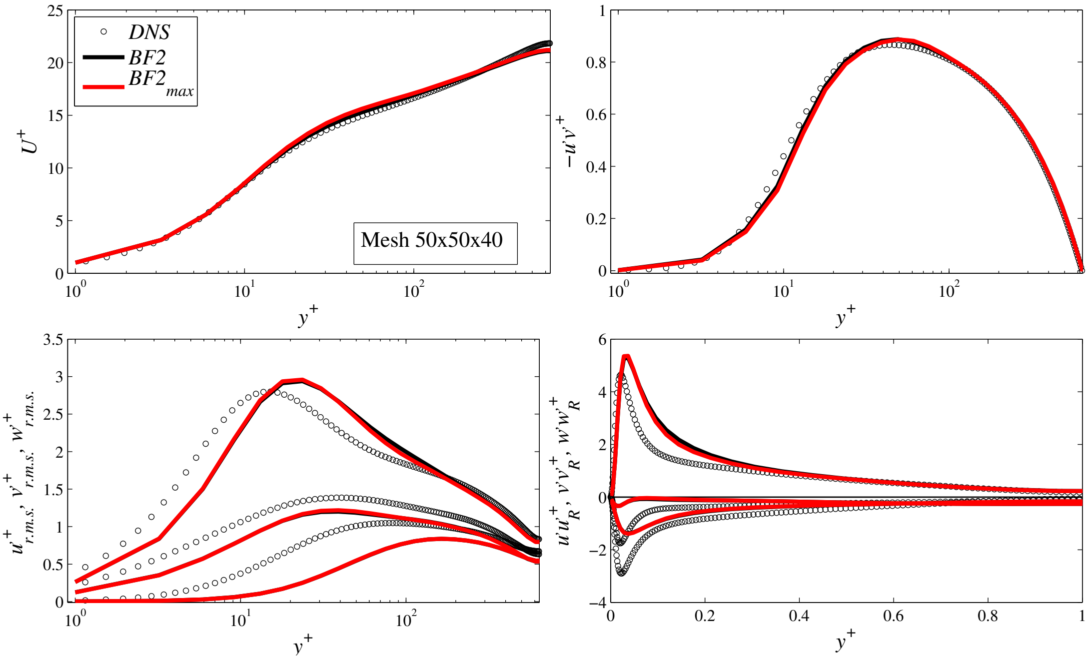

Figure 5.26: Hybrid channel flow at high Reynolds case ($Re_\tau = 640$): comparison between different blending functions (see Table 5.5). Mean velocity (top left), shear stress (top right), normal stresses (bottom left) and their reduced counterparts (bottom right).

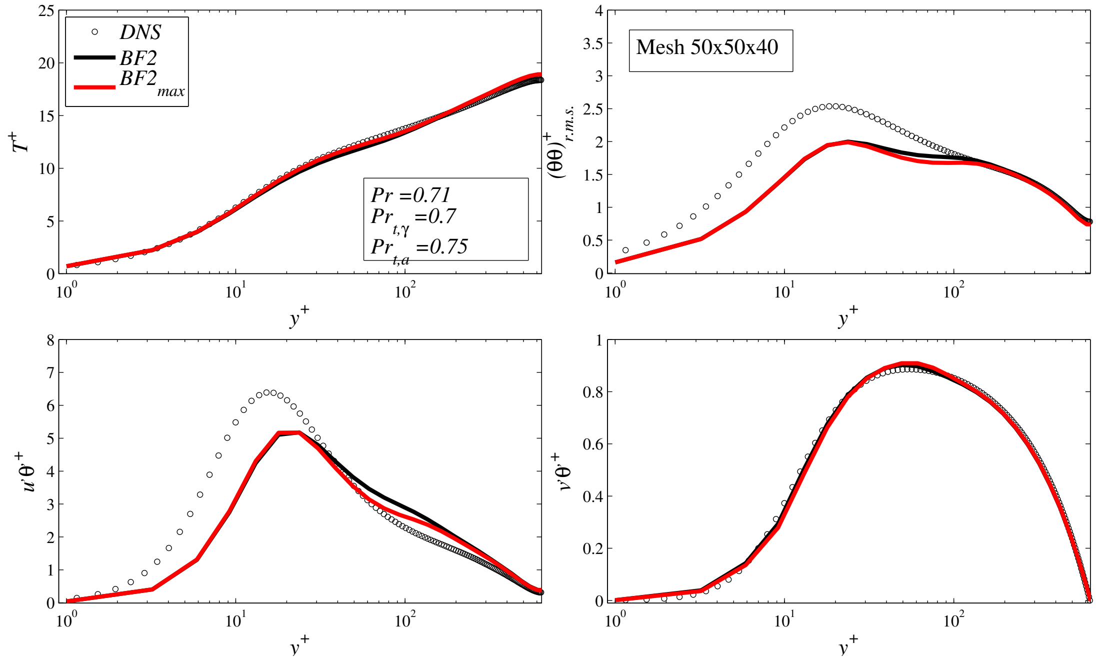

Figure 5.27: Hybrid channel flow at high Reynolds case ($Re_\tau = 640$): comparison between different blending functions (see Table 5.5).Temperature profile (top left), temperature r.m.s. (top right), heat fluxes (bottom).

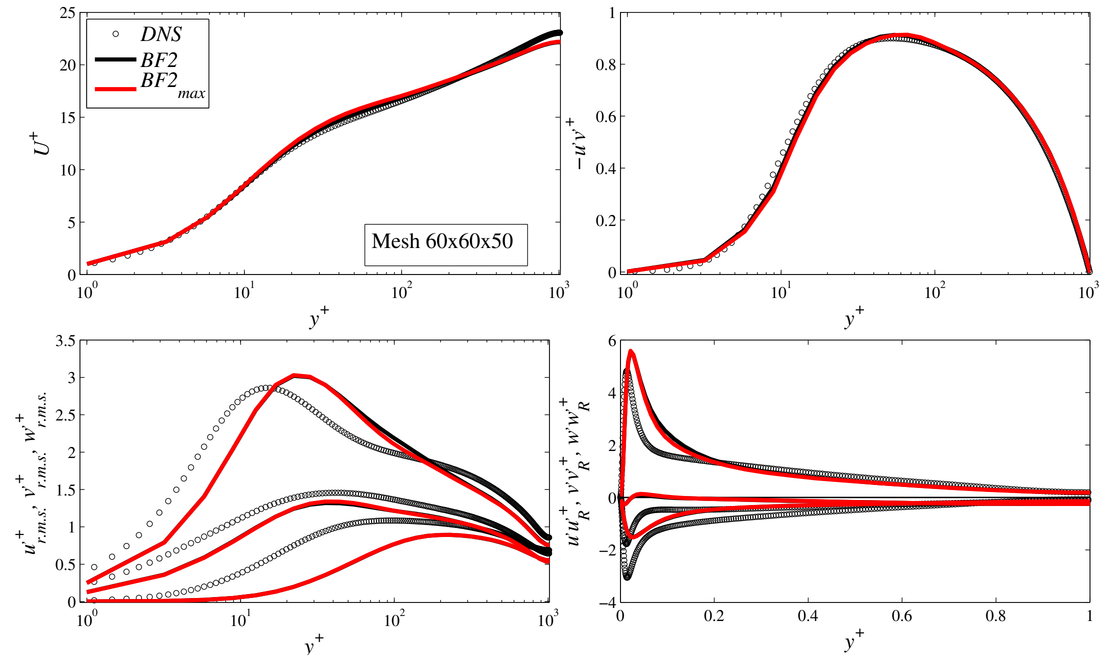

Figure 5.28: Hybrid channel flow at high Reynolds case ($Re_\tau = 1020$): comparison between different blending functions (see table 5.5). Mean velocity (top left), shear stress (top right), normal stresses (bottom left) and their reduced counterparts (bottom right).

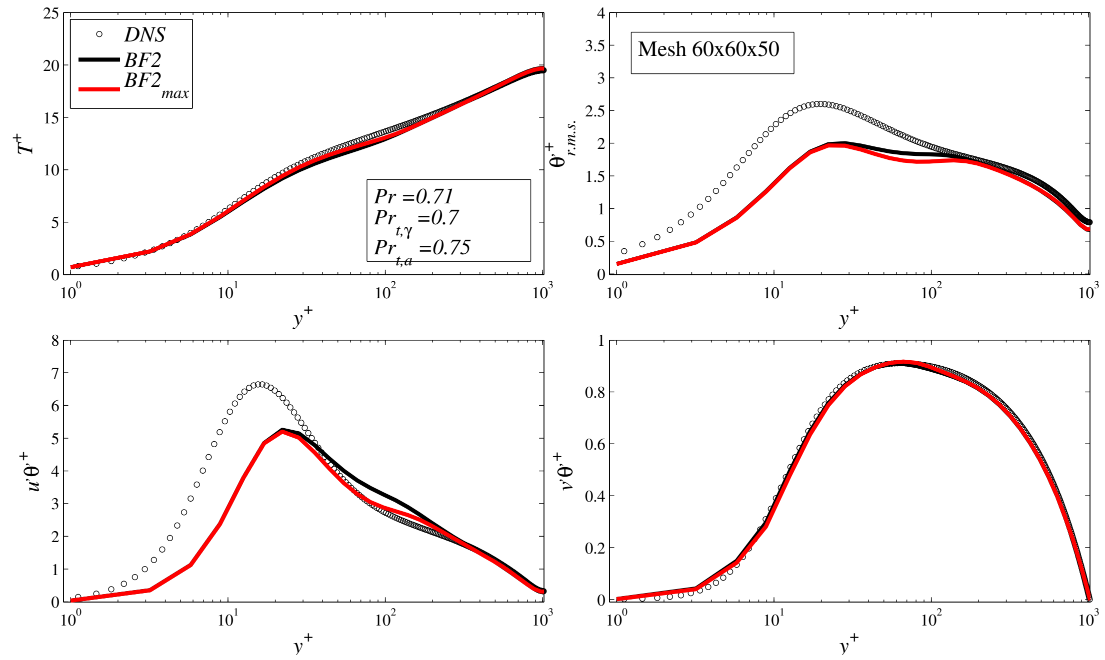

Figure 5.29: Hybrid channel flow at high Reynolds case ($Re_\tau = 1020$): comparison between different blending functions (see table 5.5).Temperature profile (top left), temperature r.m.s. (top right), heat fluxes (bottom).

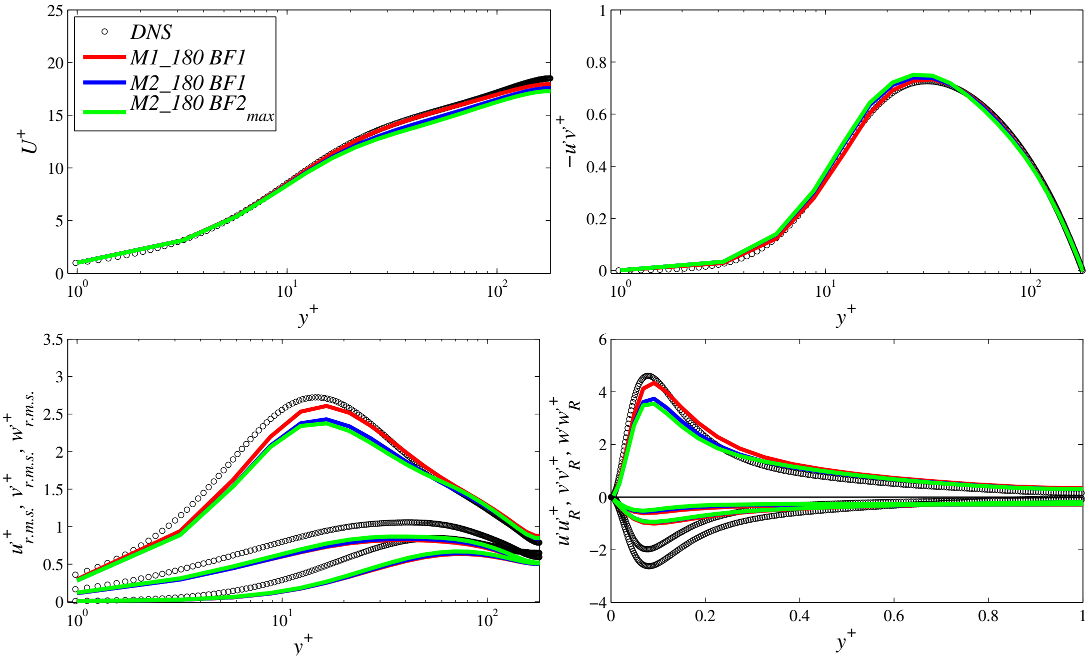

Figure 5.30: Hybrid channel flow at low Reynolds case ($Re_\tau = 180$): comparison between different mesh resolution (see table 5.5). Mean velocity (top left), shear stress (top right), normal stresses (bottom left) and their reduced counterparts (bottom right).

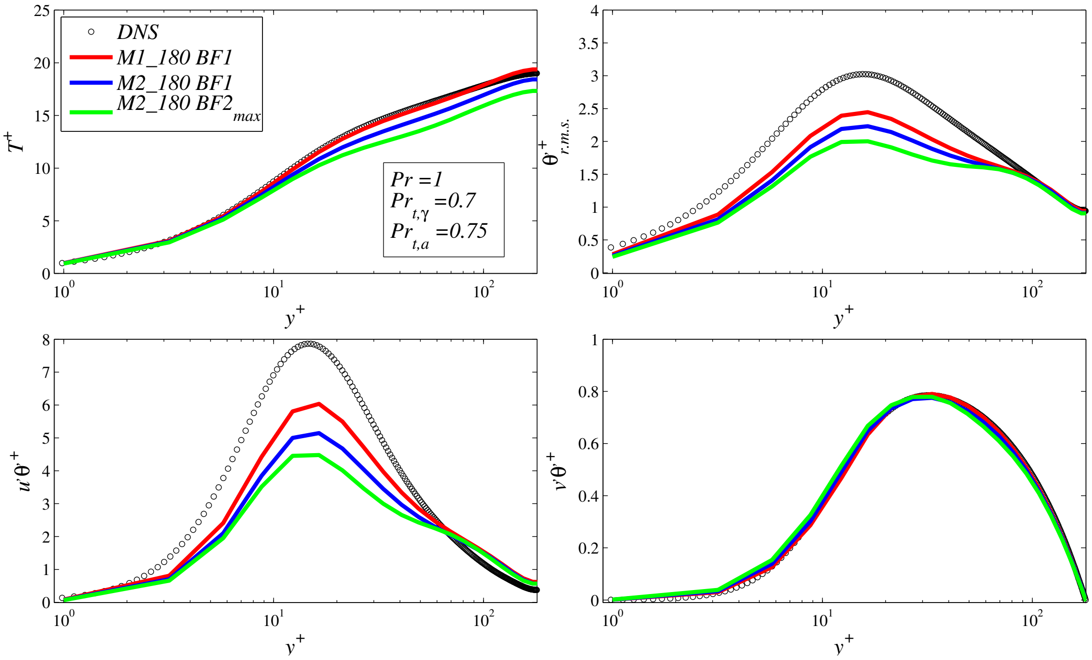

Figure 5.31: Hybrid channel flow at low Reynolds case ($Re_\tau = 180$): comparison between different mesh resolution (see table 5.5). Temperature profile (top left), temperature r.m.s. (top right), heat fluxes (bottom).

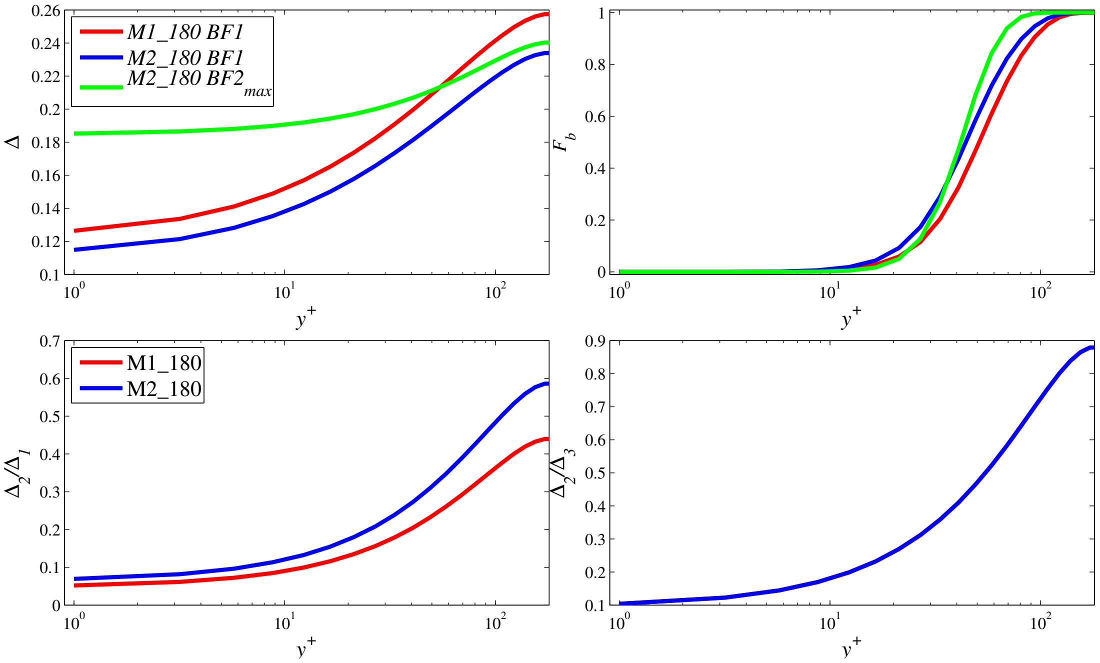

Figure 5.32: Hybrid channel flow at low Reynolds case ($Re_\tau = 180$): comparison of the blending function for different mesh resolutions. Filter width $\Delta_{\mathcal{F}_b}$ (top left) used for the calculation of the blending function $\mathcal{F}_b$ (top right). Aspect ratio of the cells in the streamwise (bottom left) and span-wise (bottom right).

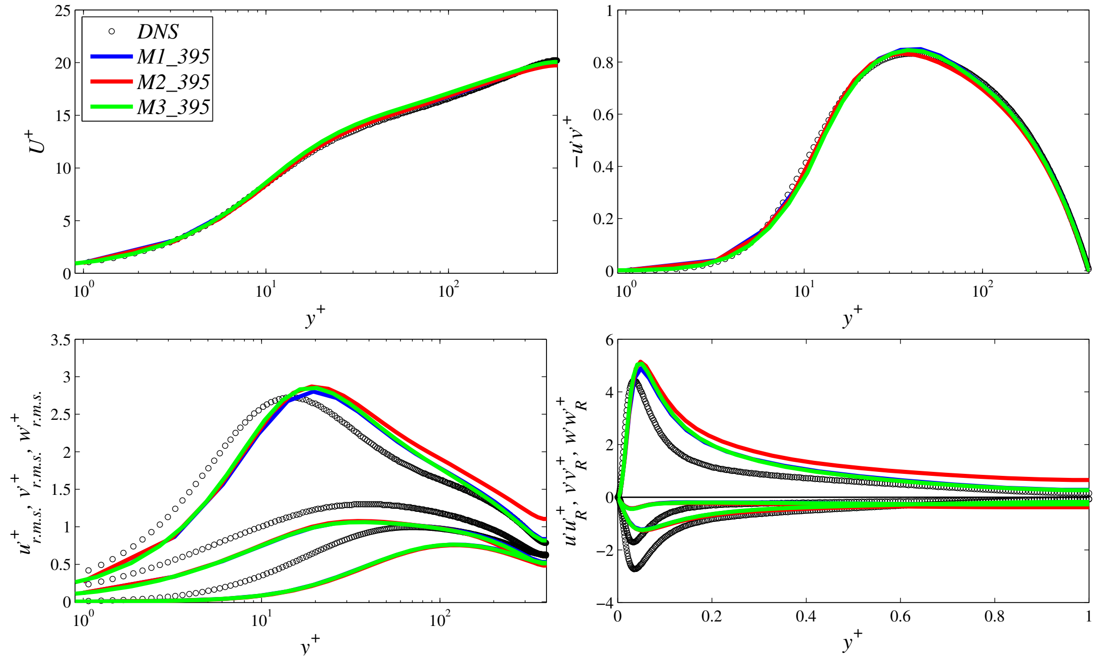

Figure 5.33: Hybrid channel flow ($Re_\tau = 395$): effect of the refinement in the wall normal direction (see table 5.5). Mean velocity (top left), shear stress (top right), normal stresses (bottom left) and their reduced counterparts (bottom right). $BF2$ is used as blending function (see Table 5.5) .

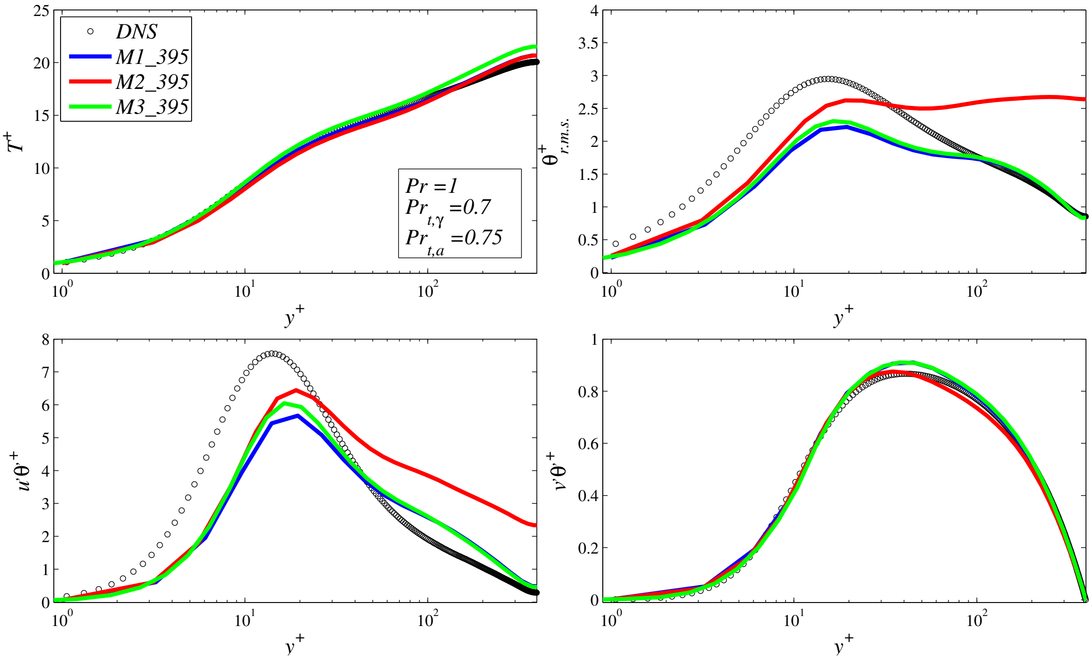

Figure 5.34: Hybrid channel flow heat transfer ($Re_\tau = 395$): effect of the refinement in the wall normal direction (see table 5.5). Temperature profile (top left), temperature r.m.s. (top right), heat fluxes (bottom). $BF2$ is used as blending function (see Table 5.5).

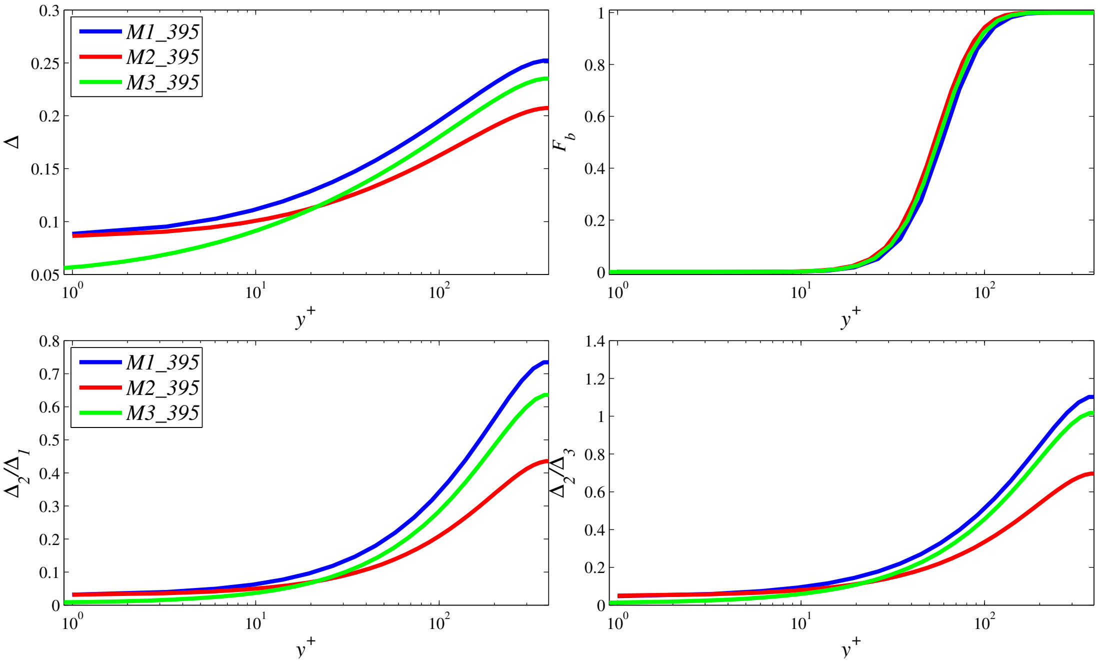

Figure 5.35: Hybrid channel flow ($Re_\tau = 395$): comparison of the blending function for different mesh resolutions. Filter width $\Delta_{\mathcal{F}_b}$ (top left) used for the calculation of the blending function $\mathcal{F}_b$ (top right). Aspect ratio of the cells in the streamwise (bottom left) and span-wise (bottom right).

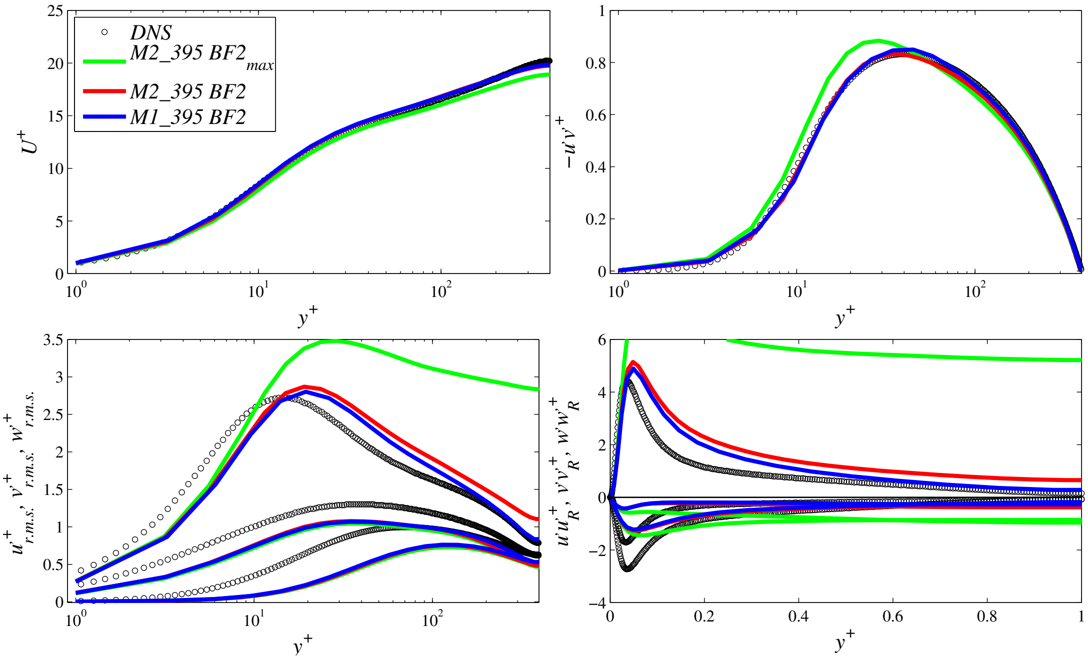

Figure 5.36: Hybrid channel flow ($Re_\tau = 395$): effect of the max correction (see table 5.5). Mean velocity (top left), shear stress (top right), normal stresses (bottom left) and their reduced counterparts (bottom right). Comparison between different blending functions .

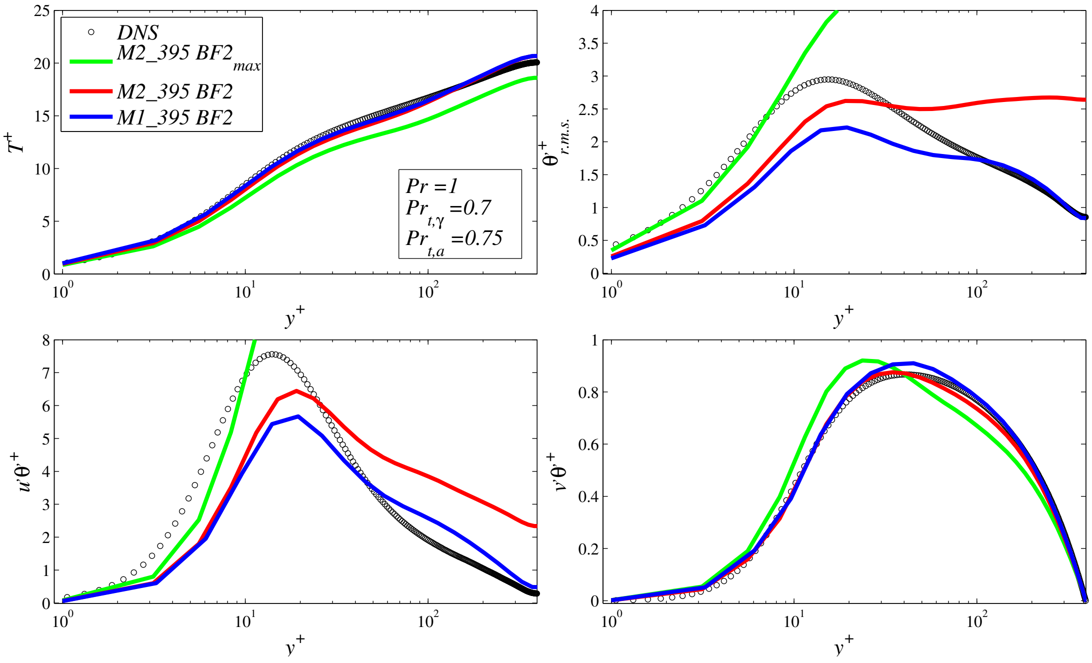

Figure 5.37: Hybrid channel flow heat transfer ($Re_\tau = 395$): effect of the max correction (see table 5.5). Temperature profile (top left), temperature r.m.s. (top right), heat fluxes (bottom).

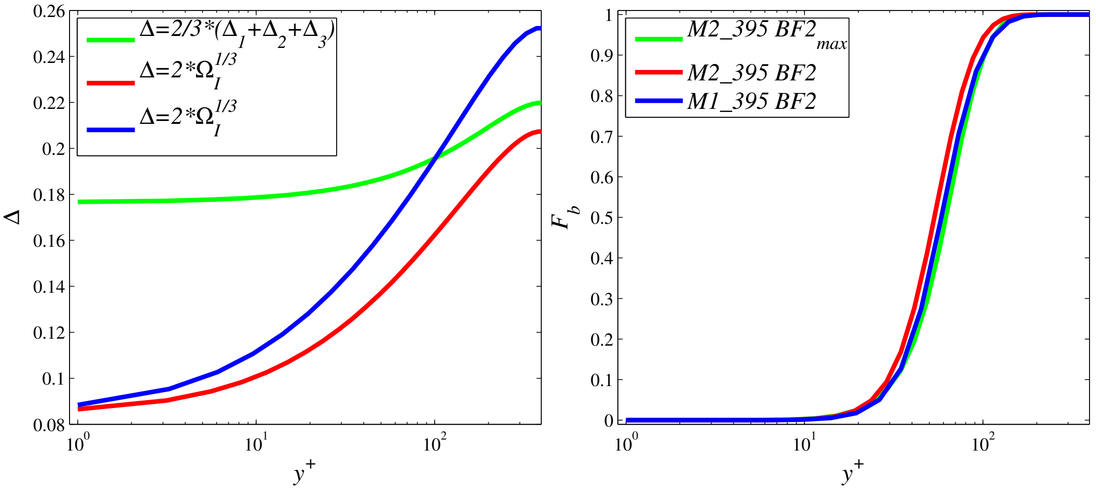

Figure 5.38: Hybrid channel flow ($Re_\tau = 395$): comparison of the blending function with the *max* correction. Filter width $\Delta_{\mathcal{F}_b}$ (top left) used for the calculation of the blending function $\mathcal{F}_b$ (top right). .

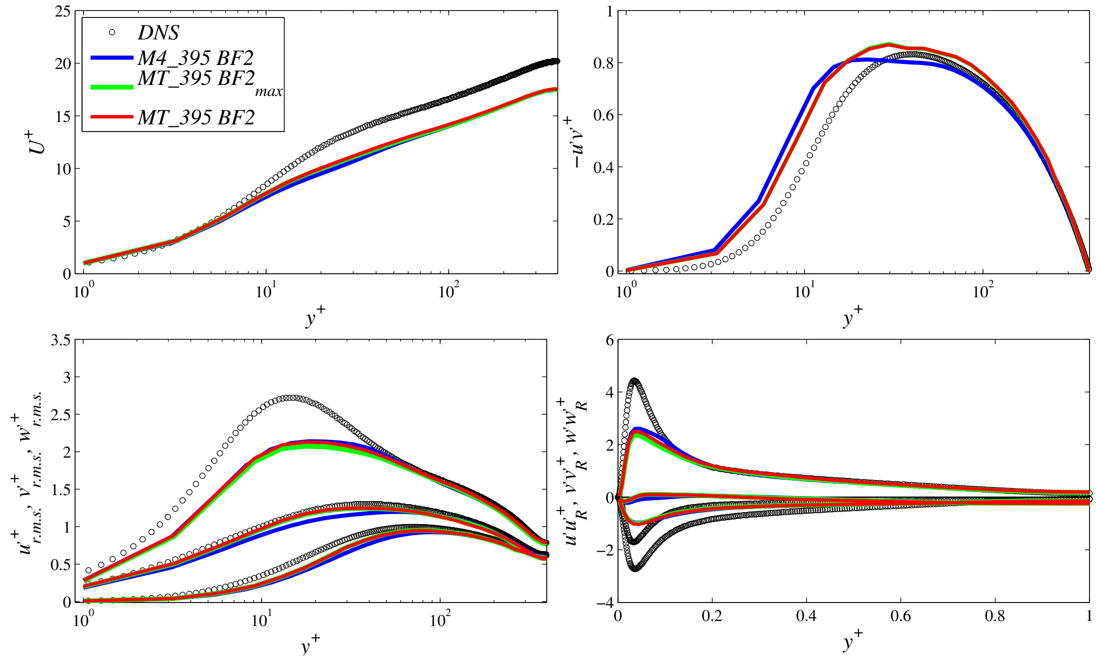

Figure 5.39: Hybrid channel flow ($Re_\tau = 395$): effect of the mesh resolution (see table 5.5). Mean velocity (top left), shear stress (top right), normal stresses (bottom left) and their reduced counterparts (bottom right). Comparison between different blending functions .

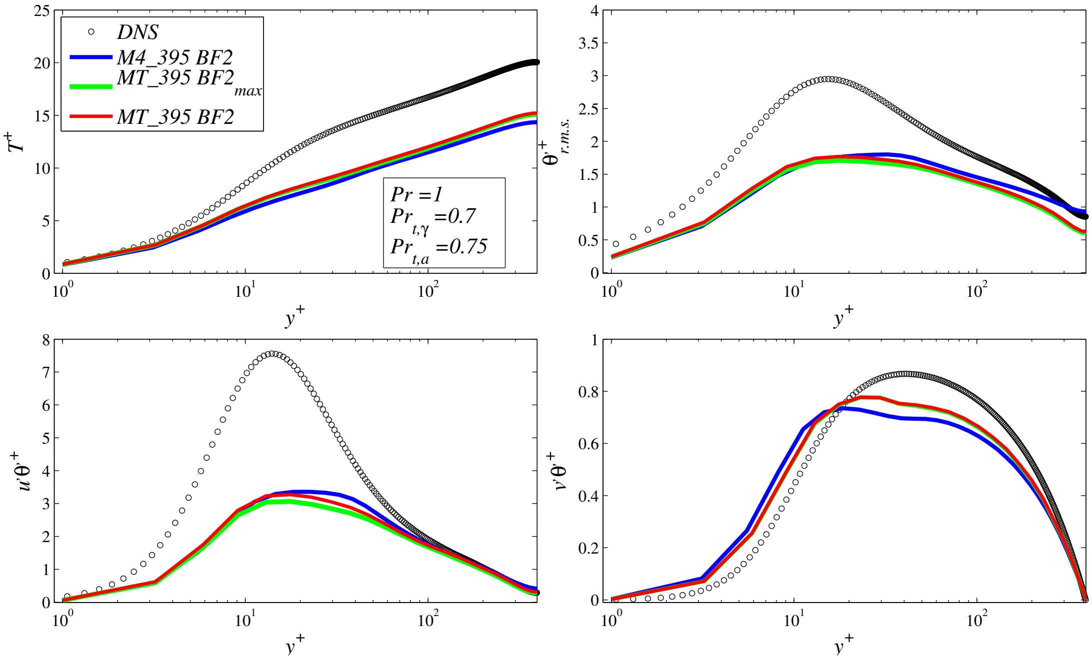

Figure 5.40: Hybrid channel flow heat transfer ($Re_\tau = 395$): effect of the mesh resolution (see table 5.5). Temperature profile (top left), temperature r.m.s. (top right), heat fluxes (bottom).

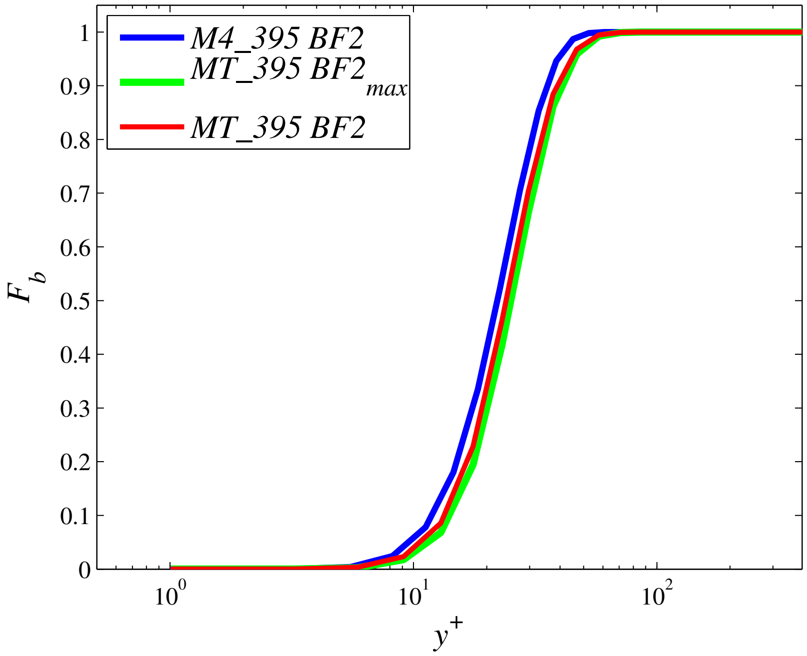

Figure 5.41: Blending function $\mathcal{F}_b$ for the Taylor mesh at $Re_\tau = 395$.

Chapter 6

FUEL ROD BUNDLE

6.1 INTRODUCTION

A Rod bundle is a key constitutive element of a very wide range of nuclear reactor designs (Pressurized Water Reactor PWR, Boiling Water Reactor BWR, Sodium Cooled Fast Reactor SFR, etc.). It is composed by a set of rods, within the nuclear fuel, arranged with different configurations: staggered, triangular or even more complicated. Those elements are cooled by a fluid flowing parallel to the rods. The coolant is different depending of the type of the reactor: from water in a PWR to Sodium in a SFR. A detailed description of the thermal-hydraulic flow field is necessary, in particular thermal and velocity fluctuations, in order to improve the efficiency and the security of the current designs. For example, in the case of SFR (Sodium cooled Fast Reactor), which is one of the proposals for the next generation IV, CFD will have a fundamental role because of the scarce availability of experimental data and their difficult realisation. Note that improvement of thermal hydraulic simulation capabilities of this kind of geometry is also of high interest for the heat exchangers.

Many experimental studies (Krauss and Meyer (1998); Rehme (1992)) found that the distribution of the turbulent intensities is different from those in pipes and plane channels. In particular, in the gap region between two sub-channels, maxima of the turbulent intensities is located far from the wall. Indeed the turbulent quantities are strongly dependent from the pitch to diameter ratio of the configuration. Higher mixing between sub-channels was also observed and several explanations were given.

Mass transfer between adjacent sub-channels can basically result from the following three different mechanisms as described byLexmond et al. (2005).

1. Diversion cross flow: it is the result of different time averaged pressure between two adjacent sub-channels.
2. Void-drift: In two-phase flows, vapour tends to concentrate in channels of higher

hydraulic diameter

3. Turbulent mixing: directly from enhanced turbulent diffusion, but also by secondary mean flow motion induced by turbulent stress anisotropy and inhomogeneity

In the case of a rod bundle arranged in a triangular array, where all the sub-channels have the same hydraulic diameter, and considering a fully developed turbulent flow without any pressure imbalance, only turbulent mixing can appear.

For long time this high mixing between sub-channels was explained with the presence of a secondary flow (Trupp and Azad (1975); Vonka (1988b)). Following a Prandtl description, secondary flows can be generated by two different mechanisms: by turning or skewing the principal flow as in a U-bend pipe or by non-uniformity of turbulence in the near wall region like in a channel of non axial-symmetric cross section. In a rod-bundle, under fully developed conditions, only this second type of secondary motion is possible. The intensity of this secondary flow was directly measured for the first time by Vonka (1988a), finding a value about 0.1% of the mean bulk velocity for a rod bundle at pitch-to-diameter ratio $P/D = 1.3$ (see Fig. 6.1) and a Reynolds numbers ranging from 60000 to 175000. Despite their weak intensity these secondary motions have a non-negligible effect on axial momentum in both radial and circumferential direction.

In nuclear reactors a high value of burn-up[1] is desirable in order to reduce refuelling down time and number of fresh fuel elements required. This can be achieved with a very small value for the pitch-over-diameter ratio (P/D). In such configurations, an energetic and almost periodic azimuthal flow pulsation is present in the gap region between two fuel elements. Rowe et al. (1974) already observed this phenomenon and it was definitely confirmed and measured by Hooper and Rehme (1984). Krauss and Meyer (1998) demonstrated that those fluctuations are the reason of higher mixing between sub-channels. Spectral measurements further enabled characterisation of the phenomenon.

These flow pulsations are described as coherent large-scale structures flowing in the stream-wise direction, superimposed on mean motions. Several experimental works showed that:

- Azimuthal velocity fluctuations in the gap region are almost sinusoidal with a dominant frequency function of the geometrical parameters and Reynolds number (Krauss and Meyer (1998));
- The phenomenon disappears below a certain Reynolds number threshold (Lexmond et al. (2005));

---

[1] Burn-up: measure of the neutron irradiation of the fuel.

- Coherent structures have a quasi-periodic distribution that is weakly dependent from the Reynolds number (Lexmond et al. (2005));
- Above a certain value for P/D (1.1 for a triangular array) the flow pulsation intensity decreases.

First attempts to approach the problem using CFD techniques are reported in Bartzis and Todreas (1979) and Seale (1979). The $k - \varepsilon$ model gives unsatisfactory results for want of capturing the secondary motion. Rapley and Gosman (1986) also confirmed the need of anisotropic models. They analysed three different P/D ratios with an algebraic stress model coupled with a $k - \varepsilon$ model. The necessity of using a more advanced turbulence model than simply isotropic EVM is pointed out by many authors in the last two decades (see for example Lee and Jang (1997); Baglietto and Ninokata (2005); Cheng and Tak (2006)). Lee and Jang investigate an array characterized by $P/D = 1.12$ using a non-linear $k-\epsilon$ model. They find good agreement with experimental results, but also an underestimation of the turbulent stresses in the gap region. In Baglietto and Ninokata (2005) and in the subsequent work Baglietto et al. (2006) a non-linear eddy viscosity model, specifically designed for this type of application, is developed and tested. The agreement with experimental results, in term of wall shear stress, is satisfactory for many configurations with the exception of the very tight lattice ($P/D = 1.06$).

Also the steady state rather than time-marching integration technique is found unsuitable for very tight geometry, because it completely ignores the previously described flow pulsations. A first attempt to use unsteady RANS approach (URANS) is introduced by Chang and Tavoularis (2005, 2007), where authors consider isothermal flow in a sector of 60° of a 37-rod bundle. Authors reported time average velocity and fluctuations and found high correlations between structure in the entire geometry. Another URANS work is presented in Merzari et al. (2008) using, as turbulence model, the already cited non-linear $k-\varepsilon$ of Baglietto and Ninokata (2005). The results are compared with the experiments of Krauss and Meyer (1998) reporting good agreement in terms of wall shear stress and turbulent kinetic energy, but with an underestimation of the dominant frequency. Authors report also the coherence pattern for the azimuthal velocity between two reference gaps, showing a coherence peak in accordance with the experiment. Consequently The authors claimed that a cross section composed by two adjacent sub-channels is sufficient, thus the finding of extended cross section (Chang and Tavoularis (2007)) is too conservative. Another interesting conclusion of Baglietto's work is that the wavelength and dominant frequency depend on the length of the computational domain in the streamwise direction

The same paper also reports a LES of a simplified geometry composed by two rectangular channel closed on 3 sides and connected by a narrow gap. The geometry is also subjected to flow fluctuations and results are in fair agreement with the experimental study of Lexmond et al. (2005). The same geometry is also used by Biemuller et al. (1996) in an earlier study in order to confirm the presence of the flow pulsations and their importance in comparison with the secondary flow.

The geometry is also tackled with LES and DNS in Baglietto et al. (2006) with P/D from 1.06 to 1.2 and Reynolds number from 6000 till 24000. The cross section of the computational domain is composed of only four elementary units, covering the gap and centres of two adjacent sub channels. In this case flow pulsations are not reported, possibly because of the short length used in the stream-wise direction, rather than the limited cross section employed. In Mayer et al. (2007), a lattice Boltzmann LES method is applied to a closed geometry composed of an hexagonal cylinder around a single fuel element. The P/D is equivalent to 1.34 and the Reynolds number is around 20,000. In this case the flow pulsations are not clearly captured and the Reynolds stresses do not compare very well with the experiment, possibly because of the lack of any wall treatment despite very large near wall cells.

A very comprehensive review of CFD applied to rod bundle can be found in Ninokata et al. (2009). In this review it is observed that, for a $P/D = 1.2$ a turbulent region develops in the gap after $Re = 4,000$ and the flow can be considered fully turbulent after $Re = 24,000$. Indeed as the geometry becomes tighter the transition is delayed. This finding is in contrast with what will be shown in the Section 6.3 of this work where the flow seems fully turbulent everywhere in the domain already at Reynolds number well below 10,000. The study gives also an average intensity of the secondary motion of about 0.4% of the bulk velocity, where the previous mentioned experimental papers gave values around 0.1%.

The flow pulsations described above may introduce vibration problems and their study is a key issue in nuclear applications. A common approach is to separate the problems, performing the CFD with the structure considered infinitely rigid and obtaining the value for the fluid velocity and pressure, and then passing this information to the structural code in order to evaluate the displacements. This approach, which is often referred as “partitioned”, can have different levels of coupling depending on how often the information is exchanged between the domains (see for instance Ahn and Kallinderis (2006)). An alternative approach is presented in Papadakis (2008), where the elastodynamics equations for Hookean solids are rewritten using the same unknown of the Navier-Stokes equations (i.e. velocity and pressure). These types of methods, so-called “Monolithic”, have the advantage that there is not any discontinuity at the interface between the two media. The novelty of this work is the use of a Finite Volume, co-located arrangement for the discretization of the governing equations for both solid and fluid.

6.2 Case description

Figure 6.1 presents the triangular infinite rod bundle pattern considered herein, with $D = 0.14\,m$. The narrow part that connects two adjacent sub-channels, from now on, will be referred as the gap region, whereas the centre of a sub-channel will be named as the open region. A first problem is to identify which is the best cross section to be used. A first choice could be a cross section composed by only four elementary units, arranged around the gap region, which is also the smallest possible (light blue in Fig. 6.1). In this case a rotational periodicity[2] is used, linking the segment $\overline{AB}$ with $\overline{A'B'}$ and $\overline{AC}$ with $\overline{A'C'}$. A second possibility is to use a larger domain, composed by two complete adjacent sub-channels (green domain in Fig. 6.1). The natural procedure to apply the periodicity is to link $\overline{DE}$ with $\overline{D'E'}$ and $\overline{FH}$ with $\overline{F'H'}$. Another possibility could be to use a rotational periodicity between adjacent sides like, for example, $\overline{DE}$ with $\overline{FH}$.

A local system of reference is used in order to report the results where x is the rod axis and the streamwise direction, r the wall normal direction and φ the tangential direction moving from the gap to the centre region. In order to be consistent with previous works from other authors, velocity components, in directions x, r and φ, are labelled u, v and w respectively as in the Cartesian notation.

In the case of the small computational domain two different configurations are taken into consideration, characterised by $P/D = 1.06$ and $P/D = 1.15$. Both the geometries are tested at $Re_B \approx 6000$, that corresponds approximately[3] to $Re_\tau \approx 400$. The dimensions of the first near wall layer, in wall units, for the two meshes are: $0.7 \leq r^+ \leq 1.06$, $7.5 \leq r\Delta\varphi^+ \leq 11$ and $16 \leq \Delta x^+ \leq 22.5$ for the lower P/D and $0.8 \leq r^+ \leq 1.1$, $6.5 \leq r\Delta\varphi^+ \leq 10$ and $16 \leq \Delta x^+ \leq 22.5$ for the higher. The final meshes count around 1.6 million cells for $P/D = 1.06$ and around 1.4 million for $P/D = 1.15$.

For the larger geometry, with two complete sub-channels in the cross section, only one P/D ratio of 1.06 is considered, but for two shear Reynolds numbers of 600 and 800 (bulk values of 6,000 and 13,000 respectively). The near wall mesh resolutions are: $0.7 \leq r^+ \leq 0.9$, $6 \leq r\Delta\theta^+ \leq 10$ and $11 \leq \Delta x^+ \leq 18$ for $Re_\tau = 400$ and $0.7 \leq r^+ \leq 1$, $7.5 \leq r\Delta\theta^+ \leq 15$, $17 \leq \Delta x^+ \leq 30$ for $Re_\tau = 800$. The resulting total number of cells is around seven million for the first case and around 14.2 million cells for the second.

---

[2] In order to link $\overline{AC}$ with $\overline{A'B'}$ a translation plus a rotation are necessary, making the original domain and the copy fully overlapping. Consequently it is not possible to use this periodical configuration because the original domain is intersecting with itself.

[3] The shear velocity u_τ is constantly changing moving from the gap to the open region. In order to evaluate the shear Reynolds number an average value, along the azimuthal direction φ is used. Consequently the definition for the shear Reynolds is:

$$Re_\tau = \frac{u_{\tau,avg} D_h}{\nu}$$

where D_h is the hydraulic diameter. The above definition is extrapolated from Baglietto et al. (2006).

In the case of $Re_\tau = 800$ the shear velocity increases from the gap to the open region, making the dimensionless grid spacing variable. Consequently, the accuracy of the skin friction can vary and the error should increase moving from the gap to the centre of the sub-channel. According to Meyers and Sagaut (2007) the error increment could be around 3%. A possible solution might be to introduce non-conformal mesh refinements in order to decrease cell stretch. This will generate many non-orthogonalities that may introduce spurious oscillations in the solution as observed in Chapter 5. In the same chapter it was also demonstrated that embedded refined meshes with a random pattern for the coarsening did not suffer from the problem, but the construction of such grids in a curvilinear geometry is extremely difficult. Small interpenetration of cells can arise in the presence of hanging nodes because on a curve, three consecutive nodes might not be aligned. In order to solve the problem a specific meshing tool has to be developed or a very laborious and long manual work is required. Indeed this test case has also a secondary motion, and its interaction with the large amount of non-orthogonalities, might introduce undesired unphysical phenomena.

A key point in the geometry definition is its length in the streamwise direction: the flow between two periodic surfaces must be uncorrelated. This is in general verified when the two-point correlations, between points located at the period face and points located at the cross section in the middle of the domain, is lower that a prescribed threshold. In general in LES of plane channels turbulent length-scales are relatively small compared with domain dimensions; in fact the ratio between hydraulic diameter and streamwise periodic length is in general around 1.5. On the other hand, in case of large-scale periodic oscillations, longer domains are required because of their development in the flow direction. Indeed the length of the domain, if not long enough, can shift the value for the dominant frequencies. The only available information is from Krauss and Meyer (1998), where a constant Strouhal number, equal to 0.93, is found which leads to a $\lambda \simeq 0.150\,m$. A linear variation with the Reynolds number is also established for the Strouhal number (see Sec 6.3.3). Consequently the wavelength λ is almost constant as the bulk velocity changes. The periodic length of the domain is set to $400\,mm$, which corresponds to more than double the wavelength λ and around twelve times the hydraulic diameter D_h. The same proportion between hydraulic diameter and streamwise length is kept for all geometries.

Budgets of turbulent kinetic energy and Reynolds stresses are computed for the low Reynolds number using the same methodology presented in the channel flow Section B.1.

To efficiently make-up for scarcity of data several temperature fields were coupled with the hydrodynamic field, since in pure forced convection regime all the scalars can be considered passive (i.e. there is no feedback from the temperature field to the velocity field). Note that a Dirichlet wall temperature boundary condition will force the temperature variance to go zero, while a Neumann, i.e. heat flux wall condition, allows high r.m.s temperature fluctuations at the wall. The Prandtl number cases vary from 0.01 to 10. A very important challenge in fuel bundles is to understand what happens in case of imbalances between sub-channels, or when a region presents a hot spot. Here a very simplified situation is analysed: a source term is introduced in the scalar equation and it is designed to be zero at the wall at the boundary of a sub-channel, maximum on the centre of one sub-channel and minimum in the adjacent. This artificial situation where a positive source in one sub-channel is surrounded by negative sources allows development of heat flux variations in various directions. For the high Reynolds number only one Prandtl number, $Pr = 0.71$, is considered along with only the Neumann BC. The majority of the results presented herein refer to the large computational domain; references to the small computational domain are explicitly mentioned.

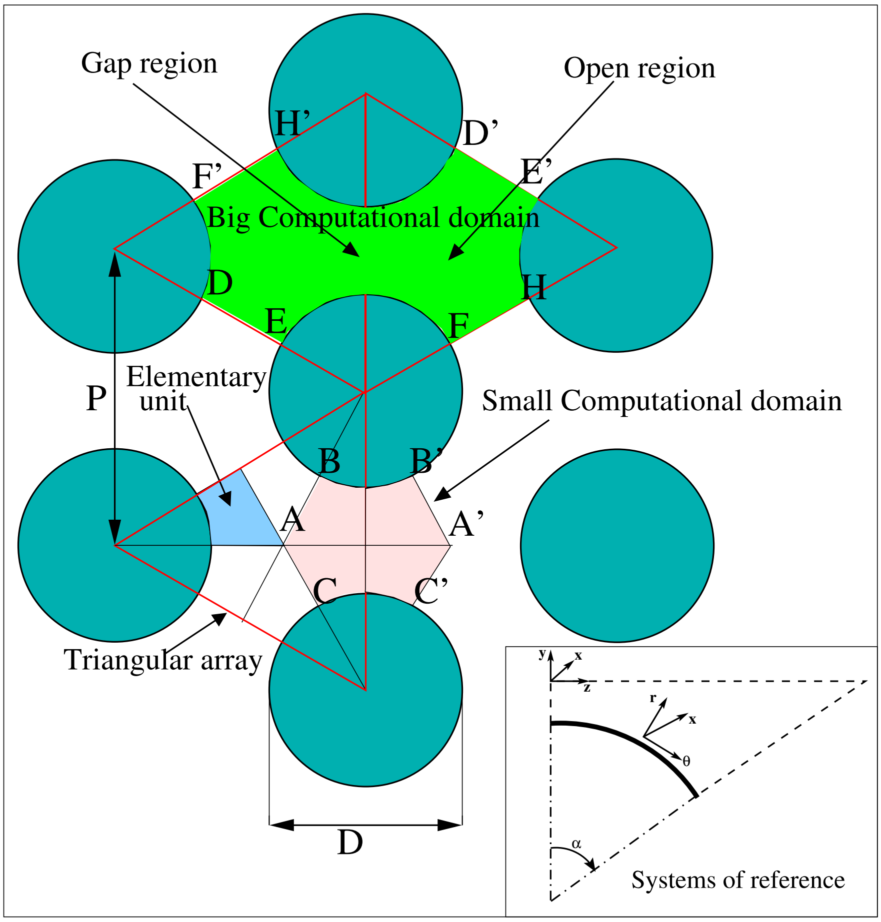

Figure 6.1: Fuel rod bundle: sketch of the geometry.

6.3 RESULTS.

The results are presented in the following order:

- Simulation quality assessment;
- Mean velocity profiles;
- Flow pulsation frequencies;
- Reynolds stress profiles;
- Second moment budgets
- Scalar fields with variable boundary values;
- Scalars with artificial channel to channel imbalance.

In all cases the Smagorinsky model (see Sec. 2.3.3.1) is used with a constant $C_s = 0.065$. The anisotropy is taken into account using the Van Driest damping as described into Sec. 2.3.4). In the case of heat fluxes a Gradient Diffusion hypothesis is used (see Sec. 2.3.5) with a constant turbulent Prandtl number $Pr_t = 0.91$. The time step used such that the instantaneous $CFL_{max} \leq 1.5$ and an average value $\langle CFL_{max} \rangle \leq 1$ for all cases. The time average is performed over at least 100 flow pass-through and afterwards a space average is also applied[4].

6.3.1 LES QUALITY CRITERIA

Pope (2000) suggests the following classification of LES following the percentage of resolved energy over the total energy:

- LES with near wall resolution (LES-NWR): the mesh is fine enough to resolve at least 80% of the energy everywhere in the domain;
- LES with near wall modelling (LES-NWM): the mesh is able to resolve at least 80% far from the wall;
- Very Large Eddy Simulation (VLES): the mesh is too coarse to resolve at least 80% of the energy everywhere in the domain.

These criteria for LES quality assessment poses a difficulty which consists in the quantification of the resolved energy and the problem is more challenging in case of implicit filtering with an effective viscosity model like the Smagorinsky model used herein. A

---

[4] The space average is performed along the homogeneous direction and along every elementary unit.

first possibility is presented by Geurts and Fröhlich (2002) where the amount of modelled energy, introduced by the LES model with respect to DNS, is quantified with a parameter called s, defined as:

$$s = \frac{\langle \varepsilon_{SGS} \rangle}{\langle \varepsilon_{SGS} \rangle + \langle \varepsilon_{\nu} \rangle} \tag{6.1}$$

where $\langle \varepsilon_{SGS} \rangle$ is the average sub-grid dissipation and $\langle \varepsilon_{\nu} \rangle$ the average molecular dissipation. The subgrid-activity can vary $0 \leq s \leq 1$, with $s = 0$ corresponding to DNS and $s = 1$ to a LES at infinite Reynolds number. The dissipation can be related to the molecular and average turbulent viscosity as demonstrated by Celik et al. (2005), leading to:

$$s \approxeq \frac{\langle \nu_{SGS} \rangle}{\langle \nu_{SGS} \rangle + \nu}. \tag{6.2}$$

Celik et al. (2005) claim that in most of LES applications $s \approxeq 1$, therefore it is difficult to use it as an estimator and they propose an alternative formulation, which takes into account also the numerical dissipation:

$$s^* = \frac{\langle \nu_{SGS} \rangle + \langle \nu_{NUM} \rangle}{\langle \nu_{SGS} \rangle + \langle \nu_{NUM} \rangle + \nu} = \frac{\langle \nu_{EFF} \rangle}{\langle \nu_{EFF} \rangle + \nu} \tag{6.3}$$

where $\langle \nu_{NUM} \rangle$ is the average numerical viscosity, which can be summed with the subgrid obtaining the effective viscosity $\langle \nu_{EFF} \rangle = \langle \nu_{SGS} \rangle + \langle \nu_{NUM} \rangle$. The problem now lies in the evaluation of the numerical diffusion. The easiest option is to assume that numerical dissipation is negligible, which correspond to $\langle \nu_{SGS} \rangle \gg \langle \nu_{NUM} \rangle$. This assumption could be acceptable if a very conservative code with high order schemes is employed. In the case of a second order, unstructured finite volume code it is not the case as demonstrated in Chapter 4. In Addad (2004) the numerical dissipation is evaluated as 30% of the average sub-grid dissipation in the case of decay of homogeneous turbulence. Celik et al. (2009) find instead a value of $\langle \nu_{NUM} \rangle \approx \langle \nu_{SGS} \rangle$. [5]

In this work the sub-grid activity s of Eq. (6.2) the modified s^* (Eq. (6.3)) are used to estimate the amount of resolved turbulent kinetic energy and the results are reported in Figs. 6.2 and 6.3 respectively. Table 6.1 gives a a summary of the results reporting the maximum and the average values for the sub-grid activity, which are in both cases below 0.20. The low Reynolds case shows a considerable part of the domain (concentrated in particular in the gap region) where the sub-grid model is rarely active.

---

[5] Celik et al. (2009) evaluate $\langle \nu_{NUM} \rangle \approx \langle \nu_{SGS} \rangle$ assuming the same weight for numerical and sub-grid energy and $h \approx \Delta$. In *Code_Saturne* , strictly speaking, the filter width $\Delta \approx 2h$ as can be derived from Equation (2.25), consequently $\nu_{NUM} = 1/4 \cdot \nu_{SGS}$, which is more close to the estimation of Addad (2004). Because the mesh presents some skewing close to the centre of each sub-channel and some stretching in the near wall region not everywhere in the domain the code can be considered second order accurate. Consequently maintaining $h \approx \Delta$ leads to a more conservative assumption.

The model starts to play a role in the open region and in particular in the sub-channel centre. This does not mean that the flow in the gap region is laminar, on the contrary, the flow is turbulent as already demonstrated. On the other hand at high Reynolds the model starts to be active also in the gap and the maximum of the activity is not only located in the sub-channel centre, but also close to the wall in the open region. A maximum value of 0.34 for s means that over the entire domain, and in both cases, the sub-grid viscosity is below the molecular viscosity. The evaluation of s^* presents the same characteristics of s, with only a shifting towards higher value of the parameter.

More accurate estimations of the numerical diffusion can be obtained from Richardson extrapolation using several meshes with increasing resolution (Celik et al. (2005, 2009)). The method consists of evaluating the effective viscosity as a polynomial function in h and Δ. In order to estimate the constant at least five different simulations are necessary which make the procedure expensive, but with some assumptions it is possible to reduce to only two different tests. This method was not use because testing two different meshes on such a big domain is too expensive. A second and more important reason is that these types of indices does not provide a clear estimation of the error, but only an indication of the level of resolution.

An alternative method to provide an error evaluation as function of model parameters such as Δ and C_s is presented by Meyers et al. (2006). The method is based on the error estimation as

$$err\left(a,b\right) = \left\| \frac{\Phi_{LES}\left(a,b\right) - \Phi_{\overline{DNS}}\left(a,b\right)}{\Phi_{\overline{DNS}}\left(a,b\right)} \right\| \tag{6.4}$$

where a and b are the arguments, Φ the function used for the comparison and $\overline{DNS}$ the filtered function given by the DNS. The method was applied in the decay of isotropic turbulence using, as arguments, the grid resolution and the Smagorinsky constant C_s, and as comparison function the energy. Several simulations are performed in order to obtain a "landscape" where valleys identify low error levels and hills identify high error level. Consequently it is possible to identify relations between the two arguments that minimize the global error. The method was also applied to channel flow in Meyers and Sagaut (2007) using as argument the resolutions in the streamwise and span-wise directions and the wall shear stress as comparing function. The drawbacks are the needs of several calculations to build the landscape and the necessity of a reference solution for the comparison. In this specific case only experimental results are available for the comparison, but the Reynolds number is too large to be approached with a wall-resolved LES.

	$Re_B = 6000$		$Re_B = 13000$	
Parameter	Max	Avg	Max	Avg
s	0.26	0.11	0.34	0.20
s^* ($\langle \nu_{NUM} \rangle \approx 30\%\ \langle \nu_{SGS} \rangle$)	0.32	0.14	0.40	0.24
s^* ($\langle \nu_{NUM} \rangle \approx \langle \nu_{SGS} \rangle$)	0.42	0.19	0.50	0.32

Table 6.1: Summary of the quality indexes for the rod bundle test case.

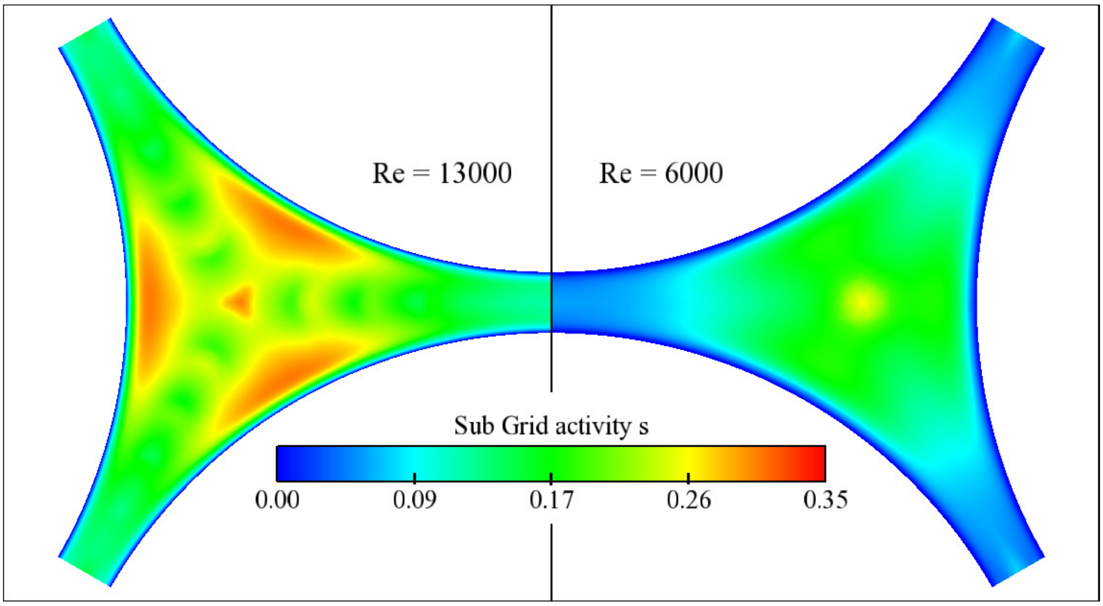

Figure 6.2: Sub-grid activity s (Eq (6.2)) for the rod bundle. On the left hand side results at $Re_b = 6000$ and on the right hand side $Re_b = 13000$.

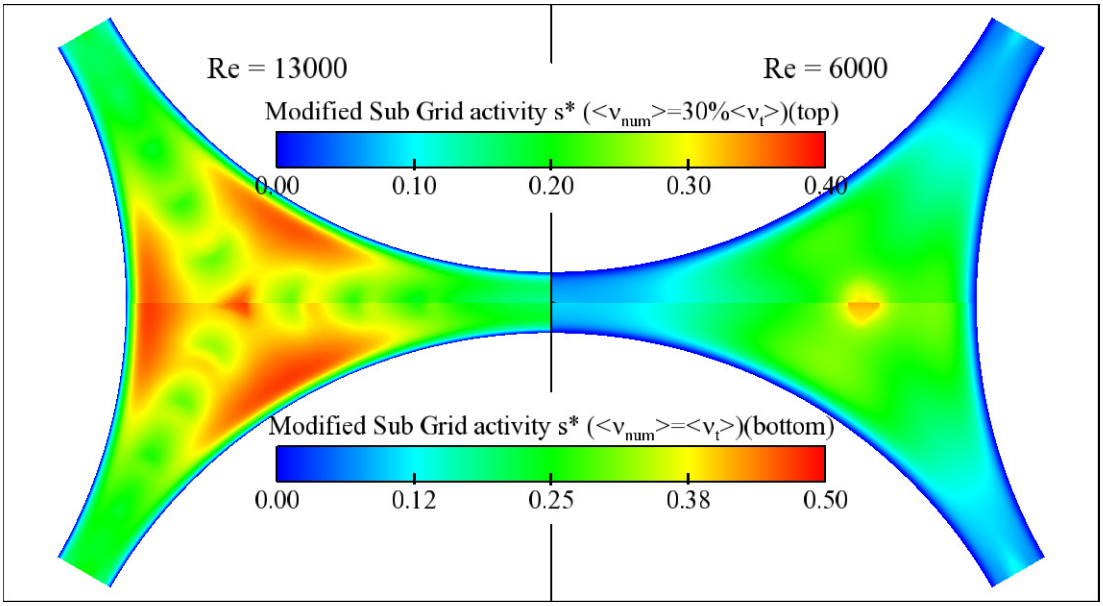

Figure 6.3: Modified sub-grid activity s^* (Eq (6.3)) for the rod bundle. On the left hand side results at $Re_b = 6000$ and on the right hand side $Re_b = 13000$. On the top hand side the numerical dissipation is evaluate as $\langle \nu_{NUM} \rangle = 30\%\ \langle \nu_{SGS} \rangle$, on the bottom $\langle \nu_{NUM} \rangle = \langle \nu_{SGS} \rangle$.

6.3.2 Flow description and mean velocity profiles

In Fig. 6.4 two instantaneous velocity fields are visualized for $Re_B = 6000$ (left) and $Re_B = 13000$ (right). From the temperature iso-surfaces a meandering behaviour is very clear in the gap region between the two sub-channels. The phenomenon is similar to the one observed in composite-bed river (see Uijttewaal and Booij (2000)) and it is generated by a coherent structure resulting from the mean axial flow velocity difference from the low speed gap to the more rapid free flow regions. From both the temperature fields the flow seems turbulent everywhere in the domain at both Reynolds numbers. These coherent elongated structures in the gap region can be seen also in Figure 6.5, while in the centre of the sub-channel they are more isotropic. A consequence of these flow fluctuations is an increase of the mixing between sub-channels, which is confirmed by the alternating positive/negative pattern displayed by the velocity fluctuations w' plotted in the middle plane section (Fig. 6.6).

A second feature of the flow is the secondary motion, which is visualised in Fig. 6.7. Every elementary unit is characterised by a weak secondary vortex rotating from the centre to the gap. The intensity of secondary motion is defined as the ratio between the secondary velocity and the bulk velocity in the streamwise direction, or rather:

$$\frac{\left\|\overrightarrow{V}\right\|}{U_B} \approx \frac{\langle u'v' \rangle}{U_B^2} \tag{6.5}$$

with $\left\|\overrightarrow{V}\right\|$ being the module of the velocity of the secondary motion. In Trupp and Azad (1975) and Vonka (1988b) the intensity of the secondary vortices is demonstrated to be similar to the ratio between the shear stress and the square of the bulk velocity. Table 6.2 lists the maximum and the average intensity of the secondary motion using both the definitions of Eq. (6.5). The intensity of the secondary motion for low Reynolds is 0.4% of the bulk velocity with a peak of more than 1%, whereas at high Reynolds the intensity show a decrease of about 50%. It is interesting to notice that at low Reynolds the approximation of the secondary motion intensity using the turbulent shear stress is not in accordance with the proper definition. This approximation of the secondary motion intensity seems to be verified only at high Reynolds as it is in all the experimental works.

The comparison of the wall shear stress with the experiment of Krauss and Meyer (1998) and the DNS of Ninokata et al. (2009) is reported in Fig. 6.8. The experiments are at higher Reynolds number with respect to the ones of this study, but they are reported in order to have an experimental reference. The profiles of the present work are in agreement with the experimental data, while the DNS profiles shows a very steep variation from the gap to the open region. Authors explain this strong variation as a consequence of a relaminarization in the gap region, which disappears with the increase of the Reynolds number. An alternative explanation could be an underestimation of the secondary motion. As already mentioned previously in the text linear EVM models do not capture the secondary motion and wall shear stress profile has a large variation from gap to open regions in comparison with what a non linear model predicts (see the comparison of profiles in Rapley and Gosman (1986)). In an analogue way the DNS at low Reynolds number might not capture (or highly underestimate) the secondary motion, with the consequence of large variation of the shear stress. The present LES at high Reynolds number confirms this, in fact the intensity of the secondary motion is lower with respect to the low Reynolds number and the shear stress profile is moderately sharper. The reason may be attributed to the coarser resolution in terms of wall units with respect to the low Reynolds case. Indeed in Ninokata et al. (2009) the wall shear profile becomes more flat as the P/D increase, whereas it is the opposite in the experiment of Krauss and Meyer (1998). Figure 6.8 reports also the velocity profiles at different azimuthal locations ($\alpha = 0^o$, 15^o and 30^o). If profiles are made dimensionless with the local shear velocity, they collapse to each other according to:

$$u^+ = 2.6 \ln y^+ + 5 \tag{6.6}$$

which is in according with Krauss and Meyer (1998)[6].

	$Re_B = 6000$		$Re_B = 13000$	
Parameter	Max [%]	Avg [%]	Max [%]	Avg [%]
$\left\Vert \overrightarrow{V} \right\Vert / U_B$	1.41	0.41	0.85	0.235
$\langle u'v' \rangle / U_B^2$	0.45	0.25	0.51	0.25

Table 6.2: Measures of the intensity of the secondary motion.

---

[6] The slope for the logarithmic layer given byKrauss and Meyer (1998) is moderately lower and equal to 2.5 instead of the 2.6 found in this work.

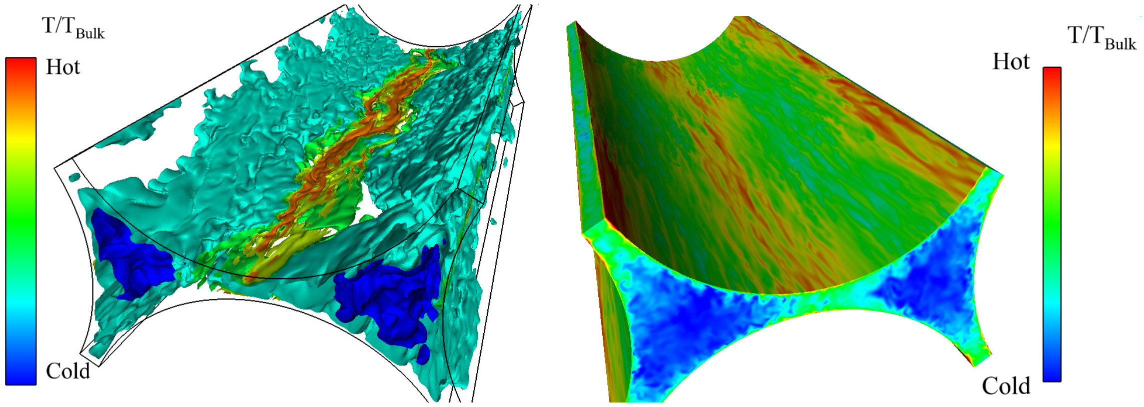

Figure 6.4: Instantaneous temperature field for the rod bundle test case. Iso-surfaces at $Re = 6000$ (left) and contours of temperature at $Re = 13000$ (right) .

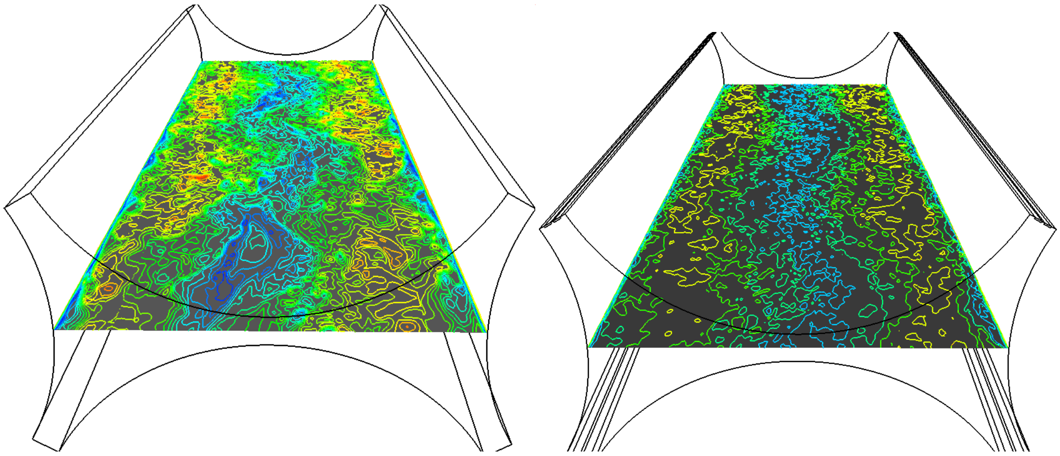

Figure 6.5: Velocity contours on the mid plane of the domain for the rod bundle test case. $Re_B = 6000$ (left) and $Re_B = 13000$ (right). In order to visualize the structure in the gap region the velocity in the streamwise direction is $u = u - \langle u \rangle_{GAP}$.

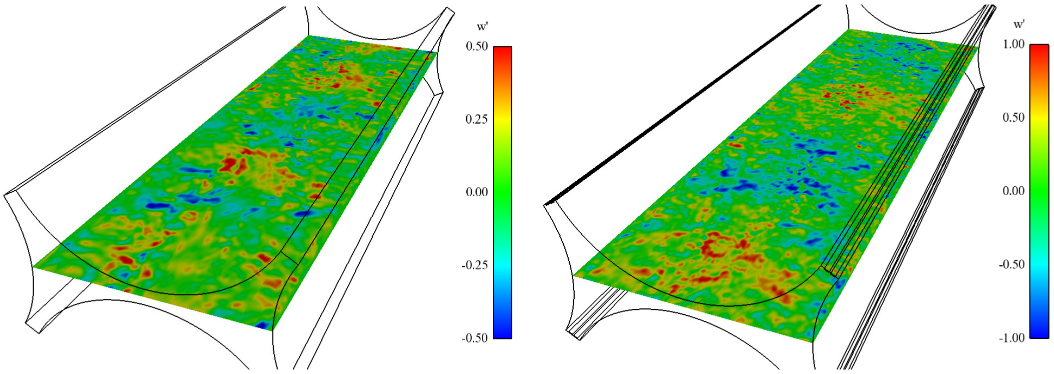

Figure 6.6: Velocity fluctuations in the z direction in the mid plane for the rod bundle test case. $Re = 6000$ (left) and $Re = 13000$ (right).

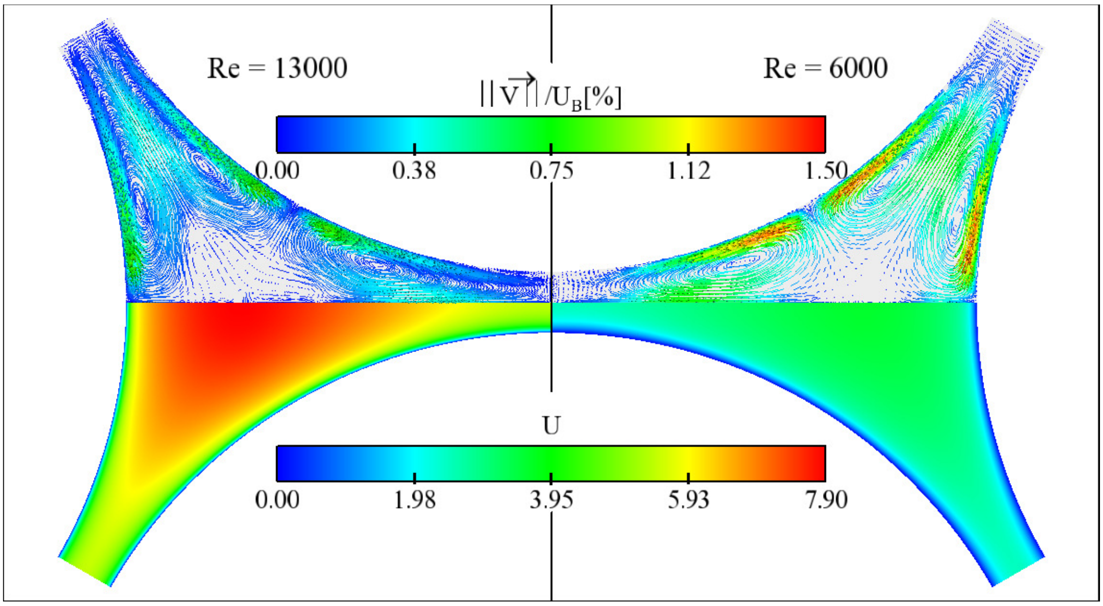

Figure 6.7: Average secondary motion and streamwise velocity for rod bundle test case. $Re_B = 6000$ (left) and $Re_B = 13000$ (right).

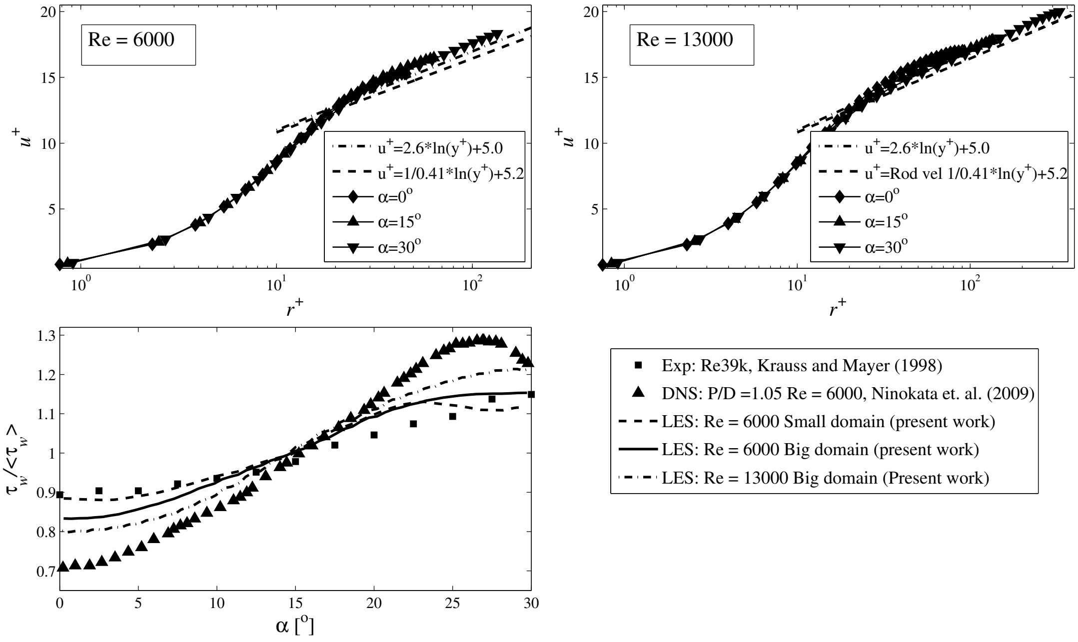

Figure 6.8: Average velocity profiles at different azimuthal location: $Re = 6000$ on the top left and $Re = 13000$ on the top right. Bottom average wall shear stress profiles.

6.3.3 Frequency analysis

In Krauss and Meyer (1998) flow pulsations are characterised by a constant Strouhal number defined as:

$$St = \frac{fD}{\langle u \rangle_{GAP}} = 0.93 \tag{6.7}$$

where f is the dominant frequency and $\langle u \rangle_{GAP}$ is the mean velocity in the gap region. Using (6.7), for a constant viscosity and rod diameter, a linear relation between Reynolds number and dominant frequency can be established, leading to following values:

$$\begin{cases} f = 13Hz \,@\, Re_B = 6000 \\ f = 30Hz \,@\, Re_B = 13000 \\ f = 112Hz \,@\, Re_B = 39000 \end{cases} \tag{6.8}$$

In order to perform a frequency analysis several probes are placed in the domain and their positions, in the reference cross-section, are visualized in Fig. 6.9. The spectra are evaluated with two different methods: the FFT in the West and Welch's method. Welch's method is based on the standard periodogram method and Bartlett's method. The signal is divided into several overlapping segments (eight in this case). Subsequently every segment is windowed. The periodogram is applied in order to evaluate the discrete Fourier transform on every window and an average over all the segment is performed. The main advantage of Welch's method is noise reduction due to imperfection of input data. More details can be found in Welch (1967); Hayes (1996). The comparison between the methods is reported in Fig. 6.10, where are plotted spectra for the reduced geometry at $P/D = 1.15$ and $P/D = 1.06$ in the middle of the gap region. The tight geometry is characterised by three dominant frequencies placed at 13, 28 and 42 Hz, which correspond to Strouhal numbers of 0.93, 2 and 3 respectively. On the contrary the wider P/D does not present any lower dominant frequency.

The first frequency is in accordance with the experimental value, while the two higher are unexpected. Indeed the values are very close to the second and third harmonics. The same problem affects also the big computational domain, and the values of the dominant frequencies are consistent between the two geometries (Fig. 6.11). Moving toward the centre of the sub-channel (points $P4$ and $P5$) the lower dominant frequency tends to disappear, whereas the two higher frequencies remain. Only points extremely close to the wall ($P7$, $P8$ and $P9$) do not possess any peaks. The same considerations can be made for temperature fluctuations and figures can be found in the appendix (Fig. C.1). The streamwise velocity fluctuation spectra are given in Fig. 6.12. In the gap region the u' spectrum is similar to the one presented above, but, in the centre of the sub-channel, all the dominant frequencies tend to disappear. Spectra at high Reynolds number, for all the variables, display the same features described above and they are attached in Appendix C (Figs. C.2, C.3 and C.4) . The first dominant frequency is equal to 30 Hz in accordance with the experimental value, and the two extra high frequencies have Strouhal numbers similar to the ones found in the low Reynolds case.

Two-point correlations between inlet and middle of the domain show that streamwise velocity fluctuations are substantially uncorrelated, while azimuthal velocity fluctuations are relatively highly correlated (see Figs. 6.13 and 6.14). This means there are elongated structures in the gap region which are mainly acting in the azimuthal direction. This fact might explain the presence of the two higher extra dominant frequencies and verification using longer domains should be carried out.

Two-point correlation between position 1 and 2 confirm the high level of correlation for the azimuthal velocity fluctuations, while, surprisingly, streamwise velocity fluctuations are relatively uncorrelated (see Figs. 6.15 and 6.16). This means that there is no transfer of axial flow-rate between left and right channels, but rather periodic bulk flow-rate across the periodic side boundaries of the domain (pressure gradient is set to zero in this direction, but nevertheless one could have non zero and periodic mass and momentum flow in this lateral direction). Conservation of momentum would imply large-scales lateral body force exchanges between fluid and solid, potentially leading to flow induced vibrations if the tubes were not infinitely rigid.

The same observations can be made for the two point correlation between points $P2$ and $P3$ (Figs. C.5 and C.6 in appendix C).

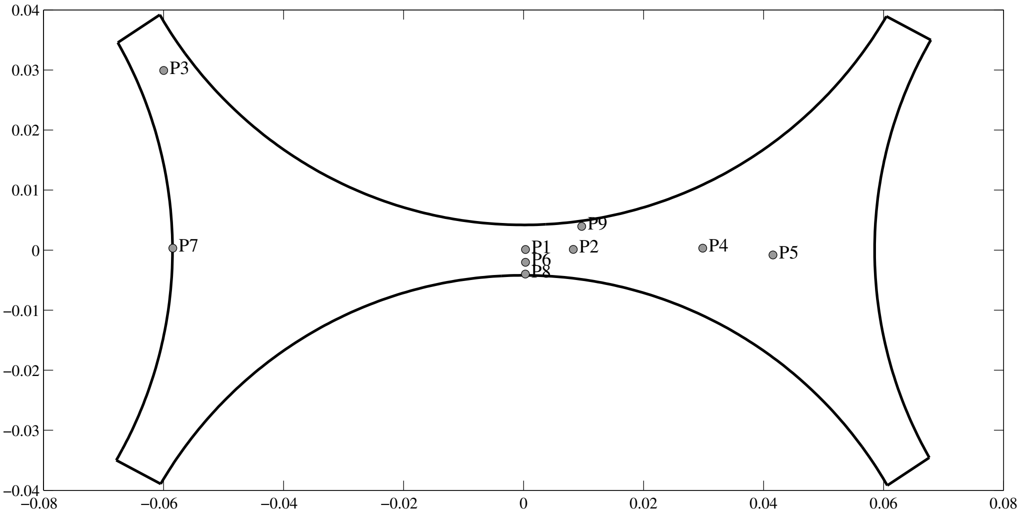

Figure 6.9: Probes location for the frequency analysis for the rod bundle test case.

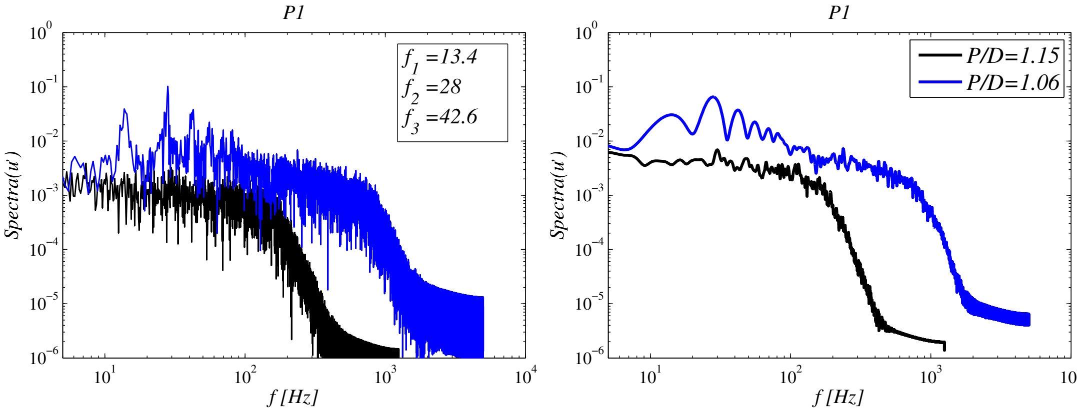

Figure 6.10: Comparison between two different methods to evaluate the power spectra of w' on point $P1$ (see Fig. 6.9). On the left FFT, on the right Welch.

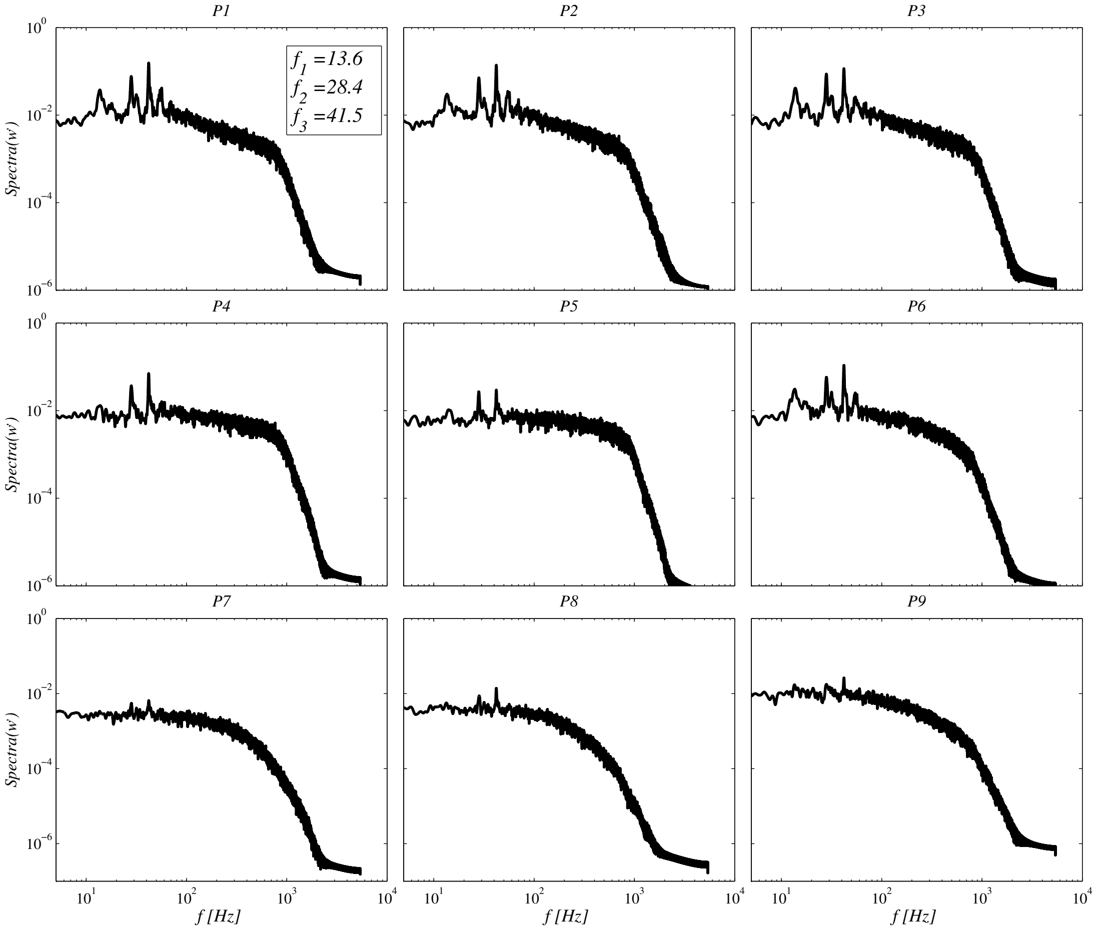

Figure 6.11: Spectra of the w' velocity fluctuations at different locations (see Fig. 6.9) at $Re = 6000$. Spectra are computed with the Welch's method.

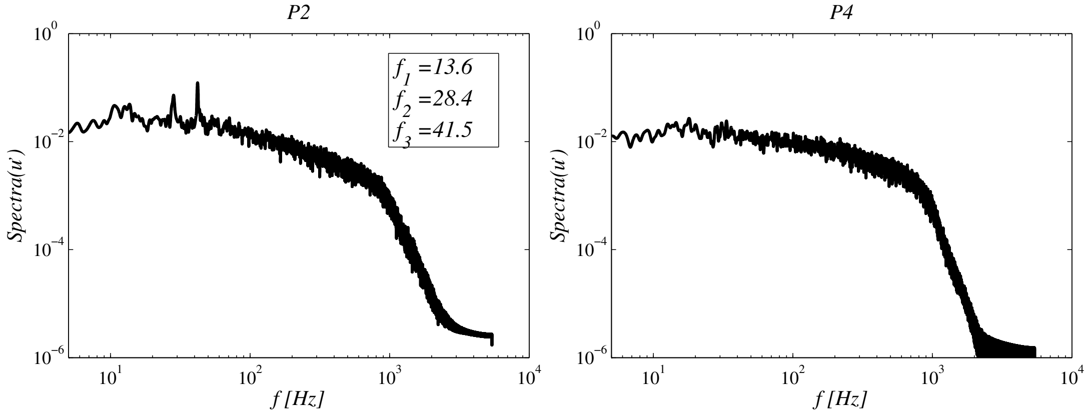

Figure 6.12: Spectra of the u' velocity fluctuations at two different locations (see Fig. 6.9) at $Re = 6000$. Spectra are computed with the Welch's method.

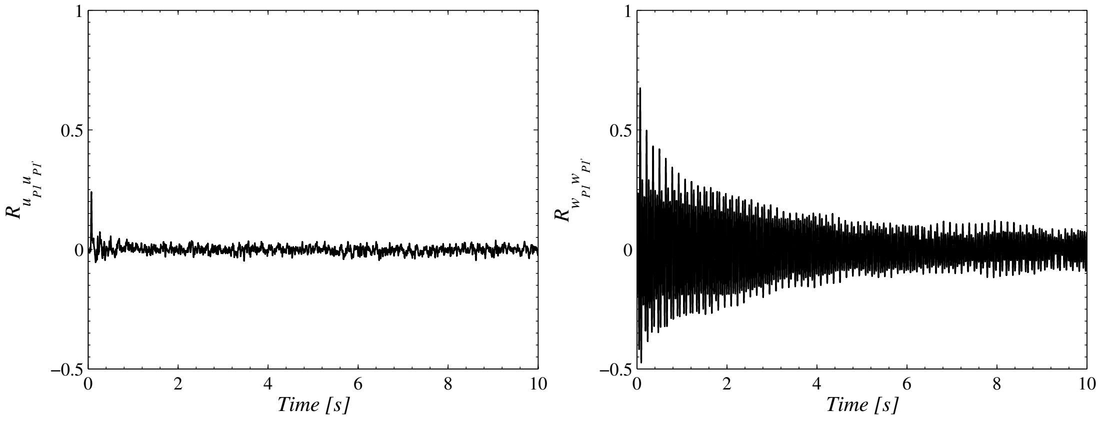

Figure 6.13: Two-point correlation for streamwise and azimuthal velocity fluctuations between inlet and middle of the domain for the location $P1$ (see Fig. 6.9) at $Re_B = 6000$.

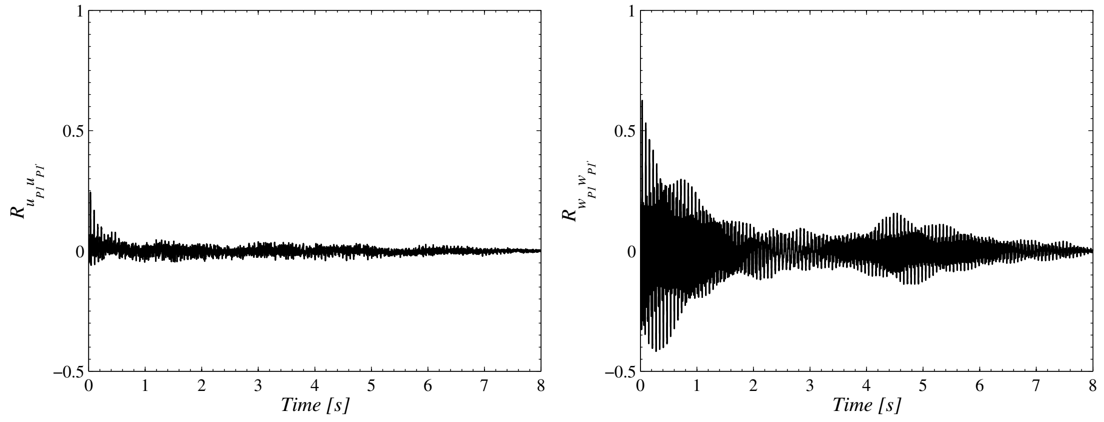

Figure 6.14: Two-point correlation for streamwise and azimuthal velocity fluctuations between inlet and middle of the domain for the location $P1$ (see Fig. 6.9) at $Re_B = 13000$.

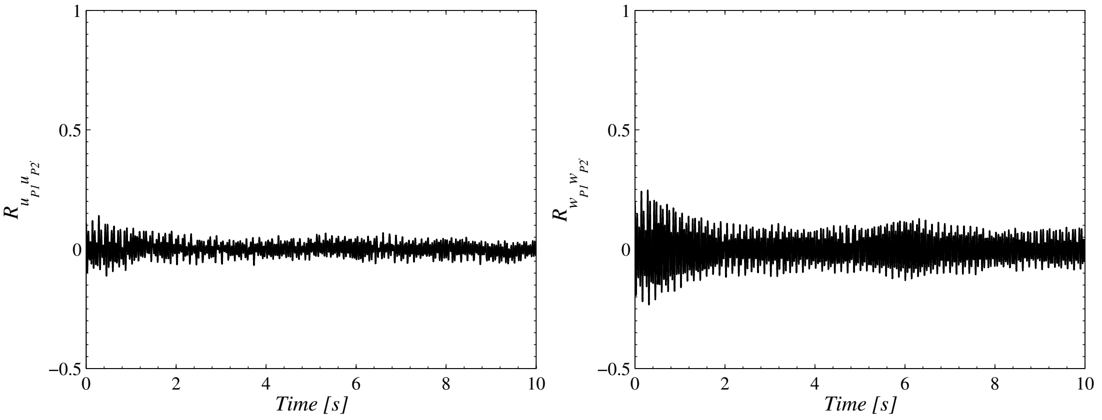

Figure 6.15: Two points correlation between point $P1$ and $P2$ (see Fig. 6.9) of the u' and w' velocity fluctuations at $Re = 6000$.

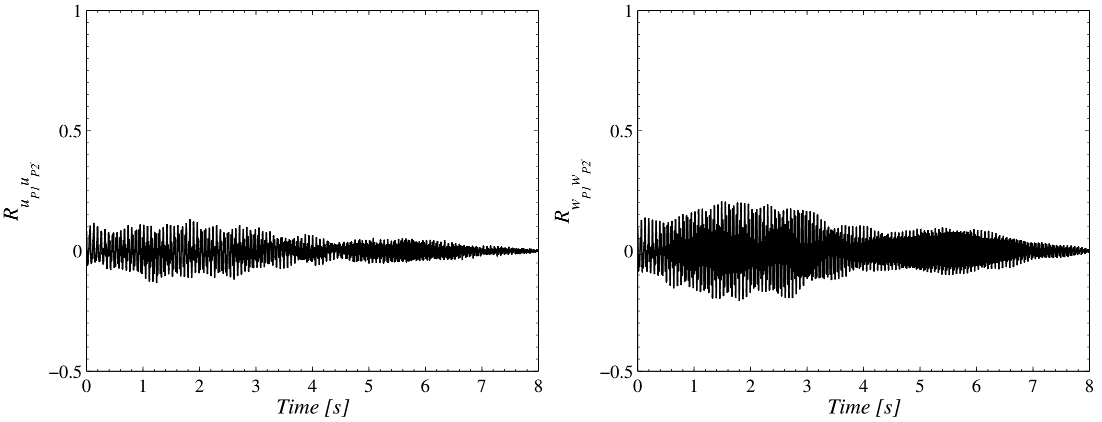

Figure 6.16: Two points correlation between point $P1$ and $P2$ (see figure 6.9) of the u' and w' velocity fluctuations at $Re = 13000$.

6.3.4 REYNOLDS STRESSES AND BUDGETS

The effect of the flow fluctuations is clearly visible on some components of the Reynolds stresses[7]. Fluctuations in the streamwise and wall normal directions display profiles similar to the one of pipes and plane channels (see Fig. 6.17). Maximum of u^{+}_{rms} is located close to the wall as this is where it is generated by the sharp gradient of the axial velocity (see Fig. 6.7), whereas an almost constant value is reached in the bulk of the domain. Wall normal fluctuations increase slowly and monotonically up the central region, as is the case in low Reynolds number channel flows.

---

[7] All stresses are made dimensionless using the friction velocity at the same azimuthal position. Budgets are made dimensionless dividing by u_τ^4 and multiply by the kinematic viscosity ν.

The particularity of this type of flow is expressed by fluctuations in the azimuthal direction. In this case there are two maxima, of about the same intensity, one located in the open region close to the wall, where there is the maximum of transfer of energy from $u_{rms}^{;+}$ to $w_{rms}^{;+}$ by the pressure strain terms. The second peak of $w_{rms}^{;+}$, in the middle of the gap region in contrast with the decrease of $u_{rms}^{;+}$, is clearly made of the coherent structures discussed previously. The peculiarity of the stresses with at least one component is in the azimuthal direction is also confirmed by Fig. 6.18, where $\langle u'v' \rangle^+$, $\langle u'w' \rangle^+$ and $\langle v'w' \rangle^+$ are plotted. $\langle u'w' \rangle^+$ and $\langle v'w' \rangle^+$ present maxima in the gap region then abruptly go to zero as necessary to respect the symmetries of the geometry and Reynolds stress tensor.

On the other hand $\langle u'v' \rangle^+$ corresponds to the main momentum transfer from axial flow to the tube walls (creating drag or head losses). It is interesting to notice that the maximum of $\langle u'v' \rangle^+$ is about half of the one of $\langle u'w' \rangle^+$, i.e. lateral transfer of axial momentum is from the high speed central region to the slower gap region rather than towards the wall.

The same considerations can be drawn for the Reynolds stresses of the high Reynolds number case with the only exception that now the maxima $\langle u'v' \rangle^+$ and $\langle u'w' \rangle^+$ are now of the same order (Figs. 6.19 and 6.20).

Figs. 6.21 and 6.22 present the budget of turbulent kinetic energy k. The production is concentrated in the near wall region, in particular in the gap, and also the dissipation follows the same trend. In contrast with usual channel flow budgets, the advection is not negligible because of the presence of the secondary motion, but, in terms of absolute values, it has a very minor role (30 times smaller than production) because of the weak intensity of the secondary motion. Moreover the advection term plays a very localized role close to wall at the middle of the open region where the colliding pair of secondary eddies eject high turbulence from the wall to the centre. Viscous diffusion is only important at the wall where it displays in a very rapid change from a maximum at the wall to a minimum around. Turbulent and pressure diffusion are relatively important in the gap region, where the turbulent transport shows its maximum. This is not surprising as large values of triple velocity correlations are usually associated with larger structures. The dissipation and the transport due to modelling were also computed in the budget, but they were found to be negligible with respect to the others terms and therefore they are not reported.

In the case of Reynolds stresses only the production and turbulent diffusion are reported, because they show the most interesting features (see Figs. 6.23, 6.24 and 6.25). Production and turbulent transport of $\langle u'u' \rangle$ and $\langle u'v' \rangle$ do not show any peculiar features and they resemble the ones already described for the turbulent kinetic energy. Production of $\langle u'w' \rangle$ presents some unusual behaviour: it is mainly concentrated in the middle of gap region, away from the wall, and it has negative values, meaning that stress and strain are not lined up. Negative production can be also noticed in $\langle v'w' \rangle$, $\langle w'w' \rangle$ and $\langle v'v' \rangle$. In particular the latter shows a rapid change from a negative to a positive peak in the open region. Turbulent diffusion also exhibits compelling profiles. For example $\langle u'w' \rangle$ has its absolute maximum in the gap region where flow pulsations are stronger and a minimum where the secondary motion is stronger.

Budgets at the high Reynolds number case display very similar features, therefore they are attached in Appendix C

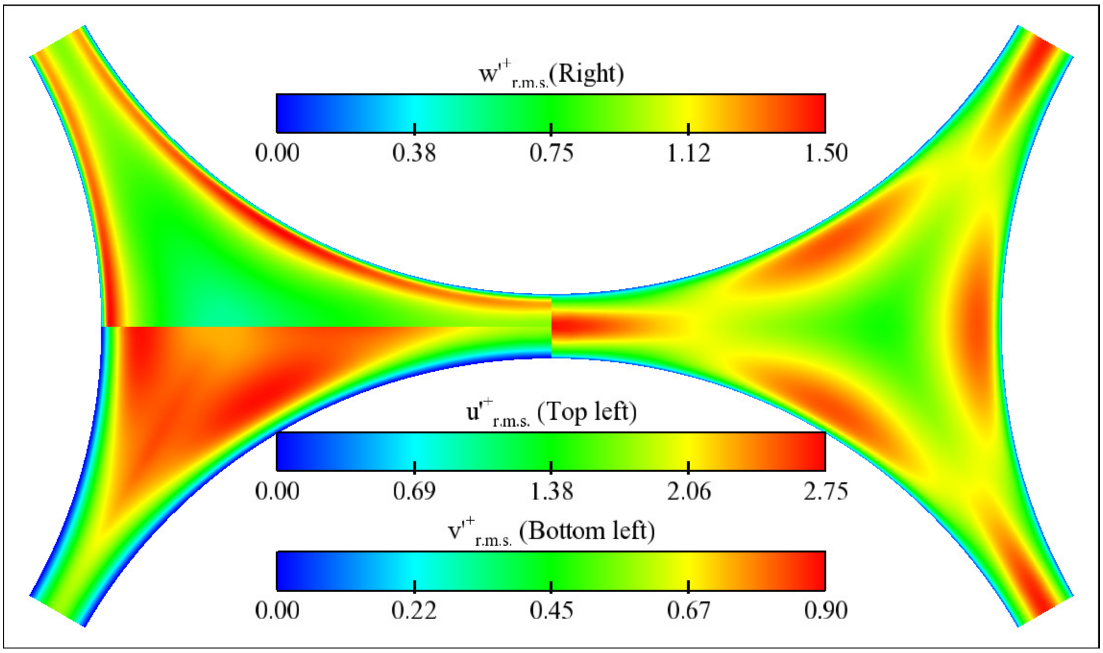

Figure 6.17: Dimensionless normal stresses for the rod bundle test case at $Re = 6000$.

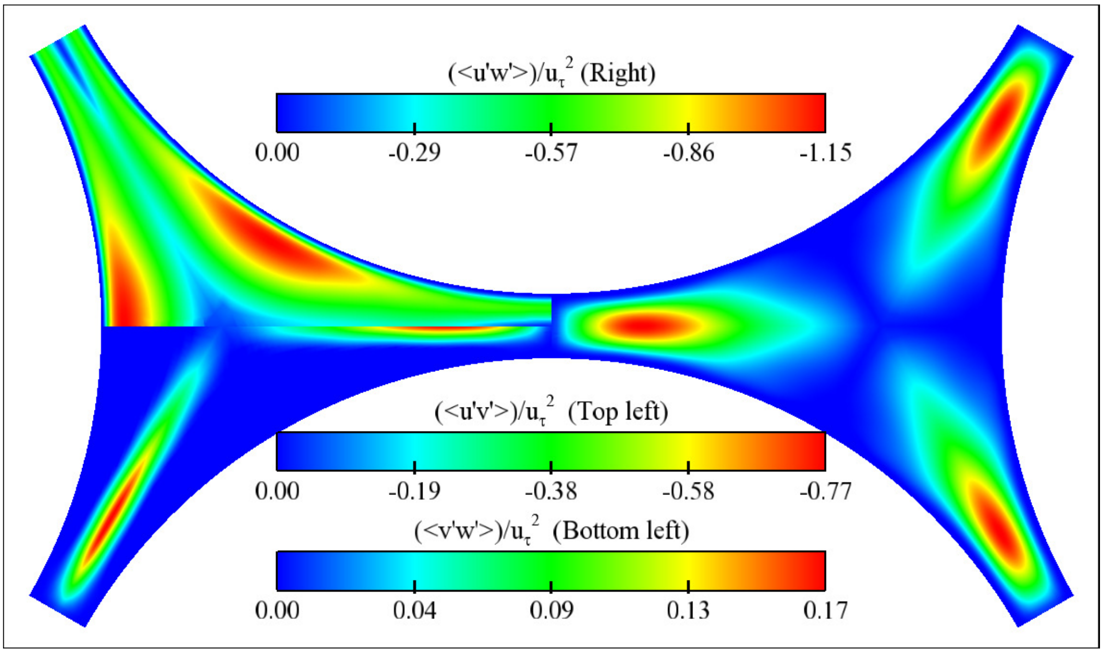

Figure 6.18: Dimensionless shear stresses for the rod bundle test case at $Re = 6000$.

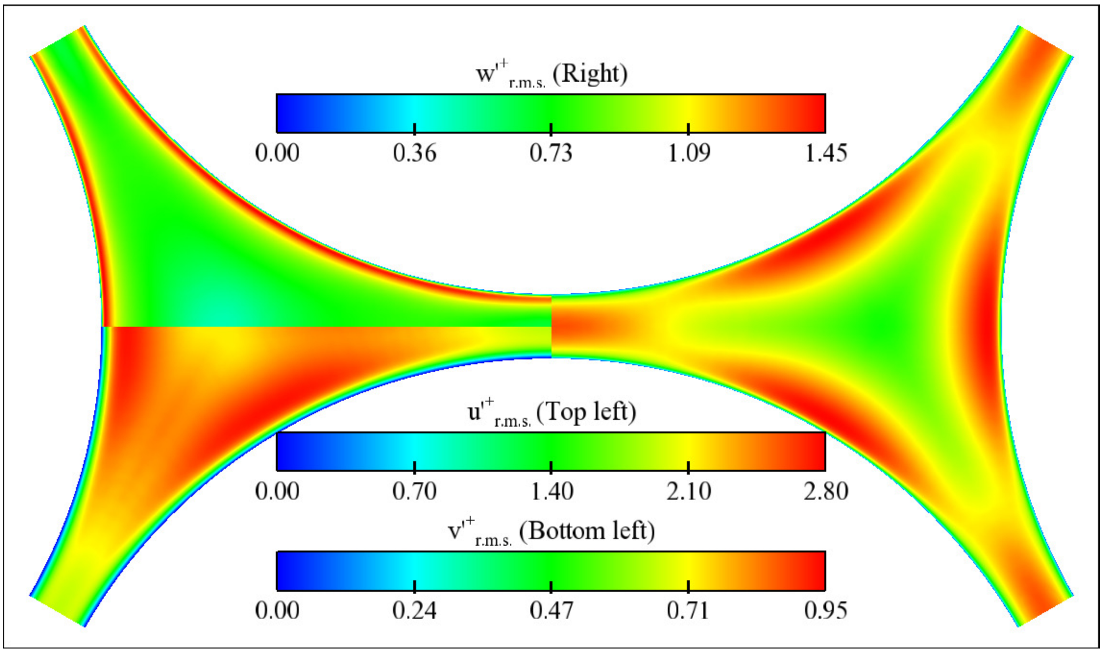

Figure 6.19: Dimensionless normal stresses for the rod bundle test case at $Re = 13000$.

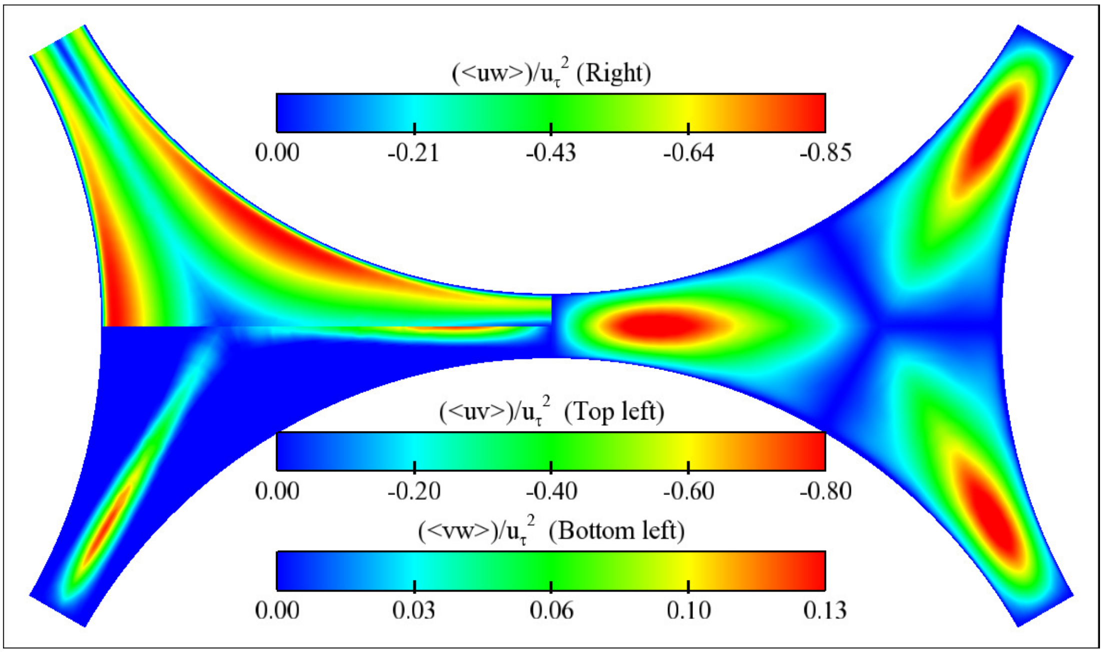

Figure 6.20: Dimensionless shear stresses for the rod bundle test case at $Re = 13000$.

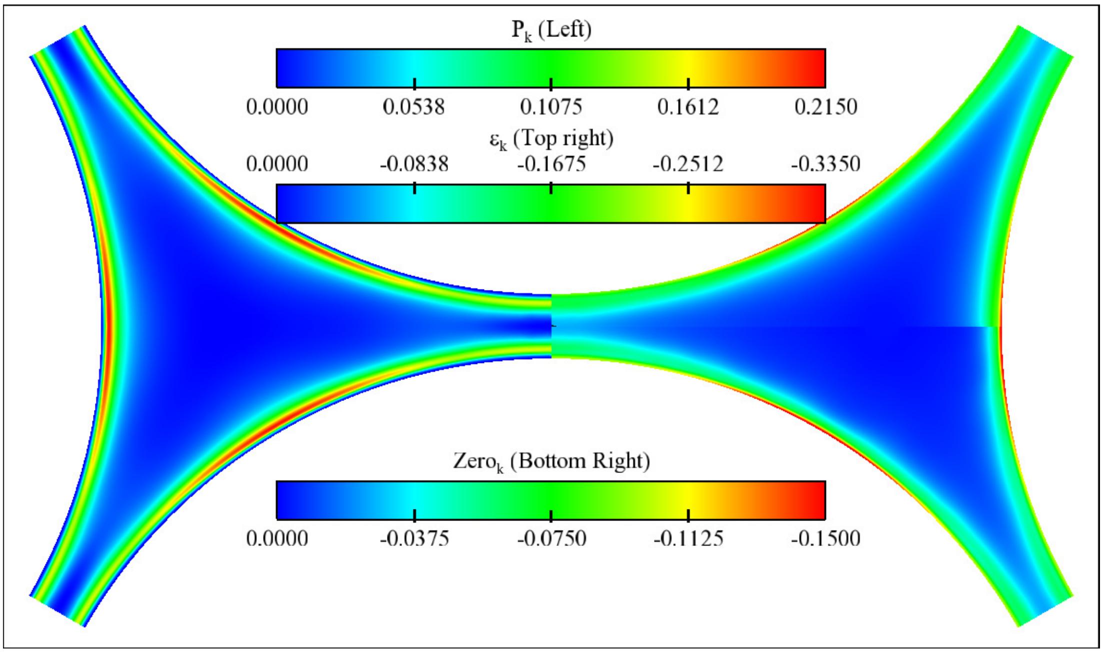

Figure 6.21: Budget of turbulent kinetic energy k at $Re = 6000$: Production P_k, dissipation ε_k and order of Zero.

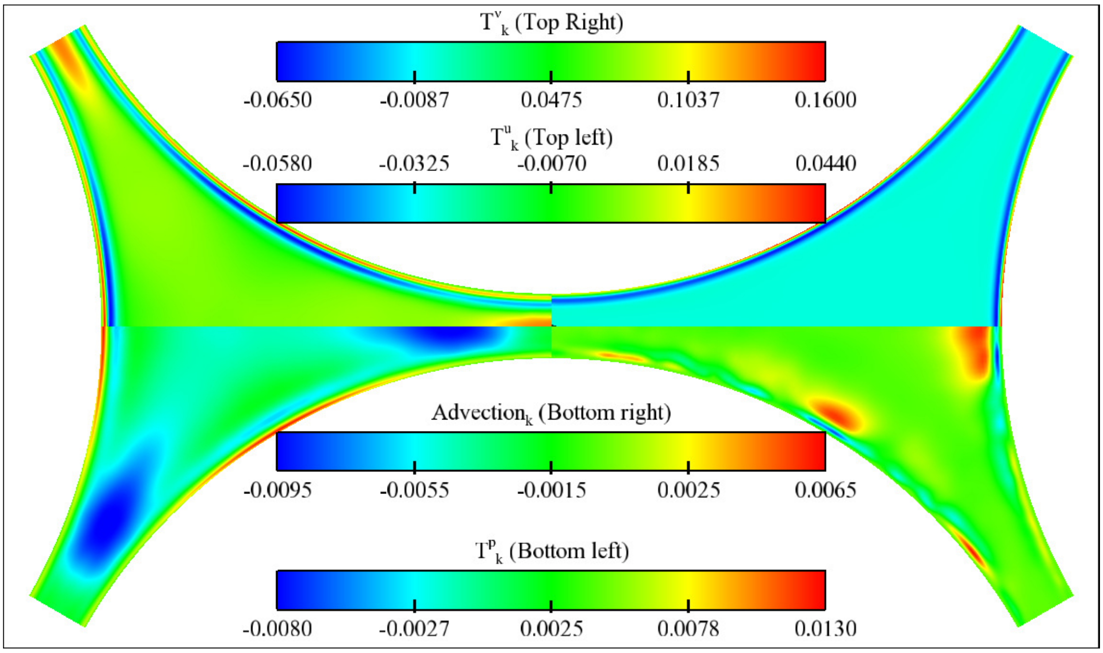

Figure 6.22: Budget of turbulent kinetic energy k at $Re = 6000$: Turbulent diffusion T^u_k, viscous diffusion T^ν_k pressure diffusion T^p_k and advection.

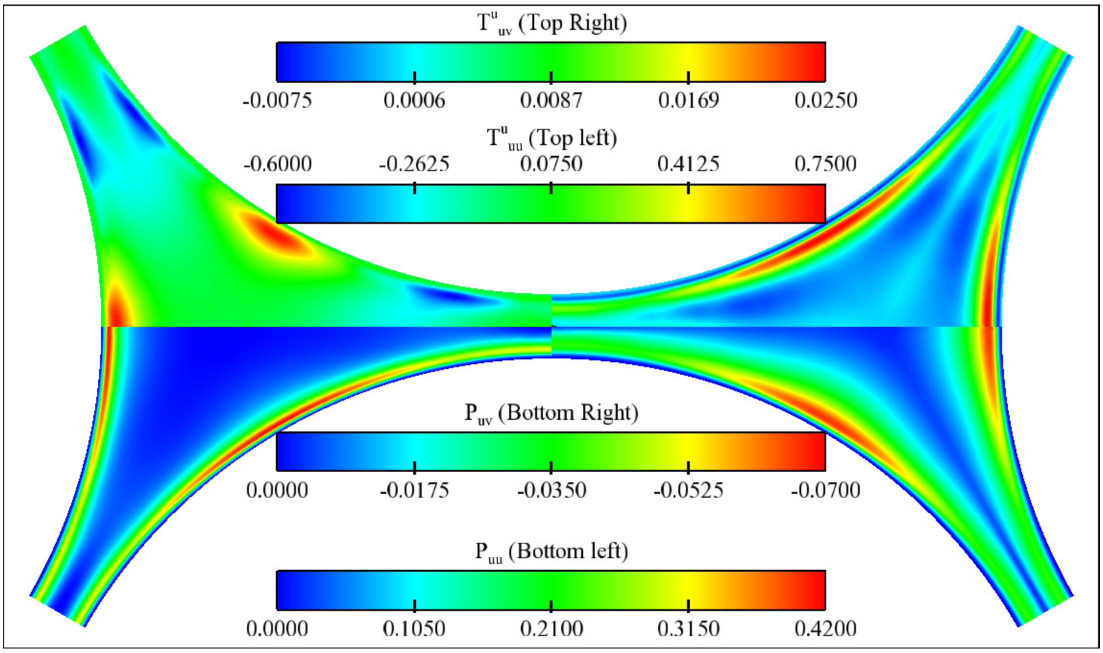

Figure 6.23: Budget of $\langle u'u' \rangle$ and $\langle u'v' \rangle$ k at $Re = 6000$: Production P and Turbulent diffusion T^u.

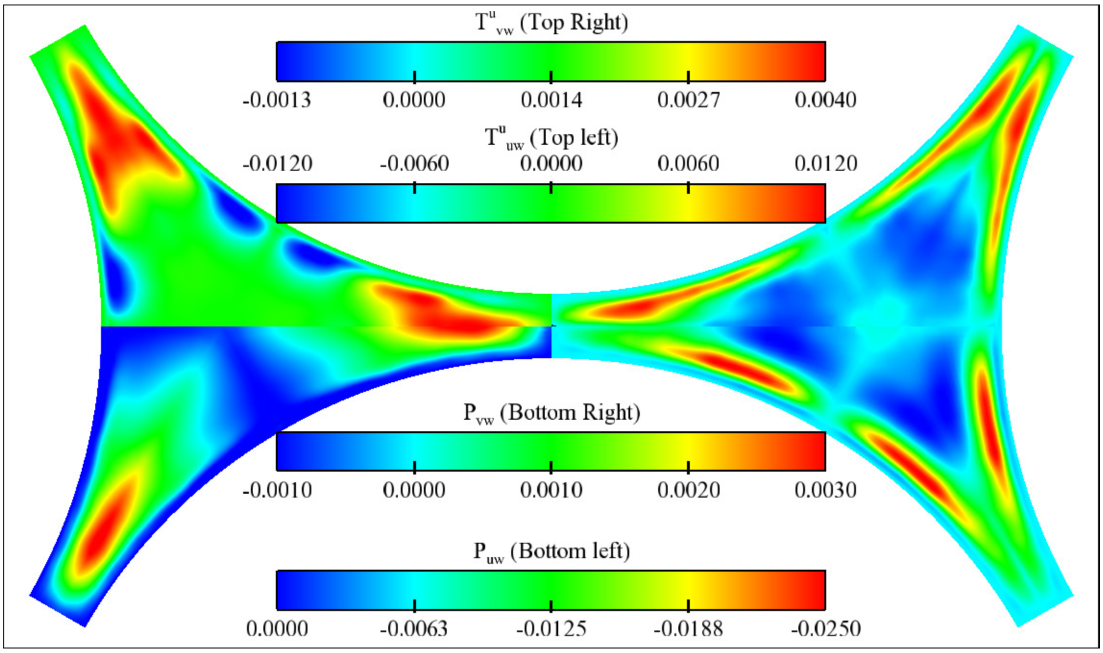

Figure 6.24: Budget of $\langle u'w' \rangle$ and $\langle v'w' \rangle$ k at $Re = 6000$: Production P and Turbulent diffusion T^u.

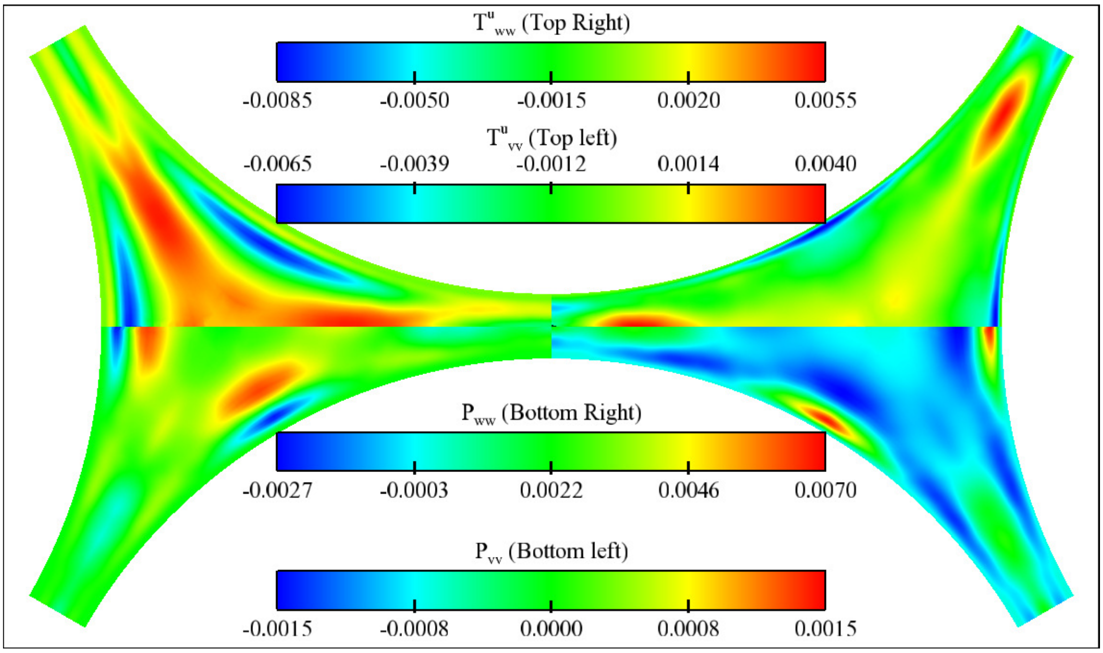

Figure 6.25: Budget of $\langle v'v' \rangle$ and $\langle w'w' \rangle$ k at $Re = 6000$: Production P and Turbulent diffusion T^u.

6.3.5 Thermal field

This section reports the results for the thermal field in forced convection[8]. The Prandtl number used is equal to 0.71 and two different types of boundary conditions (BC) are employed: a constant wall heat flux ($54\,W/m^2$ at $Re = 6000$ and $200\,W/m^2$ at $Re = 13000$) and a constant wall temperature ($300\,K$ at $Re = 6000$). The increase of energy due to the wall heating is compensated by introducing a sink term s_ϕ in the energy equation of the system (2.1), which takes the following form:

$$s_\phi = -\rho\sigma u_i \delta_{i1} \tag{6.9}$$

where δ is the Kronecker delta, with 1 being the stream-wise direction, and $\sigma = dT_B/dx_1$ the bulk temperature variation along the stream-wise direction. The estimation of the increment of bulk temperature is obtained from global enthalpy conservation, yielding:

$$\sigma = \frac{q_w S_w}{\dot{m} c_p L_{x_1}} \tag{6.10}$$

where q_w is the desired wall heat flux, S_w the wall heat surface, $\dot{m}$ the mass flow rate, c_p the specific heat capacity at constant pressure and L_{x_1} the periodic length in the stream-wise direction. A more exhaustive account about periodic boundary conditions for temperature can be found in Utriainen and Sundén (2002); Rosaguti et al. (2006, 2007).

Fig. 6.26 reports the profiles for the Nusselt number[9] and the wall heat flux. Profiles for the Nusselt number resemble the ones for the wall shear stress and the same considerations can be made. The new point to notice is the comparison between profiles obtained at Re=6,000 with the two different types of BC. The profile with imposed heat flux has steeper variation moving from the gap to open region, where it is around 10% larger than the profile with Dirichlet BC. The wall heat flux, in the case of Dirichlet BC, increases moving from the gap to the open region, reaching an almost constant value after $\alpha = 25^o$ and with an average value over the entire angular direction equal to $54\,W/m^2$ as in the constant heat flux case.

---

[8] The coefficient of volume expansion β is kept equal to zero, therefore the density is constant and not a function of the temperature.

[9] The Nusselt number is defined as:

$$Nu = \frac{hD_h}{\lambda}$$

where D_h is the hydraulic diameter, λ the thermal conductivity and $h = {}^{q_w}/_{(T_w - T_B)}$ the heat transfer coefficient. In the case of Dirichlet BC the wall heat flux is varying as function of the azimuthal angle α (see Fig. 6.26).

The dimensionless temperature profiles match the following Log-law (see Fig. 6.27):

$$T^+ = 2.5 \ln y^+ + 3.4 \tag{6.11}$$

with $T^+ = (T_w - T)/T_\tau$ and $T_\tau = q_w/(\rho c_p u_\tau)$ the local friction temperature[10]. The law is respected only when the scalar has a Neumann BC, whereas with a Dirichlet BC temperature profiles do not collapse well. The experimental results of Krauss and Meyer (1998) also report a non clear collapsing of the dimensionless temperature profiles. Map of the dimensionless mean temperature for both types of BC is displayed in Fig. 6.28. Profiles have similar trends, but the maximum dimensionless temperature for the Neumann BC is around 16, whereas for the constant wall temperature it is above 20. Contours of the temperature variance and heat fluxes at $Re = 6000$, employing a constant heat flux at the wall, are plotted in Fig. 6.29. Temperature fluctuations have a maximum in the gap region and a minimum in the centre of the sub-channel. Heat fluxes $\langle u'\theta'\rangle^+$, $\langle v'\theta'\rangle^+$ and $\langle w'\theta'\rangle^+$ mirror the stresses u^+_{rms}, $\langle u'v'\rangle^+$ and $\langle u'w'\rangle^+$ respectively. Temperature variance for the Dirichlet BC is very similar in both trends and values at the previous (constant wall heat flux) with the only exception of the wall value (see Fig. 6.30): in the Dirichlet BC case is going to zero, whereas in the Neumann case the wall value is around 1.7. Heat fluxes displays very similar trends with a variation of peak values at most equal to 20%. The only exception is display by $\langle u'\theta'\rangle^+$ in the gap region, which is flat in the case of Dirichlet BC, whereas it has a peak around $y^+ = 15$ in the case of Neumann BC. The results at high Reynolds are presented in Fig. 6.31. Temperature variance follows the one described for the same BC at lower Reynolds number, with the maximum located in the gap region.

---

[10] In the case of Dirichlet BC also the wall heat flux is varying as function of the circumferential direction and this is taken into account in the evaluation of T_τ. The heat flux is evaluated using the Fourier's law:

$$q_w = \lambda \frac{\partial \langle T\rangle}{\partial r}$$

with r being the wall normal direction.

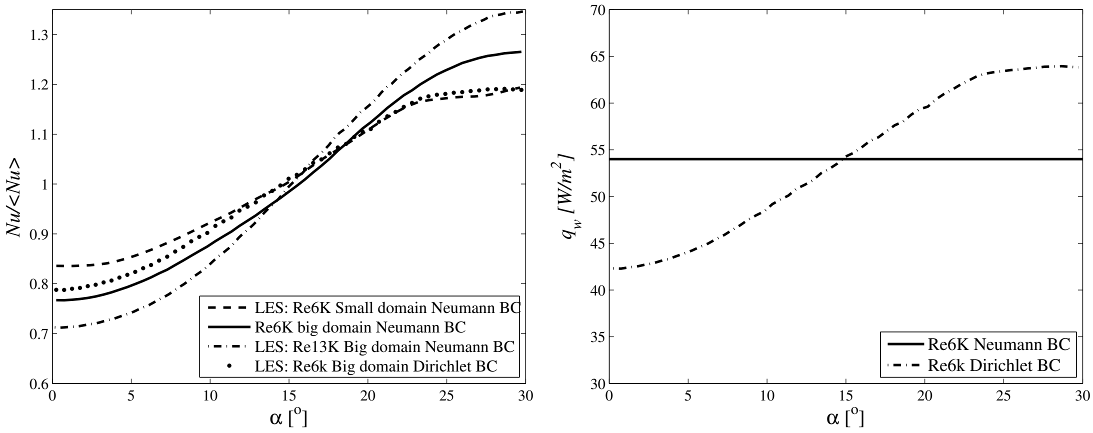

Figure 6.26: Average Nusselt profile (left) and comparison of the wall heat flux distribution between Neumann and Dirichlet BC at $Re = 6000$ (right) for the rod bundle test case.

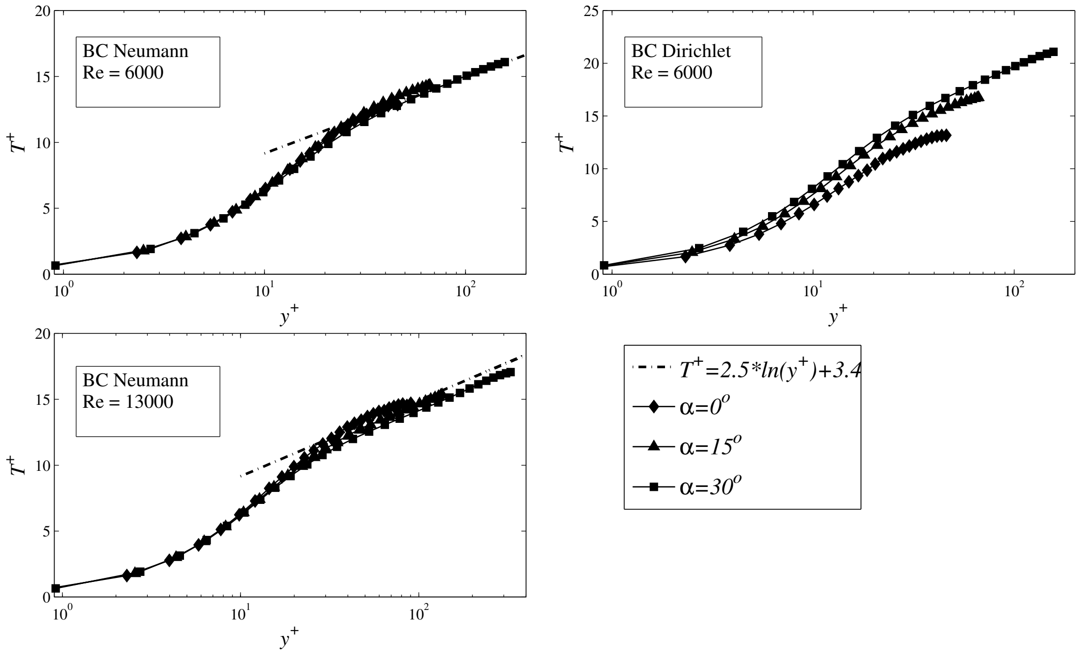

Figure 6.27: Average temperature profiles at different azimuthal location. $Re = 6000$ with constant wall heat flux (top left) for the rod bundle test case. $Re = 6000$ with constant wall temperature (top right). $Re = 13000$ with constant wall heat flux (bottom left).

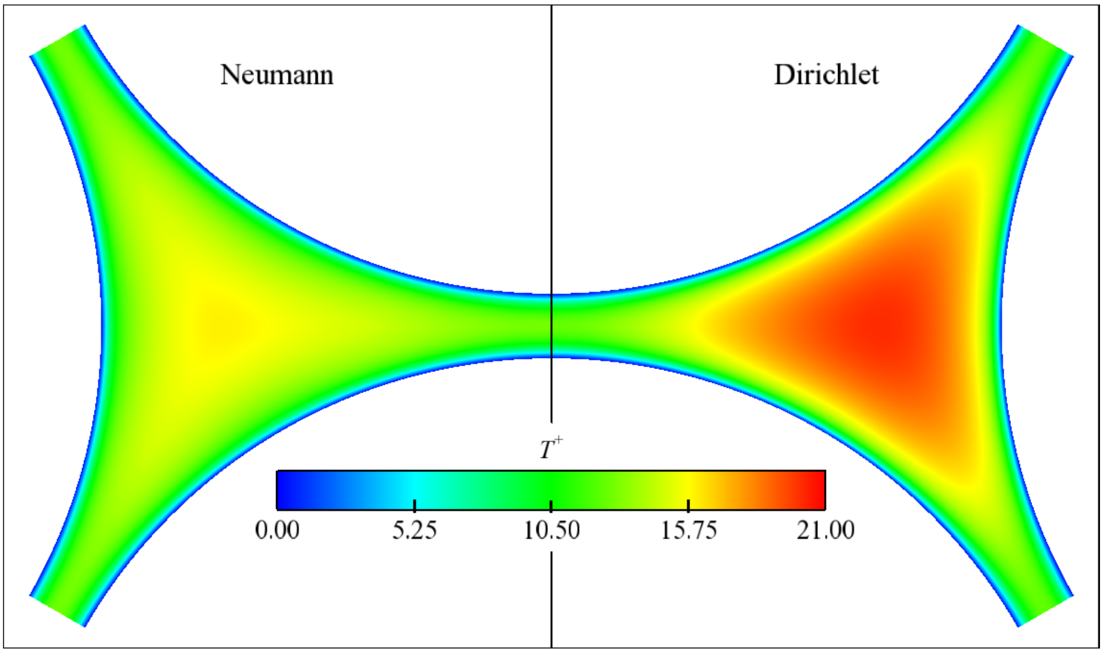

Figure 6.28: Comparison of of dimensionless temperature at $Re = 6000$ between Neumann and Dirichlet BC for the rod bundle.

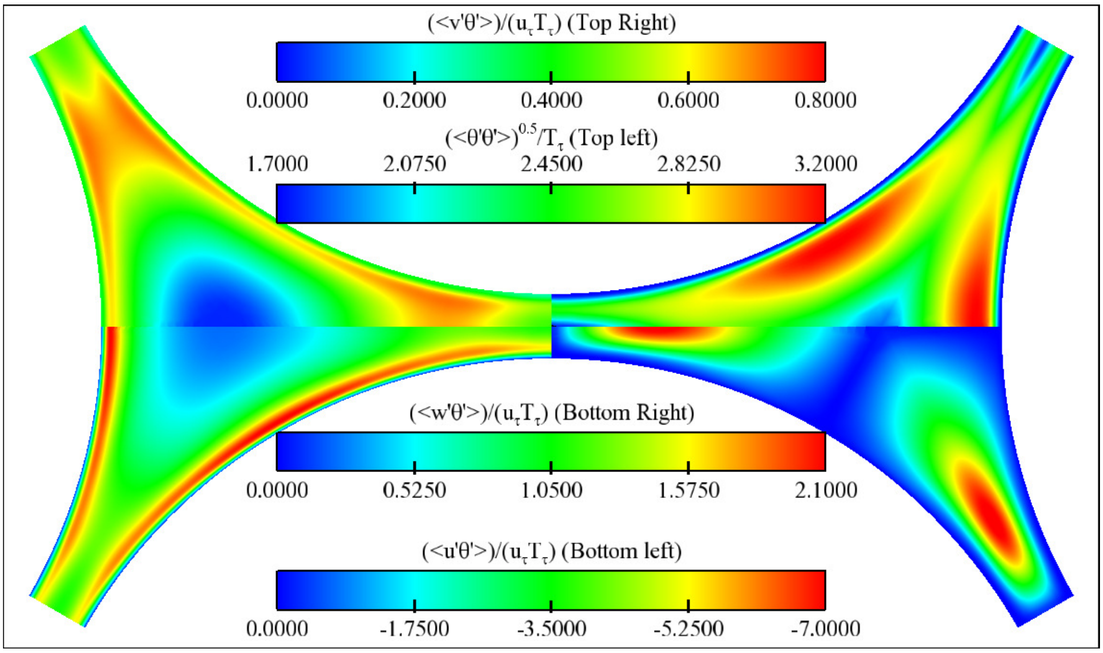

Figure 6.29: Dimensionless temperature fluctuations and heat fluxes at $Re = 6000$ using a constant heat flux for the rod bundle.

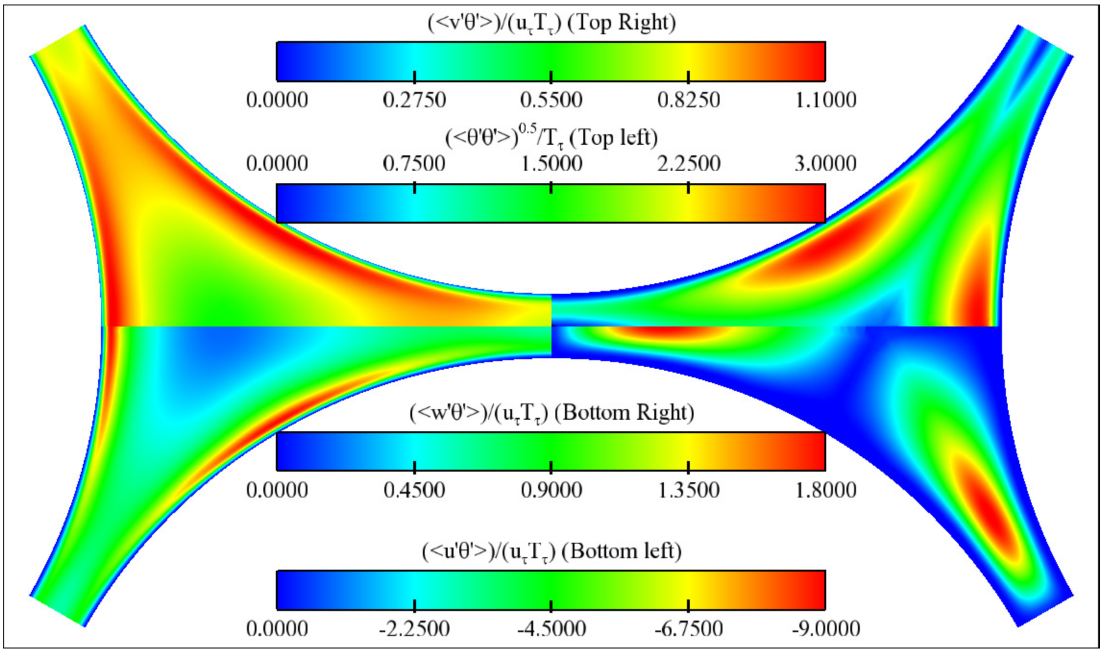

Figure 6.30: Dimensionless temperature fluctuations and heat fluxes at $Re = 6000$ using a constant wall temperature for the rod bundle test case.

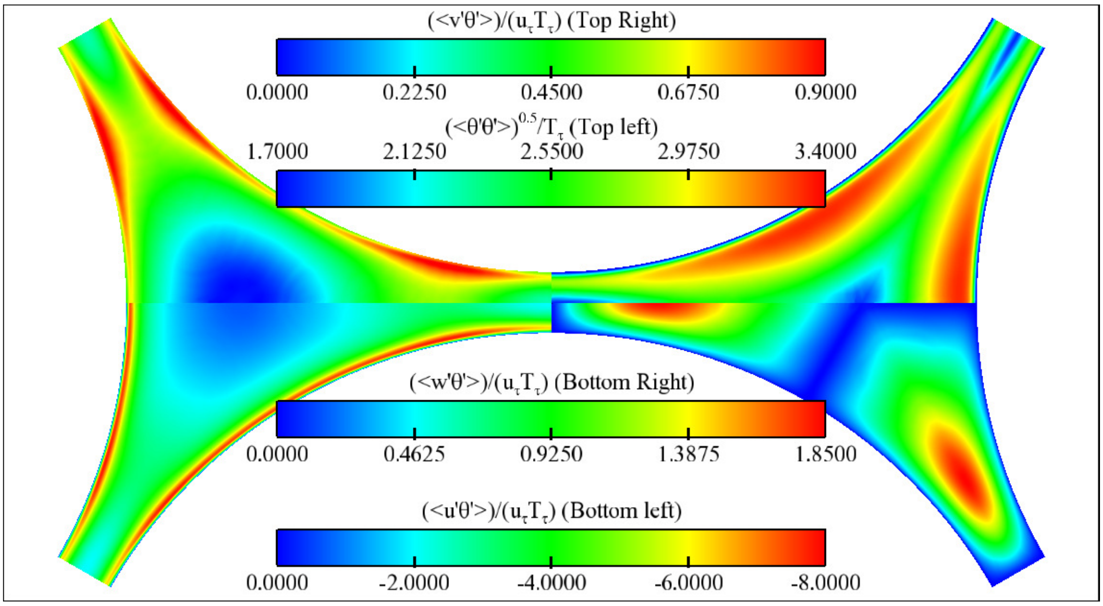

Figure 6.31: Dimensionless temperature fluctuations and heat fluxes at $Re = 13000$ using a constant wall heat flux for the rod bundle test case.

EFFECT OF PRANDTL NUMBER VARIATION

This section presents different thermal fields as a function of the Prandtl number, which varies from 0.01 to 10. The related dimensionless temperature T^+ for the first layer of cells has a wide variation according to the thickness of the thermal boundary layer. This analysis is carried imposing a constant wall temperature (Dirichlet BC). In the case of $Pr = 0.01$ T^+ is varying from 0.008 in the gap to 0.033 in the open, whereas for $Pr = 10$ T^+ varies from 7.8 in the gap to 10.5 in the open. At low Pr number, temperature slope in the wall normal direction is smoothed gradually, whereas at high Pr temperature gradient is mainly concentrated in the near wall region (see Fig. 6.32). Indeed profiles present different trends depending on the Prandtl number: the lower the Prandtl is, the more the temperature profiles are different from one azimuthal location to the next, whereas at high Pr they tend to collapse. This fact might be explained with the variation, as function of the angular direction, of the local friction temperature T_{τ}. At low Pr the wall heat flux q_w has large variation in the angular direction, variation that decreases as the Pr number increases (see Fig. 6.33) . This makes the friction temperature to have a substantial change from the gap to the open region in case of low Pr, whereas it is more uniform at high Pr. The average Nusselt number for the different scalars is reported in Table 6.3.

Re	BC	Pr	$\langle Nu \rangle$	Re	BC	Pr	$\langle Nu \rangle$
6000	Neu.	0.71	20.5	6000	Dir	0.01	6.10
6000	Dir	0.71	20.1	6000	Dir	10.0	56.3
6000	Dir	1.00	23.0	13000	Neu	0.71	37.6
6000	Dir	0.1	9.30				

Table 6.3: Average Nusselt as function of Reynolds number Prandtl number and different BC for the rod bundle test case.

Figures 6.34 to 6.37 report contours of temperature variance and heat fluxes as function of the increase of the Prandtl number. Peak values, both positive and negative, increase with the rise of the Prandtl number. For example the maximum value of $\theta^{'+}_{rms}$ moves from 0.2 at $Pr = 0.01$ to 14 at $Pr = 10$. At low Pr fluctuations and heat fluxes are concentrated toward the centre of the sub-channel, in particular temperature fluctuations are close to zero in the gap region ($Pr = 0.01$ see Fig. 6.34). As the Pr number increases heat fluxes become closer to ones described in the above section. At very high Pr number the variation of temperature fluctuations is mainly concentrated at the near wall region, then uniform throughout the domain.

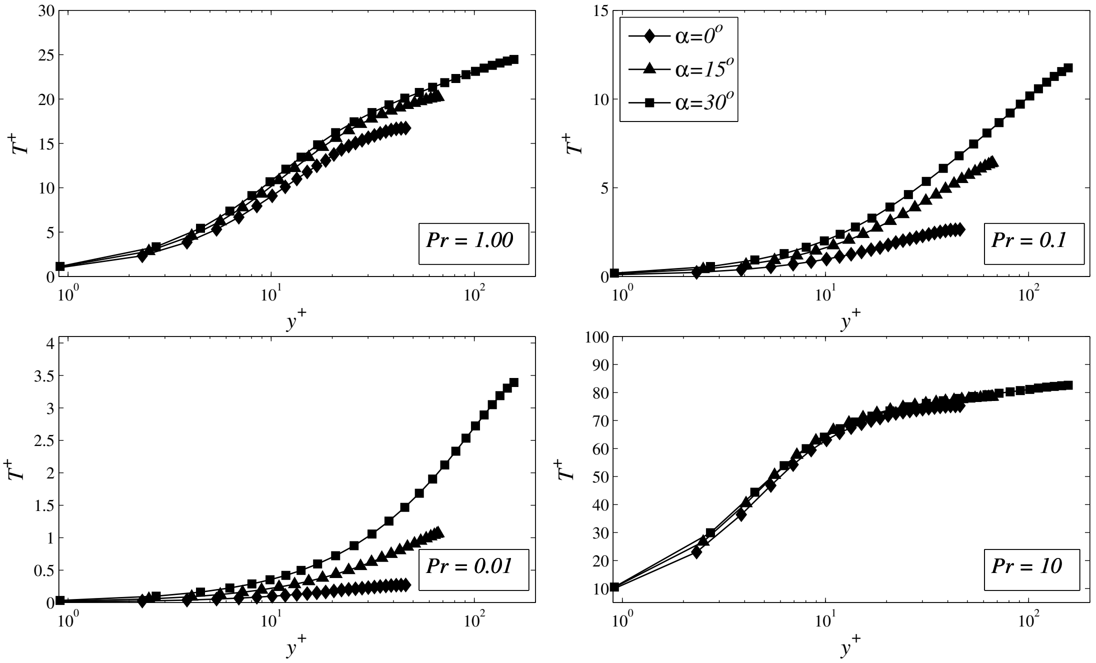

Figure 6.32: Average temperature profiles at different azimuthal location at $Re = 6000$ and for different Prandtl number: $Pr = 1$ top left, $Pr = 0.1$ top right, $Pr = 0.01$ bottom left and $Pr = 10$ bottom right.

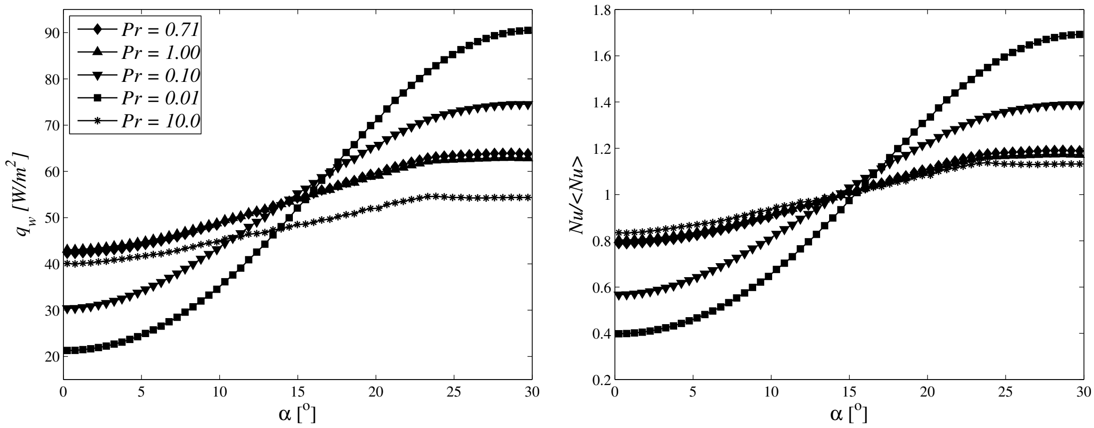

Figure 6.33: Average Nusselt profile (left) and wall heat flux at $Re = 6000$ (right) at the variation of the Prandtl number for the rod bundle test case.

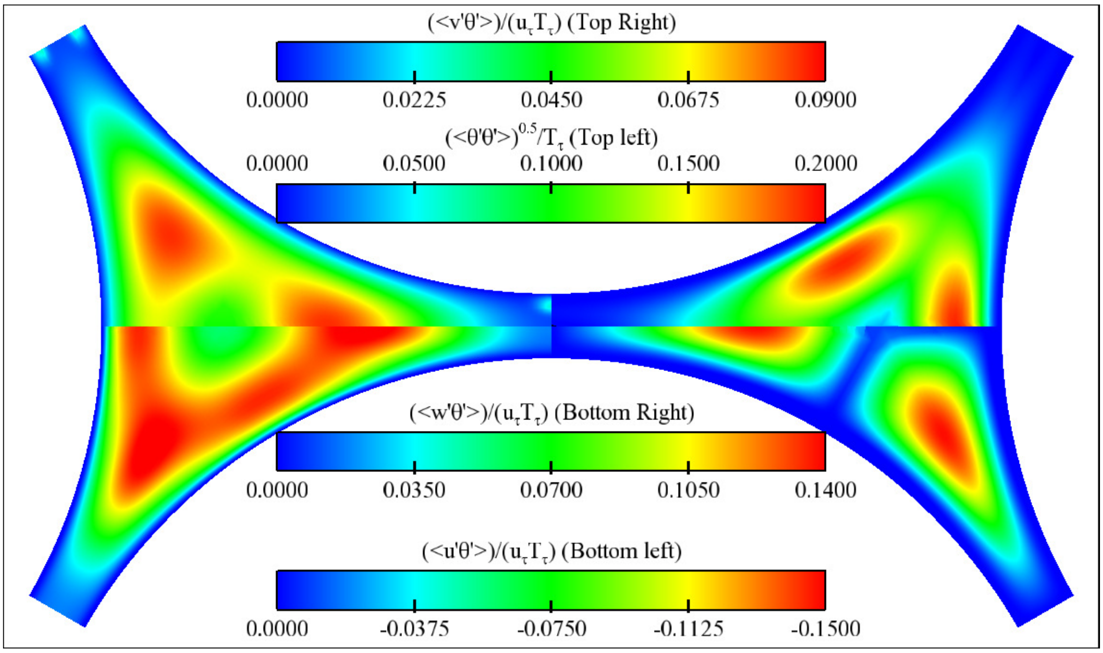

Figure 6.34: Dimensionless temperature fluctuations and heat fluxes at $Re = 6000$ with $Pr = 0.01$ for the rod bundle test case.

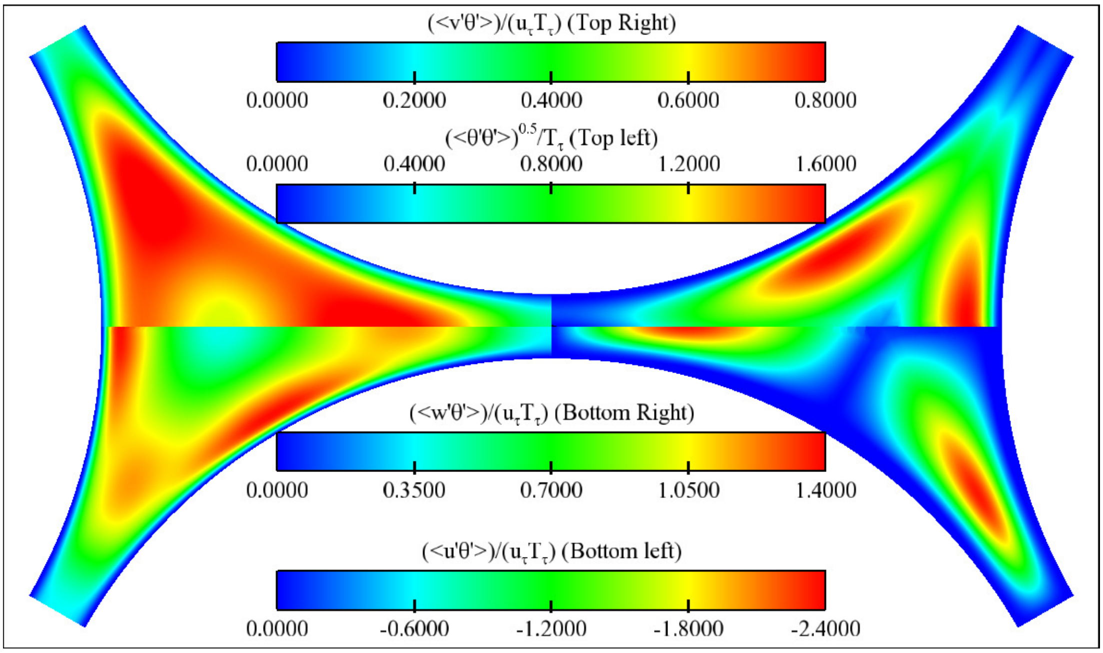

Figure 6.35: Dimensionless temperature fluctuations and heat fluxes at $Re = 6000$ with $Pr = 0.10$ for the rod bundle test case.

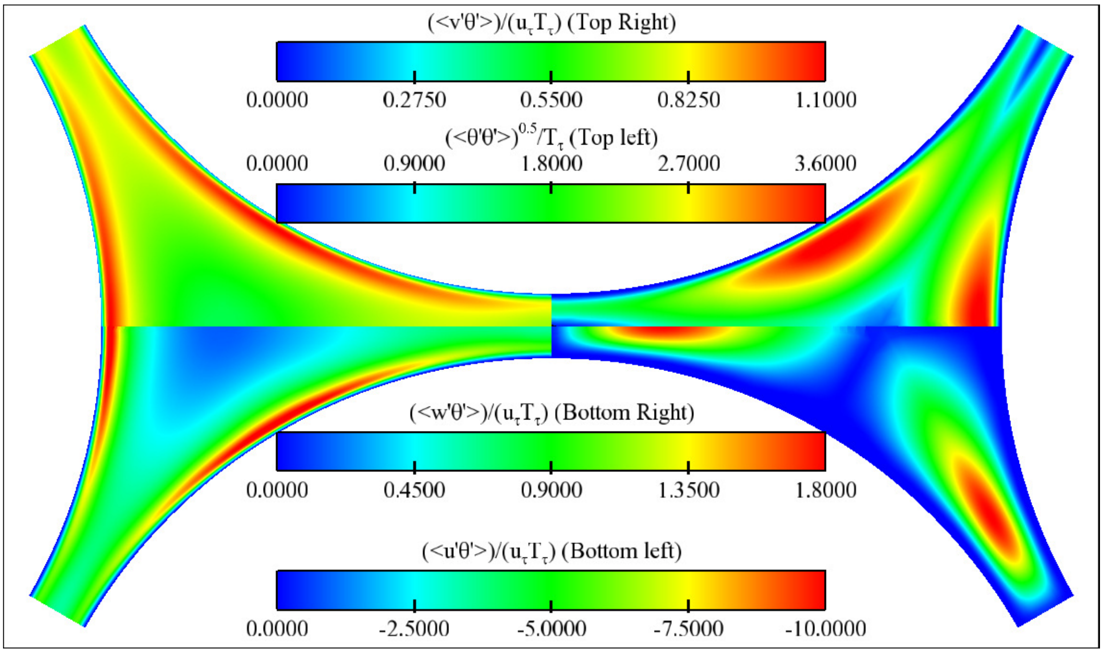

Figure 6.36: Dimensionless temperature fluctuations and heat fluxes at $Re = 6000$ with $Pr = 1.00$ for the rod bundle test case.

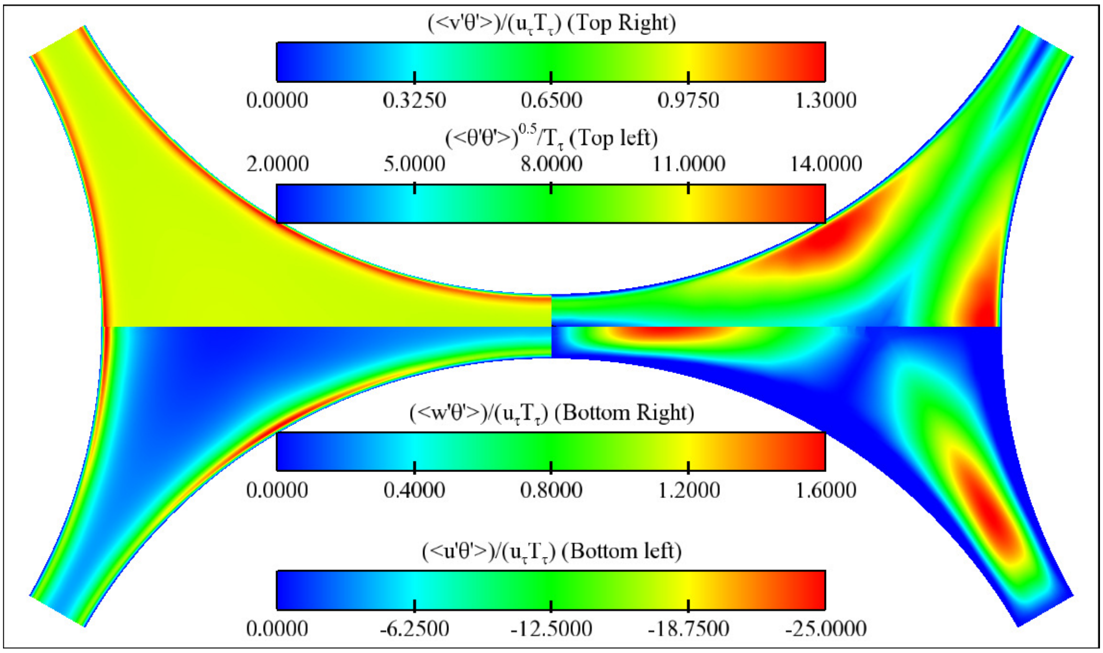

Figure 6.37: Dimensionless temperature fluctuations and heat fluxes at $Re = 6000$ with $Pr = 10.0$ for the rod bundle test case.

6.3.6 Scalar imbalance

A very characteristic concern in nuclear applications is when some imbalances, for example of temperature, are present in the cross section of a fuel rod bundle. The main interest is the variation of the fluxes in order to re-establish a uniform configuration. For this purpose a specific source term is designed to be zero at the wall and edges of a sub-channel, and maximum at the centre (see Fig. 6.38). This makes the bulk contribution of the source term, to the scalar balance, equal to zero, and correspond to a situation where a sub-channel, with positive source in the centre, is surrounded by negative sources or sink and vice-versa. This source term being anti-symmetric with respect to the symmetry line still allows generating fluxes in the gap region. This configuration is unlike to happen, but can provide some useful insights about heat fluxes variation. Moreover the influence of flow pulsations, on the inter-channels mixing, can be also investigated.

Results are shown in Figs. 6.39 and 6.40. In the first case a constant heat flux at the wall is imposed and equal to $54\,W/m^2$, in the second an adiabatic BC is instead employed.

The comparison between Fig. 6.39 with Fig. 6.40 shows some interesting features of the new thermal field. Despite the fact that the maximum of the additional source term is at most 15% of the global source term, temperature fluctuations are changing from the range $1.7-3.2$ to $1.4-6.5$. The peak is located in the gap region toward the channel characterized by the positive part of the additional source term. Also $\langle u'\theta'\rangle^+$ has a large degree of change: the maximum value has an increase of about 30% and it is located in the gap region, whereas, in the homogeneous case, it is close to the wall in the open region. The effect of the flow pulsations, i.e. enhancing the mixing between the sub-channels, is clear from $\langle w'\theta'\rangle^+$. The flux is clearly showing a path from the cold to the hot region (left to right).

The case with adiabatic wall confirms the results described above (Fig. 6.40). Results are made dimensionless using the friction temperature T_τ from the case with heated wall, because, by definition, the friction temperature of the case is equal to zero[11]. In this case the scalar variance is symmetric, whereas the fluxes are anti-symmetric. Fluxes are active in particular in the gap region as sign of an intense activity of exchange between sub-channels. It is interesting to notice that the temperature variation, with respect to the bulk, is of the order of 1%, but this produces temperature fluctuations from four to five times larger than correspondent homogeneous case with constant wall heat flux.

---

[11] In this case the wall heat flux $q_W = 0$, therefore also the friction temperature T_τ is equal to zero.

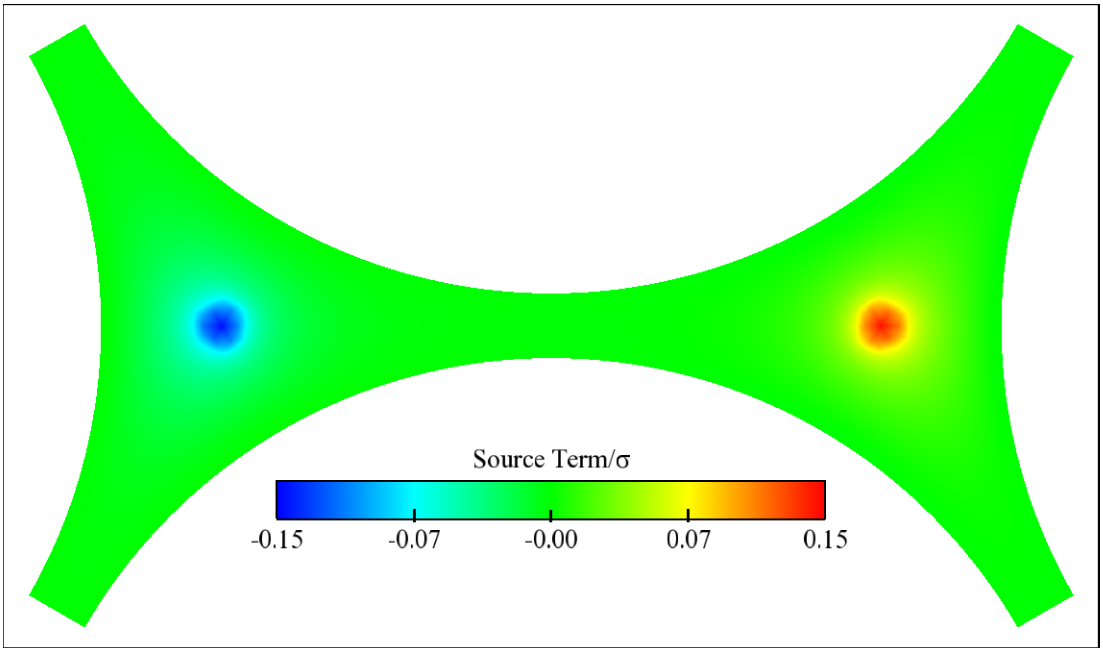

Figure 6.38: Contours of the source term used for the imbalance of scalar in the rod bundle test case. The amplitude is divided by σ, which represent the variation of bulk temperature in the stream-wise direction (Eq. (6.10)).

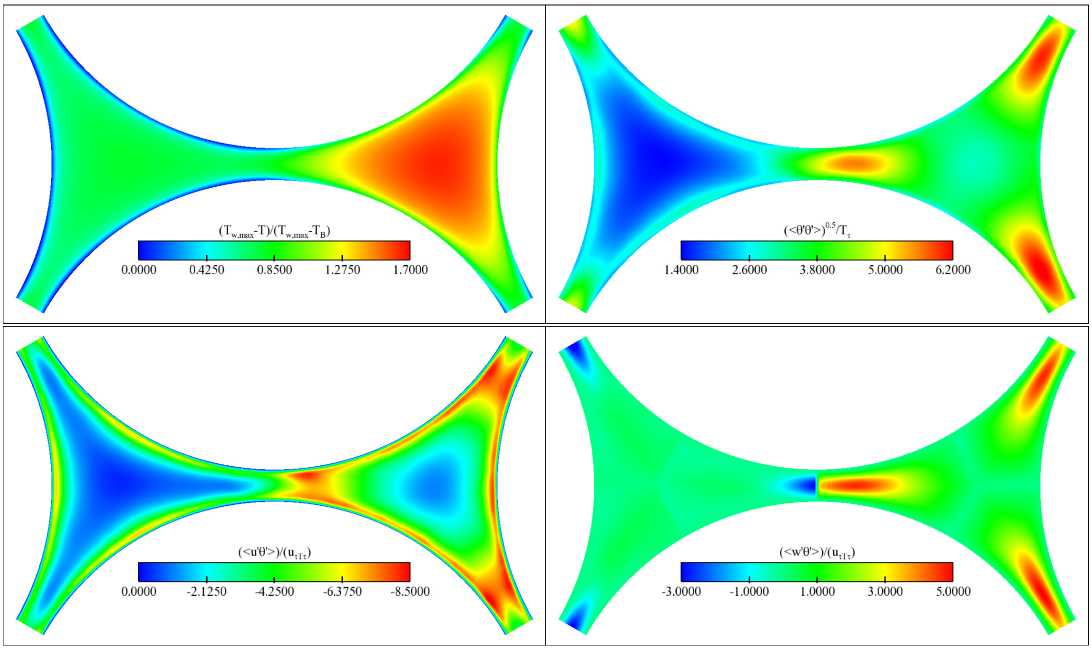

Figure 6.39: Dimensionless temperature (top left), variance (top right), $\langle u'\theta' \rangle^+$ (bottom left), $\langle v'\theta' \rangle^+$ (bottom right) for the case of scalar imbalance with constant wall heat flux for the rod bundle test case.

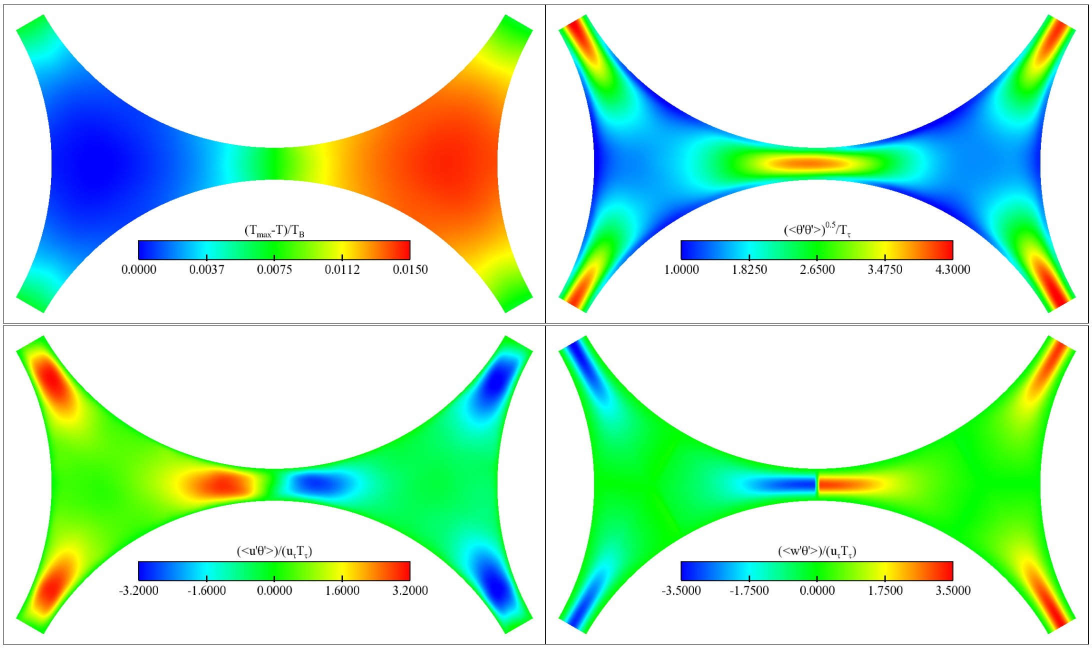

Figure 6.40: Dimensionless temperature (top left), variance (top right), $\langle u'\theta'\rangle^+$ (bottom left), $\langle v'\theta'\rangle^+$ (bottom right) for the case of scalar imbalance with adiabatic wall for the rod bundle test case. Because no heat flux is applied at the wall and the consequent shear temperature is equal to zero the T_τ of the case with constant heat flux is used to make the quantities dimensionless.

6.4 CONCLUSIONS

In this chapter the flow inside a fuel rod bundle is investigated using wall resolved LES. It is shown that more than 80% of the total energy, everywhere in the domain, is resolved, which is a necessary, but possibly not sufficient, condition for reliable results. However the sum of the terms in budget of the kinetic energy is close enough to zero, on a scale comparable with the magnitude of the production or dissipation terms, and all symmetries are well respected, which indicates sufficient statistical sampling even for large and rare events (particularly reflected by turbulent transport terms).

The secondary motion is captured at both Reynolds numbers and its intensity is equal to 0.41% the bulk velocity at $Re = 6,000$ and 0.24% at $Re = 13,000$. This last intensity seems low and might be underestimated due to the cell stretching in the stream-wise direction. The importance of the secondary motion, in the prediction of the wall shear stress, is a well-known fact, but not an easy feature to reproduce because of the extreme weakness of the vortices. All shear stress coefficient profiles are comparable with the experimental results although only qualitatively since the Reynolds number is sensibly higher. This comparison is difficult because flows with weak secondary motion, can be highly sensitive to the variation of the Reynolds number. The comparison with the DNS found in the literature is instead not very satisfactory. The DNS is showing a very steep variation from the gap to the open region, which is surprising. Such profile for the shear stress was seen in literature only when a RANS eddy viscosity model was employed, which does not capture the secondary motion. Indeed the DNS results show some contradictions with respect to the experimental results. For example the DNS reports flatter profiles of the wall shear stress as the P/D increases, whereas the experiments show an opposite trend.

Non-dimensional velocity profiles are collapsing on each other at different azimuthal locations and on the logarithmic law is in accordance with the experiments of Krauss and Meyer (1998).

The second important feature of the flow is the so-called flow pulsations, which are clearly captured in this work. Three dominant frequencies are found in the spectra for all Reynolds numbers, and their Strouhal number is consistent across all runs. The first dominant frequency is in agreement with the value given by the experiment of Krauss and Meyer (1998), whereas the two higher values are not reported. The extra frequency might be attributed to the rather limited cross section of the domain, but the bigger computational domain is also exhibiting the same phenomenon. Frequency analysis shows that the azimuthal velocity between inlet and middle of the geometry is still highly correlated and verification against even longer geometry would need to be tested.

The effect of the flow pulsations largely modifies the turbulence quantities, as it is clearly visible from the Reynolds stresses profiles. Reynolds stresses with at least one component in the azimuthal direction display unusual behaviour: they are predominantly active in the gap region and their peak value is located away from the wall. The intensity of $\langle u'w' \rangle^+$ is of the same order as or larger than the mainstream-to-wall shear stress $\langle u'v' \rangle^+$. Budgets of turbulent kinetic energy and Reynolds stresses confirm the "turbulent activity" of the gap region; in particular turbulent transport in the area is comparable with the one near the wall in the open region. In the case of $\langle u'w' \rangle$ and $\langle v'w' \rangle$ the production is mainly concentrated in the gap region and not in the open region close to the wall as for the other components.

Temperature profiles, when made dimensionless, also collapse on the "Log-law", but only in the case of a Neumann BC (imposed wall heat flux). The difference of BC produces also differences in the Nusselt profiles, in particular in the open region, for heat fluxes and temperature variance. The change on BC affects mainly the peak values of the heat fluxes, whereas profiles present similar features. Temperature variance also presents very similar trends, with the exception of the wall values, which go to zero in the case of Dirichlet BC and tend to a constant value in the case of Neumann BC.

The variation of the Prandtl number has also a large impact on the thermal field. As the Prandtl number increases temperature profiles tend to collapse, whereas low values display a large degree of change as the azimuthal angle increases. The same variation is also shown by the Nusselt profiles. Fluxes maxima tend to move toward the centre of the channel as the Prandtl decreases and peak values increase with the Prandtl. Temperature variance has a vast dependency on the Prandtl, for the present low Re numbers. At low value it tends to zero in the gap region and maximum value is located at about $\alpha = 25^o$, toward the centre of the channel. At high Prandtl number the maximum is located close to the wall, for all the azimuthal locations, and a uniform value is found in most of the domain.

In the case of non-homogeneous scalar distribution, heat fluxes show an increase of the mixing across the sub-channels, in particular peak values, in the gap region, show a large increase.

Chapter 7

CONCLUSIONS AND FUTURE WORK

This thesis has described the application of LES to test cases of nuclear interest under the framework of a finite volume unstructured code. The work can be divided into three main topics: the influence of the mesh quality on a LES calculation; the application of LES to flow in fuel rod bundles; the development of a Hybrid RANS/LES model with the addition of heat transfer modelling. This PhD thesis has been conducted in the framework of the KNOO project (Keeping the Nuclear Option Open), a five-year initiative sponsored by EPSRC in order to enhance research in the nuclear related applications.

7.1 MAJOR CONTRIBUTIONS

APPLICATION OF UNSTRUCTURED MESH TO LES

The first main objective was to provide reliable data for RANS validation using mainly LES methodology. Because of the constraint imposed by solid boundaries, mesh requirements for a wall resolved LES tend toward the resolution required by a DNS calculation, rendering the procedure prohibitively expensive. One option to alleviate the cost of near wall refinements is to use embedded meshes. The use of hanging nodes introduces some non-orthogonalities in the mesh, which results in a decrease of the conservation properties of the code (see Chapters 4) and introduces spurious oscillations in the solution (see Chapter 5). In the inviscid test case (Taylor-Green vortices), conservation properties with respect to a conformal structured mesh are recovered for unstructured meshes, reducing the level of non-orthogonalities, and this has been achieved by using specific sub-patterns at the interface between coarse and refined mesh areas (i.e. a $3-4$ sub-pattern). On the other hand in 3D fully turbulent flow (channel flow), the best results are obtained from embedded meshes with worst orthogonality (TAYLOR mesh). The

RR075 grid displays an oscillatory behaviour of the Reynolds stresses and in particular of the shear stress $\langle u'v' \rangle^+$. In addition pressure transfer in $\langle v'v' \rangle^+$ and turbulent diffusion in $\langle u'u' \rangle^+$ budgets also display oscillatory behaviour. In both the test cases considered the spurious oscillation problem could be ascribed to the velocity fluctuations in the wall normal direction v'. The channel flow performed on the TAYLOR mesh shows that averaging in time and space, along homogeneous directions, may result in an error cancellation, but this positive effect is not always present and is highly dependent from the mesh configuration. The use of locally blended Up-Wind convective scheme, activated when a slope test on the gradient fails (see Section 3.2.2), does not alleviate the problem. On the other hand the modified convective scheme helps to maintain a stable solution and avoid unphysical phenomena (i.e. increase of the total kinetic energy in the Taylor-Green vortices performed with very skewed polyhedral meshes).

Fuel Rod Bundles

The second objective of this work was to build a reliable data-set for RANS validation using LES. In order to minimize the uncertainty in the use of embedded mesh refinements, the test case of the fuel rod bundle has been investigated using a structured conformal mesh. The flow is characterised by so-called flow pulsations: coherent structures flowing in the streamwise direction are observed in the gap region. The phenomenon is characterised by a constant Strouhal number and numerical results presented herein agree well with what is reported in experiments. Spectral analysis reveals two unexpected higher frequencies, with Strouhal numbers equal to 2 and 3 respectively. In the first instance the origin of these two unexpected frequencies was attributed to the small extension of the cross section, but comparison using a larger domain reveals the same phenomenon. Two-point correlations show that azimuthal velocity between “inlet” and centre of the domain remain highly correlated and verifications employing a longer domain in the streamwise direction are ongoing.

The effect of the flow pulsations largely modifies the Reynolds stresses with at least one component in the azimuthal direction: they are predominantly active in the gap region and their peak value is located away from the wall.

Results show the importance of the capture of the secondary motion in order to predict, with high accuracy, the wall shear stress. This is not an easy task because the secondary motion intensity is only around 0.4% of the bulk velocity.

Temperature profiles, when made dimensionless, collapse on the “Log-law”, but only in the case of a Neumann BC (imposed wall heat flux). The difference of boundary conditions produces also differences in the Nusselt number profiles, in particular in the open region, heat fluxes and temperature variance. The change of boundary conditions affects mainly the peak values of the heat fluxes, whereas profiles present similar features. Temperature variance also presents very similar trends, with the exception of the wall values, which go to zero in the case of Dirichlet BC and tend to a constant value in the case of Neumann BC.

The variation of the Prandtl number has also a large impact on the thermal field. As the Prandtl number increases temperature, profiles tend to collapse, whereas low values of the Prandtl number display a large degree of change as the azimuthal angle increases. The same variation is also shown by the Nusselt number profiles. Flux apexes tend to move toward the centre of the channel as the Prandtl number decreases and peak values increase with the Prandtl number. Temperature variance has a large dependency on the Prandtl number, for the present low Reynolds numbers.

In the case of non-homogeneous scalar distribution heat fluxes show an increase of the mixing across the sub-channels, in particular peak values, in the gap region.

HYBRID RANS/LES

As previously noted, mesh requirements dictated by the near wall structures, push up the necessary grid resolution for LES towards that of DNS, making impractical the simulation of high Reynolds number cases. A second possibility to alleviate this constraint is carried out with the introduction of a Hybrid RANS/LES turbulence model. The principal achievement of this thesis is the introduction, in the Hybrid framework, of heat transfer modelling. Indeed the model permits the use not only of coarse meshes, but also a lesser growth rate of the mesh size with the Reynolds number (i.e. proportional to $Re^{1.14}$ instead of the usual $Re^{1.8}$ for LES). On such coarse meshes the model displays good agreement with DNS of mean quantities and Reynolds stresses, while on the other hand heat fluxes and temperature variance are moderately underestimated in the near wall region.

A study on the influence of mesh resolution is also carried out, with the main outcome that in case of fine meshes, the model produces an overestimation of the turbulence, which largely degrades the accuracy of results, due to a double counting of the Reynolds stresses in the near wall region. The blending function is unable to sufficiently reduce the modelled RANS contribution in the near wall region, even where the mesh resolution is adequately small to resolve the very small scales (i.e. a quasi-DNS). Some simple modifications of the blending function are suggested, but they have been proved ineffective. Indeed the definition of the blending is rather arbitrary based on past experiences.

7.2 FUTURE WORK

USE OF UNSTRUCTURED MESH FOR LES

The use of a Green-Gauss reconstruction for the gradient is a necessary but not sufficient condition to have accurate evaluation of the gradient and decrease the negative effects of the non-orthogonality. A possible solution to improve the accuracy of the calculation, without moving to a staggered arrangement or introducing penalty methods is presented in Moulinec and Wesseling (2000), where auxiliary points are created on the line perpendicular to the face and passing through the face centre. The method permits to reconstruct locally the orthogonality and also to avoid cell stretching. The solution is subsequently interpolated from cell centres to the auxiliary points, using for example a bi-linear interpolation. Here, the main problem lies in the creation of a suitable stencil for the extra points, i.e. the cell centres of all extended neighbours[1] could be used. The method would be expected to be beneficial for completely unstructured meshes, in particular in the case of polyhedral meshes. The implementation of this methodology under the framework of *Code_Saturne* is under investigation.

HYBRID RANS/LES

Several aspects of the Hybrid RANS/LES model can be improved in order to correct some of the deficiencies reported.

- The $\varphi - \overline{f}$ model used for the anisotropic contribution (see Section A.1.1) can be replaced by the $\varphi - \alpha$ model of Billard et al. (2008) (see Section A.1.2). The main advantage is the introduction of the blending parameter α, evaluated using an elliptic equation. In the formulation of this model α is used to spilt the elliptic relaxation factor f into homogeneous and near wall components. In the context of the Hybrid RANS/LES approach α can be used as base parameter in order to produce a new definition of the blending function, thereby avoiding the use of arbitrary, a priori formulation. A second advantage is that a priori RANS calculations, carried out with the $\varphi - \alpha$ model, can be used to provide a rough estimation of the blending function. Consequently the mesh generation stage is facilitated and the double counting of the Reynolds stresses can be avoided by stretching the grid in areas where RANS is performed.

- Another modus operandi to approach the blending between RANS and LES would be the introduction of a subgrid-scale energy transport model (k_{SGS}) in order to provide a mesh independent blending function. For instance the switch from RANS to LES will be allowed only when $k_{SGS} < 20\%\ k_{RANS}$ (i.e. the resolved

---

[1] Extended neighbours: cells which are sharing at least one cell vertex, even if not sharing a face.

turbulent kinetic energy is more than 80% of the total). A similar definition of blending parameter as ratio between resolved and total turbulent kinetic energy, but inserted in the framework of LES seen as a Hybrid DNS/RANS filter, is presented in Germano and Sagaut (2006).

- In the actual formulation of the Hybrid model the RANS velocity field is obtained from a running average applied to the instantaneous field. This imposes a mesh constraint in the wall normal direction because the RANS model requires the first cell centre to be placed at $y^+ \approx 1$. This imposes the usage of an expansion ratio in the wall normal direction in order to cluster cells close to the wall. As a consequence cells away from the wall, where mainly LES is performed, may not be isotropic. Two very different and opposing constraints to the mesh generation can therefore be identified: the inherent need for isotropic cells in the LES part of the domain, and the near wall refinement, in the wall normal direction required by the low RANS model. A possible solution to simultaneously meets both requirements could be the usage of over-set or CHIMERA grids (see Section 3.1). Two separated velocity fields can be employed and interpolation is used to pass information between domains. Each domain has its own mesh, which is optimized in order to meet the different requirements of the different models. The domain overlapping can be total or only partial. From a modelling point of view the former is preferable because the two domains share only physical boundaries. In the latter interfaces must also be the reconstruction of the fluctuations, moving from the RANS to the LES, is mandatory. This latter configuration might be unavoidable in case of very complex geometries like in the test case presented in Appendix D.

- The Smagorinsky model, used for the isotropic part of the subgrid stress tensor, can be replaced by Germano's dynamic model (Germano et al. (1991)). The model would expect to benefit from the advantages of this approach (see Section 2.3.3.2) and the same procedure could also be applied to the heat transfer modelling as presented in Moin et al. (1991), so as to make the turbulent Prandtl number for the LES part $Pr_{t,\gamma}$ function of time and space.

- Improvement of the RANS heat transfer modelling could also be implemented; one very effective solution is presented by Hanjalic et al. (1996), where the turbulent heat fluxes are modelled using an algebraic expression. Results show a significant improvement of the results with respect to a simple gradient diffusion hypothesis. The model is incorporated into an elliptic relaxation framework in Kenjeres et al. (2005) using a five equations $k - \varepsilon - \overline{v^2} - f - \overline{\theta^2}$ model.

Bibliography

Abe, H., H. Kawamura, and Y. Matsuo (2001). Direct Numerical Simulation of a Fully Developed Turbulent Channel Flow With Respect to the Reynolds Number Dependence. *Journal of Fluids Engineering 123*(2), 382–393.

Abe, H., H. Kawamura, and Y. Matsuo (2004). Surface heat-flux fluctuations in a turbulent channel flow up to Re_τ=1020 with Pr=0.025 and 0.71. *International Journal of Heat and Fluid Flow 25*(3), 404 – 419. Turbulence and Shear Flow Phenomena (TSFP-3).

Abe, K. (2005). A hybrid LES/RANS approach using an anisotropy-resolving algebraic turbulence model. *International Journal of Heat and Fluid Flow 26*(2), 204 – 222.

Addad, Y. (2004). *Large Eddy Simulations of Bluff Body, Mixed and Natual Convection Turbulent Flows with Unstructured FV Codes.* Ph. D. thesis, University of Manchester Institute of Science and Tecnology.

Addad, Y., U. Gaitonde, D. Laurence, and S. Rolfo (2008). Optimal Unstructured Meshing for Large Eddy Simulations. In J. Meyers, B. J. Geurts, and P. Sagaut (Eds.), *Quality and Reliability of Large-Eddy Simulations*, pp. 93 – 103. Springer Netherlands.

Ahn, H. T. and Y. Kallinderis (2006). Strongly coupled flow/structure interactions with a geometrically conservative ale scheme on general hybrid meshes. *Journal of Computational Physics 219*(2), 671 – 696.

Archambeau, F., N. Mechitoua, and M. Sakiz (2004). Code_Saturne: a finite volume code for the computation of turbulent incompressible flows - Industrial Applications. *Int. J. Finite Vol. 1*(1).

Baggett, J. S. (1997). Some modeling requirements for wall models in Large Eddy Simulation. *Center for Turbulence Research Annual Research Briefs*, 3 – 14.

Baggett, J. S. (1998). On the feasibility of merging LES with RANS for the near-wall region of attached turbulent flows. *Center for Turbulence Research Annual Research Briefs*, 267 – 277.

Baglietto, E. and H. Ninokata (2005). A turbulence model study for simulating flow inside tight lattice rod bundles. *Nuclear Engineering and Design 235*(7), 773 – 784.

Baglietto, E., H. Ninokata, and T. Misawa (2006). CFD and DNS methodologies development for fuel bundle simulations. *Nuclear Engineering and Design 236*(14-16), 1503 – 1510. 13th International Conference on Nuclear Energy, 13th International Conference on Nuclear Energy.

Baker, T. J. (2005). Mesh generation: Art or science? *Progress in Aerospace Sciences 41*(1), 29 – 63.

Bardina, J., J. H. Ferziger, and W. H. Reynolds (1983). Improved turbulence models based on large eddy simulation of homogeneous, incompressible turbulent flows. *Report TF-19*.

Bartzis, J. and N. Todreas (1979). Turbulence modelling of axial flow in a bare rod bundle. *Journal of Heat Transfer 101*(4), 628–634.

Batchelor, G. K. (1959). Small-scale variation of convected quantities like temperature in turbulent fluid Part 1. General discussion and the case of small conductivity. *Journal of Fluid Mechanics Digital Archive 5*(01), 113–133.

Benhamadouche, S. (2006). *Large Eddy Simulation with the unstructured collocated arrangement.* Ph. D. thesis, The University of Manchester.

Benhamadouche, S. and D. Laurence (2002). Global kinetic energy conservation with unstructured meshes. *International Journal for Numerical Methods in Fluids 40*(3-4), 561 – 571.

Biemuller, M., L. Meyer, and K. Rehme (1996). Large eddy simulation and measurement of the structure of turbulence in two rectangular channels connected by a gap. In *Eng. Turbul. Model. Exp. 3*, pp. 249–258.

Billard, F., J. Uribe, and D. Laurence (2008). A new formulation of the $\overline{v^2} - f$ model using elliptic blending and its application to heat transfer prediction. In *Proceedings of the* 7^{th} *International Symposium on Engineering Turbulence Modelling and Mesurements*, pp. 89–94.

Bubelis, E. and M. Schikorr (2008). Review and proposal for best fit of wire-wrapped fuel bundle friction factor and pressure drop predictions using various existing correlations. *Nuclear Engineering and Design 238*(12), 3299–3320.

Celik, I., Z. N. Cehreli, and I. Yavuz (2005). Index of Resolution Quality for Large Eddy Simulations. *Journal of Fluids Engineering 127*(5), 949–958.

Celik, I., M. Klein, and J. Janicka (2009). Assessment Measures for Engineering LES Applications. *Journal of Fluids Engineering 131*(3), 031102.

Chang, D. and S. Tavoularis (2005). Unsteady Numerical Simulations of Turbulence and Coherent Structures in Axial Flow Near a Narrow Gap. *Journal of Fluids Engineering 127*(3), 458–466.

Chang, D. and S. Tavoularis (2007). Numerical simulation of turbulent flow in a 37-rod bundle. *Nuclear Engineering and Design 237*(6), 575 – 590.

Cheng, S. and N. Todreas (1986). Hydrodynamic models and correlations for bare and wire-wrapped hexagonal rod bundles–bundle friction factors, subchannel friction factors and mixing parameters. *Nuclear Engineering and Design 92*(2), 227–251.

Cheng, X. and N. Tak (2006). CFD analysis of thermal-hydraulic behavior of heavy liquid metals in sub-channels. *Nuclear Engineering and Design 236*(18), 1874 – 1885.

Chesshire, G. and W. Henshaw (1990). Composite overlapping meshes for the solution of partial differential equations. *Journal of Computational Physics 90*(1), 1 – 64.

Chung, T. J. (1978). *Finite element analysis in fluid dynamics.* McGraw-Hill International Book Co., New York :.

Corrsin, S. (1951). On the Spectrum of Isotropic Temperature Fluctuations in an Isotropic Turbulence. *Journal of Applied Physics 22*(4), 469–473.

Davidson, L. and M. Billson (2006). Hybrid LES-RANS using synthesized turbulent fluctuations for forcing in the interface region. *International Journal of Heat and Fluid Flow 27*(6), 1028 – 1042.

Davidson, L. and S. Dahlstrom (2005). Hybrid LES-RANS: An approach to make LES applicable at high Reynolds number. *International Journal of Computational Fluid Dynamics 19*(6), 415 – 427.

Davidson, L. and S. H. Peng (2003). Hybrid LES-RANS modelling: a one-equation SGS model combined with a k-omega model for predicting recirculating flows. *International Journal for Numerical Methods in Fluids 43*(9), 1003 – 1018.

Deardorff, J. W. (1970). A numerical study of three-dimensional turbulent channel flow at large Reynolds numbers. *Journal of Fluid Mechanics Digital Archive 41*(02), 453–480.

del Alamo, J. C. and J. Jimenez (2003). Spectra of the very large anisotropic scales in turbulent channels. *Physics of Fluids 15*(6), L41–L44.

Durbin, P. (1991). Near-wall turbulence closure modeling without "damping functions". *Theoretical and Computational Fluid Dynamics 3*(1), 1–13.

Durbin, P. (1995). Separated flow computations with the $k - \varepsilon - v^2$ model. *AIAA journal 33*(4), 659–664.

Engel, F., R. Markley, and A. Bishop (1979). Laminar transition and turbulent parallel flow pressure drop across wire-wrap-spaced rod bundles. *Nucl Sci Eng* (2), 290–296.

Eriksson, S. and J. Nördstrom (2009). Analysis of the order of accuracy for node-centered finite volume schemes. *Applied Numerical Mathematics In Press, Corrected Proof*, –.

Ern, A. and J.-L. Guermond (2004). *Theory and Practice of Finite Elements.* Springer.

Ferziger, J. H. and M. Peric (1997). *Computational Methods for Fluid Dynamics.* Springer.

Fischer, P., J. Lottes, A. Siegel, and G. Palmiotti (2007). Large Eddy Simulation of wire-wrapped fuel pins I: Hydrodynamics in a Periodic Array. In *Joint International Topical Meeting on Mathematics & Computation and Supercomputing in Nuclear Applications (M&C+ SNA 2007), Monterey, California.* Citeseer.

Fröhlich, J. and D. von Terzi (2008). Hybrid LES/RANS methods for the simulation of turbulent flows. *Progress in Aerospace Sciences 44*(5), 349 – 377.

F.S. Lien, P. D. (1996). Non-linear $k - \varepsilon - v^2$ modeling with application to high-lift. *Center for Turbulence Research Annual Research*, 5–26.

Gajapathy, R., K. Velusamy, P. Selvaraj, P. Chellapandi, and S. Chetal (2007). CFD investigation of helical wire-wrapped 7-pin fuel bundle and the challenges in modeling full scale 217 pin bundle. *Nuclear Engineering and Design 237*(24), 2332–2342.

George, P. and H. Borouchaki (1998). *Delaunay triangulation and meshing.* Paris: Editions Hermes.

Germano, M. (1992). Turbulence: the filtering approach. *Journal of Fluid Mechanics Digital Archive 238*(-1), 325–336.

Germano, M. (1999). From RANS to DNS: toward a bridging model. In P. R. Voke, N. D. Sandham, and L. Kleiser (Eds.), *Proceedings Direct and Large-Eddy Simulation III*, pp. 225 – 236. Springer Netherlands.

Germano, M. (2004). Properties of the hybrid RANS/LES filter. *Theoretical and Computational Fluid Dynamics 17*(4), 225–231.

Germano, M., U. Piomelli, P. Moin, and W. H. Cabot (1991). A dynamic subgrid-scale eddy viscosity model. *Physics of Fluids A: Fluid Dynamics 3*(7), 1760–1765.

Germano, M. and P. Sagaut (2006). Formal properties of the additive RANS/DNS filter. *Direct and Large-Eddy Simulation VI*, 127–134.

Geurts, B. J. and J. Fröhlich (2002). A framework for predicting accuracy limitations in large-eddy simulation. *Physics of Fluids 14*(6), L41–L44.

Gong, J. and J. Nördstrom (2007). A stable and efficient hybrid scheme for viscous problems in complex geometries. *Journal of Computational Physics 226*(2), 1291 – 1309.

Graber, H. and M. Rieger (1972). Experimentelle Untersuchung des Warmeubergangs an Flus- sigmetall (NaK) in parallel durchstromten Rohrbundeln bei konstanter und exponentieller Warmeflussdichteverteilung. In *Atomkernenergie*, Volume 19.

Grotjans, H. and F. Menter (1998). Wall functions for general application CFD codes. *Computational fluid dynamics'98*, 1112–1117.

Grötzbach, G. (1979). Numerical investigation of radial mixing capabilities in strongly buoyancy-influenced vertical, turbulent channel flows. *Nuclear Engineering and Design 54*(1), 49 – 66.

Grötzbach, G. and U. Schumann (1979). Direct numerical simulation of turbulent velocity, pressure, and temperature-fields in channel flows. *Turbulent Shear Flows I*, 370–85.

Ham, F. (2008). Improved scalar transport for unstructured finite volume methods using simplex superposition. *Center for Turbulence Research Annual Research Briefs*, 347 – 358.

Ham, F. and G. Iaccarino (2004). Energy conservation in collocated discretization schemes on unstructured meshes. *Center for Turbulence Research Annual Research Briefs*, 3 – 14.

Ham, F., K. Mattsson, and G. Iaccarino (2006). Accurate and stable finite volume operators for unstructured flow solvers. *Center for Turbulence Research Annual Research Briefs*, 243 – 261.

Hamba, F. (2003). A hybrid RANS/LES Simulation of turbulent flows. *Theoretical and computational fluid dynamics 16*, 387–403.

Hanjalic, K., S. Kenjeres, and F. Durst (1996). Natural convection in partitioned two-dimensional enclosures at higher Rayleigh numbers. *International Journal of Heat and Mass Transfer 39*(7), 1407 – 1427.

Hayes, M. (1996). Statistical Digital Signal Processing and Modeling, by John Wiley and Sons. *New York*.

Hooper, J. and K. Rehme (1984). Large-scale structural effects in developed turbulent flow through closely-spaced rod arrays. *Journal of Fluid Mechanics 145*, 305–337.

Howard, R. and Y. Addad (2009, April). The effect of different grids and different LES models on turbulence statistics in channel flow. In *Int. Symp. on Convective Heat and Mass Transfer in Sustainable Energy*. ICHMT.

Iaccarino, G. and F. Ham (2005). Automatic mesh generation for LES in complex geometries. *Center for Turbulence Research Annual Research Briefs*, 19 – 30.

Jones, W. and B. Launder (1972). The prediction of laminarization with a two-equation model of turbulence. *International Journal of Heat and Mass Transfer 15*(2), 301 – 314.

Kawamura, H., H. Abe, and Y. Matsuo (1999). DNS of turbulent heat transfer in channel flow with respect to Reynolds and Prandtl number effects. *International Journal of Heat and Fluid Flow 20*(3), 196 – 207.

Kazimi, M. S. and M. D. Carelli (1976). Clinch River Breeder Reactor Plant heat transfer correlation for analysis of CRBRP assemblies. Westinghouse, CRBRP-ARD-0034.

Keating, A., G. D. Prisco, and U. Piomelli (2006). Interface conditions for hybrid RANS/LES calculations. *International Journal of Heat and Fluid Flow 27*(5), 777 – 788. Special issue of the 6th International Symposium on Engineering Turbulence Modelling and Measurements - ETMM6.

Kenjeres, S., S. Gunarjo, and K. Hanjalic (2005). Contribution to elliptic relaxation modelling of turbulent natural and mixed convection. *International Journal of Heat and Fluid Flow 26*(4), 569 – 586. CHT'04.

Kim, J., P. Moin, and R. Moser (1987). Turbulence statistics in fully developed channel flow at low Reynolds number. *Journal of Fluid Mechanics 177*(1), 133–166.

Kolmogorov, A. N. (1941a). Energy dissipation in locally isotropic turbulence. In *Doklady AN SSSR*, Volume 32, pp. 19–21.

Kolmogorov, A. N. (1941b). On degeneration of isotropic turbulence in an incompressible viscous liquid. In *Dokl. Akad. Nauk SSSR*, Volume 31, pp. 538–540.

Kolmogorov, A. N. (1941c). The Local Structure of Turbulence in Incompressible Viscous Fluid for Very Large Reynolds' Numbers. In *Dokl. Akad. Nauk SSSR*, Volume 30, pp. 301–305.

Kolmogorov, A. N. (1962). A refinement of previous hypotheses concerning the local structure of turbulence. *J. Fluid. Mech 13*, 83–85.

Kolmogorov, A. N. (1991). *Selected works of A. N. Kolmogorov. Vol. I*, Volume 25 of *Mathematics and its Applications (Soviet Series)*. Dordrecht: Kluwer Academic Publishers Group. Mathematics and mechanics, With commentaries by V. I. Arnold, V. A. Skvortsov, P. L. Ulyanov et al, Translated from the Russian original by V. M. Volosov, Edited and with a preface, foreword and brief biography by V. M. Tikhomirov.

Krauss, T. and L. Meyer (1998). Experimental investigation of turbulent transport of momentum and energy in a heated rod bundle. *Nuclear Engineering and Design 180*(3), 185 – 206.

Kravchenko, A. G., P. Moin, and R. Moser (1996). Zonal Embedded Grids for Numerical Simulations of Wall-Bounded Turbulent Flows. *Journal of Computational Physics 127*(2), 412 – 423.

Laurence, D. R., J. C. Uribe, and S. V. Utyuzhnikov (2005). A robust formulation of the v2-f model. *Flow, Turbulence and Combustion 73*(3), 169–185.

Lee, K. B. and H. C. Jang (1997). A numerical prediction on the turbulent flow in closely spaced bare rod arrays by a nonlinear $k - \varepsilon$ model. *Nuclear Engineering and Design 172*(3), 351 – 357.

Lee, K. D., M. Huang, Y. N. J., and R. P. E. (1980). Grid generation for general three-dimensional configurations. In *Proceedings of the NASA Langley workshop on numerical grid generation techniques* (Langley ed.). Springer Netherlands.

Lexmond, A. S., R. F. Mudde, and M. Van der Haagen (2005). Visualization of the vortex street and characterization of the cross flow in the gap between two subchannels. In *Proceedings of the 11th Nureth Avignon, France.*

Liang, C. and G. Papadakis (2007). Large eddy simulation of pulsating flow over a circular cylinder at subcritical Reynolds number. *Computers & Fluids 36*(2), 299 – 312.

Liang, C., G. Papadakis, and X. Luo (2009). Effect of tube spacing on the vortex shedding characteristics of laminar flow past an inline tube array: A numerical study. *Computers & Fluids 38*(4), 950 – 964.

Lilly, D. K. (1992). A proposed modification of the Germano subgrid-scale closure method. *Physics of Fluids A: Fluid Dynamics 4*(3), 633–635.

Mahesh, K., G. Constantinescu, and P. Moin (2004). A numerical method for large-eddy simulation in complex geometries. *Journal of Computational Physics 197*(1), 215 – 240.

Mayer, G., J. Páles, and G. Házi (2007). Large eddy simulation of subchannels using the lattice Boltzmann method. *Annals of Nuclear Energy 34*(1-2), 140–149.

Menter, F., M. Kuntz, and R. Langtry (2003). Ten years of Industrial experience with the SST model. In K. Hanjalić, Y. Nagano, and M. Tummers (Eds.), *Turbulence, Heat and Mass Transfer 4*.

Merzari, E., H. Ninokata, and E. Baglietto (2008). Numerical simulation of flows in tight-lattice fuel bundles. *Nuclear Engineering and Design 238*(7), 1703 – 1719.

Meyers, J. and P. Sagaut (2007). Is plane-channel flow a friendly case for the testing of large-eddy simulation subgrid-scale models? *Physics of Fluids 19*, 048105.

Meyers, J., P. Sagaut, and B. J. Geurts (2006). Optimal model parameters for multi-objective large-eddy simulations. *Physics of Fluids 18*(9), 095103.

Mikityuk, K. (2009). Heat transfer to liquid metal: Review of data and correlations for tube bundles. *Nuclear Engineering and Design 239*(4), 680 – 687.

Mockett, C., U. Bunge, and F. Thiele (2005). Turbulence Modelling in Application to the Vortex Shedding of Stalled Airfoils. In *Engineering Turbulence Modelling and Experiments 6*, pp. 617 – 626. Amsterdam: Elsevier Science B.V.

Moin, P. and J. Kim (1982). Numerical investigation of turbulent channel flow. *Journal of Fluid Mechanics Digital Archive 118*(-1), 341–377.

Moin, P., K. Squires, W. Cabot, and S. Lee (1991). A dynamic subgrid-scale model for compressible turbulence and scalar transport. *Physics of Fluids A: Fluid Dynamics 3*(11), 2746–2757.

Morris, P. J., L. N. Long, A. Bangalore, and Q. Wang (1997). A Parallel Three-Dimensional Computational Aeroacoustics Method Using Nonlinear Disturbance Equations. *Journal of Computational Physics 133*(1), 56 – 74.

Moulinec, C., S. Benhamadouche, D. Laurence, and M. Peric (2005). LES in a U-Bend Pipe Meshed by Polyhedral Cells. In *Engineering Turbulence Modelling and Experiments 6*, pp. 237 – 246. Amsterdam: Elsevier Science B.V.

Moulinec, C. and P. Wesseling (2000). Colocated schemes for the incompressible Navier-Stokes equations on non-smooth grids for two-dimensional problems. *International Journal for Numerical Methods in Fluids 32*(3), 349–364.

Nicolaides, R. (1993). The covolume approach to computing incompressible flows. *Incompressible computational fluid dynamics- Trends and advances, Cambridge, United Kingdom and New York, Cambridge University Press*, 295–333.

Nicoud, F., J. S. Baggett, P. Moin, and W. Cabot (2001). Large Eddy Simulation wall-modeling based on suboptimal control theory and linear stochastic estimation. *Physics of Fluids 13*(10), 2968–2984.

Ninokata, H., E. Merzari, and A. Khakim (2009). Analysis of low Reynolds number turbulent flow phenomena in nuclear fuel pin subassemblies of tight lattice configuration. *Nuclear Engineering and Design 239*(5), 855 – 866. Special Edition in honor of the retirement of Professor Neil Todreas.

Nördstrom, J., K. Forsberg, C. Adamsson, and P. Eliasson (2003). Finite volume methods, unstructured meshes and strict stability for hyperbolic problems. *Applied Numerical Mathematics 45*(4), 453 – 473.

Nördstrom, J. and J. Gong (2006). A stable hybrid method for hyperbolic problems. *Journal of Computational Physics 212*(2), 436 – 453.

Novendstern, E. (1972). Turbulent flow pressure drop model for fuel rod assemblies utilizing a helical wire-wrap spacer system. *Nuclear Engineering and Design* (1), 19–27.

Papadakis, G. (2008). A novel pressure-velocity formulation and solution method for fluid-structure interaction problems. *Journal of Computational Physics 227*(6), 3383 – 3404.

Péniguel, C., I. Rupp, J. Juhel, M. Guillaud, N. Gervais, and S. Rolfo (2009). Three Dimensional Conjugated Heat Transfer Analysis in Sodium Fast Reactor Wire-Wrapped Fuel Assembly Three Dimensional Conjugated Heat Transfer Analysis in Sodium Fast Reactor Wire-Wrapped Fuel Assembly Three Dimensional Conjugated Heat Transfer Analysis in Sodium Fast Reactor Wire-Wrapped Fuel Assembly. In *Proceedings of ICAPP.*

Peric, M. (2004). Flow simulation using control volumes of arbitrary polyhedral shape. *ERCOFTAC Bulletin* (62).

Perot, B. (2000). Conservation Properties of Unstructured Staggered Mesh Schemes. *Journal of Computational Physics 159*(1), 58 – 89.

Perot, B. and R. Nallapati (2003). A moving unstructured staggered mesh method for the simulation of incompressible free-surface flows. *Journal of Computational Physics 184*(1), 192 – 214.

Pfrang, W. and D. Struwe (2007). *Assessment of Correlations for Heat Transfer to the Coolant for Heavy Liquid Metal Cooled Core Designs.* FZKA.

Piomelli, U. and E. Balaras (2002). Wall-Layer Models For Large-Eddy Simulations. *Annual review of fluid mechanics 34*(1), 349–374.

Piomelli, U., E. Balaras, H. Pasinato, K. D. Squires, and P. R. Spalart (2003). The inner-outer layer interface in large-eddy simulations with wall-layer models. *International Journal of Heat and Fluid Flow 24*(4), 538 – 550. Selected Papers from the Fifth International Conference on Engineering Turbulence Modelling and Measurements.

Piomelli, U. and J. Liu (1995). Large-Eddy Simulation of rotating channel flows using a localized dynamic model. *Physics of Fluids 7*(4), 839–848.

Pope, S. B. (2000). *Turbulent Flows.* Cambridge University Press.

Rapley, C. W. and A. D. Gosman (1986). The prediction of fully developed axial turbulent flow in rod bundles. *Nuclear Engineering and Design 97*(3), 313 – 325.

Raza, W. and K. Kim (2008). Comparative Analysis of Flow and Convective Heat Transfer between 7-Pin and 19-Pin Wire-Wrapped Fuel Assemblies. *Journal of Nuclear Science and Technology 45*(7), 653–661.

Rehme, K. (1973). Pressure drop correlations for fuel element spacers. *Nuclear Technology 17*(1), 15–23.

Rehme, K. (1992). The structure of turbulence in rod bundles and the implications on natural mixing between the subchannels. *International Journal of Heat and Mass Transfer 35*(2), 567 – 581.

Reuteler, D. (2006). The drawings of Leonardo da Vinci. World Wide Web electronic publication.

Reynolds, O. (1883). An experimental investigation of the circumstances which determine whether the motion of water shall be direct or sinuous, and of the law of resistance in parallel channels. *Philosophical Transactions of the Royal Society of London 174*, 935–982.

Reynolds, O. (1895). On the dynamical theory of incompressible viscous fluids and the determination of the criterion. *Philosophical Transactions of the Royal Society of London. A 186*, 123–164.

Rhie, C. and W. Chow (1983). Numerical study of the turbulent flow past an airfoil with trailing edge separation. *AIAA Journal(ISSN 0001-1452) 21*, 1525–1532.

Richardson, L. F. (1922). *Weather Prediction by Numerical Process.* Cambridge: Cambridge University Press.

Rolfo, S., J. C. Uribe, and D. Laurence (2010). LES and Hybrid RANS/LES of Turbulent Flow in Fuel Rod Bundle Arranged with a Triangular Array. *Direct and Large-Eddy Simulation VII*, 409–414.

Rosaguti, N. R., D. F. Fletcher, and B. S. Haynes (2006). Laminar flow and heat transfer in a periodic serpentine channel with semi-circular cross-section. *International Journal of Heat and Mass Transfer 49*(17-18), 2912 – 2923.

Rosaguti, N. R., D. F. Fletcher, and B. S. Haynes (2007). A general implementation of the H1 boundary condition in CFD simulations of heat transfer in swept passages. *International Journal of Heat and Mass Transfer 50*(9-10), 1833 – 1842.

Rowe, D. S., B. M. Johnson, and J. G. Knudsen (1974). Implications concerning rod bundle crossflow mixing based on measurements of turbulent flow structure. *International Journal of Heat and Mass Transfer 17*(3), 407 – 419.

Sagaut, P. (2001). *Large Eddy Simulation for Incompressible Flows.* Springer.

Schumann, U. (1975). Subgrid scale model for finite difference simulations of turbulent flows in plane channels and annuli. *Journal of Computational Physics 18*(4), 376 – 404.

Scotti, A., C. Meneveau, and D. K. Lilly (1993). Generalized Smagorinsky model for anisotropic grids. *Physics of Fluids A: Fluid Dynamics 5*(9), 2306–2308.

Seale, W. (1979). Turbulent diffusion of heat between connected flow passages Part 2: Predictions using the $k-\epsilon$ turbulence model. *Nuclear Engineering and Design 54*(2), 197 – 209.

Smagorinsky, J. (1963). General circulation experiments with the primitive equations: I. The basic experiment. *Mon. Wea. Rev. 91*, 99–164.

Smith, J. G., A. Tokuhiro, W. D. Pointer, and P. F. Fischer (2009). Predictions in CFD Simulations of Wire-Wrapped SFR Fuel Assemblies. In *Proceedings of ICAPP*.

Spalart, P., S. Deck, M. Shur, K. Squires, M. Strelets, and A. Travin (2006). A new version of detached-eddy simulation, resistant to ambiguous grid densities. *Theor. Comput. Fluid Dyn. 20*(3), 181–195.

Spalart, P., W. Jou, M. Strelets, and S. Allmaras (1997). Comments on the Feasibility of LES for Wings, and on a Hybrid RANS/LES Approach. In *First AFOSR International Conference on DNS/LES, in Advance in DNS/LES*, Columbus, OH. edited by C. Liu and Z. Liu, Greyden Press.

Speziale, C., S. Sarkar, and T. Gatski (1991). Modelling the pressure-strain correlation of turbulence-An invariant dynamical systems approach. *Journal of Fluid Mechanics 227*, 245–272.

Suga, K., T. Craft, and H. Iacovides (2006). An analytical wall-function for turbulent flows and heat transfer over rough walls. *International Journal of Heat and Fluid Flow 27*(5), 852–866.

Svard, M., J. Gong, and J. Nördstrom (2008). An accuracy evaluation of unstructured node-centred finite volume methods. *Applied Numerical Mathematics 58*(8), 1142 – 1158.

Temmerman, L., M. Hadziabdic, M. Leschziner, and K. Hanjalic (2005). A hybrid two-layer URANS-LES approach for large eddy simulation at high Reynolds numbers. *International Journal of Heat and Fluid Flow 26*(2), 173 – 190.

Tessicini, F., L. Temmerman, and M. Leschziner (2006). Approximate near-wall treatments based on zonal and hybrid RANS-LES methods for LES at high Reynolds numbers. *International Journal of Heat and Fluid Flow 27*(5), 789 – 799. Special issue of the 6th International Symposium on Engineering Turbulence Modelling and Measurements - ETMM6.

Thielen, L., K. Hanjalic, H. Jonker, and R. Manceau (2005). Predictions of flow and heat transfer in multiple impinging jets with an elliptic-blending second-moment closure. *International Journal of Heat and Mass Transfer 48*(8), 1583 – 1598.

Thom, A. (1933). The flow past circular cylinders at low speeds. *Proceedings of the Royal Society of London. Series A, Containing Papers of a Mathematical and Physical Character 141*(845), 651–669.

Thompson, J., B. Soni, and N. Weatherill (1999). *Handbook of grid generation.* CRC.

Tokaty, G. (1971). *A History and Philosophy of Fluid Mechanics.* New York, U.S.A.: Dover Publications.

Tritton, D. J. (1988, November). *Physical Fluid Dynamics (Oxford Science Publications)* (2 ed.). Oxford University Press, USA.

Trupp, A. and R. Azad (1975). The structure of turbulent flow in triangular array rod bundles. *Nuclear Engineering and Design 32*(1), 47 – 84.

Uijttewaal, W. S. J. and R. Booij (2000). Effects of shallowness on the development of free-surface mixing layers. *Physics of Fluids 12*(2), 392–402.

Uribe, J. C., N. Jarrin, R. Prosser, and D. Laurence (2009). Two-velocities hybrid rans-les of a trailing edge flow. *IUTAM Symposium on Unsteady Separated Flows and their Control*, 63–76.

Utriainen, E. and B. Sundén (2002, 08). A numerical investigation of primary surface rounded cross wavy ducts. *Heat and Mass Transfer 38*(7), 537–542.

Van Driest, E. R. (1956). On turbulent flow near a wall. *J. Aerosp. Sci 23*, 1007–1011.

Vasilyev, O. V. (2000). High Order Finite Difference Schemes on Non-uniform Meshes with Good Conservation Properties. *Journal of Computational Physics 157*(2), 746 – 761.

Vincenti, W. and C. Kruger (1965). *Introduction to physical gas dynamics.* New York: John Wiley and Sons.

Vonka, V. (1988a). Measurement of secondary flow vortices in a rod bundle. *Nuclear Engineering and Design 106*(2), 191 – 207.

Vonka, V. (1988b). Turbulent transports by secondary flow vortices in a rod bundle. *Nuclear Engineering and Design 106*(2), 209 – 220.

Welch, P. (1967). The use of fast Fourier transform for the estimation of power spectra: a method based on time averaging over short, modified periodograms. *IEEE Transactions on Audio and Electroacoustics 15*(2), 70–73.

Wilcox, D. C. (1993). *Turbulence Modeling for CFD.* La Cañada, CA: DCW Industries Inc.

Winckelmans, G. S., H. Jeanmart, and D. Carati (2002). On the comparison of turbulence intensities from large-eddy simulation with those from experiment or direct numerical simulation. *Physics of Fluids 14*(5), 1809–1811.

Zhang, X., D. Schmidt, and B. Perot (2002). Accuracy and Conservation Properties of a Three-Dimensional Unstructured Staggered Mesh Scheme for Fluid Dynamics. *Journal of Computational Physics 175*(2), 764 – 791.

Appendix A

RANS FORMULATION

Since the full resolution of the Navier-Stokes equations requires the consideration of a vast range of length and time scales, RANS (Reynolds Averaged Navier-Stokes) equations are used to limit the computational cost. Reynolds decomposition splits quantities into a mean component, which is time-averaged, and fluctuating term, which represents the effects of the turbulence as:

$$\begin{cases} p = \langle p \rangle + p' \\ u_i = \langle u_i \rangle + u_i' \\ \theta = \langle \theta \rangle + \theta' \end{cases} \tag{A.1}$$

The Navier-Stokes equations can be consequently rewritten as

$$\begin{cases} \dfrac{\partial \langle u_i \rangle}{\partial x_i} = s_m \\ \dfrac{\partial (\langle u_i \rangle)}{\partial t} + \dfrac{\partial \langle u_j \rangle \langle u_i \rangle}{\partial x_j} = -\dfrac{1}{\rho}\dfrac{\partial \langle p \rangle}{\partial x_i} + \dfrac{\partial}{\partial x_j}(\langle \tau_{ij} \rangle) + s_i \\ \dfrac{\partial \langle \theta \rangle}{\partial t} + \dfrac{\partial \langle u_j \rangle \langle \theta \rangle}{\partial x_j} = \dfrac{\partial}{\partial x_j}\left(\Gamma \dfrac{\partial \langle \theta \rangle}{\partial x_j} + \left\langle u_j' \theta' \right\rangle\right) \end{cases} \tag{A.2}$$

where $\langle \tau_{ij} \rangle = \nu \left(2 \langle S_{ij} \rangle - \frac{2}{3}\frac{\partial \langle u_k \rangle}{\partial x_k} \delta_{ij} \right) - \left\langle u_i' u_j' \right\rangle$. As in the LES formulation also here there is the presence of extra-terms that represent the influence of the fluctuating motion on the mean part and they are called Reynolds stresses $\left\langle u_i' u_j' \right\rangle$ and turbulent heat fluxes $\left\langle u_j' \theta' \right\rangle$. Those terms have to be related with mean quantities and in case of an eddy viscosity model and gradient diffusion hypothesis their constitutive relations are:

$$\begin{cases} -\left\langle u_i' u_j' \right\rangle = \nu_T \left[\dfrac{\partial \langle u_i \rangle}{\partial x_j} + \dfrac{\partial \langle u_j \rangle}{\partial x_i} \right] - \dfrac{2}{3} k \delta_{ij} \\ \left\langle u_j' h' \right\rangle = -\dfrac{\nu_T}{Pt_t} \dfrac{\partial \langle \theta \rangle}{\partial x_j} \end{cases} \tag{A.3}$$

where k represents the turbulent kinetic energy, ν_T is the turbulent viscosity and Pr_t is the turbulent Prandtl number.

In this chapter the $\varphi - \overline{f}$ of Laurence et al. (2005) and the $\varphi - \alpha$ of Billard et al. (2008) are described. These two models are cited several times in this work, and they are strongly connected with the Hybrid RANS-LES model of section 2.4.

A.1 Turbulence models

The $\overline{v^2} - f$ of Durbin (1991) is an interesting turbulence model that, since its appearance, has raised high attention in both academia and industry. In this model the introduction of a transport equation for normal fluctuations $\overline{v^2}$ permits to have a better modelling of the flow in the near wall region. The second peculiarity of this model is the introduction of the elliptic relaxation function f (obtained solving a Helmholtz-type elliptic equation), in order to take into account non-local effects in the pressure/strain-rate correlation. The $\overline{v^2} - f$ is a $k - \varepsilon$ based model where the transport equations for turbulent kinetic energy and for the dissipation rate are:

$$\frac{Dk}{Dt} = \mathcal{P} - \varepsilon + \frac{\partial}{\partial x_j} \left[\left(\nu + \frac{\nu_t}{\sigma_k} \right) \frac{\partial k}{\partial x_j} \right] \tag{A.4}$$

$$\frac{D\varepsilon}{Dt} = \frac{C_{\varepsilon 1} \mathcal{P} - C_{\varepsilon 2} \epsilon}{\tau} + \frac{\partial}{\partial x_j} \left[\left(\nu + \frac{\nu_t}{\sigma_\varepsilon} \right) \frac{\partial \varepsilon}{\partial x_j} \right] \tag{A.5}$$

where $\mathcal{P}$ is the production, which includes also the buoyancy part, and $\nu_t = C_\mu \varphi k T$ is the turbulent viscosity, with $\varphi = \overline{v^2}/k$. The constants depend on the model formulation and are reported in Table A.1 for the $\varphi - \overline{f}$ and Table A.2 for $\varphi - \alpha$.

Despite its phisically realistic formulation the model has some numerical drawbacks due to the stiffness of the boundary condition for the relaxation function f. The model is very sensitive to the near-wall mesh, in particular when the y^+ of the first point is very small. The problem could be avoided by coupling the solution of $\overline{v^2}$ and f, but most of the codes are segregated, in order to require less computational power. To avoid these problems alternative formulations of the $\overline{v^2}$ and f equations were proposed in Durbin (1995); F.S. Lien (1996), but with less satisfactory results in comparison with the original formulation.

The new formulations, described herein, are based on a change of variable, solving a new transport equation for $\overline{v^2}/k$ instead of the usual $\overline{v^2}$. This reformulation permits a more convenient boundary condition, because f is going to 0 at the wall with y^2 instead than y^4 of the original formulation, improving the stability of the model. The second advantage is the absence of ε in the transport equation of $\overline{v^2}/k$. Consequently it is decoupled from the dissipation equation, increasing the robustness.

A.1.1 THE $\varphi - \overline{f}$ MODELS

The model is presented in Laurence et al. (2005) and, with respect to the original formulation, presents two changes of variables:

$$\begin{cases} \varphi = \overline{v^2}/k \\ f = \overline{f} - \dfrac{2\nu\nabla\varphi\nabla k}{k} - \nu\nabla^2\varphi \end{cases} \tag{A.6}$$

The transport equations for φ and the elliptic for $\overline{f}$ are:

$$\begin{cases} \dfrac{D\varphi}{Dt} = \overline{f} + P_k\dfrac{\varphi}{k} + \dfrac{2\,\nu_t}{k\,\sigma_k}\dfrac{\partial\varphi}{\partial x_k}\dfrac{\partial k}{\partial x_k} + \dfrac{\partial}{\partial x_k}\left[\left(\nu + \dfrac{\nu_t}{\sigma_k}\right)\dfrac{\partial\varphi}{\partial x_k}\right] \\ L^2\dfrac{\partial^2\overline{f}}{\partial x_k^2} - \overline{f} = \dfrac{1}{T}(C_1 - 1)\left[\varphi - \dfrac{2}{3}\right] - C_2\dfrac{P_k}{k} - \dfrac{2\nu}{k}\dfrac{\partial\varphi}{\partial x_k}\dfrac{\partial k}{\partial x_k} - \nu\dfrac{\partial^2\varphi}{\partial x_k^2} \end{cases} \tag{A.7}$$

where $L = C_L \max\left[\min\left(\dfrac{k^{3/2}}{\varepsilon}, \dfrac{k^{3/2}}{\sqrt{6}C_\mu\overline{v^2}S}\right), C_\eta\left(\dfrac{\nu^3}{\varepsilon}\right)^{1/4}\right]$ is the turbulent length scale and $T = \max\left[\dfrac{k}{\varepsilon}, C_T\sqrt{\dfrac{\nu}{\varepsilon}}\right]$ the turbulent time scale. The boundary conditions for the models are

$$\begin{cases} k_w = 0 \\ \varepsilon_w = \lim_{y\to 0}\dfrac{2\nu k}{y^2} \\ \varphi_w = 0 \\ \overline{f_w} = 0 \end{cases} \tag{A.8}$$

and in Table A.1 are reported the coefficients used in the model. This model is used in the Hybrid RANS/LES (Sec. 2.4) for the anisotropic contribution of the modelled stresses.

C_μ	$C_{\epsilon 1}$	$C_{\epsilon 2}$	σ_ϵ	σ_k	A	C_1	C_2	C_L	C_η
0.22	$1.4\left(1+A_1\sqrt{\frac{1}{\varphi}}\right)$	1.90	1.30	1.00	0.06	3.40	1.80	0.266	100

Table A.1: Coefficients used for the Manchester $\varphi - f$

A.1.2 THE $\varphi - \alpha$ MODELS

The model is presented in Billard et al. (2008) and with respect to the $\varphi - \overline{f}$ is based on the concept of elliptic blending introduced by Thielen et al. (2005). The relaxation function f is split into two parts: a homogeneous (f_h) and a near wall (f_w). These two are blended together through the blending coefficient α inside the transport equation for φ. The elliptic equation, resolved for the coefficient α, is:

$$\begin{cases} L^2\Delta\alpha - \alpha = -1 \\ \lim\limits_{y\to 0}\alpha = 0 \end{cases} \tag{A.9}$$

Using the α blending parameter and decomposing f in homogeneous and near wall parts, the transport equation for φ becomes:

$$\begin{cases} \frac{D\varphi}{Dt} = (1-\alpha^p)\underbrace{\left[-\varphi\frac{\varepsilon}{k}\right]}_{f_w} + \alpha^p f_h - P\frac{\varphi}{k} + \frac{2}{k}\left(\frac{\nu_t}{\sigma_k} + \alpha^p\nu\right)\frac{\partial k}{\partial x_k}\frac{\partial \varphi}{\partial x_k} + \frac{\partial}{\partial x_k}\left[\left(\nu + \frac{\nu_t}{\sigma_\varphi}\right)\frac{\partial \varphi}{\partial x_k}\right] \\ f_h = -\frac{1}{T}\left(C_1 - 1 - C_2\frac{P}{\varepsilon}\right)\left(\varphi - \frac{2}{3}\right) \end{cases} \tag{A.10}$$

where the different coefficients are listed in Tables A.2, A.3 and A.4.

$C_{\varepsilon 1}$	$C_{\varepsilon 1}$	C_{A1}	$C_{\varepsilon 2}$	σ_k	σ_ε	ν_t	C_μ
$1.44\left(1 + C_{A1}(1-\alpha^p)\sqrt{\frac{1}{\varphi}}\right)$	1.44	0.04	1.83	1	1.22	$C_\mu\varphi kT$	0.22

Table A.2: Constants of the $\varphi - \alpha$ model: k and ε equations

T	C_T	L	C_L	C_η
$\max\left[\frac{k}{\varepsilon}, C_T\sqrt{\frac{\nu}{\varepsilon}}\right]$	6	$C_L\max\left[\frac{k^{3/2}}{\varepsilon}, C_\eta\left(\frac{\nu^3}{\varepsilon}\right)^{1/4}\right]$	0.161	90

Table A.3: Constants of the $\varphi - \alpha$ model: scales

C_1	C_2	σ_φ	p
1.7	1.2	1	3

Table A.4: Constants of the $\varphi - \alpha$ model: φ equation

Appendix B

CHANNEL FLOW

This appendix reports figures, which are not included into Chapter 5. Fig. B.1 dispays the results for the RR075 mesh using the commercial CFD software Star-CD. The results are similar to the ones obtained with *Code_Saturne* demonstrating that the problem of the spurious oscillation comes from the mesh strategy employed.

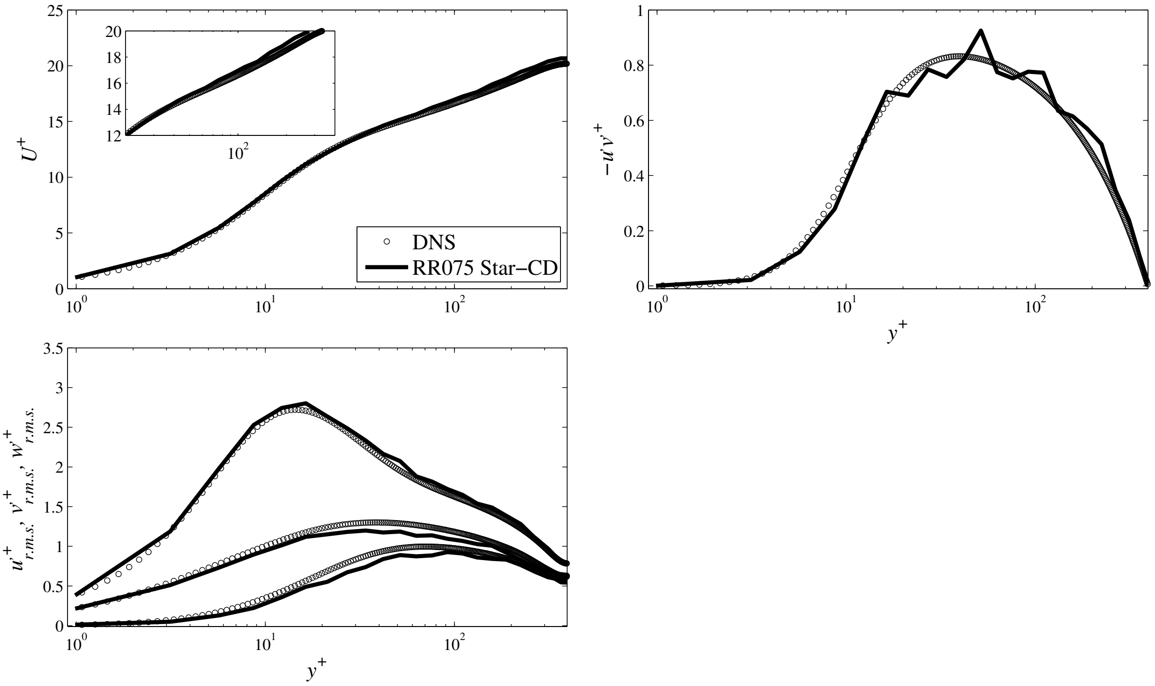

Figure B.1: LES of channel flow: verification of the spurious oscillation on the mesh RR075 with STAR-CD. Mean velocity (top left), shear stress (top right), normal stresses (bottom left) and their reduced counterparts (bottom right).

Slope test for the CD scheme.

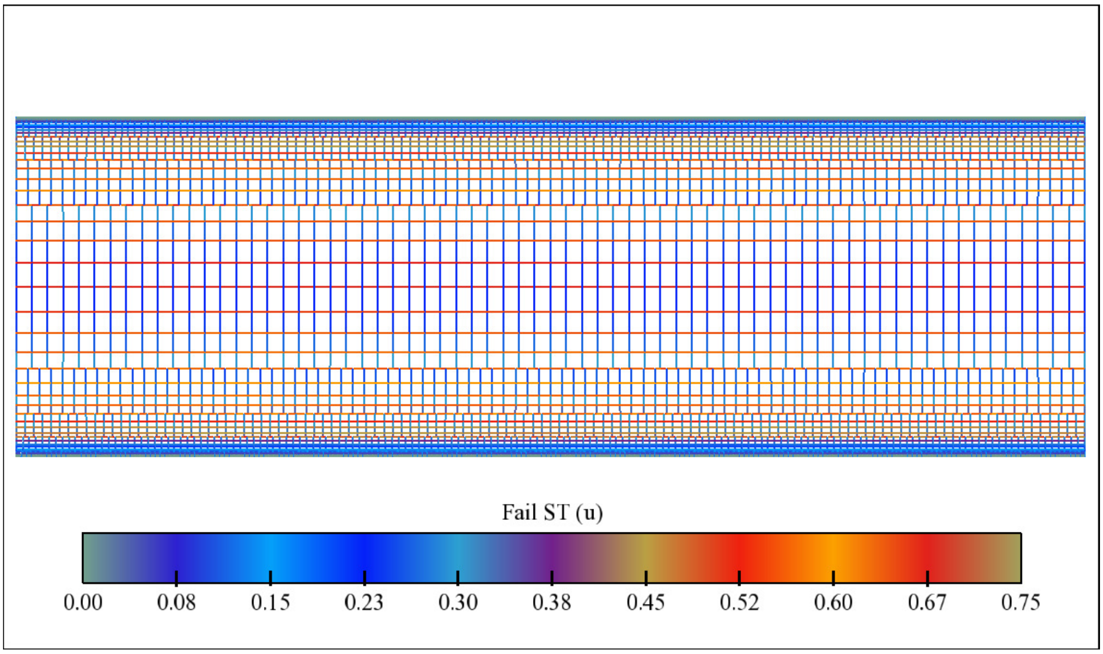

Figure B.2: Average counting of the slope test failure in the streamwise plane for the u velocity component. The cut plane is located in the middle of the domain and the average is performed over 20000 iterations ($2\,s$ of physical time). The results are plotted on the cell faces. The amount of UW is equal to 2%.

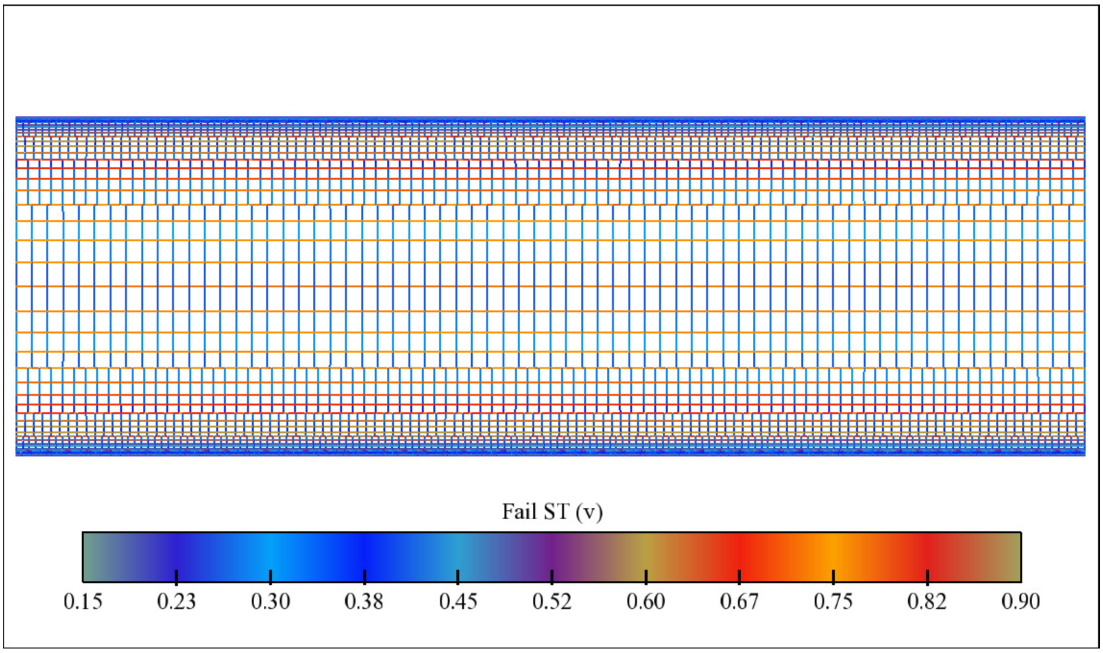

Figure B.3: Average counting of the slope test failure in the streamwise plane for the v velocity component. The cut plane is located in the middle of the domain and the average is performed over 20000 iterations ($2\,s$ of physical time). The results are plotted on the cell faces. The amount of UW is equal to 2%.

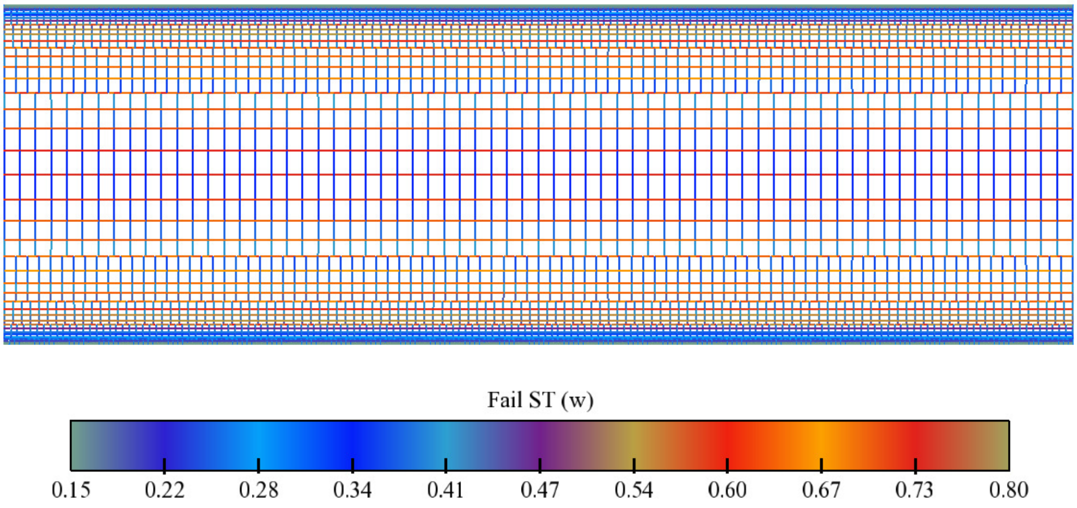

Figure B.4: Average counting of the slope test failure in the streamwise for the w velocity component. The cut plane is located in the middle of the domain and the average is performed over 20000 iterations ($2\,s$ of physical time). The results are plotted on the cell faces. The amount of UW is equal to 2%.

B.1 LES BUDGETS.

This section presents the equations used for the evaluation of budgets for the turbulent kinetic energy k and for the Reynolds stresses $\left\langle u_i' u_j' \right\rangle$. The budget for the turbulent kinetic energy k can be written as follow:

$$\begin{aligned}
\frac{Dk}{Dt} &= \underbrace{\langle u_i' u_j' \rangle \left\langle \frac{\partial u_i}{\partial x_j} \right\rangle}_{P} - \underbrace{2\nu \left\langle \frac{\partial u_i'}{\partial x_j} \frac{\partial u_j'}{\partial x_j} \right\rangle}_{\varepsilon} \\
&- \underbrace{\frac{1}{\rho} \left\langle u_i' \frac{\partial p'}{\partial x_i} \right\rangle}_{T^p} - \underbrace{\nu \left\langle \frac{\partial^2 u_i' u_j'}{\partial x_j^2} \right\rangle}_{T^\nu} - \underbrace{\left\langle \frac{\partial u_i' u_i' u_j'}{\partial x_j} \right\rangle}_{T^u} \\
&+ \underbrace{\left\langle \frac{\partial}{\partial x_k} \left(u_i \nu_t \left(\frac{\partial u_i}{\partial x_k} + \frac{\partial u_k}{\partial x_i} \right) \right) \right\rangle + \left\langle \nu_t \left(\frac{\partial u_i}{\partial x_k} + \frac{\partial u_k}{\partial x_i} \right) \frac{\partial u_i}{\partial x_k} \right\rangle}_{Model}
\end{aligned}$$

Where P is the production, ε the dissipation, T^p the velocity-pressure transfer, T^ν the transport by molecular diffusion, T^u the transport by convection. The budget contain also the contribution form the model, which is used only in the case of the fuel rod bundle (see Chapter 6). More considerations about modelling effects in conjunction with different mesh types can be found in Howard and Addad (2009). In the case of Reynolds stresses budgets becomes:

$$\begin{aligned}
\frac{D\left\langle u_i'u_j'\right\rangle}{Dt} &= \underbrace{\left\langle u_i'u_k'\right\rangle\left\langle\frac{\partial u_j}{\partial x_k}\right\rangle+\left\langle u_j'u_k'\right\rangle\left\langle\frac{\partial u_i}{\partial x_k}\right\rangle}_{P}\\
&- \underbrace{2\nu\left\langle\frac{\partial u_i'}{\partial x_k}\frac{\partial u_j'}{\partial x_k}\right\rangle}_{\varepsilon}\\
&- \underbrace{\frac{1}{\rho}\left\langle u_i'\frac{\partial p'}{\partial x_j}+u_j'\frac{\partial p'}{\partial x_i}\right\rangle}_{\Pi}+\underbrace{\nu\left\langle\frac{\partial^2 u_i'u_j'}{\partial x_k^2}\right\rangle}_{T^\nu}-\underbrace{\left\langle\frac{\partial u_i'u_j'u_k'}{\partial x_k}\right\rangle}_{T^u}
\end{aligned}$$

where Π is the velocity pressure transfer and the conventional summation on the index apply only on k. In this case the model is not considered for any test case considered in this work.

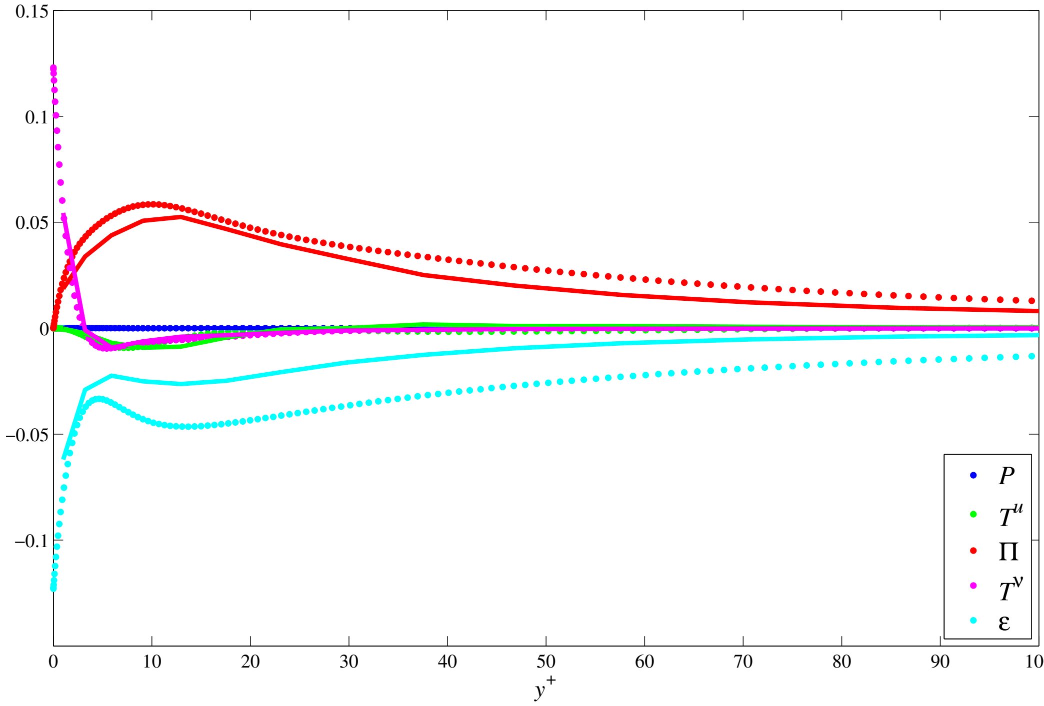

Figure B.5: Budget of $w'w'$ for the Taylor mesh: P production, T^u turbulent transport, Π velocity-pressure transfer, T^ν viscous transport, ε dissipation. Bullets points are DNS data, continuous lines LES.

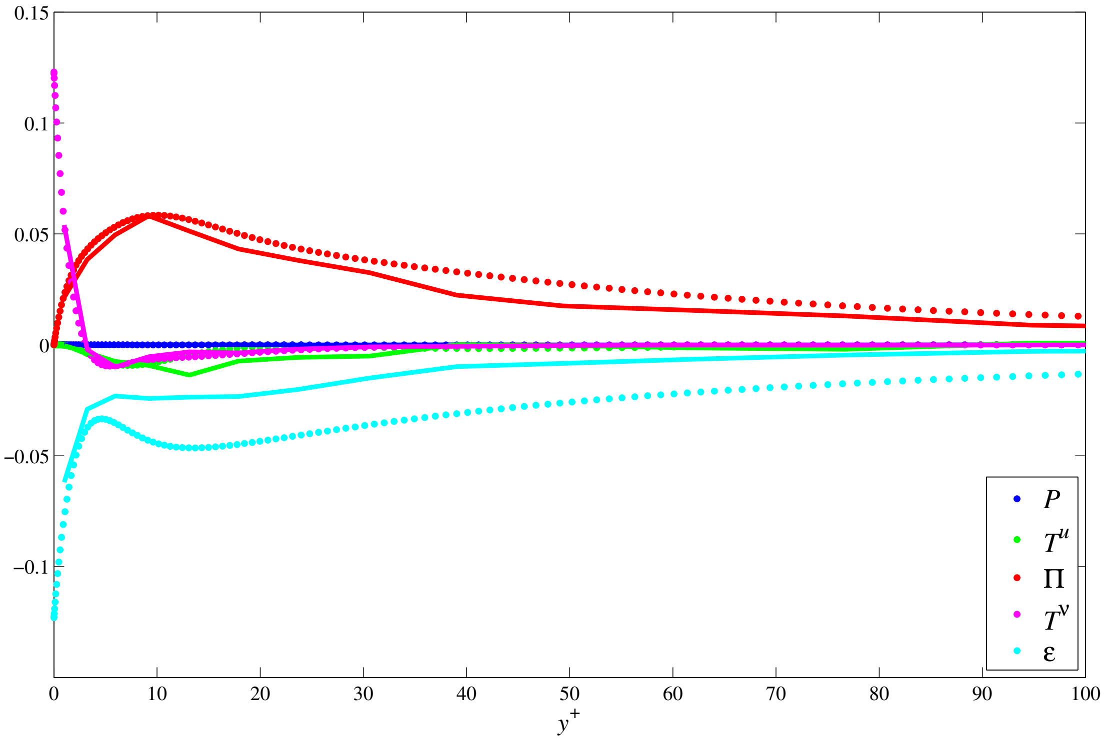

Figure B.6: Budget of $w'w'$ for the $RR075$ mesh: P production, T^u turbulent transport, Π velocity-pressure transfer, T^ν viscous transport, ε dissipation. Bullets points are DNS data, continuous lines LES.

Appendix C

FIGURES ROD BUNDLE

This chapter presents spectra at $Re = 13000$ for the fuel rod bundle test case (see Chapter 6). The spectra are confirming the observation made at low Reynolds number ($Re = 6000$), in particular the Strouhal numbers for the three dominant frequencies are 0.93, 2 and 3.

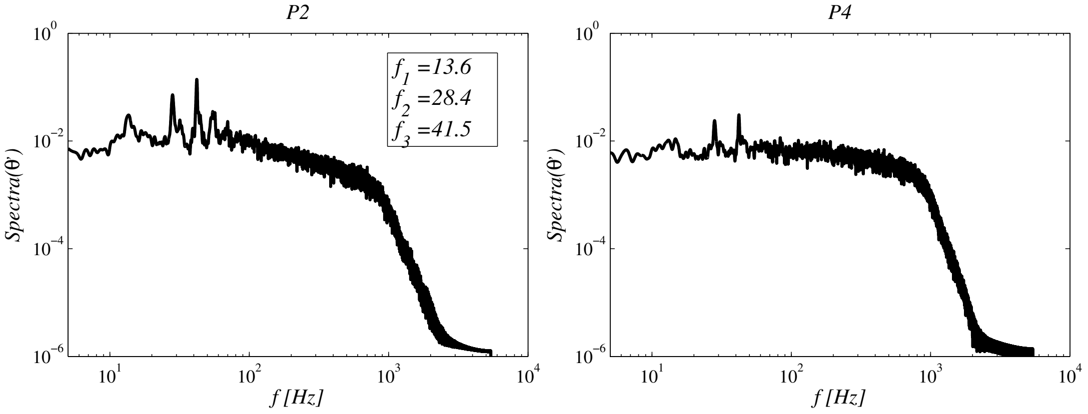

Figure C.1: Spectra of the θ' temperature fluctuations at two different locations (see figure 6.9) at $Re = 6000$. Spectra are computed with the Welch's method.

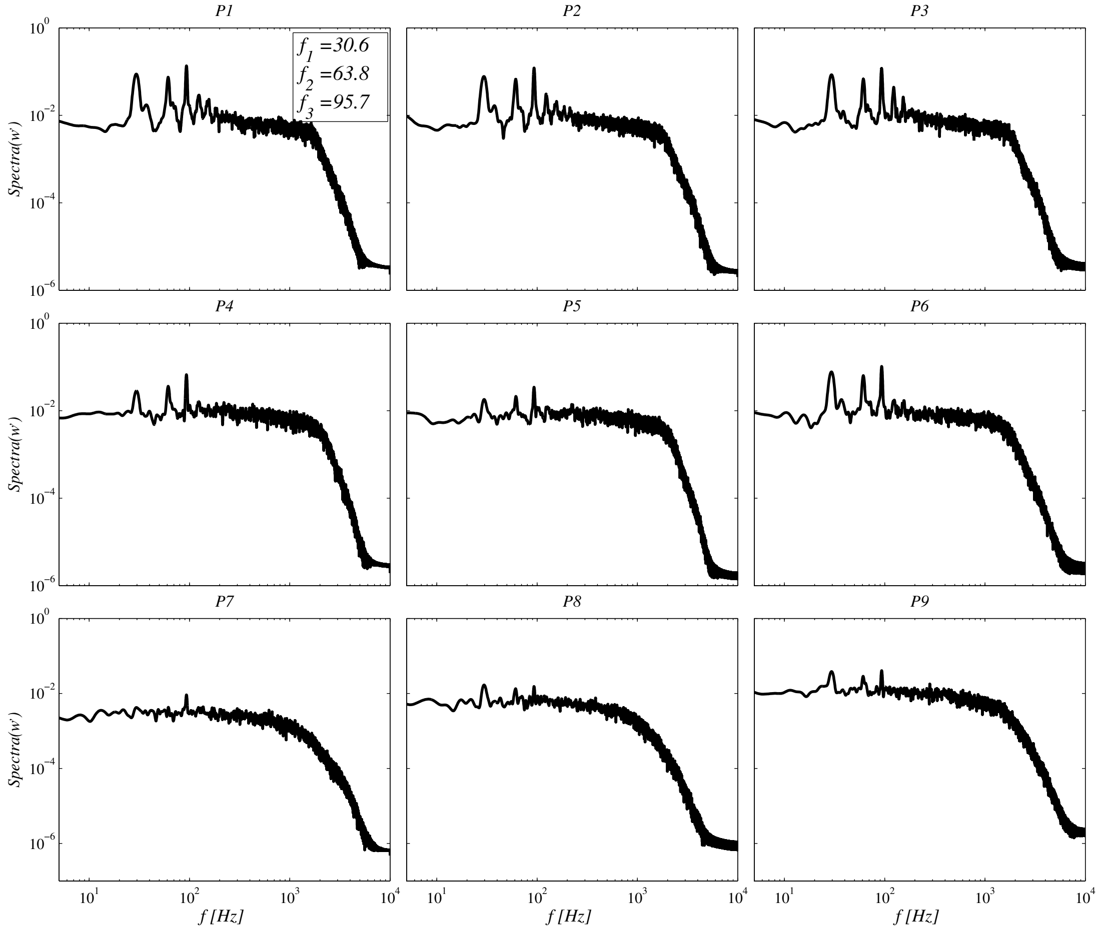

Figure C.2: Spectra of the w' velocity fluctuations at different locations (see Fig. 6.9) at $Re = 13000$. Spectra are computed with the Welch's method.

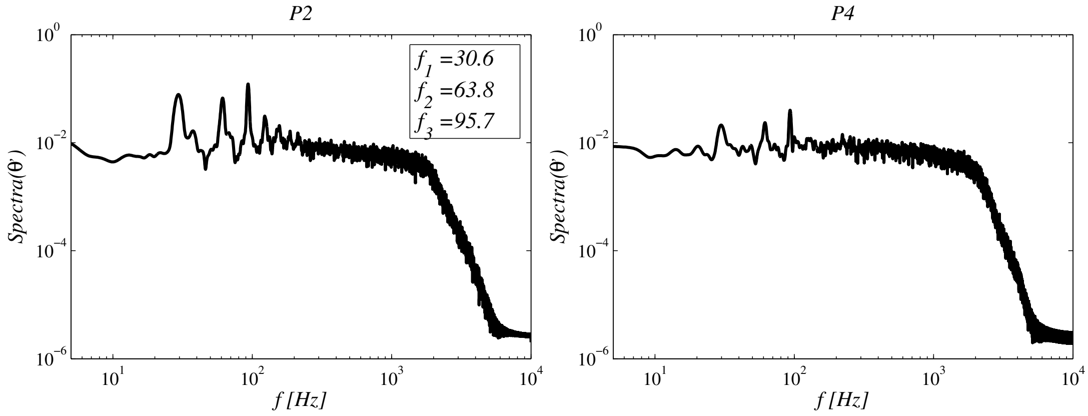

Figure C.3: Spectra of the θ' temperature fluctuations at two different locations (see Fig. 6.9) at $Re = 13000$. Spectra are computed with the Welch's method.

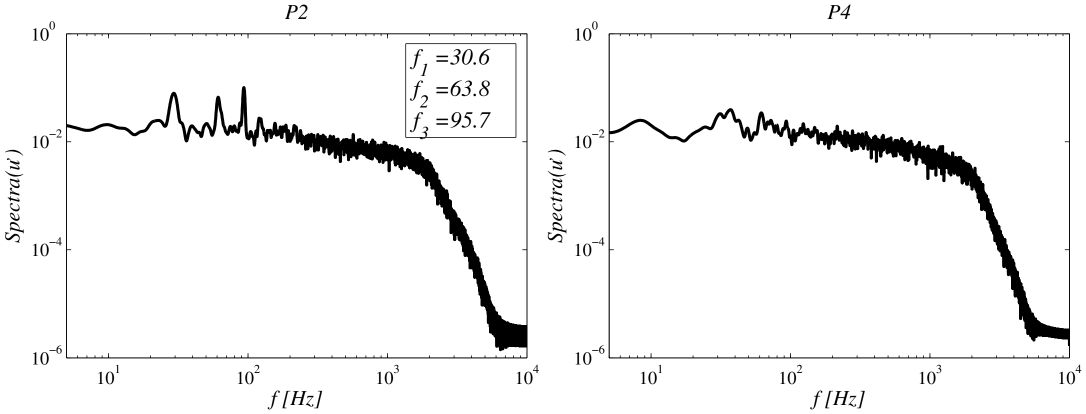

Figure C.4: Spectra of the u' velocity fluctuations at two different locations (see Fig. 6.9) at $Re = 13000$. Spectra are computed with the Welch's method.

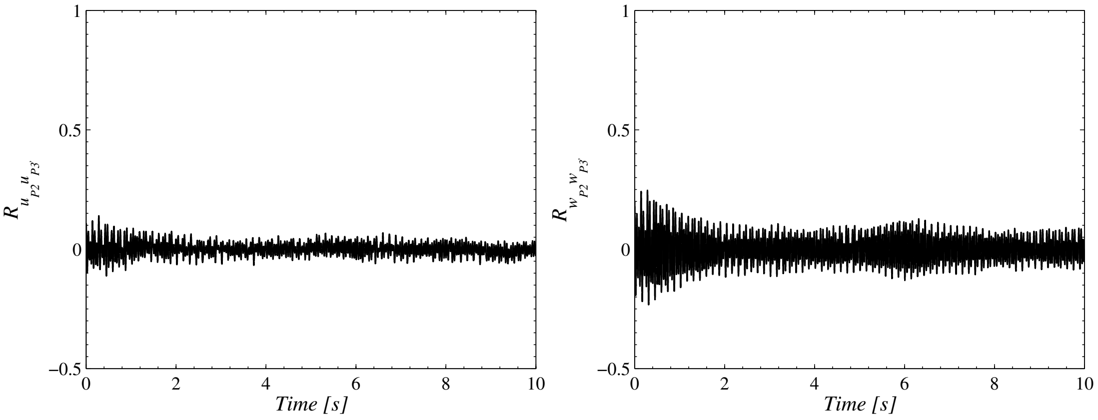

Figure C.5: Two points correlation between point $P2$ and $P3$ (see Fig. 6.9) of the u' and w' velocity fluctuations at $Re = 6000$.

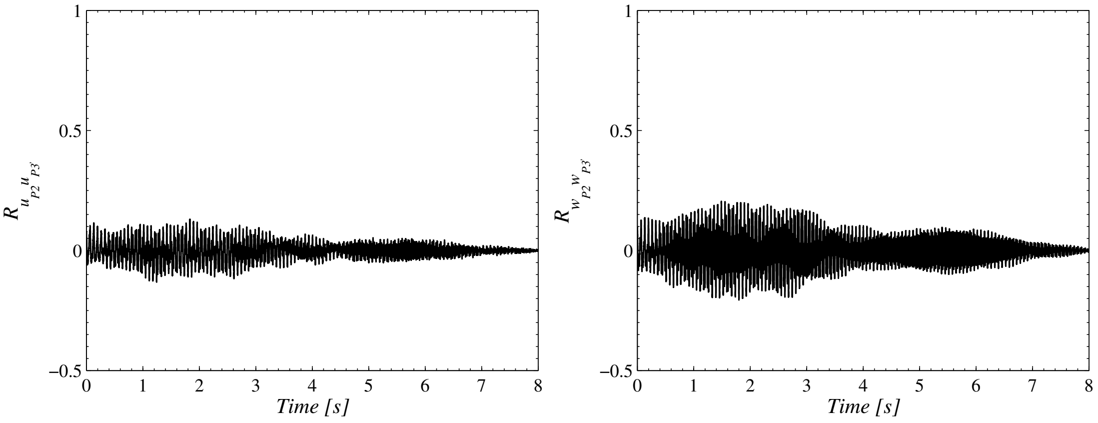

Figure C.6: Two points correlation between point $P2$ and $P3$ (see Fig. 6.9) of the u' and w' velocity fluctuations at $Re = 13000$.

Appendix D

WIRE WRAPPED FUEL ROD BUNDLE

D.1 INTRODUCTION

Fast reactors with liquid metal coolant have recently received a renewed interest due to a more efficient usage of the primary uranium resources, and they are one of the proposals for the Generation IV reactors. Fuel bundles of fast reactor are arranged into a triangular configuration and pins are wrapped with wire spacer, which follows a helical pattern around the rod axis. The primary reason of the wire is to avoid collision between adjacent pins. Moreover the presence of the wire is also reducing vibrations and avoiding the trapping of the liquid metal coolant (in general sodium). From the thermal-hydraulic point of view the wire is creating a very complex secondary motion enhancing mixing between sub-channels. From a historical point of view the effect of the wire is investigated via experimental correlations, which provide the friction factor as function of geometrical and hydraulic parameters. A first example is provided in Novendstern (1972), where the usual Blasius formula, for pipe flow, is corrected taking into account several parameters like the number and the hydraulic diameter of the different types of sub-channels of the fuel assembly. Another famous correlation is given by Rehme (1973), where a shape factor F, which takes into account the pitch-over-diameter ratio P/D and the helix-over-diameter ration H/D, is introduced. A milestone in the experimental evaluation of this type of flow is presented by Cheng and Todreas (1986), where two sets of correlations are presented. The detailed version takes into account several geometrical and different hydraulic parameters, making the correlations suitable for many configurations, but also very difficult to use. A simplified version is also presented and the two versions are converging toward the same values as the Reynolds number increases. Because the main interest of this work is toward fully turbulent, i.e. relatively high Reynolds number, only the simplified version is considered. Last correlation, which is used herein, is presented by Engel et al. (1979). In this work a modified version by Bubelis and Schikorr (2008) is used. This last work present a very large and methodical comparison of several well accepted correlations with some available experimental and numerical data. This paper is a perfect introduction of one of the key issue encountered during this work: which is the accuracy of the results? Experimental correlations have validity ranges depending on the experiments used for the definition. Pure experimental data are more reliable but very scarce. In this contest CFD can play a role in supplying a vast and very specific amount of data. An example is again present in Bubelis and Schikorr (2008) where experimental correlations are compared with RANS (Reynolds Average Navier-Stokes equations) turbulence models from Gajapathy et al. (2007). In Gajapathy et al. (2007) the CFD results are validated against correlations finding good agreement and in Bubelis and Schikorr (2008) the same correlations are validated against the CFD. Now a question is obvious: which are the data to be trusted and used as reference? A possible solution could be provided by LES and DNS as the one presented by Fischer et al. (2007). LES and DNS are able to provide a very broad and very accurate, if a proper code is used, amount of data, which can be very difficult to obtain with experimental techniques. Instantaneous flow field and extensive average results (for example Nusselt distribution along the fuel rod) will be available, making more rigorous the validation of RANS models. Because of the extremely time consuming and cost of LES and DNS (very powerful High Performing Computing, HPC, facilities are necessary), they are still limited to reduced geometry and moderate Reynolds numbers, whereas usual RANS will be devoted to the study of more industrial cases. Some RANS studies are also starting to appear like Raza and Kim (2008) and Smith et al. (2009), employing reduced geometries with a limited number of pins and results are compared with well established experimental correlations. An even more difficult task is to find heat transfer correlations for the evaluation of the Nusselt number. Several studies were conducted during the sixter and the seventer for several projects. Pfrang and Struwe (2007) presents a review of the outcome of several studies. In this work the Nusselt correlations of the EUTATOM project Graber and Rieger (1972), of Kazimi and Carelli (1976) and Mikityuk (2009) are used.

The aim of this work is firstly to investigate the ability of *Code_Saturne* to study these types of flows, underlining important parameters to take into consideration (mesh configuration, turbulence models, etc. . .). This validation is carried out using reduced geometries composed by only seven and nineteen pins with only one helix pass. Consequently periodicity is used in the streamwise direction, in order to reduce further the domain. Global results of pressure drop and global Nusselt number are compared with the previous mentioned correlations for both friction factor and Nusselt number. Two different turbulence models are used: the $k-\varepsilon$ of Jones and Launder (1972) and the second moment closure R_{ij} of Speziale et al. (1991). The wall treatment includes the use of scalable wall functions presented by Grotjans and Menter (1998) .

The mesh generation step constitutes a fairly challenging task because the wire induces a very large number of singularities in the geometry due to the fact that the wire attached to each pin is almost in contact with the surrounding pins. After several attempts with commercial mesh generators, the homemade procedure described in Péniguel et al. (2009) is followed. Several variants regarding the way to handle the connection between the wire and the pin have been investigated. It leads to an almost structured mesh with a very good control on the number of cells across two adjacent pins. Here all meshes used have at least 8 cells between two pins. Moreover only one helix pass along with periodicity in the streamwise direction in order to reduce even further the mesh size.

D.2 Flow description

The Reynolds number is varied between 5,000 and 50,000 (based on the hydraulic diameter and bulk velocity). The wall heat flux is constant and equal to $6 \cdot 10^5\, W/m^2$, which makes the Peclet number (Pe) ranging from 25 till 400. Two different helix-to-diameter ratios H/D are used, which take the value of 22 and 17. As expected, the flow field presents no symmetry in the plane perpendicular to the stream-wise direction. The presence of the wire is inducing a global swirling motion on the edge and corner sub-channels. Moreover the location of the maximum of the stream wise velocity is rotating following the pattern of the helix. In all wall channels, characterised by a high axial velocity, a large secondary vortex is also visible. It is interesting to notice that the wall sub-channel, characterised by the large bulk velocity, has also the maximum of the swirl flow velocity. On the opposite wall sub-channels, with low velocity, do not have a clear secondary motion structure. Central sub-channels are characterised by a secondary vortex for all wire angles. For those sub-channels the unbalance of the stream-wise velocity, typical of the wall sub-channels, does not appear clearly. Figure D.1 presents the comparison between mean streamwise direction velocity and secondary motion for the two turbulence models. Both flows look very similar even in their quantitative comparison. This could lead us to the wrong conclusion that the turbulence model has a minor effect on the results. As a matter of fact, if the shear velocity u_τ is compared (Fig. D.2), the two models are showing a substantial difference, making the estimation of the pressure drop relatively different.

The variation of the helix pass has a great influence on the solution as can be appreciated in Fig. D.3, where results are obtained using a $k - \varepsilon$ model. The helix-to-diameter ratio $H/D = 22$ correspond to a new design, whereas $H/D = 17$ corresponds to the old design used in the SuperPhenix reactor. The flow features are still the same, but a higher velocity and a stronger secondary motion can be appreciated. If now the $k - \varepsilon$ is compared with the second moment closure R_{ij}, a large difference can be appreciated (Fig. D.3 on the right). The $k-\varepsilon$ model is giving an almost 20% underestimation of the maximum axial velocity with respect to the R_{ij}, and also the secondary motion is weaker.

As the number of pin increases the flow does not change, as can be established from Fig D.4 (on the left). It is interesting, however, to notice that as the pins number increases the edge and corner sub-channels start to loose their predominance and the flow field is more homogeneous.

The temperature field has also a very complex pattern as can be seen from Fig. D.4 (on the right). On the fuel rod surfaces a simplified boundary condition (constant temperature) is imposed (Dirichlet BC), whereas walls of the external case are adiabatic (Neumann BC with wall normal gradient equal to zero). In reality of course only the pin itself contains fuel and therefore heat deposit. Also in this case the field can be divided into central and side sub-channels. The first-ones are characterised by higher temperatures and in particular in the gap region between two adjacent pins and by a relatively uniform temperature distribution. Side channels are more influenced by the location of the streamwise velocity maximum, which corresponds to the temperature minimum. The influence of the turbulence model, in the heat transfer is very limited, probably due to the use of scalable wall functions.

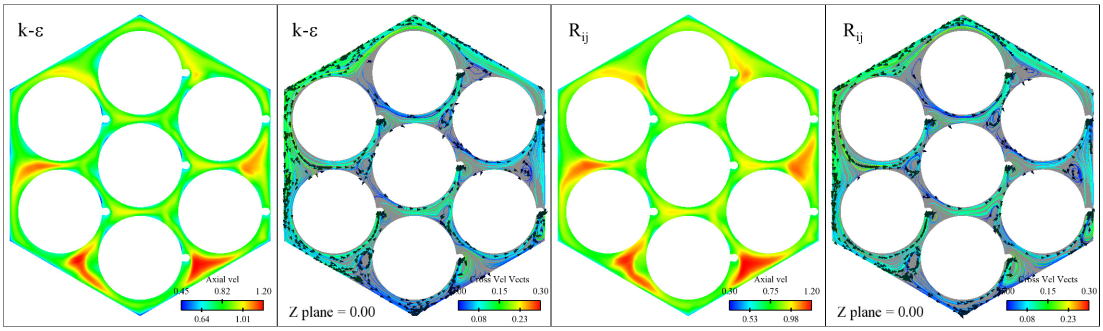

Figure D.1: Comparison of the streamwise velocity and secondary motion between $k-\varepsilon$ (left) and R_{ij} (right) turbulence models for the SFR fuel rod bundle with seven pins. P/D = 1.1, H/D = 21 and $Re = 10000$.

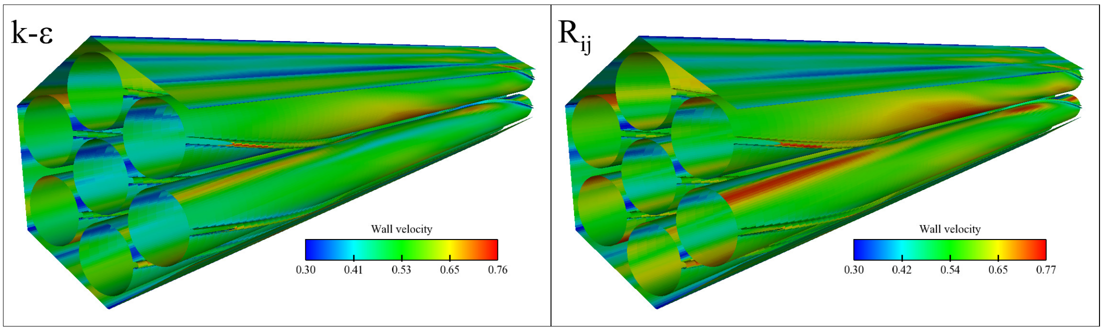

Figure D.2: Comparison of the wall velocity between $k-\varepsilon$ (left) and R_{ij} (right) turbulence models for the SFR fuel rod bundle with seven pins. P/D = 1.1, H/D = 21 and $Re = 10000$.

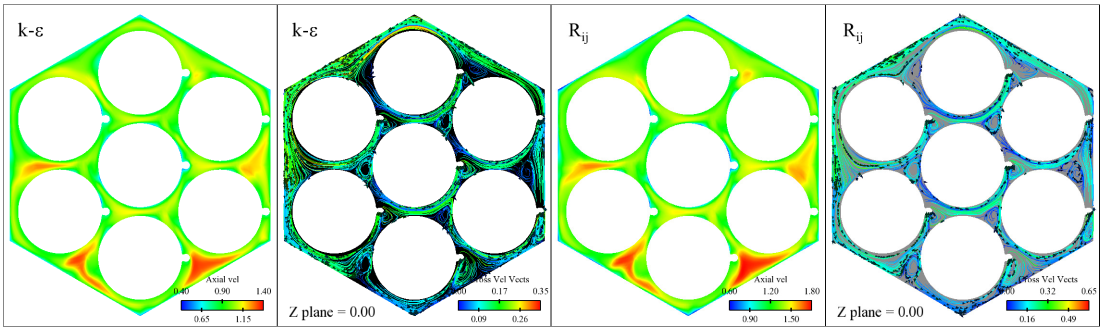

Figure D.3: Comparison of the streamwise velocity and secondary motion between $k-\varepsilon$ (left) and R_{ij} (right) turbulence models for the SFR fuel rod bundle with seven pins. P/D = 1.1, H/D = 17 and $Re = 10000$.

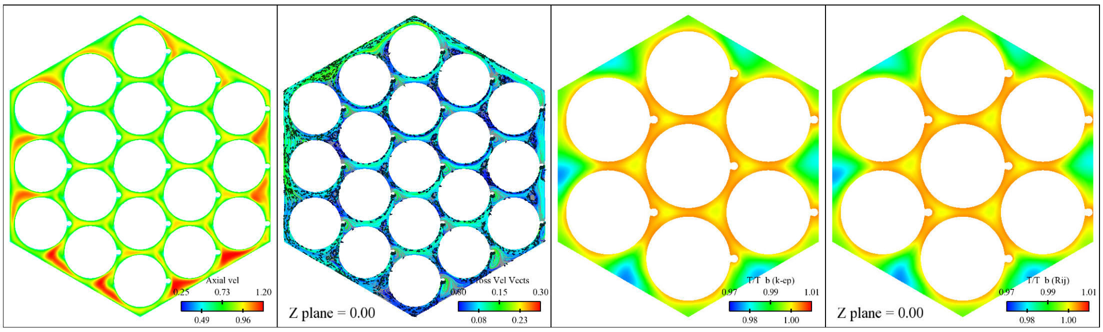

Figure D.4: Left: streamwise velocity and secondary motion for the nineteen pins configuration (R_{ij} turbulence models. $P/D = 1.1$, $H/D = 17$ and $Re = 10000$). Right: Comparison of temperature fields between $k-\varepsilon$ (left) and R_{ij} (right) turbulence models ($P/D = 1.1$, $H/D = 17$ and $Pe = 55$).

D.2.1 Friction factor and Nusselt profiles

In order to compare the results with available and well-accepted correlations, global parameters have to be evaluated. The friction factor f is defined as:

$$f = \Delta p \frac{D_h}{L_z} \frac{2}{\rho U_B^2} \tag{D.1}$$

where D_h is the hydraulic diameter, L_z the periodic length in the streamwise direction, U_B the bulk velocity and Δp the pressure drop. The evaluation of the pressure drop is very sensitive because several options are available and the results can vary considerably. For example the pressure drop can be evaluated from the wall shear as:

$$\Delta p = \frac{\tau_w}{S_{w,TOT}} \tag{D.2}$$

being τ_w the wall shear and $S_{w,TOT}$ the total wall surface. The wall shear can be estimated from the friction velocity given by the wall function as:

$$\tau_w = \sum_{i}^{wall\,faces} \rho u_\tau^2 (i) \, S_w (i) \tag{D.3}$$

where u_τ is the shear velocity at the wall, which is evaluated directly from the wall function as:

$$u_\tau (i) = \frac{u_{I'} (i)}{\frac{\ln y^+}{\kappa} + C} \tag{D.4}$$

with I' being the intersection between the wall normal direction through the wall face centre F and the projection of the cell centre on that line. κ and C are two constants equal to 0.42 and 5.2 respectively. The wall dimensionless distance is evaluated from a turbulent velocity $u_k = C_\mu \sqrt{k}$ as:

$$y^+ = \frac{d u_k}{\nu} \tag{D.5}$$

where d is the distance between I' and F and . Another possibility could be to use the imposed pressure drop used in the streamwise direction, which is equal to:

$$\Delta p = \beta L_z \tag{D.6}$$

with $\beta = \partial p / \partial x_3$ and x_3 the main flow direction. In the first case also pressure redistribution on the cross section is taken into account, whereas in the latter not. Values are relatively different, in particular at low Reynolds numbers, as can be seen in Fig. D.5 (left) for the seven pins bundle and in Fig. D.6 for the nineteen. The method of Eq. (D.2) is labeled as $\sum \rho u_\tau^2 S_w$, whereas the one of Eq. (D.6) as QDM.

In general the Reynolds stress model is giving higher value of f with respect to the eddy viscosity model, but values tend to converge as the Reynolds number increases. Indeed the same effect can be seen as the number of pins increase because of the lesser importance of edge channels on the global flow field. The data are in the range given by the experimental correlations and they seem to agree better with the one of Cheng and Todreas (1986).

The Nusselt number is instead evaluated as:

$$Nu = \frac{q_w}{(T_w - T_B)} \frac{D_h}{c_p \Gamma} \tag{D.7}$$

The comparison against the experimental correlation is plotted in Fig. D.5 (right) for the seven pins configuration. In this case the difference between the two turbulence models is almost negligible, but slightly increase with the Peclet number. The reason could be the wall treatment; consequently more accurate modelling is required. It is interesting to notice that CFD profiles are increasing with a relatively steep slope. On the other hand the experimental correlations have almost the same, and not very rapid, rate of increase, although they have different starting points.

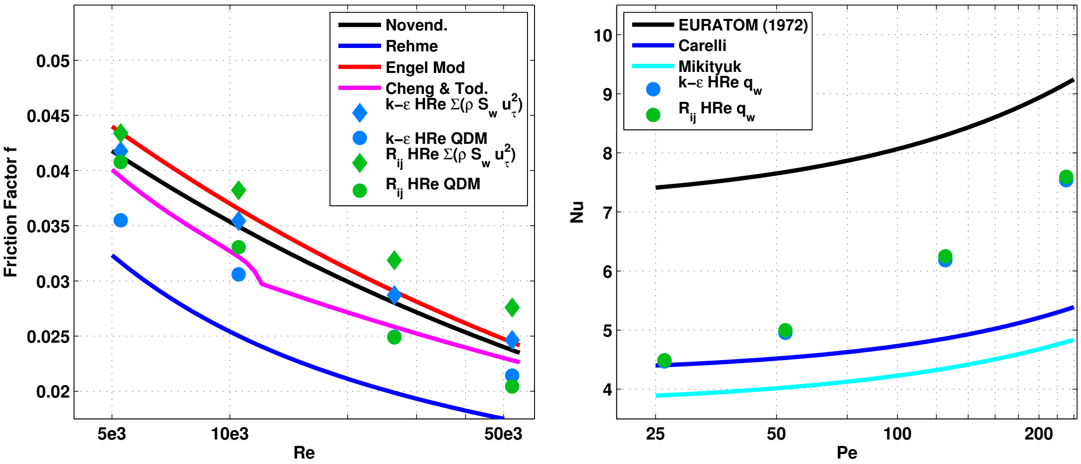

Figure D.5: Profiles of the friction factor f and Nusselt number Nu for the seven pins configuration. The friction factor is evaluated with two different approaches according to Eqs. (D.3) and (D.6).

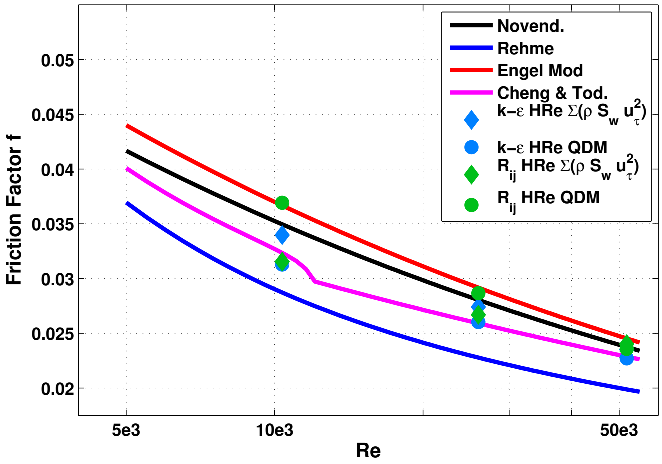

Figure D.6: Profiles of the friction factor f for the nineteen pins configuration. The friction factor is evaluated with two different approaches according to Eqs. (D.3) and (D.6).

D.2.2 Effect of the mesh configuration

Despite the fact that the geometry can be described using few geometrical parameters, the mock-up is very difficult to mesh as described in Péniguel et al. (2009). The wire is introducing many singularities that are skewing the mesh. Now an obvious question arises: with which grade of accuracy the mesh has to reproduce the geometry? Can a simplified geometry produce the same flow features and accurate global flow parameters?. An easy way to improve the orthogonality is to blend the wire with the relative pin creating what is shown in Fig. D.7 (a). A more accurate solution is to hybrid hexahedral and prism with triangular base around the wire obtaining a better geometrical description (D.7 (b)). Figs. D.7 (c) and (d) show a visual comparison between the blended and the triangular (around the wire) meshes. The flow features seems very similar, the triangular mesh is only showing very low velocities at the tips of the wire, whereas these areas are chopped out in the blended mesh. Table D.1, that reports the value of the friction factor f for the different meshes and the percentage difference with respect to the base mesh, also confirms this fact. However this conclusion is valid mainly for hydrodynamic aspects. It is likely that the better geometric definition of the wire can have a major role in the heat transfer.

Mesh Type	fric. factor f (Eq. (D.1))	Variation [%]
Base	$0.287 \cdot 10^{-1}$	0.00
Base R_{ij}	$0.319 \cdot 10^{-1}$	11.1
Triangular	$0.283 \cdot 10^{-1}$	1.39
Blended	$0.274 \cdot 10^{-1}$	4.53

Table D.1: SFR test case: comparison of friction factor f for different mesh at $Re = 25,000$ using $k - \varepsilon$.

D.2.3 Conclusions

In this chapter thermal-hydraulic of wire wrapped fuel bundle is investigated. Two different configurations, with seven and nineteen fuel rods, are taken into account, finding that the main flow features remain unchanged as the number of pins increase. Two different turbulence models were tested finding good agreement with experimental correlations. On the other hand the evaluation of the heat transfer requires more investigation. Experimental correlations for Nusselt number are largely scattered, making difficult the assessment of the CFD. Indeed the wall modelling for the heat transfer is only fist order accurate, which can make quite dubious the Nusselt evaluation. Better modelling employing low Reynolds models could be required and comparison with high Reynolds approach is on going. Another solution to the problem, which can avoid the use of refined mesh in the near wall region, could be the use of more advance wall functions as the one presented by Suga et al. (2006). As the number of pins increase the influence of side and corner sub-channels is becoming less important and flow is more homogeneous as is clearly suggested by the 19 pins configuration. In general it was difficult to find data to compare with. In this context refined LES and DNS could play an important role providing a large and reliable dataset for RANS modelling evaluation.

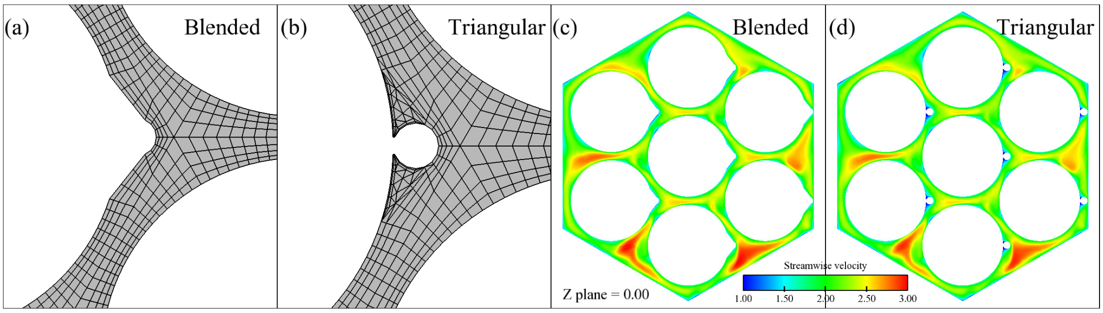

Figure D.7: Comparison between the blended mesh and the Triangular mesh for the SFR test case: (a) Blended mesh; (b) Triangular mesh; (c) Streamwise velocity blended mesh; (c) Streamwise velocity triangular mesh.